ANL-7775
RETURN TO ANL (IDAHO) LIBRARY.

775

ANL-7775

EMICAL ENGINEERING
VISION

NUAL REPORT
70

U of C-AUA-USAEC

ARGONNE NATIONAL LABORATORY, ARGONNE, ILLINOIS

The facilities of Argonne National Laboratory are owned by the United States Government. Under the terms of a contract (W-31-109-Eng-38) between the U. S. Atomic Energy Commission, Argonne Universities Association and The University of Chicago, the University employs the staff and operates the Laboratory in accordance with policies and programs formulated, approved and reviewed by the Association.

MEMBERS OF ARGONNE UNIVERSITIES ASSOCIATION

The University of Arizona
Carnegie-Mellon University
Case Western Reserve University
The University of Chicago
University of Cincinnati
Illinois Institute of Technology
University of Illinois
Indiana University
Iowa State University
The University of Iowa
Kansas State University
The University of Kansas
Loyola University
Marquette University
Michigan State University
The University of Michigan
University of Minnesota
University of Missouri
Northwestern University
University of Notre Dame
The Ohio State University
Ohio University
The Pennsylvania State University
Purdue University
Saint Louis University
Southern Illinois University
The University of Texas at Austin
Washington University
Wayne State University
The University of Wisconsin

NOTICE

This report was prepared as an account of work sponsored by the United States Government. Neither the United States nor the United States Atomic Energy Commission, nor any of their employees, nor any of their contractors, subcontractors, or their employees, makes any warranty, express or implied, or assumes any legal liability or responsibility for the accuracy, completeness or usefulness of any information, apparatus, product or process disclosed, or represents that its use would not infringe privately-owned rights.

Printed in the United States of America
Available from
National Technical Information Service
U.S. Department of Commerce
5285 Port Royal Road
Springfield, Virginia 22151
Price: Printed Copy $3.00; Microfiche $0.95

ANL-7775
General

ARGONNE NATIONAL LABORATORY
9700 South Cass Avenue
Argonne, Illinois 60439

CHEMICAL ENGINEERING DIVISION ANNUAL REPORT–1970

R. C. Vogel, Division Director
L. Burris, Associate Division Director
A. D. Tevebaugh, Associate Division Director
D. S. Webster, Associate Division Director
E. R. Proud, Assistant Division Director
J. Royal

April 1971

Preceding Annual Report:
ANL-7675 January–December 1969

TABLE OF CONTENTS

ABSTRACT . . . 1

SUMMARY . . . 1

I. FUEL CYCLE TECHNOLOGY . . . 15
A. Liquid Metal Decladding of Reactor Fuels . . . 15
1. Plant Concept Study . . . 15
2. Engineering Development–Decladding Kinetics . . . 17
3. Engineering-Scale Experiments . . . 19
4. Control of Fission-Product Iodine in a Pyrochemical Head-End . . . 21

B. CONTINUOUS CONVERSION OF U/PU NITRATES TO OXIDES . . . 22
1. Laboratory Program . . . 23
2. Engineering Program . . . 24

C. IN-LINE ANALYSIS IN FUEL FABRICATION . . . 26
1. Fuel Properties . . . 26
2. Procedure and Results . . . 27
3. Conclusions . . . 32

D. ADAPTATION OF CENTRIFUGAL CONTACTORS IN LMFBR FUEL PROCESSING . . . 32
1. Design of Centrifugal Contactor . . . 32
2. Testing Program . . . 33
3. Alternative Contactor Design . . . 33
4. Tests with Annular Contactor . . . 34

REFERENCES AND FOOTNOTES . . . 34

II. SODIUM TECHNOLOGY . . . 37
A. SODIUM CHEMISTRY . . . 37
1. Characterization of Oxygen- and Hydrogen-Bearing Species in Sodium . . . 37
2. Characterizaton of Carbon- and Nitrogen-Bearing Species in Sodium . . . 39
3. Solubility of Xenon in Liquid Sodium . . . 40
4. Development of a Process for Continuous Removal of Radioactive Contaminants from Liquid Sodium . . . 42

B. ANALYTICAL STANDARDS PROGRAM . . . 43
1. Analytical Standards Laboratory . . . 43
2. Analytical Development . . . 46

C. MONITORING OF SODIUM PURITY AND SODIUM PURIFICATION . . . 48
1. National Meter Program . . . 48
2. Direct Measurement of Chemical Activities of Impurities . . . 48
3. Oxygen Meter . . . 49
4. Carbon Meter . . . 51
5. Hydrogen Meter . . . 53
6. Detection of Leaks in Steam Generators . . . 54
7. Characterization of Cold-Trapped Sodium . . . 55

D. FISSION PRODUCT AND COVER GAS TECHNOLOGY . . . 56
1. Failed Element Detection and Location (FEDAL) Systems . . . 56
2. Radioactive Repair Engineering . . . 59
3. Nature and Control of Sodium Aerosol . . . 60

REFERENCES AND FOOTNOTES . . . 62

III. **MATERIALS CHEMISTRY AND THERMODYNAMICS** . . . 64
A. HIGH-TEMPERATURE THERMODYNAMIC STUDIES . . . 64
1. Volatilization Studies of Uranium-Plutonium Oxides by Mass Spectrometry . . . 64
2. U-Pu-O and Na-U-Pu-O Phase Studies . . . 66
3. Studies of the U-Pu-O System Containing Fission Products . . . 68
4. Thermodynamics of Carbide Fuels: Transpiration Studies of U-Pu-C System . . . 69

B. REACTOR SAFETY AND PHYSICAL PROPERTY STUDIES . . . 71
1. Enthalpies and Heat Capacities by Drop Calorimetry . . . 72
2. Vapor Pressure Over UO_2 at High Temperatures . . . 74
3. Matrix-Isolation Spectroscopy of UO_2 . . . 75
4. Speed of Sound in Molten Reactor Materials . . . 75
5. Theoretical Extrapolation of Measured Physical Property Data to Higher Temperatures . . . 77
6. Thermal Diffusivity of Reactor Materials: Liquid UO_2 . . . 77
7. Reactor Materials-Fuel Phase Studies at High Temperatures: Distribution of Fission Products Among Molten Fuel and Reactor Material Phases . . . 78

C. CALORIMETRY . . . 79
1. Thermochemistry of Plutonium Compounds . . . 79
2. Thermochemistry of Hydrogen Fluoride . . . 80
3. Enthalpies of Formation of Disodium and Monosodium Acetylides . . . 82
4. The Thermochemistry of Na_3UO_4 and Na_2O . . . 83
5. Enthalpy of Formation of Molybdenum Disulfide . . . 83
6. Enthalpy of Formation of Xenon Hexafluoride . . . 83
7. Quantum Chemical Investigations of Selected Nonmetal Monofluorides . . . 83

REFERENCES AND FOOTNOTES . . . 85

IV. **REACTOR AND ANALYTICAL CHEMISTRY** . . . 87
A. CHEMISTRY OF IRRADIATED FAST-REACTOR FUELS AND MATERIALS . . . 87
1. Fuel Analysis Techniques . . . 87
2. Electron Microprobe Analysis of Irradiated Fuels . . . 89

B. FAST-REACTOR CROSS-SECTION MEASUREMENTS . . . 95
1. Spectrum-Averaged Measurements . . . 96
2. Low-Mass Fast-Neutron Fission Yields . . . 98
3. Dosimetry Characterization of a Fast-Neutron Irradiation Environment . . . 98

C. DETERMINATION OF BURNUP OF FAST REACTOR FUELS . . . 99
1. Long-Term Irradiation in EBR-II . . . 99
2. Determination of Fast Fission Yields . . . 99

REFERENCES AND FOOTNOTES . . . 102

V. **CHEMISTRY OF LIQUID METALS AND MOLTEN SALTS** . . . 103
A. LIQUID METAL STUDIES . . . 103
1. Thermodynamics . . . 103
2. Transport Properties . . . 112

B. MOLTEN SALT STUDIES . . . 118
1. Thermodynamics . . . 118
2. Structure Investigations by Spectroscopic Methods . . . 125

C. ENERGY CONVERSION . . . 128
1. High-Specific-Energy Lithium/Selenium Batteries for Implantation . . . 128
2. High-Specific-Power Lithium/Selenium Cells for Vehicle Propulsion . . . 134
3. High-Specific-Energy Lithium/Sulfur Cells for Electric Vehicles . . . 140

REFERENCES AND FOOTNOTES . . . 148

VI. NUCLEAR SAFEGUARDS STUDY . . . 151

REFERENCES AND FOOTNOTES . . . 151

VII. FLUIDIZATION PROCESSES . . . 152
A. FLUIDIZED-BED COMBUSTION OF FOSSIL FUELS . . . 152
1. Bench-Scale Investigations . . . 152
2. Recycle of Elutriated Solids . . . 154
3. Removal of Nitrogen Oxides . . . 155
4. Removal of Added SO_2 in Natural Gas Combustion Experiments . . . 155
5. Electron Microprobe Examination of Particle Composition . . . 155
6. Desorption of SO_2 from Sulfated Limestone . . . 156
7. Relationship of SO_2 Removal to Design of Bench-Scale Equipment . . . 156
8. Modeling Study on Coal Feeding . . . 156

B. BASIC MECHANISMS OF FLUIDIZATION . . . 156
1. Fluid Dynamics for a Bubble Rising in a Finite Two-Dimensional Fluidized Bed . . . 157
2. Basic Mechanisms of Fluidized-Bed Heat Transfer . . . 157

REFERENCES AND FOOTNOTES . . . 158

CHEMICAL ENGINEERING DIVISION
ANNUAL REPORT–1970

ABSTRACT

During 1970, the research and development programs of Argonne's Chemical Engineering Division consisted of the following: (1) Fuel cycle investigations were carried out. These included liquid-metal decladding as a head-end process for LMFBR fuel, laboratory and pilot-scale work on the conversion of uranium and plutonium nitrates to oxides, development work on a centrifugal contactor for aqueous processing of LMFBR fuels, and studies of analytical procedures adaptable to in-line use in the fabrication of LMFBR fuels. (2) Work in sodium technology included studies of the chemical behavior of nonmetallic impurities in sodium, the establishment of a national program to coordinate sampling and analytical methods for determining impurities in sodium and cover gas, establishment of a national program to provide meters for monitoring levels of nonmetallic impurities in operating sodium systems and methods for detecting fuel element failure. (3) High-temperature thermodynamic and physical properties studies continued on fuels and materials of interest for LMFBRs. Studies of the U-Pu-O, Na-U-Pu-O, and U-Pu-C systems were carried out, with special emphasis being placed on the sodium-fuel interaction. High-temperature physical-property data needed for FBR safety analysis were obtained. Calorimetric studies were made of substances of interest in nuclear technology. (4) In studies of the chemical behavior of fast-reactor fuels, principal efforts were directed toward electron microprobe analysis of irradiated plutonium-uranium oxide fuel. Studies were made of fuel-cladding interactions, fission-product distribution, and oxygen gradients in irradiated mixed-oxide fuels. (5) Measurements of nuclear cross sections and fission yields for materials of interest to the FBR program continued. (6) The chemistry and thermodynamics of liquid metals and molten salts continued as important areas of studies. Thermodynamic and phase equilibrium studies of chalcogen-containing systems were carried out. Theoretical studies of gas solubilities in liquid metals were made. Transport properties of sulfur-containing systems were studied, and the surface diffusivity of iron in liquid sodium was investigated. Raman spectroscopy was used to study phosphorus-chalcogen compounds, the iodate ion, and divalent metal ions. (7) Major efforts continued to be directed toward the development of liquid metal/chalcogen secondary electrical batteries for vehicle propulsion and for powering an artificial heart. (8) A study of nuclear safeguards was undertaken to promote the accountability and protection of nuclear material. (9) Investigation continued on the combustion of fossil fuels in a fluidized bed as a means of reducing atmospheric pollutants.

SUMMARY

I. FUEL CYCLE TECHNOLOGY (pages 15 to 36)

LIQUID METAL DECLADDING OF REACTOR FUELS

The fuel elements used in the first commercial breeder reactors are expected to consist of pellets of uranium-plutonium oxide fuel contained in stainless steel tubes (cladding) that will be welded shut at both ends. Bundles of these tubes, each contained in a shroud and end fittings, will be inserted into and removed from reactors.

A head-end process for preparing discharged LMFBR fuel for solvent extraction must meet the following special requirements: The high radioactivity of this fuel dictates that it be processed inside thick-walled process cells. Its high heat-generation rate necessitates adequate heat removal throughout the purification process. Yet another requirement is that radioactive gases released when the fuel cladding is breached be disposed of safely–for example, by

containment and storage. A liquid-metal procedure is being investigated as a head-end process for stainless steel-clad oxide fuel. This procedure involves separating the stainless steel cladding from the uranium-plutonium oxide fuel by dissolving the cladding in molten zinc at 800°C, then chemically reducing the uranium-plutonium oxide to metal with magnesium-zinc-calcium at 800°C for subsequent dissolution in nitric acid.

Before a zinc decladding process can be used in a commercial fuel reprocessing plant, (1) remotely operable equipment must be designed that can accomplish the process steps inside a shielded cell, (2) stainless steel decladding rates must be determined so that process vessels can be correctly sized for a desired throughput, (3) techniques and equipment must be designed that can accomplish separation of a stainless steel-zinc melt from solid pieces of uranium-plutonium oxide, (4) the decladding procedure and equipment must be designed so that zinc splashing is avoided when fission gases escape from fuel elements during decladding, and (5) a procedure must be developed to capture the volatile radioiodine released.

Plant Concept Studies

A conceptual head-end plant processing 5 metric tons/day of LMFBR fuel has been designed for zinc decladding followed by reduction of fuel oxides to metal. Reduction, which is compatible with the zinc decladding step, is expected to effect the release of ^{131}I and other fission gases from irradiated LMFBR fuel prior to the nitric acid dissolution step of solvent extraction.

The capacity for the conceptual plant was selected to establish a parallel with recent studies at ORNL. (However, liquid-metal decladding units of much lower capacity are also attractive.) The facility is assumed to operate 24 hr/day with a plant factor of 0.75. The plant can process 36 fuel subassemblies per operating day, which corresponds to about 10,000 subassemblies per year or about seventy-two 1000-MW(e) reactors serviced.

Liquid-metal decladding followed by reduction of the oxide fuel to metal appears to be a very flexible head-end process for nuclear fuels. Several equipment and process alternatives are promising.

As an example of a decladding-reduction plant, a single design was arbitrarily selected. The principal processing unit for the liquid-metal head-end step is a furnace with three operating stations. At each of the stations inside the furnace is a process vessel, and all three vessels rest on the same rotatable platform. Decladding is performed at the first position, reduction of uranium and plutonium oxides to metal at the second position, and dissolution of precipitated uranium metal at the third. Preliminary equipment designs and descriptions of operations are presented.

Engineering Development–Decladding Kinetics

Additional information has been obtained on the rates and mechanisms of attack of stainless steel by zinc at 800°C. The zinc solutions studied contained up to 26 wt % stainless steel, and some solutions also contained 5 to 12 wt % nickel. Type 304 stainless steel tubes (3/4-in. OD, 5/8-in. wall, 4-in. long) were immersed in a bulk solution for 1 to 30 min, and the depth of zinc penetration, the weight loss, and the concentration of nickel in the bulk solution were measured.

Kinetic data show that the rate of zinc penetration into stainless steel is determined, to a first approximation, by the nickel concentration in the bulk liquid phase. The experimental results also show that practical penetration and decladding rates can be obtained in zinc slurries containing up to 26 wt % stainless steel, the highest content studied. However, a mixture containing 26 wt % steel is a paste-like slurry that is difficult to transport.

Engineering-Scale Experiments

In one concept of the liquid-metal decladding of LMFBR fuel, fuel subassemblies that are contained in a refractory metal basket are immersed in liquid zinc. Stainless steel components of the subassemblies (the shroud, cladding, and end hardware) are removed by the zinc, and the $(U,Pu,FP)O_2$ drops into the basket, which is subsequently lifted out of the melt. The objective of initial experiments was to determine the composition of basket contents after the decladding step.

The basket used for tests simulating the decladding of UO_2 consisted of top and bottom plates, four support posts, and a perforated cylindrical wall that rested on the bottom plate and was aligned by the posts. The wall contained approximately one hundred 1/16-in. holes that allowed zinc to pass into and out of the basket. After dissolution of stainless steel, the basket was lifted out of the melt and the furnace. Before the zinc-stainless steel heel could freeze in the basket, the wall was slid upward and the UO_2 and metal heel were scraped into a tray.

During decladding of charges that included UO_2 fines, significant fraction (~10%) of the fines was transported out of the basket and into the melt. To decrease the quantity of fines transported out of the basket, modification of the basket design would be necessary.

About 10% of the iron originally present in the simulated subassemblies was contained in the metal heel scraped from the basket. The quantity of zinc-steel heel roughly equalled the quantity of UO_2. Improved separation of steel from the fuel oxide would be expected by agitation of the basket contents.

Three experiments were performed to determine the

extent of zinc splashing as a result of gas released when fuel elements rupture during decladding. In each experiment, two tubes simulating fuel elements were used. Each tube contained about 25 cm^3 of argon at a pressure of about 50 atm and three close-fitting steel rods (mock fuel) having a total length of 4-1/2 in. The two tubes were positioned in a 2-in.-dia shroud and immersed to a 3-in. depth in zinc at ~800°C. Less than 2 min was generally required for the 0.01-in. thick tube wall to fail and vent the gas. In one of these experiments, two tubes were assembled in the center of a bundle or rods representing other fuel elements in a subassembly. When gas escaped from the two tubes, zinc was blown to a height of only 20 in. in the simulated subassembly. The experimental results indicate that splashing of zinc by fission gases during decladding presents no serious problems.

Control of Fission Product Iodine in a Pyrochemical Head-End

An investigation was made of the behavior of elemental iodine in an argon-iodine mixture bubbled through a molten zinc pool (at 500 and 800°C) covered by a layer of 59 mol % LiCl-41 mol % KCl salt. When an Ar-0.2 at. % I mixture was passed through a 3-cm deep zinc pool at flow rates as high as 500 ml/min (70 bubbles/sec), the iodine reacted completely with the zinc and was absorbed in the salt layer.

Results of further work on the reaction of iodine with the Zn-LiCl-KCl system indicated that ZnI_2 is formed initially by the reaction of iodine with zinc and that the second step is

$$ZnI_2 + 4KCl = K_2ZnCl_4 + 2KI$$

Due to the latter reaction, iodine is completely retained in the cover salt.

CONTINUOUS CONVERSION OF U/Pu NITRATES TO OXIDES

A process for the conversion of uranium and plutonium nitrates in nitric acid solutions to an oxide form suitable for the fabrication of fuel shapes is under investigation. This process consists of continuous fluid-bed denitration of solutions of one or more actinides, followed by fluid-bed reduction of denitration products that contain uranium. For example, mixed UO_3-PuO_2 produced by denitration is reduced with hydrogen to UO_2-PuO_2. An integrated program of laboratory studies and experimental work on a pilot scale is in progress.

Laboratory Program

Drop-denitration experiments were performed at 300 to 600°C to prepare materials for preliminary characterization and exploratory pellet tests. Starting materials were nitrate solutions of uranium, U-20% Pu, and plutonium. Selected oxide products were examined by X-ray diffraction electron-microprobe examination, and autoradiography. The major phase in UO_3-20 wt % PuO_2 material made at 450°C was identified as gamma-UO_3; possibly, PuO_2 constituted a minor phase. Plutonium nitrate solutions denitrated at 450 and 300°C produced only PuO_2; the product made at the higher temperature showed greater crystallinity. Electron-microprobe and autoradiographic examinations of mixed-oxide powder prepared at 450°C indicated that the plutonium distribution in the uranium oxide matrix was good. X-ray diffraction patterns of PuO_2 prepared by dropwise denitration at 300°C from (1) a 65% Pu(VI)-35% Pu(IV) nitrate solution and (2) a Pu(IV) nitrate solution were compared. The latter was more crystalline, but there was no other obvious difference in the patterns. UO_2-PuO_2 pellets were prepared by reducing UO_3-PuO_2 powder with hydrogen at 500 or 550°C, then pressing and sintering. Pellet densities ranged from 83 to 89% of theoretical density. Good distribution of plutonium oxide in the uranium oxide matrix was found upon examination of a pellet sample with an electron microprobe.

In other laboratory work, a dissolution procedure for UO_3-PuO_2 material produced by denitration was developed and tested. Mixed oxides produced by drop denitration at several temperatures were dissolved in nitric acid at 95–120°C and to final actinide concentrations of 0.35 and 1.5*M*. The data indicated that (1) oxide prepared at the lowest temperature, 300°C, was easiest to dissolve, (2) the oxide dissolution rate was unaffected by the dissolution temperature, (3) the dissolution rate was unaffected by the final actinide concentration when dissolution was with concentrated (16*M*) nitric acid, and (4) the fraction of plutonium dissolved was greater with concentrated acid; also the rate of plutonium dissolution was significantly higher for UO_3-20 wt % PuO_2 material than for PuO_2 alone—~99% as compared with 30–50% (in 5 hr).

Plutonium ion stability in nitric acid solutions was also studied. Data showed Pu(IV)-Pu(VI) valence distribution of plutonium ions in nitrate solution to be a zero-order function with respect to concentration of Pu(VI) during the initial 50-day period. After 50 days, the rate at which the concentration of Pu(VI) ions decreased appeared to increase. The rate of valence change in the range from 0.3 to 1.35*M* plutonium was independent of initial plutonium concentration. No spectra for trivalent or pentavalent plutonium were observed in the spectrophotometric examination of a 3*M* HNO_3 solution containing 1.35*M* plutonium.

Engineering Program

A fluidized-bed pilot plant was constructed in an

existing 3- by 4-module glovebox. The major unit is a 4-in.-dia fluidized-bed denitrator with integral filters. Auxiliaries include a feed make-up system, fluidizing-gas preheater, an off-gas condenser and condensate receiver, a demister, and a high-efficiency (AEC-type) filter for further off-gas cleanup. All process vessels are of stainless steel.

The pilot plant was checked out in a series of six denitration runs at 300°C with uranyl nitrate. Feed solutions were 1 to 2.4*M* uranyl nitrate in 0.2 or 1.0*N* nitric acid. Feed rates ranged from 50 ml/min of 1*M* uranyl nitrate to 107 ml/min of 2.4*M* uranyl nitrate; these rates correspond to 22 and 105 lb UO_3/(hr)(ft^2 reactor cross section), the upper production rate being just above the design goal of 100 lb/(hr)(ft^2). Inlet fluidizing-air flow rates were 1–1.5 ft/sec. Volume ratios of feed nozzle air-to-liquid were 330 to 640. Runs were continued for as long as 14 hr.

The following effects were observed in the six denitration runs:

(1) Slight particle growth in the bed.

(2) Fine (−200 mesh) material was produced in increasing quantity at the higher feed rates. The bulk of the fines was collected on the sintered metal filters, which are mounted directly above the bed; fines constituted about 5% of a run's product.

(3) Some coarse (+8 mesh) material formed, corresponding to about 5 to 10% of a run's product.

Product removal was effected by continuous overflow of bed material through a sidearm takeoff line, supplemented (in the final experiment) by intermittent product withdrawal at the bottom of the column. The dual withdrawal system allowed a fairly uniform bed inventory to be maintained.

Work is in progress to prepare the pilot plant for operation with plutonium.

IN-LINE ANALYSIS IN FUEL FABRICATION

Because the cost of fabrication represents a major portion of the total fuel-cycle cost for the large number of fuel subassemblies expected to be reprocessed in the LMFBR program, in-line nondestructive methods of analysis of fuel properties critical to the fabrication process are being developed. The specifications and associated precisions of fuel properties for the Fast Fuel Test Facility (FFTF) have been selected as the starting criteria for evaluation of methods of analysis.

X-ray fluorescence spectrometry is being evaluated as a direct method of measuring the uranium and plutonium contents of the oxide fuel in pellet or powder form. It has been demonstrated, utilizing powdered ThO_2-UO_2 as a stand-in for UO_2-PuO_2, that this method is promising for performing one analysis per minute. This analysis rate with a large batch size should accommodate a production rate of 1000 kg/day. Experiments must be done to determine whether the necessary precision and accuracy can be attained for material of various particle sizes and densities.

The utilization of X-ray diffraction measurement of the lattice parameter of single-phase cubic (U,Pu) oxide to determine the oxygen content (O/M ratio) of the oxide has been reviewed. Existing data on analytical methods for determining O/M ratios and the lattice parameters of single-phase $(U,Pu)O_{2\pm x}$ are summarized. Determination of the O/M ratio of hypostoichiometric oxide fuel with the required precision by measuring the lattice parameter of the fuel seems feasible.

ADAPTATION OF CENTRIFUGAL CONTACTORS IN LMFBR FUEL PROCESSING

Development of a centrifugal contactor of small diameter and large length-to diameter ratio is being studied to extend centrifugal contactor design to a configuration suitable for the plutonium isolation steps in the solvent extraction of LMFBR fuels. The principal advantages sought are a geometrically favorable design for criticality control and increased ease of operation.

The basic contactor being studied is patterned after units in use at Savannah River. In this type of contactor, organic and aqueous phases are fed into a chamber at the bottom of the contactor, where they are mixed by a rotating paddle. The mixed phases are discharged into a rotor located directly above the mixing chamber. The phases move upward, are separated by centrifugal force, and are discharged through ports located near the top of the rotor.

A stainless steel unit is being built that has a 4 3/4-in.-ID stator and a 4-in.-ID by 0.1-in.-thick wall rotor with a 12-in.-high settling zone. This unit is designed to operate at speeds up to about 3600 rpm and is expected to have a capacity of about 12 gpm.

The basic Savannah River design has been modified in the ANL unit so that the ANL unit can also be operated as an annular mixer unit with the paddle and mixing chamber removed. In this mode of operation, the organic and aqueous streams enter the annulus between the inner wall of the stator and the outer wall of the rotor and are mixed as they flow down through the annular space. The mixture enters an orifice in the bottom of the rotor and the phases are separated as the mixture moves upward inside the rotor. The phases are discharged as in the basic Savannah River design.

While the stainless steel unit was being fabricated a simplified plastic model of the annular type of contactor was built for preliminary testing. Two rotors (designated Nos. 1 and 2) differing only in their internal weir designs were built for use in the plastic contactor. Preliminary tests with water only showed that a throughput of ~10 gpm can be achieved with the No. 1 rotor. Because of restrictions in the internal flow passages, a throughput of ~5 gpm was achieved with the No. 2 rotor.

Measurements of mixing power with the contactor mounted on a dynamometer test stand showed that a high degree of mixing can be achieved in the annular mixing chamber.

II. SODIUM TECHNOLOGY (pages 37 to 63)

SODIUM CHEMISTRY

The interpretation of oxygen- and hydrogen-meter data and the control of potentially harmful processes such as corrosion and wastage require a knowledge of the identity and behavior of oxygen- and hydrogen-bearing species in sodium. A study of the phase relations in the sodium-rich corner of the sodium-oxygen-hydrogen ternary system has been initiated to meet some of these needs. In addition, an electrochemical study of sodium-oxygen solutions has been carried out which has yielded a value for the heat of solution of oxygen in sodium of 13.2 ± 0.1 kcal/mol. A $Sn\text{-}SnO_2$ reference electrode, which has a potential use in future oxygen-meter designs, has been tested in sodium-oxygen systems and found to have a number of important advantages over existing electrodes.

Because steels of differing carbon and nitrogen activity will be in contact with reactor coolant sodium, mass transport of carbon and nitrogen will occur through sodium with attendant decarburization-carburization and denitridation-nitridation of the steels. Carbon transport is thought to involve the formation of disodium acetylide (Na_2C_2) and, thus, information on the stability of this compound in sodium is of importance. Experiments have been performed which indicate that the invariant temperature for Na_2C_2 decomposition is between 550 and 600°C. Other experiments have been carried out to test the hypothesis that calcium in sodium acts as a nitrogen carrier for the nitridation of stainless steels. Experiments were made with Type 304 stainless steel tabs submerged in either pure sodium or in sodium-1 at. % calcium solutions under a nitrogen gas atmosphere at 590°C. It was found that the presence of calcium in the sodium actually inhibited the nitridation of the steel; steel tabs under pure sodium showed almost five times the nitrogen content as those under a calcium-sodium solution.

The solubility of xenon in liquid sodium was measured to satisfy the need of reactor operators and/or designers for such information. The measurements were made as functions of both temperature and pressure. The pressure dependence of the solubility was found to obey Henry's law. The temperature dependence is given by the equation $\log \lambda = 0.663 - 4500T^{-1}$, where λ is the Ostwald coefficient (the volume of xenon dissolved per unit volume of sodium) and T is the absolute temperature. The heat of solution calculated from this equation is 20.6 ± 0.7 kcal/mol.

The presence of long-lived radioactive impurities in circulating primary reactor sodium, which would result from cladding dissolution or failure or from corrosion of activated structural materials, could present a formidable reactor maintenance problem. A study was, therefore, performed to examine the feasibility of a liquid-liquid extraction technique for removing radioactive impurities from sodium. A lengthy process of elimination based on literature information and laboratory tests showed that *N,N*-diethylaniline is well suited as an extraction solvent for sodium. At 150°C, this liquid is stable in contact with sodium, has a low solubility in sodium and has wide-ranging solvency which will permit the introduction of other components that can react with the impurities.

ANALYTICAL STANDARDS PROGRAM

The long-term objective of the Analytical Standards Program is a set of sampling and analytical methods which, when combined with corrosion and purification data, will constitute the basis for a final set of purity specifications for the operation of reactor sodium systems. The short-term objectives are (1) a set of interim purity specifications and (2) a set of interim sampling and analytical methods that are uniformly applied throughout the sodium technology community.

The short-term objectives are being met through the establishment of an Analytical Standards Laboratory. This Laboratory administers and participates in the interlaboratory aspects of the Analytical Standards Program and performs the development work necessary to satisfy current analytical needs. With the assistance of two working groups, composed of representatives from major sodium technology contractors, the Laboratory has (1) issued a manual entitled "Interim Sampling and Analytical Methods for the Analysis of Sodium and Cover Gas" and (2) drafted a document entitled "Purity Specifications for Large Operating Sodium Systems." The Laboratory has also extended its analytical capabilities and initiated work in the area of particulate analysis.

The long-term objective requires the development of reliable and accurate standard methods at ANL and at other laboratories. Effort at ANL has been directed toward the investigation of the following methods: (1) high-temperature gas chromatography as a means of separating radioactive species in reactor cover gas prior to radioactivity assays, (2) proton activation as a basis for a reference method for determining total oxygen, carbon, and nitrogen in sodium, and (3) emission spectrographic analysis of a

sodium aerosol, which is generated ultrasonically and excited by an induction-coupled plasma, as a means of determining trace metals in sodium.

MONITORING OF SODIUM PURITY AND SODIUM PURIFICATION

National Meter Program

Argonne National Laboratory (ANL) has been given the responsibility of administering a National Meter Program for developing, testing, and establishing commercial availability of meters for use on FFTF and in other LMFBR systems. The meters to be developed and characterized in this program consist of monitors for oxygen, carbon, and hydrogen and a leak detector for steam generators. The FFTF schedule requires commercial availability of the oxygen and carbon meters by July 1971.

In this program, sodium technology contractors will participate in a coordinated plan to determine the capabilities of existing impurity meters that have been developed for continuous monitoring of LMFBR sodium. Completion of this plan will result in the needed characterization of the meters in the shortest possible time by taking advantage of existing facilities.

In addition to the meters themselves, prototype meter modules that include the individual meters and provide temperature and flow control are being designed for FFTF and later LMFBRs. A module is also being developed for equilibrating metal specimens with sodium to obtain measurements of the chemical activities of impurities for calibration of the meters.

Direct Measurement of Chemical Activities of Impurities

A method is being developed for calibrating impurity meters for carbon, oxygen, hydrogen, and, possibly, nitrogen, by independent chemical determinations of the activities of impurities. The type of method under development generally involves equilibration of thin specimens of a suitable metal in sodium. The equilibrium concentration of the impurity in the specimen is a measure of its chemical activity in sodium.

Oxygen activity in sodium will be determined by equilibration of vanadium wires. Distribution-coefficient data are available for the V-O-Na system, and these data will be used for oxygen-meter calibration. Equilibration methods for determining carbon, hydrogen, and nitrogen activities are also being investigated.

To use these methods for periodic on-line calibration of the various impurity meters, suitable equipment for specimen equilibration has been designed and incorporated into a modular package with the necessary devices for controlling sodium temperature and flow. This device will be tested for reactor application in radioactive sodium at EBR-II late in FY 1971.

Oxygen Meter

Electrochemical oxygen meters are being evaluated and improved, where necessary, to provide (1) reliable and reproducible measurement of the oxygen activity in sodium and (2) continuous operation of the meter at temperatures up to 900°F. The meters currently being tested have gas reference electrodes and solid thoria–7.5 wt % yttria electrolytes. Characterization of the meters will be through the national program, which will involve major LMFBR sodium technology contractors. Prooftesting of an oxygen-hydrogen meter module will be done on the Radioactive Sodium Chemistry Loop (RSCL) at EBR-II.

ANL's program currently consists of three phases: (1) characterizing the oxygen meter in nonradioactive sodium, (2) developing a meter module for use in radioactive sodium systems, and (3) testing the meter module in radioactive sodium at EBR-II. Design and fabrication work to meet these goals has been the major effort during this report period.

Carbon Meter

A carbon meter is being developed and prooftested for monitoring carbon activity in the primary and secondary sodium systems of LMFBR's. The carbon meter developed by the United Nuclear Corporation (UNC) is being given primary consideration as the on-line meter component of the carbon-monitoring station; this meter measures the rate of diffusion of carbon through an iron membrane at 1200 to 1400°F.

Characterization of the meter in stirred pots of sodium showed that it responds to the addition or removal of carbon from the sodium. Work is in progress to relate the meter readings to carbon activities determined by analyzing metal specimens which have been equilibrated with the carbon in sodium. A major effort has also been directed toward development of a modular apparatus for housing the carbon probe in reactor sodium systems.

Hydrogen Meter

An on-line hydrogen meter is being developed and prooftested for measuring the hydrogen activity in primary and secondary LMFBR sodium systems. An equilibrium diffusion-type hydrogen activity meter will be used for the on-line hydrogen meter component of the oxygen-hydrogen meter module. This meter, which measures the rate of diffusion of hydrogen through a nickel membrane, has a direct readout of the activity of hydrogen in sodium.

Data have been obtained which show that the equilibrium hydrogen pressure, as determined by the meter, is an accurate measure of the hydrogen content of the sodium.

Other studies have shown that equilibrium is reached in less than 1 hr after a step change in the hydrogen activity in sodium.

Detection of Leaks in Steam Generators

This work consists of evaluating the requirements for a leak-detection system for LMFBR steam generators and developing and prooftesting a detection system to meet these requirements. The detection system will use on-line impurity monitors for detecting the products of a sodium-water reaction. Hydrogen monitors are currently being considered for leak detection because they appear to be durable and sensitive to small changes in the hydrogen level of sodium. A signal-interpretation and alarm unit will be developed that accommodates normal hydrogen fluctuations in the sodium without giving false alarms.

The in-sodium hydrogen monitor being developed for leak detection is based on the diffusion rate of hydrogen through a nickel membrane operated under a dynamic vacuum produced by an ion pump. The rate of hydrogen diffusion through the membrane, a direct measure of the hydrogen concentration in the sodium, will be determined by monitoring the current to the ion pump.

Data have shown that the response time (~10 sec), the sensitivity, and signal-to-noise ratio are adequate for detecting water leaks before they become so large that they are self-propagating.

Plans are being made to supply an ANL hydrogen-meter leak detector to the Liquid Metal Engineering Center (LMEC) for use in their test of the Atomics International steam generator in the spring or summer of 1971.

Work is also under way to develop a leak-detection system for the secondary sodium system at EBR-II.

Characterization of Cold-Trapped Sodium

The primary goal of this work is the determination of nonmetallic impurity levels in cold-trapped sodium (as a function of cold-trap operating parameters and procedures) and interpretation of the experimental results. The methods for determining the impurities (O, C, H, N) in the sodium will be on-line impurity monitoring, and sampling and analysis. Experimental work will be carried out in a pumped-sodium apparatus, which will provide stable but adjustable impurity levels in the sodium fed to the test cold trap, and then at EBR-II. Data for both transient and steady-state operation of the test cold trap and the EBR-II primary-system cold trap will be correlated with cold-trap parameters and the feed composition.

Current work involves (1) design of the pumped-sodium system (Apparatus for Monitoring and Purifying Sodium, AMPS) for conducting definitive studies on the character of cold-trapped sodium and (2) planning for in-line oxygen and hydrogen monitors to be provided on the inlet and outlet of the EBR-II primary-system cold trap.

FISSION PRODUCT AND COVER GAS TECHNOLOGY

Failed Element Detection and Location (FEDAL) Systems

Commercial LMFBRs are expected to operate with numerous minor cladding failures. Failures that release fission gases only will be of no serious concern; however, failures that permit coolant sodium to bathe the oxide fuel either intermittently or continuously may lead to extensive leaching and/or washout of fuel. Leaching will release fission-product activity which will subsequently contaminate the primary sodium system and washout will release fuel particles, which could result in flow blockage.

For a reactor fuel pin in which sodium is contacting the oxide, a logical point to cease operation is just before the release of significant amounts of oxide particles to the coolant. Before particles are released, some leaching of fuel and consequent release of soluble fission products to the coolant would have occurred. These should be recognizable to a detection system. A satisfactory approach to failure diagnostics would be as follows: (1) selection of fission-product indicators of fuel element failures, (2) development of monitors for measuring the concentration of these indicators, (3) monitoring of these fission-product indicators during periods of reactor operations with failed fuel, and (4) characterization of failures.

Experience at EBR-II has demonstrated that a cladding hole having an area $<2\ cm^2$ is not detected by the delayed-neutron detector, which has a low signal-to-noise ratio. Fission-product indicators with half-lives longer than 57 sec (the longest half-life of delayed neutron precursors) should provide higher signal-to-noise ratios and thus allow the detection of smaller defects. (A defective area of $2\ cm^2$ is greater than the cladding area adjacent to an oxide fuel pellet; it is, therefore, important to detect much smaller hole sizes.)

Cesium, rubidium tellurium, and iodine are fission product elements that migrate strongly toward the cladding in an oxide fuel element and are easily dissolved when sodium contacts the cladding-oxide interface at cladding defects.

Because of the high background in the primary sodium from ^{24}Na activity, direct on-line application of gamma spectrometry for analysis of fission-product activity is not expected to be successful. Therefore, separation methods which will eliminate or greatly decrease the ^{24}Na activity and which are suitable for on-line application are being considered. Development work has started on equipment for the on-line measurement of fission product iodine in reactor sodium. The method involves an indirect determination of ^{135}I by separation and counting of its daughter, ^{135m}Xe.

Xenon tagging is under development by the EBR-II

Project for locating failed experimental fuel; however, if commercial LMFBRs continue operations with numerous defective fuel elements that are releasing fission-product gases to the cover-gas space, additional approaches for locating failed fuel in the reactor will be needed. One possible solution is to build a gas trap into the top end of each fuel assembly. The trap would be a device with a low pressure drop, which would be inefficient for removal of gas bubbles from sodium at full sodium flow. At greatly reduced sodium flow, such as that existing at reactor shutdown, the trap would become efficient in collecting gas bubbles released from defective fuel pins. (At reactor shutdown, when sodium flow is reduced, fission-gas bubbles are released from a defective fuel pin as the dynamic pressure outside the fuel pin drops.) Each trap would be sampled for fission-gas content after reactor shutdown with a sampling tool attached to the already existing refueling mechanism, and the gas samples would be routed, in turn, through a single line to a shielded detector.

Nature and Control of Sodium Aerosol

The presence of sodium aerosol in reactor cover gas can interfere with the movement of mechanical parts of the reactor, clog the gaps between the moving parts, and transport fission products and other impurities from the sodium phase to the cover-gas phase. A program was, therefore, undertaken to study the properties of sodium aerosols and the mechanism of aerosol formation.

At sodium temperatures above 300°C, most of the sodium transported in the cover gas will leave the sodium pool as sodium vapor. As this vapor cools, it condenses to aerosol very close to the sodium surface, and thermal convection transports the aerosol particles in the gas phase, where agglomeration and settling processes take place. Measurements of some of the properties of sodium aerosol have been made as a function of temperature. Results indicate that sodium aerosol concentration can exceed the concentration resulting from the vapor pressure by factors greater than 9. An aerosol concentration of 35 g/m^3 was measured above sodium at 500°C. Preliminary measurements of the particle-size distribution of sodium aerosol in argon over sodium at 400°C were made with a Casalla jet impactor. The mass mean diameter of the aerosol was ~4 μm.

III. MATERIALS CHEMISTRY AND THERMODYNAMICS (pages 64 to 86)

HIGH-TEMPERATURE THERMODYNAMIC STUDIES

A mass-spectrometric Knudsen effusion study of vapor species over $U_{0.8}Pu_{0.2}O_{2-x}$ was carried out over a range of oxygen-to-metal (O/M) ratios of 1.92 to 2.00 and a temperature range of 1630 to 2130°C. A brief description of this published work is given.

A mass spectrometric study of the U-O-Na and U-Pu-O-Na systems was initiated. The objective of the study is to establish O/M ratios for U-Pu-O fuel (or the oxygen content of the sodium) required to prevent sodium-fuel interactions.

The metal-rich boundary of the U-Pu-O fluorite phase was measured for 19.8 and 44.1 at. % plutonium. Measurements were also carried out to establish the phase diagram for the hyperstoichiometric region for Pu/(U + Pu) ratios of 0.2 to 0.8 at temperatures from 200 to 1200°C. Phase and reaction studies were initiated on the interaction of LMFBR fuel with sodium coolant.

Equipment was constructed to study the chemistry of the U-Pu-O-Cs system and other fuel-fission product systems. The U-Pu-O-Cs system is important in potential cladding attack by fission product I_2 and cesium.

Activities of uranium and carbon in U-C and uranium, carbon, and oxygen in U-C-O were measured. Oxygen contamination of UC was shown to result in lower carbon activity, higher uranium activity, and an increase in the overall stability of uranium carbide.

REACTOR SAFETY AND PHYSICAL PROPERTY STUDIES

Three complementary calorimetric systems for the measurement of high-temperature enthalpy increments are available for our use. Depending on the material to be studied and temperature range to be covered, one may choose (1) the resistance-heated drop calorimetric system (600–1600°K), (2) the electron-beam-heated drop calorimetric system (1300–2500°K), or (3) the induction-heated drop calorimetric system (2500–3600°K).

Enthalpy data from the first system are reported for $RuO_{1.98}$, and literature references are given for work which we completed on uranium dioxide, Na_3Bi, uranium diboride, and sapphire. Measurements of the enthalpy of uranium dioxide were completed using system (3) with the highest temperature reached being 3523°K. Modification of the calorimeter system for work with $(U,Pu)O_2$ is in progress.

Vapor pressure measurements over liquid UO_2 using a transpiration technique were performed up to 3390°K. The data obtained in these preliminary measurements are in good agreement with literature in the range where other data exist and agree well with an extrapolation of lower-temperature results.

A program utilizing matrix-isolation spectroscopic

techniques to obtain molecular parameters of fuel vapor species has been undertaken. These data may be subsequently utilized in computations of the uranium oxide equation of state at elevated temperatures. Construction and testing of the experimental apparatus were completed. The availability in the CEN Division of a Fourier transform infrared spectrometer system will greatly facilitate the interpretation of the spectral data.

Measurements were made of the speed of sound in molten sodium from 182 to 1001°C. This extends the temperature range of previously available data by about 200°C. Good agreement with values reported by other workers was found in the region of temperature overlap. Work is in progress to extend these measurements to still higher temperatures.

Calculations of vapor pressures and phase composition in fuel oxide and fission product systems were carried out based upon thermodynamic considerations and mass constraints. Results showing the effects of initial fuel composition and percent burnup are presented and briefly discussed. Work is now complete on revisions which will take into account solution effects.

Values of the thermal diffusivity of UO_2 in the liquid state are of importance to the reactor safety program. This information is needed to evaluate means of safely cooling the core of an LMFBR in the event of a meltdown incident. We have selected a method by which the thermal diffusivity is determined from the phase change in a thermal wave passing through a sample. This wave is produced by heating the sample with a sinusoidally modulated electron beam. These experiments will be performed in a dual-gun electron-beam furnace, formerly used as a high-temperature tensile test furnace. Extensive electronic modifications to the system are being made. Cell design and temperature and phase-shift measuring procedures are also being tested. We plan to obtain thermal diffusivity data for liquid UO_2 between its melting point and about 3500°K and for solid UO_2 from 2300°K to the melting point.

Knowledge of the distribution of fission products to the phases which are produced in the event of a meltdown of the core of an LMFBR is required in order to predict the fission-product heat distribution after an incident. This information will be used to assure that means are available for cooling the products of the meltdown. One phase of an experimental program is to determine the distribution of fission-product elements between molten UO_2 and molten stainless steel. The fission products to be studied (Nb, La, Mo, Zr, and Ru) are among those that contribute to the major portion of the heat produced soon after shutdown of a fast reactor and that have properties suitable for the experimental method used. We have performed experiments in an arc-melting furnace to determine how zirconium distributes between liquid phases of UO_2 and iron. The experiments to date establish what one would predict thermodynamically: zirconium would be distributed to the oxide phase in the event of a core meltdown incident.

The distribution of fission-product elements between liquid UO_2-concrete and molten steel is also under study because of the possible interaction of molten fuel components with the concrete which will lie below the core of a reactor such as FFTF. A preliminary experiment with the concrete-UO_2-iron mixture plus some inactive fission product oxides, contained in a zircon crucible welded into a tantalum capsule, has been performed in a resistance-heated furnace, and it appears that this method of investigation is satisfactory.

CALORIMETRY

In a continuing program to provide accurate thermochemical data for plutonium compounds, the enthalpy of formation has been determined by oxygen bomb calorimetry for two plutonium carbides. A specimen of arc-melted plutonium monocarbide was prepared in the Materials Science Division by O. L. Kruger, and its standard enthalpy of formation, $\Delta Hf^{\circ}_{298.15}(PuC_{0.878\pm0.003}, c)$ was determined to be -11.41 ± 0.68 kcal mol^{-1}. A specimen of arc-melted plutonium sesquicarbide was prepared at Los Alamos Scientific Laboratory by J. A. Leary, and the preliminary value obtained for its enthalpy of formation, $\Delta Hf^{\circ}_{298}(PuC_{1.466}, c)$, is -19.4 ± 0.7 kcal mol^{-1}.

As part of the effort that has been going on for some years to clear up the uncertainties in the thermochemistry of hydrogen fluoride, additional measurements have been made this year on (1) the energy of reaction of hydrogen and fluorine to produce liquid hydrogen fluoride, (2) the enthalpy of solution of liquid hydrogen fluoride in water, and (3) the enthalpy of neutralization of liquid hydrogen fluoride by dilute sodium hydroxide. It appears that the thermochemistry of HF is now firmly established.

In connection with the sodium-cooled reactor program, the enthalpies of formation of disodium acetylide and monosodium acetylide were determined by solution calorimetry to be $\Delta Hf^{\circ}_{298}(Na_2C_2, c) = +4.77 \pm 0.40$ kcal mol^{-1} and $\Delta Hf^{\circ}_{298}(NaHC_2, c) = +23.10 \pm 0.27$ kcal mol^{-1}. Na_2C_2 may play an important role in the transport of carbon in sodium-cooled reactors.

Preliminary studies, also by solution calorimetry, are being carried out on Na_3UO_4 and Na_2O. Na_3UO_4 has been shown to be the species likely to be in equilibrium with sodium and uranium dioxide in the presence of excess oxygen. The literature values for the enthalpy of formation of Na_2O, a necessary auxiliary datum for the study of Na_3UO_4, are discordant.

The determination of the enthalpy of formation of molybdenum disulfide by fluorine bomb calorimetry yielded the value $\Delta Hf^{\circ}_{298}(MoS_2, c) = -65.8 \pm 1.2$ kcal mol^{-1}.

The potential of phosphorus trifluoride as a fluorine stripper (ANL-7225, p. 152), is being put to a test by calorimetric measurements of the enthalpy of the reaction

$$3PF_3(g) + XeF_6(c) \rightarrow Xe(g) + 3PF_5(g)$$

in a study of the enthalpy of formation of xenon hexafluoride. Published values for the enthalpy of formation of xenon hexafluoride vary between −70.4 and −126 kcal mol^{-1}.

As part of a continuing effort to rationalize previously observed bond energy trends and establish a scheme to predict reliable thermodynamic data for fluorine-containing molecules, free radicals, and ions, a considerable effort over the past year has been spent in the calculation of accurate wave functions for gaseous diatomic fluoride molecules and ions. Calculations have now been made for OF, SF, SeF, NF, and PF.

IV. ANALYTICAL AND REACTOR CHEMISTRY (pages 87 to 102)

CHEMISTRY OF IRRADIATED FAST-REACTOR FUELS AND MATERIALS

Studies of the chemical behavior of fast-reactor fuels during irradiation are continuing, with the principal efforts being directed toward development of analytical techniques for examining fuels on a micro scale and the application of these techniques for collecting data on irradiated mixed-oxide fuel specimens.

A method has been developed for determining the relative radial distribution of krypton in irradiated mixed-oxide fuel. The method involves volatilization of the krypton by laser-beam sampling, and subsequent beta-counting of ^{85}Kr. The data obtained will contribute to the development of fuel-swelling models for mixed-oxide fuels.

A solid-state energy-dispersion detector (lithium-drifted silicon) is being tested for application to electron microprobe analysis of irradiated fuels. This type of detector is expected to offer an increase in sensitivity and a decrease in the time required for analysis, as compared with conventional wavelength-dispersion devices.

Electron microprobe analyses have been performed on a variety of irradiated mixed-oxide fuel specimens. These studies have been directed toward examining uranium-plutonium redistribution and fission product distribution, with particular emphasis on processes that appear to limit attainment of the target burnup, e.g., fuel-cladding interactions and swelling. Electron microprobe data obtained on these fuel specimens are presented. Vapor-phase transport is believed to be the principal mechanism involved in the migration of fission products and fuel and cladding constituents during irradiation.

FAST-REACTOR CROSS-SECTION MEASUREMENTS

Measurements of cross sections and cross-section ratios, for materials of interest to the fast breeder reactor program, are continuing. This program emphasizes measurements requiring chemical techniques and is primarily devoted to measurements of material irradiated by neutrons within the energy region bounded by 10 keV–10 MeV.

Results are reported for measurements of capture-to-fission cross-section ratios from 64 samples of uranium and plutonium isotopes irradiated throughout the core and blanket regions of EBR-II. A program is under way to measure the yields of tritium from fast-neutron-irradiated reactor fuels. Two experimental methods are being developed; the status of each is described.

Other work has involved studies conducted in collaboration with other divisions of ANL. A study was made of the helium generation in sections of control- and safety rod thimbles from EBR-II; the results have led to the conclusion that nitrogen is a significant source of helium in fast-reactor-irradiated steels. In addition, extensive measurements of foil-activation rates were conducted in the ZPR-3 critical assembly, which has been mocked-up to simulate irradiation conditions in EBR-II. These data will provide a means of comparing experimental results with reactor physics calculations.

DETERMINATION OF BURNUP OF FAST-REACTOR FUELS

A long-term irradiation in EBR-II of encapsulated samples of ^{232}Th, ^{233}U, ^{235}U, ^{237}Np, ^{238}U, ^{239}Pu, ^{240}Pu, and ^{241}Pu, which began in December 1966, has been completed. These samples, which were irradiated in both the core and the axial blanket of the reactor, will be used to determine fast fission yields and nonfission nuclear transformations. The burnup of the fissile nuclides ranges from about 10 to 15% for the blanket samples and from 20 to 25% for the core samples.

Short-term irradiations have been carried out in EBR-II mockup experiments in Assemblies 60 and 61 of ZPR-3 (1) to determine the ^{235}U, ^{238}U, and ^{239}Pu absolute fast fission yields of gamma-active fission products that have high fission yields and half-lives of less than 100 days and (2) to establish the variation of fission yields with neutron energy in fast reactor spectra. The irradiation packages contained gram amounts of ^{235}U, ^{238}U, and ^{239}Pu as foils and nanogram amounts of these nuclides in contact with mica fission-track detectors. The number of atoms of each fission product per gram of material was determined by gamma-spectrometric assays of the foils; the number of fissions per gram of material is being determined by means

of the mica fission-track detectors. Absolute fission yields will be calculated upon completion of the fission-track counting.

Relative fission yields, calculated from the gamma-spectrometric data, have been used to establish the variation of the absolute fission yields of burnup monitors with neutron energy. From these results, the following conclusions have been drawn. (1) For the neutron spectral distribution between Rows 2 and 12 of EBR-II, the fission yields of the ^{235}U and ^{239}Pu burnup monitors are constant. (2) For the neutron spectral distribution between Row 2 of EBR-II (the location of the long-term irradiation samples) and a spectrum somewhat softer than that expected for FFTF, the fission yields of the ^{239}Pu burnup monitors are constant (^{239}Pu will be the principal fissioning nuclide in FFTF fuel). The fission yields to be determined from the long term irradiation in EBR-II will thus be applicable to burnup measurements in FFTF.

V. CHEMISTRY OF LIQUID METALS AND MOLTEN SALTS (pages 103 to 150)

The study of the chemistry and thermodynamics of liquid metals and molten salts continues to increase in importance in many areas of science and technology. The continuing programs in this area include studies of the thermodynamics, transport properties, and structures of a number of liquid metals and alloys, fused salts, and mixtures in which the major component is a liquid metal or a molten salt.

The thermodynamic investigations involve the determination of the liquid-solid phase diagrams, activity coefficients, vapor-liquid equilibria, and the solubilities of various solids, gases, and liquids in liquid phases. The studies of transport processes include diffusion of neutral species on surfaces and in bulk phases and the migration of charged species in electric fields. Studies of the structure of molten salts have been performed primarily by Raman spectroscopy and have aided in the interpretation of the chemical and thermodynamic behavior of various salts.

A number of recently initiated programs on electrochemical energy conversion, involving lithium/chalcogen cells with molten-salt electrolytes, are continuing under the sponsorship of the National Heart and Lung Institute, the U.S. Army (Fort Belvoir), and the Environmental Protection Agency. These programs involve the design, construction, and testing of lithium/selenium and lithium/sulfur cells and will eventually involve the construction and operation of full-sized batteries for particular applications.

LIQUID METAL STUDIES

Thermal, chemical, microscopic, and X-ray analysis have been used to determine the phase diagram of the lithium-selenium system. The melting point of Li_2Se, the only intermediate phase found, was determined to be 1302°C. A miscibility gap extends from 0.5 to 30.5 at. % lithium above the monotectic temperature of 350.1°C. Mutual solid solubility of the terminal phases has not been found. On the basis of preliminary results, the lithium-sulfur system is believed to be very similar to the lithium-selenium system.

The recent optimism with regard to obtaining power from controlled thermonuclear fusion reactions has prompted the extension of experimental studies of liquid metals and molten salts to include systems of potential importance to controlled thermonuclear reactors (CTR). Because of (1) the need to maintain well-confined, well-controlled tritium inventories in deuterium-tritium fueled CTR devices and (2) the anticipated use of liquid lithium as a coolant and blanket medium, studies of the thermodynamic properties of lithium-hydrogen-metal systems have been initiated in which the metals under investigation are candidate structural materials for fusion reactors. These studies include the determination of phase diagrams for ternary systems containing hydrogen and lithium in contact with refractory metals, measurements of hydrogen activities and diffusivities, and investigations of hydrogen-transport phenomena.

A physically realistic model for solutions of gases in liquid metals has been developed. In contrast to earlier models, this model explicitly accounts for the effects of the conduction electrons in a liquid metal. The model has been shown to provide a fairly reliable calculation of the solubility of the noble gases (He, Ar, Xe) in liquid sodium.

First and second nearest-neighbor bond energies were calculated for a variety of liquid metals from heat-of-vaporization and surface-energy data using a simple pair-wise interaction model of cohesive forces. The first nearest-neighbor interaction was found to be attractive while the second nearest-neighbor interaction was repulsive. The longer range repulsive interaction was not surprising in view of the Friedel oscillations known to exist in the potential functions for ion-ion interactions in a metal. However, the calculations demonstrated that the presence of long-range repulsive interactions in metals are also suggested by simple bond-energy calculations.

A method of analysis of grain-boundary grooving kinetic data has been developed which permits, in cases where both surface and volume diffusion are operative in groove growth, the separation of and simultaneous determination of surface and volume coefficients. This analytical technique makes grain-boundary grooving a more powerful tool for diffusion studies.

The electrical conductivities of liquid sulfur and P_4S_3 were determined over the approximate temperature ranges from 300 to 430°C and from 200 to 360°C, respectively.

Measurements were made both with direct current and with alternating current at frequencies from 0.1 to 10 kHz. These data, together with earlier results, show that the conductivity of sulfur increases markedly upon the addition of up to about 10 at. % phosphorus.

An understanding of transport mechanisms is essential to total understanding of the chemical and electrochemical processes taking place in sulfur cathodes (which are used in lithium/sulfur secondary cells). To gain insight into these mechanisms in sulfur-containing systems, a study was undertaken of the transport of reaction products in cathodes containing sulfur and sulfur-phosphorus compounds. Experimental Li/LiBr-RbBr/Li in S or /Li in P_4S_{10} electrochemical cells were run so as to deposit a known amount of lithium at the cathode-electrolyte interface. Microscopic examination and sulfide analysis were used to determine the concentration profiles of lithium-containing reaction products in the porous cathode structure. The results indicate that very little product is transported into the cathode structure.

MOLTEN SALT STUDIES

The solubility of Li_2Se in lithium halides was found to be unaffected by changes in the anion composition. However, the addition of larger cations such as rubidium appears to cause a decrease of the Li_2Se solubility. The total selenium solubility of Li_2Se-selenium mixtures in lithium halide eutectics is significantly greater than the individual solubilities of Li_2Se and selenium. This is attributed to the formation of polyselenides of the type Se_x^{-n} when selenide and selenium are present together. The solubility of lithium halide eutectics in liquid selenium was found to be extremely low and unaffected by the presence of Li_2Se. The total dissolved sulfur from sulfur-Li_2S mixtures in lithium halides was much greater than for sulfur or Li_2S alone. As in the case of the selenium-selenide mixtures, this behavior was attributed to the formation of polychalcogenide ions, S_x^{-n}.

Pseudo-ternary lithium selenide-selenium-alkali halide systems have been examined by emf, thermal, and microscopic methods. The alkali halide components considered are the LiBr-RbBr and LiF-LiCl-LiI eutectic mixtures. Consideration of these systems has helped to explain apparent discrepancies between thermal-analytical and emf results on the lithium-selenium binary system. An interesting feature of these ternary systems is a large region of three-liquid equilibrium. The results of the emf investigations have yielded activity coefficients for lithium in lithium-selenium alloys and have given the standard free energy of formation of Li_2Se at 360°C as −94 kcal/mol.

Laser-Raman spectroscopic studies of phosphorus-chalcogen systems have been extended to include solid and liquid P_4S_7 and solid $P_4Se_3 . P_4S_7$ appears to undergo some cross-linking of terminal sulfur atoms in the liquid state in a manner similar to that found in previous studies of P_4S_{10} (ANL-7675, p. 138). Raman spectral results for P_4Se_3 support the contention that it is isostructural with P_4S_3. Raman spectra of iodate-nitrate melts indicate that the iodate ion is pyramidal in molten-salt solution and that its behavior is similar to that of nitrate ion with respect to the influence of the alkali metal cation environment on the molecular vibrations of the anion. The complete Raman spectrum of tetrahedral $MgCl_4^{-2}$ has been recorded and a normal coordinate analysis has been carried out. Raman spectral studies of ZnI_2-LiCl-KCl melts containing 5 or less mol % ZnI_2 indicated that most of the zinc (II) was combined as $ZnCl_4^{-2}$ and that no detectable amount of ZnI_2 was present. This explains the low ZnI_2 partial pressures above ZnI_2-LiCl-KCl melts even at temperatures near 650°C.

ENERGY CONVERSION

A program on the development of a lithium/selenium secondary battery of high specific energy (110 W-hr/kg) to be used as an implantable power supply for an artificial heart or heart-assist device has continued. Electrical performance studies involving eighteen single-cell tests indicated that a 1.1-kg battery of five 7.5-cm dia lithium/selenium cells will be capable of providing an energy of 120 W-hr at a power level of 10 W. According to calculations, this battery would fall within acceptable limits of weight and size for implantation. An unsealed five-cell battery was operated at 12 W for 1.5 hr. A hermetically sealed six-cell battery was operated in an air environment for several hours and was relatively insensitive to motion as well as orientation. Improvement in cycle life is an important objective of the continuing program.

Another program continues with the objective of developing 7.5-cm dia lithium/chalcogen cells with paste electrolytes for application in secondary batteries to provide electrical drive power to supplement the conventional power system in hybrid Army vehicles. The cells are to be capable of 1 to 3 W/cm^2 short-time peak power densities and have lifetimes of 1000 to 2000 hr and 1000 to 2000 charge-discharge cycles. An energy storage capacity density of 0.5 W-hr/cm^2 at the 1-hr discharge rate (0.27 A/cm^2) and a short-time peak power density of 2.3 W/cm^2 have been demonstrated. Recent efforts have resulted in cells with improved charging characteristics (a Faradaic efficiency of 0.92) and with the capability of delivering 52% of the theoretical capacity density at the 1-hr rate. Cycle lives of 10 to 13 cycles have been obtained during operating times of 120 hr, but with decreasing performance. The life-limiting factor has been the transference of selenium through the paste electrolyte to the lithium electrode, causing an increase of internal resistance and a loss of capacity. Investigations are presently being directed toward eliminating this problem.

Ionic resistivities of past electrolytes composed of lithium aluminate and the LiF-LiCl-LiI eutectic were measured. Compositions of the samples ranged from 40 wt % salt to 60 wt % salt. The observed resistivity ratios (resistivity of paste/resistivity of salt) exceeded the resistivity ratios calculated from Maxwell's equation for conduction in heterogeneous systems (assumed for present purposes to represent the minimum attainable values) by factors of no more than 1.1 to 1.4.

A procedure has been developed for fabrication of 7.5-cm dia paste electrolytes by the molten-salt infiltration of disks pressed from pure powdered lithium aluminate. The important property of disks made by this procedure is their low porosity as indicated by their low permeability to gaseous helium, typically less than 0.04 ml(STP) $min^{-1} cm^{-2} atm^{-1}$ for 0.25-cm thickness.

Chromium, beryllium, and aluminum are the most corrosion-resistant materials tested for application as electrically conductive construction materials, showing corrosion rates less than 0.8 mm/yr at 375°C. Polymeric materials appear to be unsatisfactory for use as hermetic seals and electrical insulators.

The objective of the work formerly sponsored by the National Air Pollution Control Administration and currently sponsored by the Environmental Protection Agency is to develop secondary batteries suitable for powering electric automobiles. Batteries for this application should have a minimum specific power of 220 W/kg, a specific energy of 220 W-hr/kg or more, a lifetime of at least 1000 charge-discharge cycles, and a cost of less than $10/kW-hr. Electrical performance tests were conducted on a series of small (~1- to 2-cm^2 electrode area) single cells consisting of a lithium anode, a sulfur, P_4S_{10}, or P_4S_3 cathode, and a molten-salt electrolyte. In general, the open-circuit potentials of the lithium/sulfur and lithium/P_4S_{10} cells were from 2.1 to 2.3 V, and the short-circuit current densities ranged between 4.8 and 8.5 A/cm^2. A new, laminated-cathode design that was tested gave a capacity density of 0.52 A-hr/cm^2 at a current density of 0.52 A/cm^2. Supporting studies were conducted on materials of construction, seals and insulators, the solubilities of cathode reactants in molten salts, and battery design calculations for electric vehicles.

VI. NUCLEAR SAFEGUARDS STUDY (page 151)

A study on nuclear safeguards has been undertaken for the AEC's Office of Safeguards and Material Management (OSMM). The study will include materials accountability, physical protection, and surveillance. Results of the study will be used by OSMM in developing general criteria for future U.S. plants to assure that adequate safeguards are established and maintained.

The study is being performed mainly by ANL's Chemical Engineering Division. However, significant assistance is being given by persons from other parts of ANL. The initial efforts were devoted to becoming familiar with existing reactor fuel conversion, preparation, and fabrication facilities. Preliminary general design criteria have been formulated. Initial drafts of the criteria were made available to OSMM by the end of 1970 for internal and later external comment.

VII. FLUIDIZATION PROCESSES (pages 152 to 158)

FLUIDIZED-BED COMBUSTION OF FOSSIL FUELS

Fluidized-bed combustion of fossil fuels is being studied at Argonne National Laboratory as a method of reducing the quantity of atmospheric pollutants (oxides of sulfur and nitrogen) released. This work is part of a large program, under the direction of the National Air Pollution Control Administration, on various aspects of fluidized-bed combustion research. Numerous governmental agencies and industrial firms are involved in this program.

The fluidized-bed combustion concept involves feeding, into a hot fluidized bed of solids, powdered fuel and an additive (such as particulate limestone) that will react with SO_2. The solids consist of small particles of noncombustible material, such as ash or partially sulfated limestone, held in a dense suspension by a stream of air passing upward through them. As the fuel burns in the bed, the SO_2 released by combustion of the coal reacts with the additive, forming $CaSO_4$. An objective of experimental work is to determine the conditions necessary to achieve a high degree of SO_2 removal from the flue gas and efficient utilization of the limestone or other additive material.

The program at ANL has emphasized the pollution abatement aspects of fluidized-bed combustion and has consisted largely of bench-scale experimentation along with a few laboratory investigations. The major equipment item of the bench-scale fluidized-bed pilot plant is a 6-in.-dia combustor equipped with resistance heaters and air-cooling chambers for temperature control. Metered fluidizing air for the combustor is preheated in an electrically heated, packed pipe. Coal and additive are fed into carrier air streams by means of screw feeders and transported to the combustor, being introduced at a feed point just above the gas distributor. Flue gas leaving the combustor is passed

through two in-series cyclones, a final filter, and a gas-analysis system.

The major results of the experiments performed during the report period are as follows:

1) In coal-combustion experiments performed with starting beds of partially sulfated limestone of large particle size, SO_2 removals were independent of the type of additive. The three additives tested at identical operating conditions were limestone No. 1359, limestone No. 1360, and dolomite No. 1337.

2) In coal-combustion experiments with starting beds of limestone and with limestone No. 1359 additive, SO_2 removal was 91% at combustion temperatures of 1500 to 1550°F and was lower at temperatures above and below this temperature range.

3) Velocity of the fluidizing gas was shown to affect SO_2 removal in coal-combustion experiments with a starting bed of limestone. The highest SO_2 removal, 83%, was obtained at the lowest of three gas velocities tested, 3.5 ft/sec.

4) SO_2 removals were determined at several additive feed rates in experiments of extended duration with a bed of partially sulfated limestone and with No. 1359 limestone additive of 490-μm particle size. SO_2 removals were increased at higher additive feed rates.

5) The use of −325 mesh Tymochtee dolomite additive resulted in poorer SO_2 removals than with 650-μm Tymochtee dolomite, apparently because of inadequate residence time of the fine dolomite in the fluidized-bed combustor.

6) Laboratory-scale experiments indicated that the reactivity with SO_2 of partially sulfated limestone contained in elutriated solids is comparable to the reactivity of fresh SO_2.

7) A reduction in NO emission in the flue gas, which has been observed when limestone is injected into the bed in coal-combustion experiments, is apparently related to the presence of sulfate in the bed.

8) It was noted that heating a bed of partially reacted limestone above 1700°F results in some desorption of SO_2, possibly because of partially reducing conditions in the bed.

BASIC MECHANISMS OF FLUIDIZATION

Fluid Dynamics for a Bubble Rising in a Finite Two-Dimensional Fluidized Bed

A theoretical study was made to determine the effect of finite bed dimensions on (1) particle circulation patterns and (2) gas-flow patterns for a single bubble rising in a fluidized bed. It is predicted from this study that (1) the bed particles move upward at the column center and downward near the column walls, (2) particle movement is primarily in the vertical direction, with horizontal particle movement occurring at the bottom and top boundaries of the bed, and (3) the side walls and the top and bottom boundaries of the bed have a compressive effect on the gas cloud that surrounds a rising bubble; the compressive effect increases with a decrease in the ratio of bubble velocity to interstitial gas velocity.

Basic Mechanisms of Fluidized-Bed Heat Transfer

Measurements relating the heat-transfer coefficient to the fluidized-particle residence time at a heater surface were made by periodically injecting bubbles into a bed to cause particle movement while the bed was at the point of minimum fluidization. Heat transfer was measured from a heater installed in the reactor wall. Particles were photographed through a transparent surface with a motion picture camera at 120 frames per second. Residence times were measured by analyzing the film and noting the times of arrival and departure of tracer particles at the transparent surface. Heat-transfer coefficients as a function of particle residence time were determined for three bed materials—glass beads having diameters of 1.51×10^{-3} ft and 1.17×10^{-3} ft and copper shot having a diameter of 1.93×10^{-3} ft. Agreement was good between data for copper and glass particles and values predicted by a previously proposed heat-transfer model. These experiments validated the heat-transfer model; originally, the predictions of this model were compared with heat-transfer data for moving packed beds.

ARGONNE NATIONAL LABORATORY

Chemical Engineering Division Annual Report

U of C-AUA-USAEC

1970

ANNUAL REPORT

I. FUEL CYCLE TECHNOLOGY [1]

(D. S. Webster, J. W. Simmons)

A. LIQUID METAL DECLADDING OF REACTOR FUELS

(R. D. Pierce, M. J. Steindler [2])

The fuel elements used in the first commercial breeder reactors (LMFBRs) are expected to consist of uranium oxide-plutonium oxide pellets in 1/4-in. dia stainless steel tubes welded shut at both ends. About 200 fuel elements will be contained in a stainless steel shroud and end fittings to form a subassembly.

The head-end operations must accomplish separation of the fuel from the cladding and most volatile fission products and conversion of the fuel to a form suitable for dissolution in nitric acid. Head-end processes that are suitable for LWR fuels are unlikely to be suitable for spent LMFBR fuels, which will have about ten times the heat-generation rates and radioactivity levels of current fuels.

A relatively simple molten-metal decladding technique is being developed as a head-end procedure for aqueous processing of LMFBR fuels. This procedure, performed in a tightly sealed furnace, includes direct dissolution of the cladding in a liquid metal, separation of the resulting steel-zinc solution from the fuel oxides, and reduction of the fuel oxides to metal. Decladding is started by immersing the fuel-containing zone of a subassembly in a pool of molten zinc at 800°C. After the immersed stainless steel components of the subassembly have disintegrated and the unaffected fuel oxide pellets have fallen to the bottom of the crucible, the steel-zinc melt is pressure-siphoned out of the crucible. Next, a Mg-Zn-Ca alloy is charged into the crucible in preparation for the reduction step; the melt is then stirred with an agitator, and the uranium-plutonium oxide reacts with the alloy forming metallic uranium and plutonium product. The product alloy is pressure-transferred out of the crucible and fed to a nitric acid dissolution step.

The problems related to high heat generation of breeder reactor fuel are met by providing a continuous flow of cooling gas over subassembly surfaces during transfer of fuel to the crucible and by immersion of the fuel in liquid metal during decladding and purification steps. To control the highly radioactive volatile isotopes in LMFBR fuel, dilution of radioactive gases with other gases is minimized. Substantially all of the radioactive gases, released while the fuel is in the sealed furnace, are pumped into a gas-handling system and subsequently into standard gas cylinders for storage.

1. Plant Concept Study (I. O. Winsch, T. R. Johnson, M. Krumpelt, W. J. Walsh)

A conceptual head-end plant processing 5 tons/day of LMFBR fuel has been designed for zinc decladding followed by reduction of fuel oxides. A conceptual head-end plant for zinc decladding followed by voloxidation was described in ANL-7675, pp. 20–21. Reduction and voloxidation are candidate process steps designed to effect the release of ^{131}I and other fission gases from irradiated LMFBR fuel prior to nitric acid dissolution. The reduction alternative appears to be preferable because of higher process reliability in achieving efficient fission-gas removals and relative ease in interfacing with the zinc decladding step.

LMFBR fuel subassembly designs and the aqueous processing steps are still in a period of evolution and development, and head-end processing requirements are presently uncertain. In order to provide a basis for the plant design, a single set of processing conditions was selected.

A plant capacity of about 5 tons/day was selected to establish a parallel with recent processing studies at ORNL [3]. The facility is assumed to operate 24 hr/day with a plant factor of 0.75. The plant can process 36 fuel subassemblies per operating day, which corresponds to about 10,000 subassemblies per year, and, in the case of the Atomics International (AI) Conceptual Design [4], about seventy-two 1000-MW(e) reactors can be serviced and 4.8 tons/day of fuel processed. It is assumed that core fuel and axial and radial blankets will be processed together in the head-end unit since the ORNL separations processes [3] being developed are based on homogenized fuel input. The head-end plant could operate somewhat more efficiently if the radial blanket were processed in a separate campaign in the same facility.

The Atomics International Follow-On Study "Final Reference Design" [4] was selected as an example of LMFBR fuel charged to a liquid-metal decladding process. The subassemblies are each 15 ft long and 5.667 in. across the flats. The core subassemblies each contain 217 non-vented fuel elements, which have a core region 42.8 in. long and upper and lower axial blankets of 15 and 12 in. respectively. The bottom hardware is cut off prior to processing, and the upper hardware is not immersed during decladding.

a. Zinc Declading-Reduction

Liquid-metal decladding followed by reduction appears to be a very flexible head-end process for nuclear fuels. Several equipment and process alternatives are promising.

To provide an example of a decladding-reduction plant, the following procedure and design were arbitrarily selected: Fuel subassemblies are shipped, unloaded, and stored in a pool (probably under sodium) and the bottoms are cropped. An array of three subassemblies is raised into a

transfer turret for transport. Forced-gas cooling may be employed to prevent excessive cladding temperatures during transfer of subassemblies to a furnace with three operating stations. The furnace is the principal processing unit for the liquid-metal head-end step. A concept of this unit is represented in plan and elevation views in Figs. I-1 and I-2. At each of three positions inside the furnace, resting on a rotatable platform, is a process vessel. Decladding is performed at one position, reduction of uranium and plutonium at the second position, and uranium dissolution at the third.

After the transfer turret is affixed to the furnace at the decladding station, gates are opened at the decladding port and in the transfer turret, and the fuel is lowered through the cover salt until it is immersed to a depth of a few inches in the zinc. The system is held at 800°C throughout a run. After the bottom cladding of the fuel elements has dissolved and the fission gases have vented (about 15 min), the fuel is lowered so that the zinc covers the fuel completely. For the case of vented fuel elements or if it turns out that gases vent slowly from the plenum through the pellets, the above step may be omitted, and instead, the subassemblies may be lowered immediately to a position that immerses the entire fuel zone in zinc. A period of about one hour is then allowed for removal of the cladding. Next, the zinc-steel mixture is pressure-transferred out of the process vessel through a transfer line. A maximum pressure of about 20 psi is required for zinc transfer. This zinc is recycled twice through the decladding step before

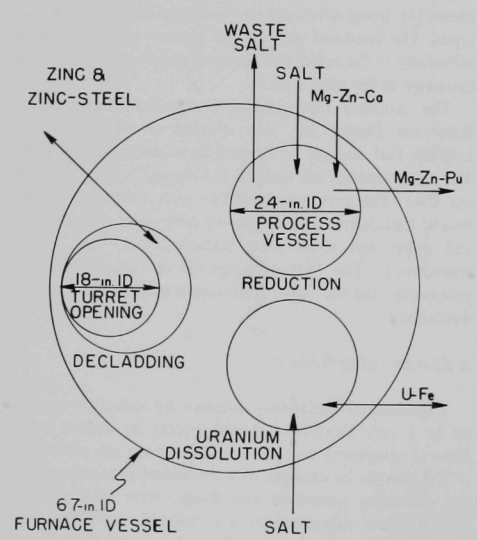

Fig. I-1. Head-End Processing Unit—Plan View. ANL Neg. No. 308-2535.

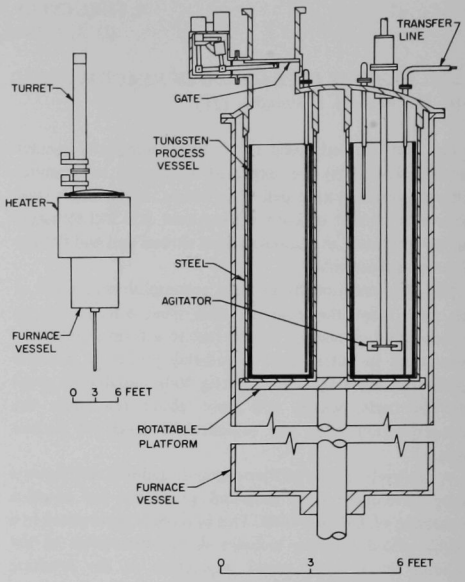

Fig. I-2. Head-End Processing Unit—Elevation View. ANL Neg. No. 308-2376.

being either discarded or recovered from the waste steel by vacuum distillation. The salt remains in the vessel during this step.

After the zinc is removed, the three vessels in the head-end furnace are rotated (clockwise 120°, see Fig. I-1). Prior to rotation, the vessels (on the platform) must be lowered about 7 ft so that they are not obstructed during rotation by agitators and transfer lines (see Fig. I-2). After rotation, the vessels are raised to the operating level. The mechanisms and seals for raising, lowering, and rotating these vessels are below the heated zone.

Once rotated to the reduction position, a process vessel is charged with Mg-Zn-Ca alloy and additional salt in preparation for the reduction step. Agitation for about 90 min promotes reduction of fuel oxide. At the end of this period, agitation is stopped and the metal and salt phases separate. The salt phase is pressure-transferred out of the vessel as waste; the Mg-Zn-Pu solution (~10 wt % plutonium) is pressure-transferred from the vessel as recovered product and is cast as an ingot. Maximum pressures of about 5 and 12 psi, respectively, are required for the two transfers. The uranium remains as a precipitated phase in the bottom of the vessel. Next, a small amount of fresh Mg-Zn alloy is charged to the vessel to wash the precipitated uranium and extract additional plutonium. This wash solution is also pressure transferred out of the vessel and

combined with the product solution. (During the reduction step, a decladding step is performed simultaneously in the preceding station.) The vessels are again lowered, rotated 120°, and raised to new positions. At the uranium dissolution position, an alloy of U-12 wt % Fe is added to the vessel and the uranium in the vessel is dissolved, producing U-5 wt % Fe. This dissolution has been experimentally determined to occur in about 10 min, after which the uranium solution is transferred out of the vessel for recovery. The high density of this solution necessitates a transfer pressure of 75 psi. (Alternative solvents for the uranium are available, but U-Fe is attractive because it can contain a very high concentration of uranium at 800°C and because iron is the only reagent required.)

The process vessel is then inspected for fissile-material content by neutron-irradiation techniques. If excessive fissile material is present, no fuel is charged to the vessel at the decladding station and corrective measures are taken when the vessel reaches the reduction station. If the fissile-material content is acceptable, salt is added in preparation for the next decladding run. Sufficient oxidant (possibly $MnCl_2$) is employed in this salt to assure that any uranium heel remaining in the process vessel is oxidized.

With further rotation of the three process vessels, the decladding-reduction-dissolution cycle continues. The three steps normally proceed simultaneously. The vessels are rotated 120° once every 2 hr; 36 subassemblies are processed per day, equivalent to nearly 5 tons of fuel per day. The quantities of constituents of inlet and outlet process streams are listed in Table I-1.

Ingots of the waste salt and waste zinc may be cast in disposable steel molds, or the zinc may be recovered by vacuum evaporation and recycled to reduce the waste volume.

These wastes are monitored for fissile-material content and recycled if necessary. The bulk of the nobler elements is separated from the plutonium with the uranium, thereby removing a source of sludge in the acid dissolution step.

TABLE I-1. Inlet and Outlet Process Streams

Basis: one operating day
(quantities in tons except where noted otherwise)

Feed	
Fuel	
UO_2	4.17
PuO_2	0.44
Fission Products	0.19
Steel	6.7
Reagents	
Zinc	17.7
Salt	9.0
Magnesium	1.8
Calcium	1.5
Iron	0.2
Products	
Mg-Cu-Pu (10 wt % Pu)	3.9
U-Fe (95 wt % U)	3.8
Wastes	
Zinc-Steel	18.3 (750 gal)
Salt	11.3 (1500 gal)
Steel (compressed)	4 (200 gal)
Gas	16 ft^3 at 225 psi

Dissolution of the Mg-Zn-Pu ingot in the acid dissolution step of a solvent extraction process would consume approximately 4.7 times as much acid as would be required for dissolution of an equivalent amount of UO_2-PuO_2 fuel. The Mg-Zn-Pu solution could be concentrated by evaporating off most of the zinc and magnesium prior to acid dissolution. If U-Fe alloy is dissolved in addition to Mg-Zn-Pu, the total acid consumption would be about 5.9 times that for an equivalent amount of UO_2-PuO_2. The cost of the greater acid consumption is insignificant (~0.0008 mill/kW-hr), but the effects on dissolver design, gas handling, and waste disposal might be important. The effects on the succeeding process steps of adding magnesium, zinc, and iron cations must also be evaluated. Dissolution kinetics in nitric acid have been demonstrated to be very good if the plutonium is in a magnesium or Mg-Zn solution; the absence of iodine and tritium and of nobler metals (particularly ruthenium) from the plutonium dissolver is an obvious advantage.

Fission-gas containment. The cover gas in the processing vessel during decladding is composed of xenon, argon, and krypton. It is not maintained at a specific composition but is the mixture that results from the gases that enter the decladder, i.e., its composition depends on the type of fuel being processed and its fission-gas content. The major addition of argon occurs when the transfer turrets are evacuated (after fuel decladding) and refilled with gas from the cell gas system; if the turret were not refilled with cell gas, process cell contamination with radioactive gases would occur during discharge of the upper portion of the subassembly from the turret and during charging of the next load of subassemblies to the turret. Since the input of argon to the decladder is low, the fission gases are collected in highly concentrated form. For the reference fuel, the composition is about 64% Xe, 29% Ar, and 7% Kr.

The gas used to make pressure transfers of solutions between vessels is compressed to 100 psi and stored for reuse. Accumulated gases are removed periodically and further compressed to 225 psi for permanent storage in cylinders.

2. *Engineering Development-Decladding Kinetics*

(I. O. Winsch, T. R. Johnson, J. J. Stockbar, T. F. Cannon, R. W. Clark)

Removal of stainless steel from LMFBR fuel elements is being investigated as a head-end process to prepare discharged fast reactor fuels for subsequent processing steps in fuel recovery plants. Additional information has been obtained on the rate and mechanism of attack of stainless steel by zinc at 800°C. Earlier data (ANL-7675, pp. 22-23) had shown that liquid zinc rapidly penetrates stainless steels at 800°C, even when the bulk solutions are saturated with iron and chromium. Metallographic examinations reported

earlier (ANL-7675, pp. 36-37) indicated that the mechanism of attack is the leaching of nickel from the austenitic solid phase and the freeing of grains of iron-chromium alloy, which then are carried by zinc into the bulk solution.

In the experiments completed during this report period, stainless steel dissolution rates were determined from the depth of zinc penetration into solid stainless steel samples immersed in Zn-Fe-Ni-Cr mixtures for known periods of time. The effects on the rates and mechanisms of liquid-metal decladding of (1) stainless steel and nickel concentrations in the melt and (2) agitator speed were studied.

a. Experimental Conditions

Several experiments (ZDS series) were conducted to determine the relative rates of zinc dissolution and penetration of stainless steel by zinc containing known concentrations of stainless steel and nickel.

The test procedure was to immerse a weighed sample of Type 304 stainless steel tube (3/4-in. OD, 5/8-in. ID, 4-in. long) for a specified time in ~10 kg of Zn-Fe-Cr-Ni melt [5] held at 800°C in a 5 1/2-in.-ID tungsten crucible. The tube was immersed vertically, and the melt was stirred with an agitator, 2 in. in diameter and 0.53 in. high and having two blades pitched at a 45° angle. The agitator speed was varied from 0 to 500 rpm, but in most tests it was 100 rpm. After a tube was exposed for 1 to 30 min, it was removed from the zinc solution. The concentrations of iron, chromium, and nickel in the melt were not changed significantly by the dissolution of metal from a single sample tube. After tests at one melt composition were completed, additional stainless steel or nickel was added to the melt, and stainless steel dissolution rates were measured in melts having the new compositions.

Some of the tubes that had been exposed were placed in a vacuum retort to remove adhering zinc, then weighed. The difference between the tube weight before immersion and the tube weight after retorting was the weight loss due to dissolution in zinc.

All of the tubes were sectioned, polished, and etched. The thicknesses of the inner and outer reaction zones and of the unaffected steel were measured. The difference between the original thickness of the tube wall and the final thicknesses of unaffected steel after immersion was the depth of penetration of zinc into the stainless steel.

The composition of the liquid metal phase was determined by analyses for iron, chromium, and nickel or, in cases where samples were not obtained, the composition was calculated. This calculation was based on the assumptions that all of the nickel added was in the liquid phase, that the cosolubilities of iron and chromium in zinc at 800°C are 5.8 wt % and 1.0 wt %, respectively, and that the solid phase in equilibrium with the saturated zinc solution contains 45 wt % zinc. This composition of the solid phase is based on the iron-zinc phase diagram [6]. The actual cosolubilities in the quaternary system have not been studied in detail, but the values of iron and chromium given above are averages of values found in our dissolution studies. In most cases, the calculated liquid compositions agreed well with the compositions determined by analysis of filtered samples. However, the analysis of a filtered sample taken at the end of ZDS-13 was approximately 3 wt % Fe, 0.6 wt % Cr and 8.5 wt % Ni compared with the calculated values of 5.8 wt % Fe, 1.0 wt % Cr, and 12.8 wt % Ni. This analysis is being checked.

b. Results and Discussion

This work indicates that the rate at which zinc penetrates into Type 304 stainless steel is primarily related to the nickel content of the liquid zinc phase. In run ZDS-12, depths of zinc penetration were determined for test pieces exposed to melts containing 15 to 26 wt % stainless steel and with agitator speeds of 0 and 500 rpm. With 15 to 19 wt % stainless steel in the melt, the nickel concentration in the solution was 1.42 to 1.97 wt % and the zinc penetration depth was 0.44 to 0.46 mm for a 5 min immersion time. With 20 to 26 wt % stainless steel in the melt, the melt contained 2.14 to 3.22 wt % nickel, and the penetration depth in 5 min was 0.41 to 0.42 mm. The agitator speed had no appreciable effect on the penetration depth.

The penetration of Type 304 stainless steel by zinc as measured in four experiments (ZDS-5, -6, -12, and -13) is shown in Fig. I-3. In this graph, total compositions represent the total amounts of stainless steel and nickel added to the zinc, and liquid compositions represent values calculated as described above.

The data show that penetration of the stainless steel was rapid during the first 5 min of immersion, as indicated by the positive intercepts when the curves in Fig. I-3 were extrapolated. After about 5 min of immersion time, the

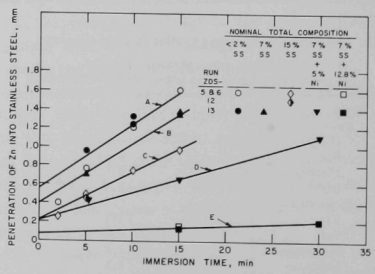

Agitator Speed: 100 rpm for ZDS-5, -6, and -13
0 and 500 rpm for ZDS-12

Liquid Compositions:

Curve:	A	B	C	D	E
Fe (%)	<1	5.2	5.8	5.8	5.8
Cr (%)	<0.2	1.0	1.0	1.0	1.0
Ni (%)	<0.1	0.6	1.4	5.5	12.8

Fig. I-3. Penetration of Type 304 Stainless Steel by Zinc at 800°C. ANL Neg. No. 308-2536.

penetration rate decreased and the thickness of the reaction layer appeared to reach an equilibrium thickness, indicating that the rate of dissolution or removal of solids from the reaction layer and the rate of penetration were equal. The reaction layer had little strength at 800°C. Once the zinc penetrated the steel cladding completely, the remaining cladding crumbled and for all practical purposes the fuel was declad. It is believed that the penetration data are the most pertinent to the decladding studies.

On the basis of measurements made to date, the steady-state penetration rate can be represented satisfactorily as a function of only the calculated nickel concentration, i.e., by

$$R_{SS} = a(C^*_{Ni} - C_{Ni})^2 \qquad (1)$$

where R_{SS} is the steady-state penetration rate, mm/min; a is a constant; C^*_{Ni} is the nickel concentration in bulk solution at zero penetration rate, weight fraction; and C_{Ni} is the calculated nickel concentration in bulk solution, weight fraction. Figure I-4 shows the measured penetration rates as a function of calculated nickel concentrations and also shows a curve representing the above expression with $a = 0.236$ and $C^*_{Ni} = 0.17$ weight fraction.

The iron and chromium concentrations in the bulk solution, as well as the nickel concentration, influenced the penetration rate during the first 5 min of immersion, as shown by the different values for the intercepts of the extrapolated curves in Fig. I-3. The concentrations of the three steel constituents affected the thickness of the reaction layer. Layers were thicker on samples exposed to solutions containing larger amounts of steel constituents. Upon exposure of test pieces to solutions saturated with iron and chromium and containing 5 to 13 wt % Ni, the samples grew in size and lost little if any weight, although the penetration rate was significant and could be predicted by Eq. 1.

At present, not enough measurements have been made

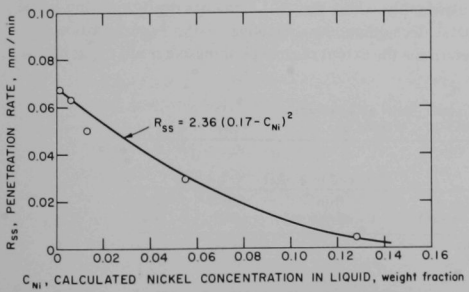

Fig. I-4. Steady-State Penetration Rate of Type 304 Stainless Steel by Zinc. ANL Neg. No. 308-2537.

to allow quantitative conclusions relating reaction layer thickness and weight loss to agitation rate and solution compositions. However in melts not saturated with iron and chromium, the weight loss of samples was observed to be linear with exposure time and to depend on the concentrations of iron, chromium, and nickel in the melt and on the agitation rate.

In experiment ZDS-12, the limit to which the zinc solution could be loaded with stainless steel at 800°C was investigated, as well as the penetration rate. The highest stainless steel content was 26 wt %. It was found that only 25% of this paste-like zinc stainless steel mixture could be poured from the crucible into a mold, but that zinc containing 20 wt % steel can be transferred.

c. Conclusions

The results of these experiments indicate that high penetration rates would occur in zinc mixtures containing up to 26 wt % stainless steel, but that zinc-26 wt % stainless steel would be difficult to transport as a fluid.

Kinetic data show that, to a first approximation, the rate of penetration of stainless steel by zinc is determined by the nickel concentration in the bulk solution. Iron and chromium concentrations appear to affect the dissolution rate also, but to a lesser extent, during the initial period when a reaction layer is forming, the dissolution rate decreases with increased iron and chromium concentrations Knowledge of the relationship of stainless steel dissolution rate to nickel concentration in the liquid phase will be useful in developing a stainless steel decladding process.

3. Engineering-Scale Experiments (I. O. Winsch, T. F. Cannon, J. J. Stockbar)

a. Basket-Draining Experiments

In one concept of liquid metal decladding of LMFBR fuel, three fuel subassemblies are contained in a basket during decladding in liquid zinc. After the stainless steel components of the subassembly (the shroud, cladding, and end hardware) are removed into the zinc the basket (which contains UO_2-PuO_2) is lifted out of the zinc melt.

Several experiments have been performed to evaluate basket design and decladding techniques on the basis of the composition of the fuel oxide-metal heel in the drained basket. The basket initially used in these experiments consisted of a Mo-30 wt % W frame enclosed by a 70-mesh tungsten screen that allowed zinc to pass into and out of the basket. The screen proved too fragile for the operations performed and was replaced in the following three experiments with an 0.030-in. wall tantalum cylinder containing approximately one hundred 1/16-in. holes (Fig. I-5). The tantalum cylinder was 6 in. high, the holes were spaced at

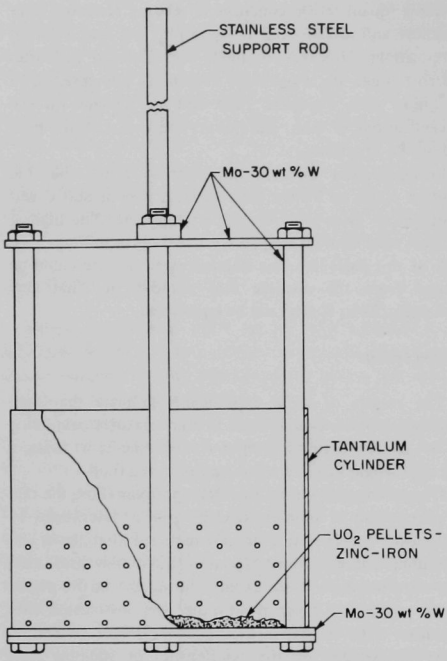

Fig. I-5. Experimental Decladding Basket (5-3/4-in. Dia by 10-3/4-in. High) at the End of a Decladding Experiment. ANL Neg. No. 308-2538.

1-in. intervals on the circumference and at 1/2-in. intervals up the lower 3 1/2 in. of the wall.

At the beginning of an experiment, the basket was charged with a stainless steel tube (4-in. OD, 1/8-in. wall, and 5-in. height) and UO_2 pellets or crushed pellets of a selected particle size distribution (see Table I-2). (At present, the particle size distribution for declad, irradiated LMFBR fuel is not known.) The melt, contained in a tungsten vessel, consisted of 65 kg of zinc covered with 3 kg of $MgCl_2$-30 mol % NaCl-20 mol % KCl. The basket and contents were immersed in zinc at 800°C, and the contents of the vessel were agitated at 300 rpm with a 3 3/4-in. slant-blade paddle. After a 2.5-hr exposure, the basket was removed from the melt. Before the basket cooled, the tantalum wall was slid upward, and the contents were scraped from the base of the basket into a stainless steel tray. The composition of the zinc-steel-oxide residue in the basket was determined by dissolving the material scraped from the basket in an acid solution, acid-cleaning the basket to remove unscraped material, and analyzing the combined solutions. The results for the runs in which the tantalum cylinder was employed are presented in Table I-2.

For two runs in which a portion of the UO_2 charge was present as crushed pellets, a significant loss of oxide fines (~10%) from the basket was observed. The loss was greater when the oxide charge consisted entirely of fines. If the basket concept is to be applied to decladding fuel that contains an appreciable fraction of oxide fines, modification of the basket design may be necessary.

Any waste zinc-steel that is to be discarded must have a low plutonium content. Therefore, if this decladding technique is adopted, some provision will be made to remove any $(U,Pu)O_2$ fines (perhaps by filtration of the melt) prior to discard.

A second objective of decladding is to achieve maximum separation of fuel oxide from stainless steel. In the three basket-draining experiments performed, about 10% of the iron originally in the simulated subassemblies was contained in the zinc-stainless steel heel. The quantity of heel roughly equalled the quantity of UO_2. Sloshing or other agitation of the basket contents may improve the separation of the steel from the fuel oxide.

b. Gas-Release Experiments

Three experiments have been performed simulating the release of fission gas from irradiated fuel elements in a fuel subassembly when the fuel elements rupture during liquid metal decladding. An objective of the experiments was to determine the extent of zinc splashing as a result of gas release.

TABLE I-2. Basket-Draining Experiments (Melt: 65 kg of zinc, 3 kg of $MgCl_2$-30 mol % NaCl-20 mol % KCl)

	Basket Charge			Retained in Basket			
	Uranium Oxide		Stainless				
Run	Pellets[a] (kg)	Fines (kg)	Steel (kg)	Uranium (% of charge)	Iron (% of charge)	Zinc (kg)	Salt (kg)
SD-3	0.50	0	0.95	100	11	0.46	0.03
SD-4	0.25	0.11[b]	0.96	97.5	16.3	0.84	0.07
SD-5	0	0.20[c]	0.96	86.4	6.2	0.49	0.09

[a]0.21-in. dia by 0.25-in. length.
[b]-14 +25 mesh, 0.05 kg
-25 +45 mesh, 0.035 kg
-45 +80 mesh, 0.025 kg
[c]+14 mesh, 0.10 kg
-80 +170 mesh, 0.05 kg
-170 +325 mesh, 0.05 kg

Irradiated fuel elements containing fission-product gases were simulated with argon-filled Type 304 stainless steel tubes (0.25-in. OD by 0.010-in. wall by 5.5-in. length). The bottom end of each tube was welded to an ~2-in.-long by 0.222-in.-dia steel rod, plugging that end of the tube. Each tube was charged with two 0.25-in. lengths and one 4-in. length of 0.222-in.-dia stainless steel rod. The other end of the tube was attached by means of compression fittings to an additional length of 0.25-in.-dia tubing and a pressure gauge. The total gas volume in each of these tube assemblies was about 25 cm^3. The tubes were each pressurized with argon, after which the valve leading to the argon supply was closed.

In each of two experiments, two tube assemblies were fastened inside a 2-in.-OD stainless steel tube (simulating a shroud) that had a 5/8-in. opening in the bottom. This assembly was immersed to a depth of 3 in. in a zinc melt.

In the first experiment, the zinc temperature was 785°C and the shroud was sealed except at the bottom. During immersion, the pressure in each tube, originally 54 atm, increased to 61 atm. After 4.9 min, the pressure in one tube decreased slowly; after 5.7 min, the pressure in the other tube decreased rapidly. The tube assembly was then removed and inspected. Uniform corrosion of the exposed surfaces had occurred, and the gas had escaped through small cracks in the tube wall. The rods had remained in the tubes. Some zinc was blown out of the crucible (3-in. freeboard) by the gas escaping from the bottom of the shroud.

For the second experiment, six 1/4-in. holes were drilled 11 in. above the bottom of a 2-in.-dia, 37-in.-long tube simulating a shroud. Two simulated fuel elements were mounted in the 2-in.-dia shroud and immersed to a depth of 3 in. in molten zinc at 800°C. In one tube, the pressure rose from 49.6 to 52 atm and in the other it rose from 48.6 to 52 atm in 1.75 min. Rapid pressure release occurred after 1.5 and 1.75 min, respectively, for these two tubes.

Inspection after the run showed that the stainless steel plugs had separated from the tube bottoms, but the rods had remained inside the tubes. Some zinc had splashed 37 in. to the top of the shroud, but no splashing outside the shroud had occurred.

In the most recent experiment, again two pressurized simulated fuel elements were used, but these tubes were in the center of a bundle of fifteen 1/4-in.-dia steel rods (each wrapped with a 0.048-in.-dia spacer wire) that simulated other fuel elements in a subassembly. The spacing between tubes and rods was similar to that expected for fuel subassemblies. The bundle was placed inside the vented, 2-in.-dia shroud used in the second experiment. The simulated subassembly was immersed to a depth of 3 in. in zinc held at 795°C. The pressure increased from 52.7 to 54.4 atm and from 56.1 to 58.5 atm in the tubes. Gas was released rapidly after 1.87 and 1.95 min. Inspection of the tube after the run indicated that the steel plugs had separated from the tubes. Zinc had splashed around the tubes and rods inside the shroud to a height of only 20 in. There was no evidence that zinc has splashed outside the shroud.

The experimental results indicate that zinc will be splashed by fission product gases during zinc decladding but will present no serious problems.

4. Control of Fission-Product Iodine in a Pyrochemical Head-End (M. Krumpelt, J. J. Heiberger)

Reprocessing of 30-day-cooled fast reactor fuel by a Purex process requires decontamination factors for iodine [7] of 10^7-10^8 in the head-end to avoid accumulation of iodine in the organic streams. A pyrochemical head-end comprising decladding in molten zinc and reduction of the oxide fuel to metal is being investigated. The fuel is immersed in liquid metals in both of these steps, and the volatile iodine that is released when the cladding dissolves in the zinc melt reacts with the zinc. The degree of reaction of iodine with zinc in the decladding step has been determined experimentally, and the results are presented here.

The basic assumptions were as follows: (1) iodine exists in the fuel element mainly as elemental iodine and to only a small extent as CsI and FeI_2; (2) when the lower end of a fuel element is immersed in zinc, the cladding ruptures and the elemental iodine (mixed with xenon and krypton) flows from the fuel-element plenum through the annulus and is released through the breach in the cladding; (3) the gas mixture from the fuel element is emitted into the zinc pool as a sequence of bubbles.

In experiments simulating the release of fission-product gases from fuel elements, an argon-iodine mixture was generated by passing argon carrier gas over iodine crystals (labelled with ^{131}I) in a U-tube held at a constant temperature. The argon-iodine mixture was then bubbled through a 5-mm-ID tube into a pool of liquid zinc that was covered by a 2-cm-deep layer of 59 mol % LiCl-41 mol % KCl. The gas stream was next passed through a safety trap and then through a 0.1*M* $Na_2S_2O_3$-1*M* NaOH scrubber solution to remove any unreacted iodine. Although iodine at first reacts with zinc, none of the iodine was in the zinc phase at the conclusion of an experiment. To determine the amount of iodine that had reacted with zinc, all of the LiCl-KCl was dissolved in water at the end of an experiment and aliquots of this solution and of the scrubber solution were counted. From the ratio of the two counting rates, the decontamination factor of the zinc pool was calculated. In various experiments, the depth of the zinc pool, the gas flow rate, the iodine content in the carrier gas, and the temperature of the zinc were varied. The experimental parameters and results are listed in Table I-3.

The counting rate in the aqueous scrubber solution never

TABLE I-3. Iodine Absorption in Zinc

Expt.	Depth[a] of Zinc Pool (cm)	Temp of Zinc (°C)	Concentration of Iodine in Ar (at. %)	Ar-I_2 Flow Rate (ml/min)	Amount of Iodine Transported (mg)	Cover Salt Activity [counts/(min) (aliquot)]	Scrubber Activity [counts/(min) (aliquot)]
1	17	500	0.1	65	22	3×10^4	Background[b]
2	10	800	0.1	65	35		Background
			0.1	150	38		Background
			0.2	150	76	1×10^5	Background
3	3	800	0.2	150	205		Background
				300	205		Background
				500	205	5×10^5	Background
4	3	500	0.2	150	205		Background
				300	205		Background
				500	205	3×10^5	Background
5	3	500	3×10^{-3}	300	17	7×10^5	Background
6	10	800	0.2	150	630	1.2×10^6	Background
7	Salt Only	800[c]	0.1	150	25	7.0×10^3	7.3×10^3

[a]Cover salt depth was 2 cm in all runs.
[b]Error in background is ±8 counts/min.
[c]Temperature of salt phase.

exceeded the background level. Iodine was completely absorbed at a zinc pool depth of only 3 cm and with flow rates of 500 ml/min, which corresponded to 70 bubbles/sec through the pool. The flow rate of gas through the zinc pool had no apparent effect on the reaction, and the reaction was extremely rapid.

To prove that iodine capture in the zinc-salt melt rather than reaction with apparatus components or a malfunction of the aqueous scrubber was the reason for counts in the scrubber remaining at background, an experiment was conducted with zinc absent. At the end of this experiment, one half of the iodine was detected in the aqueous scrubber and the other half was in the cover salt.

Further study of the reaction of iodine in the Zn-LiCl-KCl medium indicated that it probably occurs in two steps. Initially, ZnI_2 forms by the reaction of iodine with zinc. However, iodine would not be retained in the zinc-salt melt as ZnI_2 since this compound has a vapor pressure of 760 Torr at 625°C. At 800°C (the normal temperature of the bath), ZnI_2 would be expected to evaporate from the melt if it did not undergo further reaction.

A Raman spectroscopic analysis [8] was made of a sample of molten salt prepared by bubbling iodine through zinc and a LiCl-KCl cover layer until the mole fraction of iodine in the salt was 0.05 (see Section V.B.2 of this report). The only observed peak in the Raman spectrum at 450°C was attributed to $ZnCl_4^{2-}$. This finding suggests that the second step is a reaction between ZnI_2 and LiCl-KCl:

$$ZnI_2 + 4KCl = K_2ZnCl_4 + 2KI$$

Owing to this reaction, iodine is completely retained in the cover salt, and no iodine will escape from a pyrochemical head-end. In a plant operation, the cover salt would be discarded as dry active waste.

Other possible chemical states of fission product iodine, CsI and FeI_2, have not been investigated experimentally. Based on free energies of formation, any CsI present would not be expected to react further in the decladding or reduction steps but to collect in the cover salt. Any ferrous iodide present would be reduced by metallic zinc to ZnI_2 and iron. These data suggest strongly that adequate control of iodine in pyrochemical head-end steps is feasible under process conditions.

B. CONTINUOUS CONVERSION OF U/Pu NITRATES TO OXIDES (A. A. Jonke, N. M. Levitz, G. J. Vogel, D. E. Grosvenor, S. Vogler, F. G. Teats, R. V. Kinzler)

A necessary and presently expensive step in the nuclear fuel cycle for LMFBR fuels is the conversion to an oxide form of uranium and plutonium nitrate in nitric acid solutions produced in nuclear fuel reprocessing plants. This conversion must provide the fuel fabricator with powdered fuel oxides suitable for the fabrication of fuel shapes (e.g., pellets) on a safe, reliable, economic basis. In addition, it is in itself desirable to convert plutonium nitrate in nitric acid solutions to a powder form since powder is more easily and safely shipped than liquid.

Current conversion processes consist of a number of steps, among which are precipitation, filtration, and calcination. An alternative to these processes that offers potential economic advantages and uniform product is continuous fluidized-bed denitration of uranium-plutonium nitrate in nitric acid solutions to form UO_3-PuO_2 powder, followed by fluidized-bed reduction to UO_2-PuO_2. The denitration and reduction steps are based on extensive fluidized-bed denitration technology developed for uranyl nitrate and waste aluminum nitrate solutions [9]. An integrated program for laboratory studies and experimental work on a pilot scale is described. The program includes calculational studies on the process scale-up potential for geometrically favorable column shapes, such as slabs, and an evaluation of powders as fuel materials.

1. Laboratory Program

The laboratory program is directed toward an early characterization (composition and structure) of the products from denitration of U-20% Pu feed solutions and hydrogen reduction of the denitration product, and an evaluation of pellets formed by pressing and sintering. Other subjects under study or under consideration include the following:

1) Development of a procedure (to be used in the pilot-plant program) for dissolving the mixed-oxide products of denitration.

2) Determination of (a) the plutonium valence state after dissolution of uranium-plutonium materials and (b) the rate of change in valence as a result of standing.

3) Determination of the effect of the plutonium valence (IV and VI) in the nitrate solution on the properties of the oxide product.

4) Measurement of the solubility limits for plutonium in uranium-plutonium nitrate solutions in the region of interest, i.e., in solutions containing ~2.0*M* total metal ions including 20% plutonium.

a. Drop Denitration

Laboratory-scale drop-denitration experiments provided product material for initial examination and analysis. In these experiments, solutions containing uranyl nitrate alone, plutonium nitrate alone, and U-20% Pu nitrate (1.5*M* total metal ions) were fed dropwise to a hot surface maintained at a temperature of 300 to 600°C. Approximately 6 g of oxide was prepared in each experiment.

Selected oxide products were analyzed with the following results. X-ray diffraction examination of the product formed at 500°C showed that uranium was present mainly as gamma-UO_3; material prepared at lower temperatures (~400°C) contained gamma-UO_3 and $UO_3 \cdot H_2O$. The only plutonium form identified was PuO_2 of poor crystallinity; examination of UO_3-PuO_2 samples prepared at 300 and 450°C showed that oxide prepared at the higher temperature was slightly more crystalline. Plutonium dioxide products made at 300°C from a 65% Pu(VI)-35% Pu(IV) nitrate solution and from a Pu(IV)-only nitrate solution showed similar diffraction patterns; the latter product appeared to be more crystalline.

Electron microprobe examination of a mixed UO_3-PuO_2 product prepared at 450°C showed good distribution of PuO_2 in the UO_3 matrix. Two types of examinations were made, scanning of 8 by 10-μm and 80 by 100-μm areas and single-spot scanning, all with a 0.5-μm-dia beam. It was shown that segregation does not occur, since in a check of 30 individual spots, not a single spot was found to be completely free of plutonium or of uranium (although the concentrations of plutonium varied considerably). The good distribution of plutonium in the powder was confirmed by autoradiography, using a cellulose nitrate film "etched" by plutonium alpha radiation.

b. Development of a Dissolution Procedure for Denitration Product

A procedure for dissolving UO_3-PuO_2 in nitric acid was developed in a series of scouting laboratory studies. This step is needed for the pilot-plant program to permit recycling of denitration products and thereby minimize plutonium inventory requirements. Dissolution tests were made with UO_3-20% PuO_2 and with PuO_2 alone that had been prepared by drop denitration at 300, 450, and 600°C. Nitric acid molarities were 5 to 16, and dissolution temperatures were 95 to 120°C.

Data indicated that (1) oxide prepared at the lowest temperature (300°C) was easiest to dissolve, (2) the rate of oxide dissolution was not affected significantly by the dissolution temperature (95 or 120°C), (3) the dissolution rate was not affected by a higher final actinide concentration (0.35*M* and 1.5*M* total metal ions) when dissolution was with 16*M* nitric acid, and (4) a higher fraction of plutonium was dissolved in 16*N* acid than in 5*N* acid. Also, the PuO_2 in mixed UO_3-PuO_2 dissolved more rapidly than PuO_2 alone in 16*M* nitric acid at 120°C; 99% dissolution was achieved in 5 hr in the case of the mixed oxide as compared with 30–50% dissolution for PuO_2 alone in a similar period.

c. Stability of Plutonium Ions in Nitrate Solutions

Simulated feed solutions were used to examine the stability of plutonium ions in nitrate solutions. The change in valence distribution of plutonium (VI) and (IV) ions in nitrate solutions containing 1.35*M* plutonium was measured spectrophotometrically. The amounts of Pu(VI) and Pu(IV) were calculated from the optical spectra. These data are shown in Fig. I-6 along with data reported by Crawley [10] for 0.82*M* Pu in 5.3*M* HNO_3 solution and earlier ANL data for a solution containing 1.2*M* $UO_2(NO_3)_2$, 0.3*M* Pu, and 2–4*M* HNO_3.

For the initial 50-day period, the concentration of Pu(VI) is a linear function of time, indicating a zero-order reaction with respect to Pu(VI). After 50 days, the rate at which the concentration of Pu(VI) ions decreases apparently increases. The rate of valence change in the range from 0.3 to 1.35*M* plutonium is independent of the initial plutonium concentration. No spectra for trivalent or pentavalent plutonium were observed in the spectrophotometric examination of the 3*M* HNO_3 solution containing 1.35*M* plutonium.

d. Oxide Reduction and Pellet Formation

Conversion of UO_3-PuO_2 powder to UO_2-PuO_2 powder

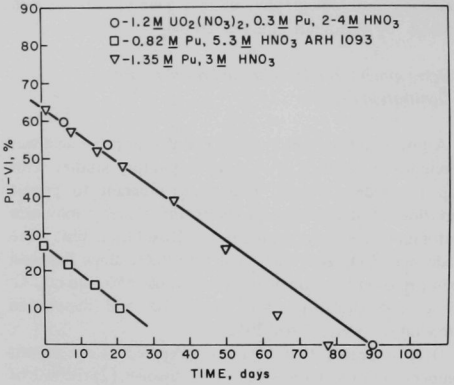

Fig. I-6. Reduction of Pu(VI) in HNO_3. ANL Neg. No. 308-2331.

is a necessary step in the LMFBR fuel cycle. The UO_2-PuO_2 powder will be subsequently formed into pellets. Exploratory laboratory reduction and pelletizing tests were performed to determine the sinterability of fuel oxide prepared by denitration. In these tests, UO_3-PuO_2 powder was prepared by a dropwise addition of a nitrate solution containing 1.65*M* total U + Pu into a quartz tube at 300°C. The UO_3-PuO_2 powder was reduced to UO_2-PuO_2 powder with hydrogen at 500 or 550°C in a stainless steel crucible. The UO_2-PuO_2 powder was then pressed into pellets (~1/4 in. in diameter by ~0.2 in. long) which were sintered.

Two pellets were prepared by pressing at 87,000 psi; two other pellets were first pressed at low pressures (~1500 psi), then granulated through a 45-mesh sieve, and finally pressed at 87,000 psi. Next, one pellet from each of the above pairs was sintered at 1650°C for 4 hr, and the other two pellets were sintered at 1750°C for 90 min; an argon atmosphere was used in all tests. Pellet densities ranged from 83 to 89% of theoretical. The combination of prepressing, granulation, and the higher sintering temperature gave the highest density to date. Material reduced at the two different temperatures (500 and 550°C) and otherwise treated identically had the same final density (84% of theoretical). The results of these preliminary tests suggest that satisfactory $(U,Pu)O_2$ fuel pellets can be prepared by appropriate selection of pelletizing and sintering conditions.

One of the UO_2-PuO_2 pellets with a density 84% of theoretical was chemically analyzed, and was also physically examined with an electron microprobe (for homogeneity) and by X-ray diffraction. In the chemical analysis, oxygen content was determined by vacuum fusion, and the uranium and plutonium concentrations were determined amperometrically. The uranium, plutonium, and oxygen concentrations were 70.70, 17.60, and 11.75 wt %. The oxygen-to-metal atom ratio was 1.98, and the uranium-to-plutonium atom ratio was 4.0.

A pellet sample was examined by counting the characteristic X-rays of uranium and plutonium with an electron microprobe. Counting data obtained by two different scanning procedures and by scanning several different areas of the pellet appeared to indicate good homogeneity. No segregation of uranium or plutonium was observed. Trace stainless steel constituents that had been picked up during sintering were identified in the pellet.

A lattice parameter of 5.4602Å for the oxide was measured. Only a single set of diffraction lines was in evidence, indicating the presence of a single oxide phase. The measured lattice parameter was compared with the lattice parameter predicted from an earlier observed relationship between oxygen-to-metal ratio and the lattice parameter at a stated plutonium content (see Progress Report for April–May 1970, ANL-7688, pp. 214–215). The value for a_0 predicted by that relationship is 5.4610Å, which compares favorably with the experimental value.

2. *Engineering Program*

A fluidized-bed denitration pilot plant has been constructed for study of mixtures of uranium nitrate and plutonium nitrate solutions. Because of the broad experience with cylindrical columns in earlier denitration work [9], initial investigations will be done with a stainless steel cylindrical fluidized-bed denitrator 4 in. in diameter, which is considered critically safe for feeds containing up to 20% plutonium. A parallel effort will be the development of a slab-shaped column that offers nuclear criticality advantages when scaled up for high-plutonium systems.

a. Denitration Process

In the fluidized-bed denitration process, a heated bed of oxide particles (typical of the denitration product) is fluidized with air. Feed solution is sprayed into the bed through an atomizing nozzle. The liquid droplets either strike the particles and thermally decompose (depositing a fresh oxide layer) or decompose in the gas phase (forming small solid particles); the former phenomenon predominates. An overflow arrangement keeps the bed inventory in the denitrator constant. The off-gas contains NO_2, NO, O_2, and water, the composition varying with the temperature of denitration.

The denitration reaction is endothermic; the heat required for denitrating uranyl nitrate hexahydrate (UNH) alone at 230°C would be about 260,000 Btu/(lb) (mol uranium). Decomposition of our solutions, which typically are more dilute than UNH and contain excess nitric acid, will require an even larger heat input. The usual

denitration temperatures are 275 and 400°C.

b. Equipment

Figure I-7 is a simplified drawing of the pilot plant for the denitration experiments. The equipment consists of a fluidizing-gas preheater, a fluidized-bed denitrator, feed solution preparation and metering tanks, secondary filter, condenser, condensate receiver, demister, heater, and HEPA (High Efficiency Particulate Aerosol) filters. Instrumentation consists of appropriate temperature and pressure sensors with local or panelboard readouts, controllers, recorders, and a data logger. The major process items are installed in an existing 3- by 4-module glovebox.

The fluidized-bed denitrator consists of three separately flanged parts–the cone-shaped gas-distributor section at the bottom of the denitrator, the denitration section, and the filter chamber. The denitration section is fabricated of 4-in.-dia, schedule 40, Type 304 stainless steel pipe, 32 in. long. A spray nozzle and temperature or pressure sensors can be positioned at 3-, 6-, or 9-in. levels. The denitration section is heated by twelve 2000-W Watlow [11] resistance heaters, copper-spray-bonded to the exterior wall.

The filter chamber, mounted directly above the bed, is fabricated of 4-in.-dia, schedule 40, Type 304 stainless steel pipe, 47 in. long, and contains two sintered stainless steel filters [12]. The filters are each 18 in. long and have a nominal 10-μm pore size. The filters can be blown back manually or automatically. During a run, the two filters would be blown back alternately. Blowback air at 100 psig from the laboratory supply is stored in a 400-psi-rated stainless steel cylinder.

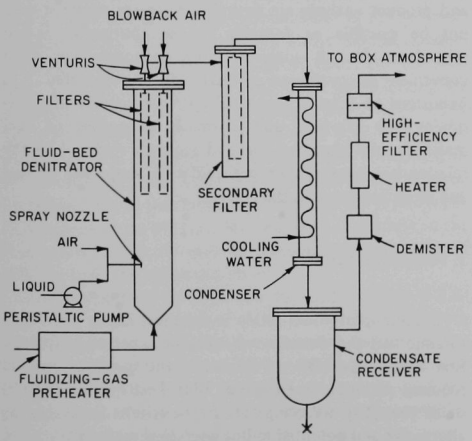

Fig. I-7. Equipment Components of 4-in.-dia Denitration Pilot Plant. ANL Neg. No. 308-2539.

c. Shakedown Experiments in the Pilot Plant

A series of six denitration experiments were made with uranyl nitrate solutions to check out equipment operability. The experiments, carried out "through the gloves" to simulate future work with plutonium-containing materials, were made over a wide range of operating conditions to determine any particle-size effects (i.e., growth or diminution trends in bed particle size). The operating conditions for these experiments are summarized in Table I-4. All runs were made at a denitration temperature of 300°C. The initial bed in each case comprised about 7200–8500 g of UO_3 with an average particle size of 162 μm, a bulk density of 4.2 g/cm^3, and a sulfate content of about 800 ppm. The presence of sulfate was not intentional; sulfate was merely a constituent of the available bed and feed stock.

Feed solutions were 1 to 2.4*M* uranyl nitrate in 0.2 or 1.0*N* nitric acid. The feed rates, which ranged from 50 ml/min of 1*M* uranyl nitrate to 107 ml/min of 2.4*M* uranyl nitrate, were equivalent to production rates of 22 to 105 lb UO_3/(hr)(ft^2 reactor cross section). The upper value is just above the design goal of 100 lb/(hr)(ft^2).

The inlet fluidizing air was fed at rates equivalent to a velocity of about 1 to 1.5 ft/sec (at column conditions). Air fed at the spray nozzle and decomposition gases augmented the gas stream volume so that the total gas flow rate was approximately double that of the fluidizing air. Volume ratios of nozzle air-to-liquid feed were 330 to 640.

Runs were judged on the bases of mechanical operability, ease of startup and shutdown, ability to maintain uniform feed rate and fluidized-bed level, and sufficient heat input capacity for the design goal of 100 lb UO_3/(hr)(ft^2). Results were generally good except in Run U-2, which was terminated within one hour of startup when a large temperature spread and unusual fluctuations in the differential pressure of the bed were observed. The bed was found to be agglomerated virtually into a single mass, but the cause was not determined. The duration of other runs was 3 to 14 hr.

Data were obtained on elutriation of fines (–200 mesh) from the bed, fines formation, particle growth (increase in average bed particle size), and the formation of agglomerates (+8 mesh). Are considered preliminary and conclusions tentative because runs were of relatively short duration and since results for uranium-plutonium systems may differ from those for uranium alone. The design goal of 100 lb UO_3/(hr)(ft^2) was reached when 2.0*M* uranyl nitrate was fed at about 100 ml/min.

Of the total UO_3 produced in a given run, about 5% was in the form of fines and about 5 to 10% as small agglomerates (+8 mesh). The relatively high linear gas velocities in the column, about 3 ft/sec including the decomposition gases, resulted in the bulk of the fines being elutriated from the bed and deposited on the sintered metal filters. For process application, it may be necessary to

TABLE I-4. Operating Conditions for Shakedown Experiments in Denitration Pilot Plant

Denitration Temperature: 300°C

Run No.	Run Duration (hr)	Starting Bed Weight (g)	Fluidizing Air Velocity (ft/sec)	Feed Solution Composition (*M*)		Feed Rate (ml/min)	Ratio of Nozzle Air to Liquid [scfm/(cm^3)(min)]	Duration of Each Blowback Pulse (sec)
				U	Excess HNO_3			
U-1	3	7244	1	1	1	50	-	0.5
U-2	2/3[a]	7318	1	1	1	100	-	0.5
U-3	10[b]	7678	1.5	1	1	75-100	500-640	0.5
U-4	14	7847	1.5	2.4	0.3	60-100	480-520	0.5-1.0
U-5	9.4[c]	8495	1.4	2.0	0.2	80-107	330-480	0.5-1.0
U-6	6	~8400	1.2	2.1	0.4	80	465	0.1

[a]Unscheduled shutdown because the bed became agglomerated; reason not known.
[b]Unscheduled shutdown because of plugged product overflow line.
[c]Unscheduled shutdown because of fines buildup on the sintered metal filters, resulting in excessive filter pressure drop.

offset the filter section so that the fines can be removed continually. This fines fraction can then be blended with the bulk product and fed directly to the reduction step.

A uniform bed inventory could not be maintained solely by continuous overflow of bed material because partial plugging of the sidearm takeoff line occurred. Therefore, in Run U-6, simultaneous withdrawal of material at the bottom of the column was tried. Although there was bridging of coarse material that accumulated in the conical section, a fairly uniform bed inventory was maintained by intermittent withdrawal of ordinary bed solids, whose flow was not restricted by bridging of large bed particles. The formation of coarse material needs to be eliminated, or else a means should be developed for removing coarse particles, perhaps by a larger bottom opening or a mechanical device (e.g., a screw). Coarse material can be recycled to a feed make-up system or be ground and blended with the bulk product stream for subsequent reduction. Additional work also is needed on the mechanics of solids overflow from fluidized beds.

Slight particle growth in the bed was evident from sieve analyses of product samples taken at half-hour intervals. Product sampled at the overflow point and at the bottom withdrawal point had similar particle growth patterns and comparable particle-size distributions, an indication that good mixing was occurring in the bed. From work to date, it cannot be predicted whether the growth trends would continue throughout a run or whether a steady-state particle-size distribution would be attained. Demonstration runs of long duration will be made to obtain information on this question.

The current program has given an insight into the characteristics of denitration pilot plant operation and has shown that the equipment and instrumentation were functioning properly. Work with uranium-plutonium is being planned. Critically safe auxiliary items (e.g., a dissolver to permit recycle of UO_3-PuO_2 and a feed storage vessel) are being designed. Sealing of windows and glovebox leak-rate tests will also be done prior to work with plutonium.

C. IN-LINE ANALYSIS IN FUEL FABRICATION

(A. A. Jonke, M. J. Steindler, J. G. Schnizlein, T. Gerding)

Reduction of the cost of LMFBR fuel fabrication is necessary to improve the competitive economic position of power-producing nuclear reactors. The economics of the fuel cycle will be strongly affected by analytical capabilities since in the absence of sufficient experimental data relating the effects of various fuel properties to fuel performance, rigorous specifications have been set for ceramic FBR fuel.

For operation of large-capacity fabrication plants on a sound economic basis, rapid, automated, and perhaps continuous in-line analytical methods for process control and product analysis are desirable. In cases where it may not be possible or desirable to use continuous in-line procedures for all analyses, more economical or more convenient discontinuous methods will be considered. It is important to develop analytical methods capable of determining the physical and chemical properties of fuel materials with the precision and accuracy required by the relationship between the preirradiation properties of fuel and its performance in the reactor.

1. Fuel Properties

Uranium-plutonium oxide is the most highly developed ceramic fuel and consequently may be expected to fuel the first commercial FBR. In this work, the specifications and required precisions for the Fast Flux Test Facility (FFTF) oxide fuel [13] are being used as the criteria for evaluating alternative and potential in-line analytical methods.

Initially, analytical methods for the determination of plutonium content (Pu/U ratio) and oxygen/metal (O/M) ratio are being evaluated because these determinations are necessary in every conceivable fabrication procedure. The specifications, precisions, and acceptable methods of measurement [14] of these properties are discussed below to provide insight to choices of potential in-line analytical methods.

a. Plutonium Content

Plutonium concentrations being considered for various LMFBR fuels range from 8 through 30%. The more probable contents appear to be 15, 18, 20, and 25%. Ternary phase diagram studies by Markin and Street [15] indicate that oxide material in the substoichiometric O/M region and containing up to 40% Pu is single phase at room temperature and above.

Controlled-potential coulometry is the method currently recommended for determining plutonium and uranium content of mixed-oxide fuel [16]. An alternative technique for determining the Pu/U ratio is in-line X-ray fluorescence, which is being evaluated here. X-ray fluorescence analysis is a sensitive, nondestructive method: exciting radiation (from an X-ray tube or a radioactive source) impinges on the sample and causes the emission of radiation that is characteristic of the elements present in the sample; by this method, uranium and plutonium concentrations can be determined rapidly and accurately.

b. Oxygen-to-Metal Ratio

The initial ratio of oxygen-to-metal (O/M) in the charged mixed-oxide fuel affects the compatability of the fuel with cladding during irradiation, as well as the thermal conductivity. The probable desired range of values for the O/M ratio is from 1.95 to 1.99. The O/M specifications are currently 2.07 ± 0.03 for UO_2 powder and 1.975 ± 0.025 for PuO_2 powder. The O/M value of 1.97 ± 0.02 for mixed-oxide or coprecipitated oxide pellets is attained in the sintering process. Since the O/M ratio changes during irradiation due to the thermal gradient and the oxidation of fission-product metals (i.e., Mo, Ba, Sr, Zr, and Nb) in the fuel, additional study may be required before a value of O/M for fuel fabrication can be set.

For determining the O/M ratio for oxide samples of 2 to 100 mg, a thermogravimetric method [17] of analyzing for oxygen is currently specified. An alternative method for the determination of the O/M ratio that may be adaptable for in-line use will be tested. This method depends upon the measurement of lattice parameters of the fuel material by X-ray diffraction techniques.

2. Procedure and Results

a. Determination of Plutonium Content

The analysis of the uranium and plutonium content of FBR oxide fuel by X-ray fluorescence of solutions is routinely practical to a relative precision of ±2%. At other sites, X-ray fluorescence has been applied to the analysis of (U,Pu) nitrate solutions, both inactive samples [18] and samples from process streams containing radioactivity [19] When the background count is taken into consideration, the relative standard deviation for these measurements [18] ranges from about 20 to 0.6% over the analytical range, 0.003 mg Pu/ml in the presence of 10 and 0.003 mg U/ml in the presence of 3.5 mg Pu/ml.

The most rigorous specification on plutonium content of FFTF fuel appears to be that for the core zone, which requires a relative precision of 0.5%. To attain this precision in analyzing solid oxide as powder or pellets, it is planned to define the effects of material properties such as high absorption coefficients, crystallite size, scattering by voids and surface roughness, and enhancement (secondary fluorescence). These matrix effects must be proved to be insignificant or measurable.

In this experimental program to demonstrate the practicality of this analytical technique, the effects of instrumental choices and sample presentation procedures are currently being studied. Careful attention is being paid to counting statistics since it is generally agreed that the precision of X-ray fluorescence analysis is limited by counting statistics.

Liebhafsky [20] has calculated the loss of intensity in each of nine identified processes for a flat-crystal spectrograph fluorescence apparatus. The two greatest losses of fluorescence intensity in X-ray fluorescence spectrometry are in the fraction of X-rays absorbed and re-emitted by the sample, 4.4×10^{-6}, and the fraction emerging from the collimators (geometric factor), 1.6×10^{-5}.

The fraction of X-rays absorbed and re-emitted by the sample is generally described as being due to a matrix effect. Since it is the largest loss factor, it has been the subject of considerable research in recent years. Two kinds of matrix effects are pertinent, absorption and enhancement. Absorption includes the effects of scattering from a surface, voids, and crystallites, as well as the absorption described in terms of mass absorption coefficients of other elements present. Enhancement or secondary fluorescence occurs when the characteristic radiation from one element has enough energy to excite the characteristic radiation of one or more other elements in the sample. This occurs in uranium-plutonium oxides because PuLα excites ULα. In thorium-uranium oxides, ULα excites ThLα.

A disadvantage of quantitative analysis by a fluorescence technique would be a requirement for a set of standards covering a range of important variables, such as composition (element concentration and matrix content), density, crystallite size, and absorption coefficients. However, Criss and Birks [21,22] have formulated methods (utilizing modern computers) whereby X-ray fluorescence can be calculated from fundamental parameters. Application of these methods should significantly minimize the number of standards necessary, and preliminary calculations have been carried out for our system.

Instrumental considerations. The effect on count rates of the size of the mask covering the sample and the effects on peak resolution and background counts of collimator spacings have been studied. This experimentation was performed with U-Th oxide. Because of their identical atomic number relationship, results for U-Th should be similar to results for Pu-U without the problems of plutonium hazards. Part of the data obtained with U-Th oxides will be subsequently verified in experiments with Pu-U oxides.

Mixtures were prepared containing 10, 20, 30, and 40 wt % UO_2 in ThO_2. All four powders were examined with the X-ray spectrograph [23] at eight power levels of the X-ray generator and three sizes of masks (1/4-, 1/2-, and 3/4-in. diameter) covering the sample. These data make possible the presentation of relative intensity values (Table I-5 and Fig. I-8). Consistent with expectations, the matrix effect of absorption was shown for uranium and that of enhancement for thorium. Consideration of the fluorescence spectra and absorption edges of Th, U, and Pu (Ref. 21, pp. 71–75) suggests that thorium emission may be enhanced by uranium fluorescence and that uranium emission may be enhanced by plutonium, but to a smaller degree.

A series of experiments was performed [23] with several pairs of collimators and a sample of 20 wt % UO_2-80 wt % ThO_2 powder. Pairs of collimators were evaluated on the bases of whether resolution of the uranium and thorium peaks was adequate and whether the background count had increased to a degree that would interfere with the precision of counting. Ratemeter scans were obtained

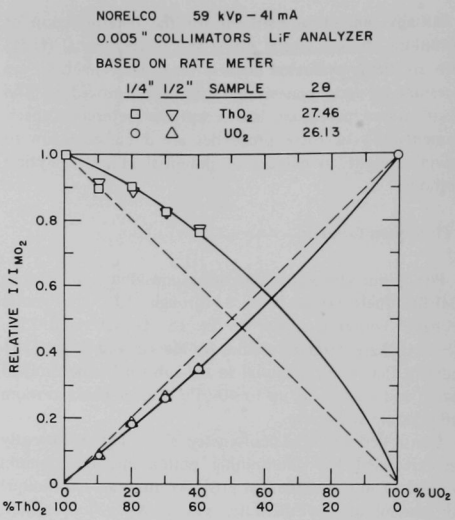

Fig. I-8. X-Ray Fluorescence: ThO_2-UO_2. ANL Neg. No. 308-2540.

for various combinations [24] of collimators having spacings of 5, 20, and 125 mils. The goal was to increase the count rate of each fluorescence peak without significantly reducing resolution or causing an excessive increase in background, both of which reduce precision.

The data (Table I-6) illustrate that by use of two collimators with 20-mil spacing rather than 5-mil spacing, the count rate for uranium was increased by a factor of 10. The precision of counting (far-right column) was improved from 8.0 to 2.6, demonstrating that the increased background at the greater slit spacing is not deleterious.

The half-width of both the thorium and uranium peaks increased at greater slit widths, but, except for the uranium peak obtained when the 125-mil collimator was used, resolution was satisfactory. Figure I-9 illustrates that, with

TABLE I-5. Relative Spectrometric Intensities for UO_2 and ThO_2 in ThO_2-UO_2 Mixtures of Four Compositions

Sample	1/2-in. Mask		1/4-in. Mask		Relative Intensities,[a] I/I_{MO_2}			
					UO_2		ThO_2	
	U(cps)	Th(cps)	U(cps)	Th(cps)	1/2-in.	1/4-in.	1/2-in.	1/4-in.
UO_2	10304	-	2765	-	1.0	1.0	0	0
40 UO_2·60 ThO_2	3584	8960	960	2419	0.348	0.347	0.773	0.762
30 UO_2-70 ThO_2	2688	9600	720	2624	0.261	0.260	0.829	0.827
20 UO_2-80 ThO_2	1856	10394	499	2861	0.180	0.180	0.889	0.901
10 UO_2-90 ThO_2	832	10624	230	2842	0.081	0.083	0.917	0.895
ThO_2	-	11584	-	3174	0	0	1.0	1.0

[a] I/I_{MO_2} is the ratio of the intensity of the Lα line for a UO_2-ThO_2 mixture to the intensity of the Lα line for the pure oxide.

TABLE I-6. Comparison of Line Intensities at Several Collimator Spacings

80% ThO_2-20% UO_2 powder; X-ray tube with W target; power: 45 kVP, 11 mA; 3/8-in. dia mask; LiF diffraction crystal

Collimator Spacing (mils)		Th $2\theta = 27.46°$				U $2\theta = 26.13°$					
Exit	Detector	Half Width (degree)	Gross (cps)	Bkgd. (cps)	Net (cps)	Half Width (degree)	Gross (cps)	Bkgd. (cps)	Net (cps)	Ratio[a]	σ[b]
5	5	0.33	1203	30	1173	0.34	232	30	202	1	8.0
5	20	0.48	2080	61	2019	0.60	384	61	323	1.7	6.5
20	5	0.61	6157	160	5997	0.62	1126	173	953	5	3.8
125	5	0.75	8576	358	8218	[c]	1869	384	1485	7	3.9
20	20	0.78	12480	410	12070	0.91	2547	448	2099	10	2.6

[a]Ratio = (net count rate with uranium)/(net count rate with 5-mil slit width in both collimators).
[b]Relative standard deviation based on counting statistics for uranium.
[c]Not measurable because of lack of resolution.

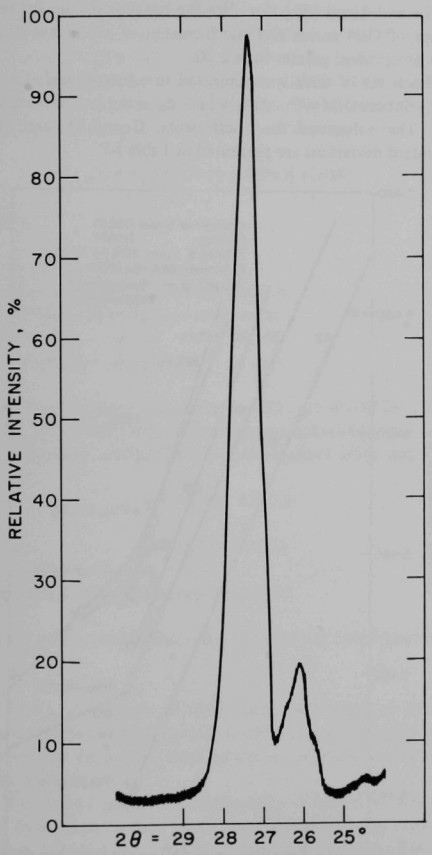

Fig. I-9. X-Ray Fluorescence Spectrogram for 80% ThO_2-20% UO_2 (power, 45 kVp and 11 mA; exit and detector collimators, 0.020 x 4 in.; full scale, 12800 cps). ANL Neg. No. 308-2541.

two 20-mil collimators, separation of peaks was adequate. This instrumental configuration will be used in subsequent experiments.

In another series of experiments, the X-ray tube was operated at 59 kV and 41 mA, and a count rate for uranium of 7×10^3 cps was obtained. At this count rate, a counting precision of ±0.5% at the 95% confidence level should be obtainable in a counting time of about 1/2 min. If the thorium peak and background are counted sequentially, as required on our Norelco instrument, the estimated total counting time for each pellet would be ~1 min. This analysis rate with a large batch size should accommodate a production rate of 1000 kg/day.

b. Oxygen Content of Fuel

The O/M ratio of $(U,Pu)O_2$ fuel is believed to be one of the more important factors controlling the changes in fuel during irradiation. The O/M ratio presently specified for FFTF driver-fuel pellets is 1.97 ± 0.02. The recommended FFTF analytical method for measuring O/M ratio is based on the weight change of a sample upon heating. Heating the sample to 800°C in a He-6% H_2 gas stream saturated with H_2O at 800°C is claimed [14] to produce an O/M ratio of 2.000. Measurements are claimed to be reproducible to 0.001 O/M unit, but the accuracy of the method is not known because of a lack of standards.

Markin, Walter, and Bones [25] have reviewed the various methods of O/M determination applied to O/U, O/Pu, and O/(U + Pu). These authors describe a method in which hypostoichiometric mixed oxide is first oxidized with oxygen to $(U,Pu)O_{2+x}$, and hyperstoichiometric oxide is then reduced with CO at 850°C. The results were compared with those from (1) a high-temperature galvanic cell, (2) polarographic determination of U(VI), and (3) oxidation to U_3O_8. The claimed accuracy of the CO method is ±0.001 O/M for hyperstoichiometric oxide and ±0.002 O/M for the two-stage process (including preliminary oxidation) required for hypostoichiometric oxide.

The analytical methods currently relied on which have acceptable precision and accuracy are slow and destructive.

A method based on physical properties such as the lattice parameter might prove to be rapid and nondestructive and adaptable for in-line use. The basis for such a method is outlined below. Any reservations about its applicability would need to be dispelled by experimental work.

Extensive studies of the U-Pu-O ternary system by X-ray diffraction have been performed at Harwell [15,26–29] and Karlsruhe [30]. For oxide with the O/M ratio carefully controlled at 2.00, Vegard's relationship between UO_2 and PuO_2 has been demonstrated, i.e., lattice cell size changes linearly with a change of plutonium content.

It is generally accepted that deviations in oxygen stoichiometry are accompanied by an effective change of valence of either the uranium or plutonium in the hyper- or hypostoichiometric regions [15,26], respectively. The addition of oxygen oxidizes uranium toward a valence of five, and the removal of oxygen reduces plutonium toward a valence of three.

In the hyperstoichiometric region, Brett and Fox [26] have demonstrated a linear relationship between the lattice parameter and compositions between PuO_2 and hypothetical "U_2O_5" for the cubic phase in equilibrium with orthorhombic (U_3O_8-type) phase. Markin and Street [15] contend that the theoretical Vegard plot should be drawn with respect to U_4O_9. However, lattice parameters are 5.4285 and 5.4275Å for $(Pu_{0.11}U_{0.89})O_{2.34}$ and $(Pu_{0.15}U_{0.85})O_{2.30}$, respectively, which appears to support the relationship with "U_2O_5." Lynds and others [31] demonstrated that for the uranium oxides two relationships are involved. UO_{2+x} and U_4O_{9-y} are two different entities; UO_{2+x} has interstitial oxygen, whereas U_4O_{9-y} is a defect structure. The relationships to lattice parameter are

$$UO_{2+x}; \quad a_0 = 5.4705 - 0.094x \; (0 < x < 0.125)$$

$$U_4O_{9-y}; \quad a_0 = 5.4423 + 0.029y \; (0 < y < 0.31)$$

It seems reasonable that a similar relationship between the lattice parameter and O/M ratio should exist in the ternary system

In the hypostoichiometric region, Gardner *et al.* [27] have determined, by high-temperature X-ray diffraction, the lattice parameter for the cubic phase PuO_{2-x}, which is in equilibrium with Pu_2O_3, is stable above 600°C, and has an O/M ratio greater than 1.61. Although PuO_{2-x} is commonly indexed as a body-centered cubic structure, the lattice parameter of the related face-centered structure is one-half that for the bcc structure.

Markin and Street [15] have proposed a phase diagram for the ternary Pu-U-O system and have determined some lattice parameters for various plutonium (III) contents. Their lattice parameter data support a linear relationship for the lattice parameter between UO_2 and "$PuO_{1.5}$."

Some modifications have been proposed by workers at Karlsruhe [31], but they do not affect the hypostoichiometric, single-phase region between 8 and 20% Pu which is of interest for FBR fuel.

Data have been located in the literature relating the lattice parameter to O/M ratio for ternary materials containing between 10 and 40% Pu (for which adequate analyses for Pu and O_2 can be presumed). The data for 15, 18, 20, 25, 30, and 42% Pu are presented in Fig. I-10. The data from Markin and Street [15] for 42% Pu cover the largest range of O/M ratios and indicate that the slope is 0.0047Å per 0.02 O/M ratio [32]. The data of Gibby [33] for 25% Pu indicate that the slope is 0.0060Å per 0.02 O/M ratio. The data of Schmitz [34] for 18% Pu indicate a significantly different slope but were measured over a limited range. No line was drawn through the earlier data of Baily and Lyon [35] for 20% Pu because of the limited range of O/M ratios and the inclusion of a point with an oxygen content greater than 2.00.

Each set of data was subjected to a least-squares fit of the relation $O/M = C - Da_0$ where a_0 is the lattice parameter. The values of the coefficients, C and D, and the standard deviations are presented in Table I-7.

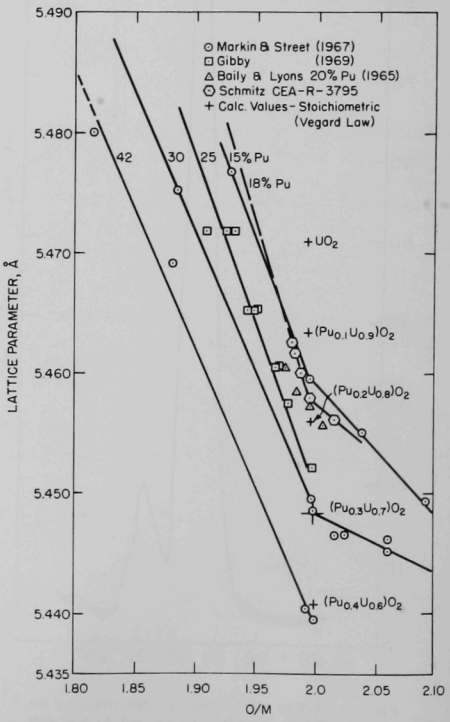

Fig. I-10. Lattice Parameter for Pu-U Oxides as a Function of O/M Ratio. ANL Neg. No. 308-2542.

TABLE I-7. Least-Squares Coefficients and Standard Deviations for Relations of O/M Ratios and Unit Cell Dimension for Pu-U Oxides

$O/M = C - Da_0$

Pu/(U + Pu)	Source of O/M and a_0 Values[a]	No. of Data	C	D	$\sigma_{O/M}$
0.15	M + S	2	22.0	3.66	-
0.18	Schmitz	4	17.8	2.89	0.0004
0.25	Gibby	14, 7[b]	22.5	3.75	0.008
0.30	M + S	4	24.4	4.12	0.002
0.42	M + S	4	25.5	4.33	0.003

[a]M + S is T. L. Markin and R. S. Street, Ref. 15; Schmitz is Ref. 34; Gibby is Ref. 33.
[b]Fourteen values of O/M and seven values of lattice parameter, a_0.

The compatibility of all the data makes it appear reasonable to treat them as one relationship. The relationship between lattice parameter and O/M ratio for $(U,Pu)O_2$ of known Pu/(Pu + U) ratio will allow normalizing to the Vegard law for stoichiometric oxide (O/M = 2.00). A single linear relationship combining the generally accepted Vegard law for stoichiometric oxides has the following form:

$$a = \alpha + \beta(\mathrm{Pu}) + [\gamma + \delta(\mathrm{Pu})]\ (\mathrm{O/M}) \qquad (1)$$

where

a is the lattice parameter
(Pu) is the plutonium atom fraction
(O/M) is the oxygen-to-metal ratio
$\alpha = a_{UO_2} - 2\gamma$
$\beta = a_{PuO_2} - a_{UO_2} - 2\delta$

Imposing weighted values of a for $UO_{2.0}$(5.4705) [31] and $PuO_{2.0}$(5.3952) [36], a least-squares calculation provides the following coefficients and their standard deviations:

$$\gamma = -0.321 \pm 0.020$$

$$\delta = 0.229 \pm 0.058$$

Equation 1 may thus be represented by

$$a = 6.1127 - 0.534(\mathrm{Pu}) - 0.321(\mathrm{O/M}) + 0.229(\mathrm{Pu})(\mathrm{O/M}) \qquad (2)$$

For a 1% change of O/M ratio, the change in lattice parameter is 0.0055Å, which is easily measurable since it is about ten times the usual precision of lattice-parameter measurements.

Figure I-11 presents a relationship of lattice parameters to O/M ratio within the substoichiometric single-phase region between the Vegard relationships for UO_2-"PuO_2" and UO_2-"$PuO_{1.5}$." The cross-hatch bands indicate the limits of the single-phase regions based on the phase-diagram of Markin and Street [15]. Dashed lines represent values from the correlation, and points represent interpolations from the experimental data presented in Fig. I-10.

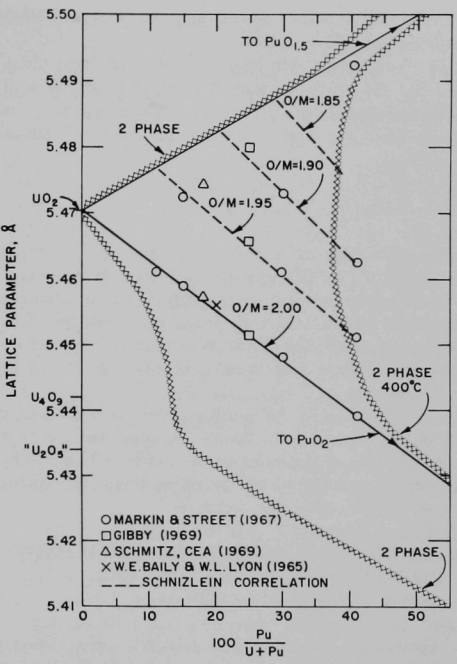

Fig. I-11. Lattice Parameter for U-Pu Oxides as a Function of Plutonium Content. ANL Neg. No. 308-2543.

Data collected by White [37] during fabrication of mixed oxides in three sintering atmospheres at 1650°C include lattice parameters, as well as O/M measurements obtained by a thermogravimetric method (oxidation-reduction) and a chemical method (fusion) [38]. The right-hand column of Table I-8 presents O/M values obtained by translations of White's lattice parameters by means of Eq. 2. The O/M ratios derived from lattice parameters are in agreement with O/M ratios determined by

TABLE I-8. Results of O/M Determinations on $U_{0.8}Pu_{0.2}O_{2-x}$ Sintered for Four Hours at 1650°C

Sintering Atmosphere	O/M Ox-Red[a]	O/M Chem[b]	a_0 (Å)	O/M by Correlation[c]
Vac (10^{-6} Torr)	1.977	1.982	5.459	1.987
He-6% H_2	1.972	1.976	5.460	1.984
He	1.985	1.992	5.457	1.994

[a]Thermogravimetric method. Oxide held at 850°C in He-2% O_2 for 2 hr and then in CO-10% CO_2 for 3 hr.
[b]Inert-gas fusion method, ANL-7264 (1967).
[c]From Equation 2.

the thermogravimetric method and the inert-gas fusion method for the three samples.

It is concluded, upon consideration of pertinent literature and the above correlation of lattice parameter with O/M, that analysis of O/M within the desired precision is feasible by X-ray diffraction measurement of lattice parameters.

3. Conclusions

Rapid nondestructive methods of analysis for critical properties of LMFBR fuel materials need to be developed. The use of X-ray fluorescence spectrometry to determine Pu/U ratios is feasible. Analysis times are expected to be about one minute. The influences on precision of variations of crystallite size and powder density are yet to be evaluated.

On the basis of previously published values and a correlation derived from them, it appears that the O/M ratio of uranium/plutonium oxides can be determined by measuring the lattice parameters of the hypostoichiometric oxides by X-ray diffraction techniques.

D. ADAPTATION OF CENTRIFUGAL CONTACTORS IN LMFBR FUEL PROCESSING (G. Bernstein, D. Grosvenor, J. Lenc, N. Quattropani)

Centrifugal contactors with relatively large diameter (10-in.) bowls are presently being used at Savannah River (SR) to process production-reactor fuels by the Purex process [39,40]. Demonstrated advantages of these contactors include minimized radiation damage to the solvent and quick flushout of equipment at the end of a processing campaign. These units have high throughputs, 40 to 60 gpm; however, because of their size, their use is limited to dilute plutonium systems.

Application of a Purex-type process to short-cooled LMFBR fuels is now under intensive development. These fuels are characterized by high plutonium content, and in order to develop a safe, high-throughput process, relatively concentrated plutonium solutions will have to be processed, particularly in the plutonium-isolation portion of the flowsheet. With appropriate modifications, centrifugal contactors appear to be well suited for safe processing of fuel solutions containing relatively high plutonium concentrations.

A program has been undertaken to extend the centrifugal contactor design developed at SR [41–46] to a configuration suitable for the plutonium isolation steps during solvent-extraction processing of LMFBR fuels. The principal advantage sought is an increase in nuclear safety by limiting the diameter of the unit to a critically favorable dimension, while maintaining a relatively high capacity by increasing bowl length and operating speed. The main objective of the study is to determine the performance characteristics of centrifugal contactors having larger length-to-diameter ratios than those employed in the SR units.

1. Design of Centrifugal Contactor

A centrifugal contactor has been designed for testing and is currently being fabricated. The main components of the unit (Fig. I-12) include (1) a cylindrical rotor mounted on a central shaft and spinning within a stator casing and (2) a mixing section (just below the rotor) containing a mixing paddle that is attached to the rotor shaft. The design is an adaptation of the Savannah River design with a restriction placed on the stator diameter in order to maintain a critically favorable diameter for plutonium process solutions. A stator ID of 5 in. is critically safe for plutonium concentrations as high as 200 g/liter on the basis of data [47] on safe diameters of infinite water-reflected cylinders of $Pu(NO_3)_3$ solutions without credit for ^{240}Pu. Purex-type process flowsheets for which this type of contactor may be employed will utilize plutonium concentrations below this level. On the basis of these criteria, a stator ID of 4 3/4 in. and a rotor ID of 4 in. were selected.

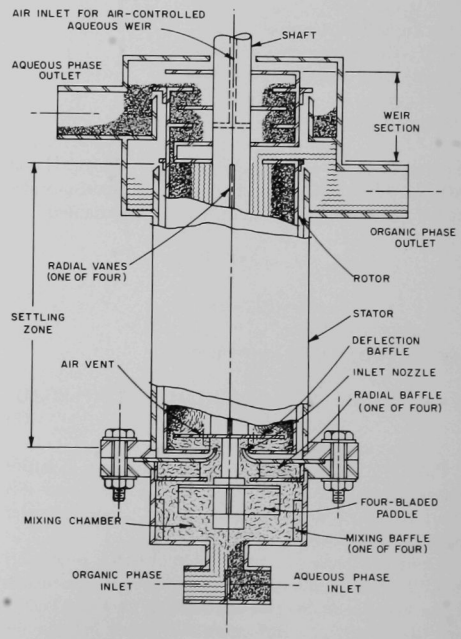

Fig. I-12. Experimental Long-Bowl Centrifugal Contactor. ANL Neg. No. 308-2377.

In the unit shown, aqueous and organic phases enter the mixing chamber located below the rotor. Radial baffles located in the base of the mixing chamber direct the mixed phases into the bottom of the spinning rotor, where they are quickly accelerated to the rotor speed by four vertical vanes attached to the rotor shaft. The two phases are separated by centrifugal force as they move upward through the rotor and are separately discharged through ports near the top of the rotor. A stable emulsion band of the two phases exists in the rotor under normal operation [48]. An air-controlled aqueous-phase weir is used to adjust the position of this emulsion band so that it is between the clear-phase organic overflow weir and aqueous underflow baffle. This feature (which was developed at Savannah River) permits operation over a broader range of phase density ratios and flowrates than could be achieved with a simple fixed weir.

The rotor is supported only at the top in order to avoid problems that might be encountered if bearings were operated in corrosive solutions. Accordingly, the permissible length of the rotor and permissible operating speed are limited by the critical speed of the shaft and rotor assembly. At the critical speed, any vibration resulting from rotor imbalance is strongly reinforced and can lead to excessive deflection, high stresses, and possible failure of the equipment. The spindle assembly that has been obtained for the contactor being fabricated can accommodate a 1 1/4-in.-dia shaft. Calculations indicated that with a 15-in.-long rotor the rotor assembly would have a first critical speed of about 5400 rpm. Since the generally recommended safe operating speed for rotating bodies is about 70% of the critical speed, operating speeds of about 3600 rpm should be permissible with the 15-in.-long rotor.

The weir section of the rotor occupies the upper 3 in. of the rotor length; the remaining 12 in. is available for use as a settling zone. The length-to-diameter ratio of three for the settling zone and the operating speed of 3600 rpm will extend the study of operating characteristics beyond the range covered by the SR units, which have a settling-zone length-to-diameter ratio of about 1.3 and an operating speed of 1750 rpm.

2. *Testing Program*

The testing program to be carried out with the contactor now being fabricated is designed to establish separating capacities with an aqueous stream consisting of nitric acid solution and an organic stream consisting of tributyl phosphate in refined kerosene or *n*-dodecane diluent. Performance data from these tests will be compared with performance data from tests of the SR units. On the basis of the SR tests, a tentative relationship was developed to correlate settling capacity with rotor speed, diameter, and length. Using this relationship, a settling capacity of about 12 gpm at a rotor speed of 3500 rpm is expected for the Argonne unit. The data from the proposed tests will be used to establish the validity of the relationship or to refine and extend it to include the higher speeds and larger length-to-diameter ratio employed.

In addition to tests with nitric acid and organic solvents, tests will be made with inactive uranium feed solutions to evaluate the mass-transfer efficiency of the contactor. One of the variables to be studied in these tests will be the effect of different geometries of mixing paddles. In the contactor design shown in Fig. I-12, the bottom section can be removed to permit replacement of the mixing paddle with one of a different design. In addition, it is possible to remove the mixing paddle entirely and replace the bottom section of the contactor with a special housing equipped with a shaft seal to permit a mixing paddle to enter the bottom of the mixing chamber. This paddle would be driven by an independent motor drive, allowing investigation of the effects of operating the rotor and the mixing paddle at different speeds.

3. *Alternative Contactor Design*

Another physical modification of the ANL centrifugal contactor design permits conversion of the contactor into an annular mixing unit. The annular mixer design has been tested with models built of acrylic plastic during fabrication of the stainless steel centrifugal contactor. The basic features of the annular centrifugal contactor are shown in Fig. I-13. The aqueous and organic phases enter through

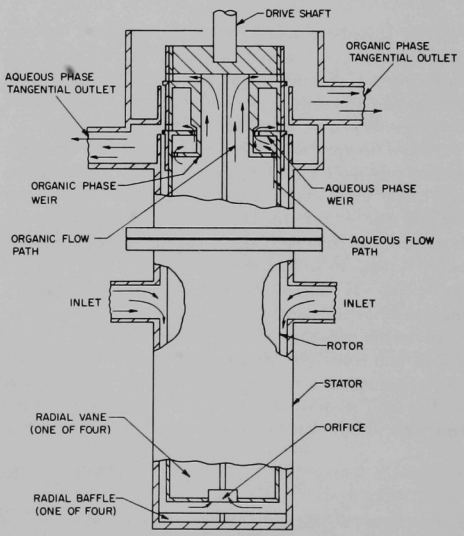

Fig. I-13. Annular Mixer Centrifugal Contactor. ANL Neg. No. 308-2544.

inlet lines on the wall of the stator and are mixed by skin friction as they flow downward through the annular space between the spinning rotor and the stator. The rotor OD is 4 in.; two stators with ID's of 4 1/2 and 5 in. have been used; the settling zone is 12 in. long. At the base of the stator, four radial baffles convert some of the kinetic energy of the spinning fluid into pressure. The mixed phases flow through an orifice into the rotor and are quickly brought up to rotor speed by four radial vanes which extend to the top of the rotor. The two phases are separated under centrifugal force, flow over weirs, and are discharged through separate ports into collecting rings, as in conventional centrifugal contactors.

In the unit shown in Fig. I-13, a simple mechanical weir is used to control the flow of the separated phases. Because the range of density ratios that can be accommodated with a particular mechanical weir arrangement is limited, two rotors (Nos. 1 and 2) have been made which differ only in their weir dimensions. An alternative to mechanical weirs would be more versatile air-controlled weirs similar to those used in the SR units [42].

The principal advantages sought in the annular design as compared with the SR design are simpler fabrication, lighter weight (which may be significant insofar as critical speed is concerned for a rotor with a high length-to-diameter ratio), and potential hydrodynamic support of the spinning rotor by the fluid in the annular space.

4. Tests with Annular Contactor

Tests have been performed with the plastic annular contactor to gain insight into some of the operating characteristics of this design. Most of these tests were performed with water as the sole fluid to measure relative flow capacity and mixing power input.

Tests with the No. 1 rotor installed in the contactor showed that the total throughput of water varied with the size of the rotor orifice and the height of water in the annulus, but was independent of rotor speed over a range from 1000 to 1650 rpm. Maximum throughputs were 6.6 and 9.9 gpm for orifice diameters of 3/4 and 1 1/8 in., respectively. The higher the level of water in the annulus, the greater the throughput.

In tests in which the No. 2 rotor fitted with a 3/4-in.-dia orifice was installed in the contactor, the maximum throughput varied from 3.6 gpm at 1240 rpm to 5.1 gpm at 1770 rpm. The differing effects of rotor speed when the two rotors were installed suggests that orifice size controlled the flow through the No. 1 rotor, but internal resistance (a result of smaller internal passages in the No. 2 rotor) controlled the flow through the No. 2 rotor. The pressure for forcing fluid through the orifice is provided by the height of fluid in the annulus, which is limited to about 12 in. in the present design. In the SR design, the mixing paddle acts as a pump and can deliver the mixed phases to the rotor orifice at a greater pressure than that expected in the annular design. Accordingly, it is anticipated that maximum throughput would be lower with an annular contactor than with a contactor of the SR design.

Mixing-power input tests were also made while the contactor was mounted on a dynamometer test stand. For these tests, the rotor orifice was sealed so that no power was consumed in pumping fluid through the rotor. When the contactor was tested with the 4 1/2-in.-ID stator and ~9-in. water depth in the annulus, mixing power input ranged from 0.01 hp at 910 rpm to 0.07 hp at 1870 rpm. With a water level of ~5 in. in the annulus, power input was about 70% of these values. Power input was increased by ~50% in tests with a 50-50 mixture of water and refined kerosene in the annulus. These tests indicated that mixing-power input will be high relative to the anticipated flow rates so that good phase contacting can be expected with the annular type of mixer.

Several tests have been performed in the contactor test facility to evaluate performance of the unit with a two-phase system using 0.1*M* HNO_3 and Ultrasene [49]. Good phase mixing but inadequate phase separation was achieved with the No. 2 rotor. Essentially all of the organic phase was discharged with the aqueous phase, suggesting that the weirs would function better with solutions having a greater density difference. In tests with a higher density aqueous phase (1*M* aluminum nitrate, 1.2 g/cc), the organic phase was free of any aqueous phase contamination. However, the aqueous phase contained about 4–5% organic phase.

Subsequent examination of the No. 1 rotor indicated that contamination had apparently been caused by small cracks in the plastic discharge tube for the organic phase, which permitted the organic phase to leak into the aqueous phase discharge passage.

Modification of the No. 1 rotor to permit it to operate in the contactor test facility resulted in distortion. As a result, the rotor could not be operated at high speeds. No two-phase tests were made with the modified rotor.

Since fabrication of the stainless steel contractor is nearly complete, no further tests are planned in the plastic unit.

REFERENCES AND FOOTNOTES

1. A summary of this section is given on pp. 1 to 5.
2. Supervisor of work described in Subsection 4 of this section.
3. "Aqueous Processing of LMFBR Fuels–Technical Assessment and Experimental Program Definition," USAEC report ORNL-4436 (1970).
4. "Atomics International Follow-On-Study-Task II Report," USAEC report AI-AEC-12791, Vols. 1, 2, and 3 (1969).

5. In two runs, the melt contained 1% sodium; however, this concentration of sodium was found to have no effect on the decladding rate.
6. M. Hansen, K. Anderko, *Constitution of Binary Alloys*, p. 738, McGraw-Hill, New York (1958).
7. "Aqueous Processing of LMFBR Fuels–Technical Assessment and Experimental Program Definition," USAEC report ORNL-4436, p. 171 (1970).
8. The Raman spectroscopic studies were made by V. A. Maroni of this Division.
9. A. A. Jonke, E. J. Petkus, J. W. Loeding, S. Lawroski, *Nucl. Sci. Eng. 2*, 303 (1957).
10. D. T. Crawley, "Pressure Buildup and Plutonium Nitrate Solutions in Sealed Shipping Containers," ARH-1093 (July 15, 1969).
11. Product of Watlow Electrical Co., St. Louis, Missouri.
12. Product of Pall Trinity Micro Corporation, Cortland, New York.
13. C. A. Strand, Battelle Northwest Laboratory, private communication (1969). The specifications for composition, properties, and impurities for FFTF fuel are listed in Table 1, pp. 60–62, ANL-7735 (Chemical Engineering Division Fuel Cycle Quarterly Report, April, May, June 1970).
14. "Analytical Chemistry Methods in Support of Driver Fuel Fabrication," USAEC report BNWL-1024 (Oct. 25, 1968).
15. T. L. Markin, R. S. Street, *J. Inorg. Nucl. Chem. 29*, 2265 (1967).
16. J. E. Rein, R. K. Zeigler, C. F. Metz, "LMFBR/FFTF Fuel Development Analytical Chemistry Program, Phase II," USAEC report LA-4407 (1970).
17. W. L. Lyon, "Oxygen-to-Metal Ratio in Solid Solutions of UO_2 and PuO_2," USAEC report GEAP-4271 (1963). (See Subsection C.2.b for a brief description of the thermogravimetric method.)
18. D. Ertel, "Simultaneous Determination of Uranium and Plutonium by X-ray Fluorescence," *J. Radioanal. Chem. 2*, 205 (1969).
19. D. Ertel, W. Wettstein, "Simultaneous X-Ray Spectrometric Determinations of Uranium and Plutonium in Solutions of Irradiated Fast Breeder Fuels," KFK-1121 (1970).
20. H. A. Liebhafsky, "X-ray Absorption and Emission in Analytical Chemistry," p. 27, John Wiley & Sons, Inc., New York (1960)
21. L. S. Birks, *X-ray Spectrochemical Analysis, Chemical Analysis,* Vol. 11, Interscience Publishers, New York (1969).
22. J. W. Criss, L. S. Birks, *Anal. Chem. 40*, 1080 (1968).
23. Experimental work performed by R. Schablaske, Analytical Section, Chemical Engineering Division.
24. Our Norelco X-ray spectrum analyzer utilizes a collimator between the sample and the crystal and a collimator between the crystal and the detector.
25. T. L. Markin, A. J. Walter, R. J. Bones, "The Determination of Oxygen/Metal Ratios for Uranium, Plutonium and (U,Pu) Oxides," UKAEA report AERE-R-4608 (1964).
26. N. H. Brett, A. C. Fox, *J. Inorg. Nucl. Chem. 28*, 1191 (1966).
27. E. R. Gardner, T. L. Markin, R. S. Street, *J. Inorg. Nucl. Chem. 27*, 541 (1965).
28. G. Dean, "Proceedings 3rd Int. Conf. on Plutonium," London, pp. 806–827 (1965).
29. T. L. Markin, E. J. McIver, "Proceedings 3rd Int. Conf. on Plutonium," London, pp. 845–57 (1965).
30. H. M. Mattys, *Actinide Rev. 1*, 165 (1968).
31. L. Lynds *et al., Advan. Chem. Ser.–Non-Stoichiometric Compounds 39,* 59 (1963).
32. A precision of 0.02 O/M is specified for FFTF fuel.
33. R. L. Gibby, "The Effect of Oxygen Stoichiometry on the Thermal Diffusivity and Conductivity of $U_{0.75}Pu_{0.25}O_{2-x}$," USAEC report BNWL-927 (1969).
34. F. Schmitz, "Structures and Properties of $(U,Pu)O_2$ Containing Non-Active Fission Products. A Simulation of Irradiated Nuclear Fuel," French report CEA-R-3795 (1969) (see USAEC report BNWL-TR-43).
35. W. E. Baily, W. L. Lyon, "Electrical Properties of Pu-U Mixed Oxide System," USAEC report GEAP-4675 (1965).
36. C. Sari, U. Benedict, H. Blank, "Metallographic and X-ray Investigation of Plutonium Oxides at Room Temperature," EURATOM report EUR-3564 (1967).
37. G. D. White, Argonne National Laboratory, private communication (1967).
38. H. T. Goodspeed, D. Pettis, "Macrodetermination of Oxygen in Uranium Dioxide Composites by Inert-Gas Fusion," USAEC report ANL-7264 (1967).
39. In the Purex process, uranium and plutonium in irradiated fuel are separated from each other and from fission products by solvent extraction. The solvent is tributyl phosphate in a kerosene-type diluent, and the aqueous phases contain nitric acid.
40. E. R. Irish, W. H. Reas, "The Purex Process–A Solvent Extraction Reprocessing Method for Irradiated Uranium," USAEC report HW-49483A (April 1957).
41. D. S. Webster, C. L. Williamson, J. F. Ward, "Flow Characteristics of a Circular Weir in a Centrifugal Field," USAEC report DP-371 (June 1961).
42. D. S. Webster, C. L. Williamson, J. F. Ward, "Hydraulic Performance of a 5-inch Centrifugal Contactor," USAEC report DP-370 (August 1962).
43. A. T. Clark, Jr., "Performance of a 10-inch Centrifugal Contactor," USAEC report DP-752 (September 1962).
44. A. A. Kishbaugh, "Performance of a Multi-stage Centrifugal Contactor," USAEC report DP-841 (October 1963).
45. D. S. Webster, A. S. Jennings, A. A. Kishbaugh,

H. K. Bethmann, "Performance of Centrifugal Mixer-Settler in the Reprocessing of Nuclear Fuel," USAEC report DP-MS-67-71 (October 1967).
46. A. S. Jennings, "A Miniature Centrifugal Contactor," USAEC report DP-680 (March 1962).
47. H. K. Clark, "Handbook of Nuclear Safety," USAEC report DP-532, Table IV.28, p. 442 (January 1961).
48. In Fig. I-12, the aqueous-organic interface in the rotor is shown as a distinct line; actually, the interface is characterized by an emulsion band.
49. Refined kerosene; product of Atlantic-Richfield Co.

II. SODIUM TECHNOLOGY [1]

(L. Burris, J. E. Draley, F. A. Cafasso, P. A. Nelson)

A. SODIUM CHEMISTRY (F. A. Cafasso, J. G. Eberhart)

The program on the chemistry of liquid sodium is directed toward the development of a sound scientific foundation for understanding the behavior of sodium's common nonmetallic contaminants—carbon, nitrogen, oxygen, and hydrogen—so that analytical methods can be developed for these contaminants, and potential corrosion problems in sodium systems can be predicted from existing corrosion data. Recent effort in the program has been devoted to (1) elucidating the phase relations in the Na-Na_2O-$NaOH$-NaH system, (2) determining the heat of solution of oxygen in sodium, (3) determining the stability in sodium of disodium acetylide—a compound believed to be important in carbon transport, and (4) studying the interactions of nitrogen and calcium in sodium and thereby assessing the role of calcium in enhancing nitridation of steels in sodium systems, and (5) developing a process for continuous removal of radioactive contaminants from sodium. Included in the program is a research effort which does not fall in the above categories, but which provides information useful in fuel element detection and location (FEDAL) schemes, namely, determination of the solubility of xenon in liquid sodium.

1. Characterization of Oxygen- and Hydrogen-Bearing Species in Sodium

a. The Sodium-Rich Corner of the Sodium-Oxygen-Hydrogen Ternary System (K. M. Myles, R. D. Wolson)

This investigation seeks to understand the behavior of oxygen- and hydrogen-bearing species in liquid sodium. The results will directly assist in the development and evaluation of analytical methods for the qualitative and quantitative monitoring of oxygen and hydrogen impurities in sodium. In addition, information will be obtained that will provide a strong foundation for future investigations of cold trapping, caustic stress corrosion, mass transport, and other related topics. The initial effort is being directed toward the elucidation of the phase relations in the Na-Na_2O-$NaOH$-NaH system.

The problems associated with the reaction of sodium with O_2 and H_2 have been extensively studied in various laboratories. For the most part, the emphasis in these studies has been on safety considerations and on developing a broad understanding of the chemical and mechanical interaction of the reaction products with other LMFBR components. Details of the actual chemical reactions and the nature and distribution of the resultant species have received only limited attention. Nevertheless, several reviews [2–4] have recently been made of the available information on the phase relations that exist between Na, Na_2O, NaOH, and NaH. In each case, the conclusion was reached that essentially no unequivocal information is available on the Na-Na_2O-$NaOH$-NaH ternary system and that the respective binaries, i.e., the systems Na-Na_2O, Na_2O-$NaOH$, $NaOH$-NaH, and NaH-Na, have been determined only fragmentarily. Although the available information is sparse, it has served us as a basis for the construction of two very tentative but self-consistent versions of the Na-Na_2O-$NaOH$-NaH diagram. The assumption was made that either Na_2O-$NaOH$ or $NaOH$-NaH is a quasi-binary section and, thus, that the Na-Na_2O-$NaOH$-NaH section of the larger Na-O-H ternary can be treated independently. Also, the hydrogen partial pressure was considered to be sufficiently large so that NaH melts congruently. Both diagrams show a region of liquid immiscibility in accord with Shikhov [2]; neither diagram, however, is wholly consistent with all reported data.

Our experimental program is addressed to (a) determining which of the two diagrams is more reliable, (b) refining the selected diagram, and (c) studying the interactions between hydrogen- and oxygen-bearing species in sodium at LMFBR temperatures.

To determine which of the two diagrams is more reliable, heat-treated mixtures of Na, Na_2O, NaOH, and NaH will be examined at room temperature by X-ray powder diffraction techniques. A selection between the diagrams may be possible on the basis of the phases present and/or absent. Preliminary experiments are under way.

To refine the selected diagram and to study the hydrogen-oxygen-sodium interactions at elevated temperatures, the method selected is that of simultaneously determining (a) the activities of oxygen and hydrogen in the various phase fields and (b) the nature and concentration of the species in the vapor in thermodynamic equilibrium with the liquid and solid ternary phases. A correlation of these parameters with known additions of Na_2O, NaOH, and NaH to liquid sodium should provide insight into the nature of O-H interactions and should delineate the phases and phase-region boundaries of the ternary system.

An apparatus for this purpose has been designed. The main component is a large ($\sim$1000 cm^3) nickel Knudsen cell that is heated by a standard wire-wound furnace. Vapor from the cell effuses through several orifices (effectively converting the vapor into a molecular beam) and into a precision quadrupole mass spectrometer. A critical analysis of the mass data should provide identity information that is directly related to the particular solid and liquid phases present in the Knudsen cell. Also inserted into the Knudsen cell are oxygen- and hydrogen-activity probes. The outputs of the two probes will be monitored for the discontinuities

that are produced by transgressions of the various phase-region boundaries. The information derived from the use of the two probes in these experiments will also be useful in evaluating the response of the probes themselves to various operating conditions.

b. Electrochemical Studies of Oxygen in Liquid Sodium
(G. P. Stavropoulos)

Application of galvanic-cell methods for monitoring oxygen activity in liquid sodium was first proposed by G. W. Horsley in 1959. A systematic effort to use a solid electrolyte in the measurement of some of the thermodynamic properties of the sodium-oxygen system was started by Alcock and Stavropoulos [5] in 1963, and has been continued by scientists at Brookhaven National Laboratory since 1967. To further our understanding of solutions of oxygen in sodium, work was started in two areas: (1) the measurement of the heat of solution of oxygen in liquid sodium and (2) evaluation of a tin-tin oxide reference electrode for use in oxygen meters. These studies are being carried out in a cell of the type $Sn\text{-}SnO_2/ThO_2\text{-}Y_2O_3/O$ (dil. sol'n in Na), in which the reference electrode is $Sn\text{-}SnO_2$ and the working electrode is the system under investigation.

The heat of solution of oxygen in sodium. Determination of the heat of solution of oxygen in sodium involved measuring, as a function of temperature, the open-circuit, reversible electromotive force of a cell in which the working electrode consisted of a dilute solution of oxygen (1–100 ppm) in sodium, maintained at constant composition. For solutions as dilute as those studied, solute-solute interactions are insignificant and the solute-solvent affinity is strong; hence the heat of solution may be expected to be independent of oxygen concentration. Moreover, with the reasonable assumptions that Henry's law is applicable and that the heat of solution is nearly independent of temperature, thermodynamic considerations indicate that the cell emf should vary linearly with temperature. This linear relationship may be seen in Fig. II-1, where the data collected at ANL and those previously obtained by the author [5] are presented. Also shown are curves for oxygen levels of 1, 10, and 100 ppm calculated with the aid of existing solubility information [6]; these curves are given so that the oxygen concentrations at which the emf measurements were made may be estimated.

The experimental data for each curve were fit, by the method of least squares, to an equation of the form $E(\text{mV}) = a + bT$. From the average value of $a(375 \pm 2\ \text{mV})$ and the following equations for the free energy of formation of SnO_2 and Na_2O

$$(500\text{–}1000^\circ\text{K})\ \Delta G_f^\circ(SnO_2) = -(140.0 \pm 0.3) + (0.0511 \pm 0.0003)T\ (\text{in kcal/mol}) \quad (1)$$

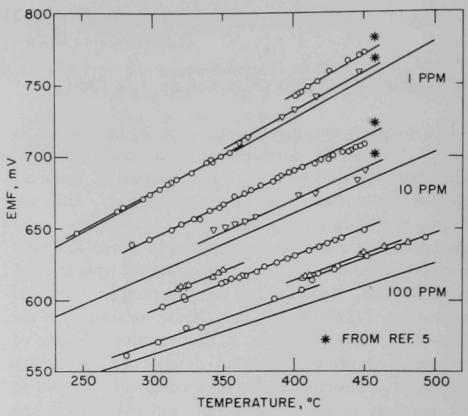

Fig. II-1. Experimental and Calculated Emf-versus-Temperature Data for the Cell: $Sn\text{-}SnO_2/ThO_2\text{-}Y_2O_3/O$ (dil. sol'n in Na). ANL Neg. No. 308-2378.

$$(500\text{–}1000^\circ\text{K})\ \Delta G_f^\circ(2Na_2O) = (200.9 \pm 3.0) + (0.068 \pm 0.002)T\ (\text{in kcal/mol}) \quad (2)$$

the partial molar heat of solution of oxygen in sodium was determined to be 13.2 ± 0.1 kcal/mol. This value may be compared with values obtained in other studies: 13.1 ± 0.8 kcal/mol (average of four values) by Stavropoulos [5], 12.0 ± 0.2 kcal/mol (average of five values) by Minushkin [7], 11.2 kcal/mol from Eichelberger's solubility equation [8], and 12.8 ± 0.3 kcal/mol from an assessment [9] of the solubility data of Rutkauskas [6] and of Noden and Bagley [10]. The agreement with the value derived from the latter solubility results leads to the suggestion that even at oxygen levels much larger than those studied here (the solubility of oxygen in sodium, e.g., is ~3000 ppm at 550°C) solute-solute interactions are negligible and dilute solution behavior is exhibited by sodium-oxygen solutions.

Assessment of the $Sn\text{-}SnO_2$ electrode as a candidate reference system for oxygen meters. The use of the $Sn\text{-}SnO_2$ reference electrode in the measurements discussed above makes possible its comparison with other reference electrodes in use for oxygen meters–for example, the $Na\text{-}Na_2O$ electrode (liquid sodium saturated with oxygen) or the oxygen gas electrode.

The $Sn\text{-}SnO_2$ electrode was found to have a number of important advantages. (1) Because of the oxygen activity of the $Sn\text{-}SnO_2$ system, the ionic transport number of oxygen in the $ThO_2\text{-}Y_2O_3$ electrolyte is unity; this is not the case when the oxygen gas electrode is used. Thus, a separate determination of the ionic transport number, which is made when gas electrode cells are used, is unnecessary for the interpretation of emf measurements. (2) No corrosive

interactions occur between the $Sn\text{-}SnO_2$ electrode and the $ThO_2\text{-}Y_2O_3$ electrolyte; the corrosion problem encountered with $Na\text{-}Na_2O$ electrodes is thus avoided. (3) Because of the lack of corrosion, the tendency of the electrolyte to break (observed in cells of other designs) as a result of changes in operating temperature is significantly reduced. (4) Because of the high boiling point of tin, the problem of containing electrode vapors, encountered in cells with $Na\text{-}Na_2O$ reference electrodes, is avoided.

The $Sn\text{-}SnO_2$ system has two disadvantages however. (1) It must be removed from the electrolyte tube before the cell temperature is permitted to drop below the melting point of tin; otherwise, breakage of the electrolyte may occur on reheating. (2) In case of breakage, Sn may enter the loop or reactor [11] system on which the cell is installed; such contamination may prove undesirable.

In the present work the $Sn\text{-}SnO_2$ reference system has been used with great success. A single $ThO_2\text{-}Y_2O_3$ electrolyte tube has been used for 2200 hr and has been cycled between room temperature and 500°C several times.

2. *Characterization of Carbon- and Nitrogen-Bearing Species in Sodium*

a. Carbon Chemistry (J. P. Ackerman, J. W. Allen)

Carburization and decarburization of steels are corrosion phenomena known to occur in sodium systems. Disodium acetylide, Na_2C_2, has been postulated [12] to be the species responsible for carbon transport in liquid sodium-steel systems. To aid in evaluating this postulate, information on the thermal stability of Na_2C_2 in sodium was needed. Experiments which were made to collect the required data are described later.

The decomposition of pure Na_2C_2 (no sodium added) gives rise to gaseous sodium and solid carbon; according to the phase rule the system is thus monovariant, and the extent of decomposition (as measured by the pressure of sodium in the system) is a function of temperature. However, the system becomes invariant in the presence of liquid sodium, and it can be in equilibrium only at one discrete temperature. Liquid sodium may become part of the system in two ways: (1) by purposeful addition (as was done in this study) or (2) by decomposition of "pure" Na_2C_2 until the pressure of sodium in the system equals the vapor pressure of pure sodium and sodium condenses. The invariant temperature is the same in either case.

Experiments to determine the invariant temperature have been of two kinds: X-ray and chemical. The X-ray experiments, described in the preceding report (ANL-7675, p. 64), showed that (a) pure Na_2C_2 undergoes a tetragonal-to-cubic phase change when heated to 275°C, and (b) the cubic structure persists to at least 500°C. Thus an invariant temperature above 500°C was indicated.

The chemical experiments involved heating copper or graphite-lined copper capsules containing 2 g of sodium and 0.1 to 0.2 g of Na_2C_2 to temperatures in the range 550–700°C, then cooling them and analyzing the contents for acetylide. To avoid contamination from air, the capsules were loaded and welded shut in a helium-filled glovebox and heated in helium-filled furnaces; they were then returned to the glovebox, cut open, and placed in a vacuum system for chemical analysis. The results showed that Na_2C_2 is undecomposed in sodium that has been heated to 550°C for two weeks. At 600°C, 25% of the Na_2C_2 is decomposed after one week. At higher temperatures, the decomposition is faster: after two weeks at 650°C or one day at 700°C, essentially no acetylide is left. It appears, therefore, that the invariant temperature for the $Na_2C_2\text{-}Na$ system lies in the range 550–600°C.

b. Nitrogen Chemistry (A. K. Fischer)

The study of the chemistry of nitrogen in liquid sodium has two principal objectives. The first is to provide information on the existence, identification, and chemical behavior of nitrogenous species in sodium so that analytical methods can be developed for these species. The second is to elucidate the roles that these species play in transporting, through sodium, the nitrogen that nitrides reactor components.

To begin the program, a study of the interaction of nitrogen and calcium in sodium was undertaken. This approach was taken after a literature search showed that (a) nitridation of stainless steel in the presence of molten sodium is a genuine phenomenon and (b) the function of calcium as a nitrogen carrier in sodium was a common conjecture. An analogous carrier role could also be postulated for magnesium, since both alkaline earths are present in reactor sodium, and the known chemistries of their nitrides are similar. Ultimately, the program will also include studies to elucidate the roles of other selected nitrogenous species such as amide, nitrite, cyanide, cyanamide, and cyanate.

The experimental procedure for the nitrogen-calcium studies was, briefly, as follows. A solution of 1 at. % calcium in sodium contained in a Type 304 stainless steel reaction vessel was agitated under a constant pressure of 720 Torr of nitrogen gas. Gas absorption was followed gasometrically to determine the stoichiometry of the reaction. After the absorption curve was sufficiently defined (about one week), a filtered sample of the liquid sodium phase was withdrawn for determination of its calcium and Kjeldahl-nitrogen content. Several Type 304 stainless steel tabs that had been included in the original sample loading and that had been submerged under the sodium throughout the experiment were analyzed for nitrogen, and other constituents as desired.

The system for measuring nitrogen absorption consisted of a cylindrical reaction vessel and furnace well contained in a rocking furnace which, in turn, was connected to a

constant-pressure gasometric manifold by means of flexible stainless steel tubing. The furnace assembly rocked through a vertical position so that the sodium in the cylindrical reaction vessel flowed a short distance up and down the vessel walls, and the tabs always remained submerged in the sodium. In each experiment, a new reaction vessel was used, so that there was no question of nitride carryover from one experiment to another.

The following experiments have been conducted: (1) two experiments with 0.01 mol calcium in 0.99 mol sodium at 590°C; (2) one "dry" experiment (no sodium or calcium) at 590°C; (3) one blank experiment with 1.00 mol sodium (no calcium added); and (4) one experiment with 0.01 mol calcium in 0.99 mol sodium at 390°C. The results of the gasometric experiments conducted so far are shown in Fig. II-2, where nitrogen uptake is plotted as a function of time. The two experiments at 590°C with 0.01 mol calcium in 0.99 mol sodium agreed within experimental error and are shown by one averaged curve.

The "dry" experiment was designed to measure the nitrogen uptake resulting from nitridation, in the absence of sodium and calcium, of Type 304 stainless steel (the material of construction for the reaction vessel and furnace well). The finding that no nitrogen was absorbed indicates that the steel, the only possible nitrogen absorber, was not nitrided. However, in experiments which were carried out in the presence of sodium or sodium-calcium solutions, significant nitrogen absorption was observed. For these experiments, the initial rise in the curves is interpreted as reflecting the reaction between nitrogen and dissolved reactive constituents (of which calcium is the major one) in the sodium, and the linear portions, in the 590°C experiments, as reflecting the absorption of nitrogen by the steel. The horizontal portion of the curve for the experiment with sodium-calcium at 390°C is a feature also exhibited by

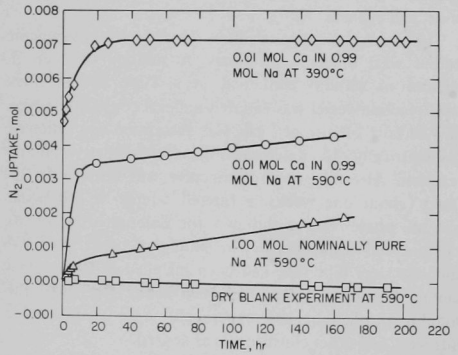

Fig. II-2. Nitrogen Absorption Curves at 390 and 590°C and 720 Torr. ANL Neg. No. 308-2379.

the curve for the "dry" experiment. Since the dry experiment at the higher temperature of 590°C showed that no nitridation of steel occurred, it is reasonable to expect that at the lower temperature of 390°C, the horizontal portion of the curve also reflects a period of no nitridation of steel.

The interpretation, offered above, of an initially rapid interaction between calcium in solution in sodium and nitrogen is analogous to that suggested by Addison and Davies [13] for lithium-sodium solutions and nitrogen at 400°C. In this connection, it is also noteworthy that the calcium does not remain in solution in sodium. Analysis of filtered samples of the solutions taken at the end of the experiments showed less than 10 ppm calcium. Also, a stainless steel tab that had been submerged in the solution did not reveal any significant calcium uptake. These facts are consistent with the interpretation offered above and with the hypothesis of relatively rapid formation, in sodium, of an insoluble calcium-nitrogen compound.

Analyses of submerged tabs showed that nitridation of Type 304 stainless steel is inhibited, not enhanced, when calcium is added to the sodium. Tab analyses showed 330 and 1800 ppm nitrogen for 1 at. % calcium and no added calcium, respectively, and 370 ppm nitrogen for untreated tabs. These analytical findings parallel the visual appearance and weight changes of the tabs. Tabs removed after the completion of calcium-enriched experiments emerged with their original, shiny appearance and with no change in weight. On the other hand, tabs from the nominally pure sodium runs emerged with a dull grey appearance and showed an increase in weight. The weight increases were 1 to 2 mg (in 0.9-g tabs), and these agreed well with the analytical results for nitrogen content. One possible explanation for the inhibiting effect of calcium on nitridation is that the calcium removes nitrogen carriers from the sodium. These carriers are presumably impurities that have not yet been identified.

The amount of nitrogen that is ascribed to interactions with calcium and impurities in the experiments with 1 at. % calcium at 590°C is 3.37×10^{-3} mol. The difference between this amount of nitrogen and the corresponding quantity (5.6×10^{-4} mol) from the experiment with 1 mol of nominally pure sodium gives the amount of nitrogen interacting with calcium and an apparent overall Ca-N stoichiometry of $Ca_{1.78}N$.

The conclusion that emerges from these experiments is that calcium does not enhance nitridation, but, in fact, inhibits it. This finding tends to refute the conjecture cited in the literature that calcium, in sodium, functions as a nitrogen carrier in the nitridation process.

3. *Solubility of Xenon in Liquid Sodium* (E. Veleckis, W. A. Kremsner)

The solubility of noble gases in liquid sodium is of

considerable interest because of the use of sodium as a coolant in nuclear reactors. Helium and argon are generally used as reactor cover gases and krypton and xenon are fission product gases which are released to sodium through fuel-pin cladding failures. The solubilities of helium [14], argon [15], and krypton [16] in liquid sodium have been measured previously. The study of the solubility of xenon was undertaken to provide data for evaluating schemes, currently under development at Argonne, for detecting and locating fuel-cladding failures in LMFBR systems.

The method used for the xenon solubility measurements is due to Grimes *et al.* [17]. This method incorporates several important features for determining very low solubilities of gases in liquids at elevated temperatures. Our adaptation of the method involves (a) saturating liquid sodium with natural xenon at a preselected temperature and pressure, (b) transferring a known portion of the saturated sodium to another container where the dissolved gas is stripped from sodium by sparging with helium, (c) separating the stripping gas from the gas mixture by selective absorption, and finally, (d) analyzing the remaining gas by gas chromatography to determine the xenon originally dissolved in sodium. (Xenon analyses were made with a Beckman GC-5 chromatograph.)

In employing this procedure, special precautions are taken to assure representative solubility measurements. (1) Good contact of the saturating gas with sodium is provided by prolonged bubbling of gas through the sodium. (2) The saturated sodium is allowed to sit undisturbed for a long period of time to promote the coalescence and escape of bubbles. (3) Only the bottom portion of sodium is transferred to the stripper, and the transfer rate is low to avoid the sodium-gas or sodium-container interfaces which are expected to be richer in xenon. (4) Efficient stripping of the dissolved xenon from sodium is effected by first cooling sodium to ~150°C, a temperature at which the gas solubility of xenon is negligible, and then sparging with helium for 2 hr.

Solubility determinations were carried out as a function of both pressure and temperature. The pressure dependence was determined in 16 experiments carried out at approximately 500°C and at xenon pressures ranging from 2 to 8 atm. The purpose of these experiments was to establish whether Henry's law is obeyed by solutions of xenon in sodium. The results are shown in Fig. II-3 where the mole fraction solubility of xenon, x_{Xe} (corrected to exactly 500°C), is plotted against the xenon pressure, P. The experimental data were fitted to a linear, two-constant equation and yielded a least-squares slope (the Henry's law constant) of $K_H = 2.8 \times 10^{-9}$ atm^{-1}. On the basis of statistical F-tests made on the value of the intercept and the linearity of the line, the displacement of the line from the origin was found to be insignificant; hence, the data can be represented by Henry's law, $x_{Xe} = K_H P$. This can also be seen in Fig. II-3 by the position of the 95% confidence

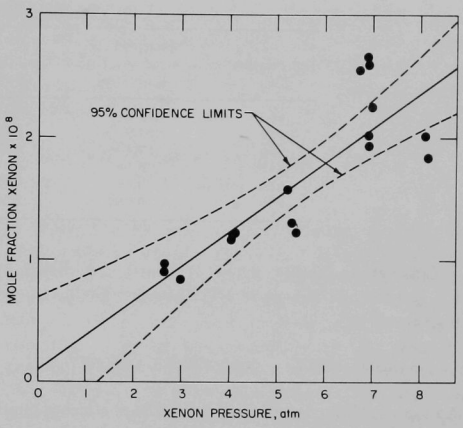

Fig. II-3. Pressure Dependence of the Solubility of Xenon in Sodium at 500°C. ANL Neg. No. 308-2380.

limits for the predicted mean values of x_{Xe} [18]. A solubility relationship of the form $x_{Xe} = KP^n$, which includes Henry's law and Sieverts' law as special cases, was also tested. A linear least-squares analysis of log x_{Xe} vs. log P yielded a slope of $n = 0.9 \pm 0.3$, which is a further indication of the adequacy of a Henry's law representation of the solubility data.

The temperature dependence of xenon solubility in sodium was determined from 47 experiments carried out at approximately 50-degree intervals between 350 and 600°C. The results are presented in an abbreviated form in Table II-1 in terms of mean solubilities. The mean solubilities were obtained by making a temperature correction on each value [19] and then averaging each set. The corrections were made using the temperature-dependence equation obtained from least-squares analysis of the complete data. The relative standard deviations and the number of determinations at each temperature are shown in columns 4 and 5 of Table II-1.

The solubilities in Table II-1 are expressed in two forms: (1) the Henry's law constant, K_H, in ppb/atm (i.e., grams of gas dissolved in 10^9 grams of sodium per atmosphere of gas pressure) and (2) the Ostwald coefficient, λ (the volume of gas per unit volume of sodium), both the solute and solvent being at the temperature and pressure of the experiment. The Ostwald coefficient is related to the Henry's law constant by the equation

$$\lambda = (RTd_{Na}/10^9 M_{Xe})K_H$$

where R is the gas constant, T is the absolute temperature, d_{Na} is the density of liquid sodium [20], M_{Xe} is the atomic weight of xenon.

TABLE II-1. Solubility of Xenon in Liquid Sodium

Temperature (°C)	Henry's Law Constant, K_H (ppb/atm)	Ostwald Coefficient, λ	Relative Std. Deviation (%)	Number of Determinations
600	91.1	4.01×10^{-5}	-	1
550	37.9	1.60×10^{-5}	9	6
500	17.4	6.98×10^{-6}	17	17
450	6.56	2.50×10^{-6}	18	9
400	3.06	1.10×10^{-6}	6	7
350	0.799	2.70×10^{-7}	17	7

Complete solubility data (47 points) are shown in Fig. II-4 as a plot of log λ vs. $1/T$. The regression line can be represented by

$$(350\text{–}600^\circ\text{C}) \qquad \log \lambda = 0.663 - 4500T^{-1}$$

An error analysis showed that at the 95% confidence limits the deviation of the mean value of log λ is ±0.019 and the corresponding error in λ, ±4.4%. The heat of solution of xenon in liquid sodium, calculated from the slope of the line in Fig. II-4, is 20.6 ± 0.7 kcal/mol [21].

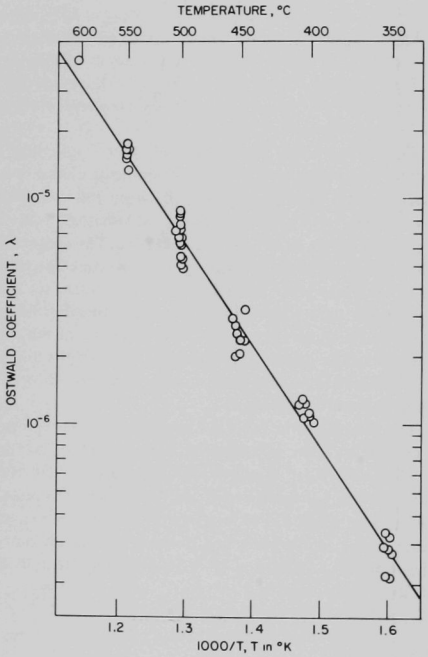

Fig. II-4. Temperature Dependence of the Solubility of Xenon in Sodium. ANL Neg. No. 308-2381.

The information available on the solubility of noble gases in liquid alkali metals has recently been reviewed [22]. The only other experimental study on the solubility of xenon in liquid sodium appears to be that of Mitra [23]. His procedure, however, contained experimental inconsistencies and yielded xenon solubilities 10^5 higher than those reported here. Xenon solubilities of that magnitude are inconsistent with expectations and with extrapolations based on the available data for other noble gases in sodium. A theoretical model that satisfactorily accounts for the measured solubilities of noble gases in liquid sodium has been developed at ANL (see Section V.A.1.c, this report). As shown in Fig. V-3, xenon solubilities predicted by this model are in good agreement with the measured solubilities.

4. Development of a Process for Continuous Removal of Radioactive Contaminants from Liquid Sodium
(H. M. Feder, C. Postmus)

Radioactive impurities may be introduced into the circulating primary sodium system of a fast breeder reactor by activation and dissolution of structural and cladding materials, from vented fuel elements, and from leaking and defective fuel elements. The presence of radioisotopes resulting from the neutron activation of sodium (e.g., sodium, neon, and magnesium) is unavoidable; however, these isotopes are generally short-lived and pose no problem for equipment maintenance after a reasonable waiting period. Longer-lived radioactivities in sufficient quantity, however, would present formidable contact-maintenance problems. Because no methods have been established for the removal of radioactive contaminants from flowing sodium streams, no current plans exist for coping with the problem, except to rely on quality assurance and control. To provide an alternative approach, research was undertaken to seek a method of radioactive-contaminant removal. After consideration of various possibilities, attention was focussed on the potential of a liquid-liquid solvent extraction system operating at 150°C on a bypass loop of the sodium circuit. Necessary characteristics of a liquid extracting phase for such a function are as follows: (1) one or more of the components must be capable of reacting

with the harmful impurities and extracting them without reacting with sodium; (2) the extracting phase must have a very low solubility in sodium so that thermal decomposition of dissolved materials in the core of the reactor does not create an additional problem; and (3) other properties of the extracting phase (e.g., boiling point, density, cost and availability, thermal and radiation stability, corrosiveness) must be suitable for the intended use.

As a first step, a search was instituted for a suitable fluid solvent phase. The search proceeded by a process of elimination. Materials were eliminated as candidates on the basis of the following criteria: (1) substances known to be reactive to hot sodium, or possessing functional groups known to be reactive, (2) all substances not readily available from commercial sources, (3) substances known to be corrosive toward stainless steel, (4) all substances melting above 25°C or boiling below 180°C, or having densities differing from that of liquid sodium by less than 0.02 g/cc, and (5) all uncommon substances that possessed more common analogs. The materials that survived these eliminations were a small number of low-melting fused salts and a larger number of organic solvents. Attention was first directed toward the latter; representative materials were obtained in sufficient quantity for further testing and subjecting to drying (over CaH_2, $CaSO_4$, or Molecular Sieves, as appropriate) and vacuum distillation. The next elimination step consisted of observing the behavior of stirred mixtures of ~100 cm^3 of solvent and ~25 g of sodium on heating in an evacuated glass vessel to 150°C. Observation of precipitation, gassing, color change, film formation, or self-heating was taken as evidence of insufficient long-term stability. Tests were made under both continuous and intermittent heating conditions, in the presence and absence of stainless steel, and for periods of time of up to two weeks. The types of substances subjected to these tests were saturated aliphatic and aromatic hydrocarbons, aliphatic and aromatic amines, disubstituted amides, aliphatic polyethers, tertiary phosphines, and aliphatic nitriles. Despite efforts to eliminate substances likely to be reactive, the results varied widely—a good indication that the chemical literature on the elementary reaction of sodium with many substances is very far from complete.

Excellent stability under the test conditions was exhibited by two classes of test materials: the straight-chain alkanes, e.g., *n*-decane, and the aromatic amines, e.g., *N,N*-diethylaniline. The latter substance (preferred because of its wide-ranging solvency) was made the subject of an extensive literature search and was further tested for thermal stability at temperatures up to 180°C in contact with sodium. The stability of solutions of *N,N*-diethylaniline and potential metal-complex formers such as sodium acetylacetonate and sodium cyclopentadienide was also tested. These tests gave encouraging results, and further tests of the behavior of *N,N*-diethylaniline and its complex-forming solutions toward radiation, toward 150°C sodium in a small stainless steel pumped circuit, and as a trace-metal extractant were planned. At this stage, however, the research was suspended in favor of more immediate LMFBR requirements.

B. ANALYTICAL STANDARDS PROGRAM

(R. J. Meyer, F. A. Cafasso)

Within the national sodium technology program, the development of analytical methods for determining impurities in sodium has received increasing attention in recent years, and significant advances have been made in this area. However, little effort has been made to standardize the methods in current use, and the result has been that impurity-sensitive (and often discrepant) experimental data from different laboratories have proven to be difficult to intercompare and interpret. If sodium technology is to advance rapidly, the research and development efforts of all major sodium technology contractors must be put on a common, intercomparable, and reliable basis.

As a first step toward achieving this goal, ANL has been requested to establish and manage an Analytical Standards Program. The long-term objective of this program is a set of specifications (RDT Standards) which stipulate (a) the maximum permissible impurity levels in operating reactor and experimental sodium systems (including cover gases); (b) standard sampling and analytical methods for determining impurity levels in these systems; (c) impurities that must be controlled to assure system integrity and to permit intercomparison of experimental data; and (d) methods to control impurities. The short-term objectives of the program are (1) a set of interim purity specifications and (2) a set of interim sampling and analytical methods, selected from existing technology, that are uniformly applied throughout the sodium technology community.

The short-term objectives are being met through the establishment of an Analytical Standards Laboratory. Work related to meeting the long-range objectives has been directed toward development of analytical methods for which a need exists.

1. Analytical Standards Laboratory (F. A. Cafasso, M. H. Barsky, H. S. Edwards, M. D. Adams, S. B. Skladzien, A. F. Panek, R. C. Haglund, L. E. Ross)

Operation of the Analytical Standards Laboratory is a combination of administrative and laboratory work. The administrative activities involve coordination of the Analytical Standards Program; the laboratory activities involve participation in the standards program and the satisfaction of current analytical needs, particularly those of the Fast Flux Test Facility (FFTF).

a. Administrative Activities

The initial effort of the Analytical Standards Laboratory was an assessment of the steps necessary to meet the short-term goals of the program. The following conclusions were reached:

1) Sampling and analytical needs of the sodium technology community must be periodically assessed.

2) Sampling and analytical methods must be selected from existing technology to satisfy, as well as possible, the immediate analytical needs of the sodium technology community. Acceptable methods, their use, limitations, and range of applicability must be specified and updated whenever appropriate.

3) Areas of sampling and analysis, where additional development work is required, must be defined, and work in different laboratories in these areas must be coordinated. Continuous surveillance of new developments must be maintained so that interim methods may be updated or replaced as appropriate.

4) Uniform application of acceptable methods must be demonstrated by sample-interchange programs.

5) Acceptable impurity limits for sodium and cover-gas systems must be defined and updated as warranted by new developments. Impurity control methods also must be specified and periodically updated.

Successful implementation of the standards program requires the close cooperation of all laboratories participating in the sodium technology effort. Accordingly, ANL organized two advisory working groups to assist in implementing this program—a Reactor Standards Working Group and a National Standards Working Group. The two groups differed only in the scope of their interests.

The Reactor Standards Working Group, composed of representatives from RDT-AEC, Liquid Metals Engineering Center, WADCO Corp., EBR-II, and ANL-Illinois, met at ANL-Illinois in July 1970. At this meeting, agreement was reached on interim sampling and analytical methods to be used, and a draft of a document prepared by ANL, "Purity Specifications for Large Operating Sodium Systems," was reviewed. The group also agreed to start sample-interchange tests for oxygen (via the amalgamation method), carbon (via the oxyacidic-flux method), hydrogen (via the amalgamation-reflux method), and individual trace metals (via the distillation-atomic absorption method) using EBR-II primary and secondary sodium as a source of samples. Accordingly, arrangements were made with EBR-II personnel to provide samples for these tests. Appropriate samples were taken from EBR-II in November 1970 and analysis of these samples was started.

After the Reactor Standards Working Group had attained its objective of satisfying the immediate sampling and analytical needs of the reactor community, it was merged with the National Standards Working Group. The latter group, which is composed of representatives from RDT-AEC, Atomics International, Liquid Metals Engineering Center, General Electric Valecitos, Westinghouse Advanced Reactor Division, WADCO Corp., and ANL-Illinois, is presently concerned with satisfying the sampling and analytical needs of the national R&D programs, and eventually will be concerned with establishing the specifications for the monitoring and control of impurities in sodium and cover-gas systems on a national scale.

ANL recently completed the preparation of a manual of interim analytical and sampling methods that incorporates the methods to be used by both reactor and nonreactor laboratories. Each analytical procedure specifies (1) the method to be used to obtain a representative sample (an overflow sample obtained in a cup or a bypass sample obtained in a section of tubing), (2) the method for obtaining an aliquot of the sample, if this is needed, (3) the method of separation, and (4) the method of measurement. These methods are listed in Table II-2. The vanadium-wire method for determining oxygen activity is intended primarily for use in calibrating oxygen meters (see Section II.C.2). However, it may be used as an analytical method for sodium systems that have an oxygen activity $\leqslant$15 ppm and that are equipped to maintain sodium in a part of the system at a temperature of 750°C for 4 hr.

As a part of the development of purity specifications for large operating sodium systems, mentioned above, EBR-II analytical data on primary and secondary sodium were accumulated and converted to graphic form. This graphic representation proved to be very useful for recognizing trends and changes in impurity content, and it evoked considerable interest from personnel of other laboratories. Consequently, an in-house computer program has been modified to provide the data in publishable form to EBR-II, which will issue the data in a report.

b. Laboratory Activities

Certification of interim methods will require the testing of these methods by ANL as well as by other laboratories in the sodium technology program. Accordingly, the analytical capabilities of ANL have been extended so that full participation in this testing will be possible. General equipment, such as inert-atmosphere boxes and monitoring equipment, has been installed. Assembly of gas-handling and gas chromatographic equipment, to be used in the analysis of sodium for carbon and hydrogen, is complete. A laboratory distillation apparatus and an atomic-absorption instrument (to be used in the analysis of sodium for trace metals) have been assembled and tested. Some effort has also been made to investigate a spectrographic method for determining trace metals and to establish a procedure for particulate analysis. The latter two areas of work are discussed below.

Spectrographic method for trace metals. Emission spectrography was evaluated as a method for determining trace

TABLE II-2. Interim Methods for the National Analytical Standards Working Group

Analysis	Analytical Method	Sampling Method	Aliquoting Method
A. Sodium Samples			
Hydrogen	Amalgamation-reflux-gas chromatographic	Bypass	Section
Carbon	Oxyacidic flux-gas chromatographic	Bypass	Extrusion
Nitrogen	Kjehldahl-colorimetric	Bypass	Section
Oxygen (total)	Amalgamation-flame emission	Bypass	Extrusion or Section
Oxygen (activity)	Vanadium-wire equilibration-inert gas fusion	None	None
Nonvolatile metals	Distillation-spectrographic, atomic absorption, or flame emission	Overflow	None
Volatile metals	Dissolution-spectrographic, atomic absorption, or flame emission	Overflow	None
Chloride and bromide	Dissolution-colorimetric	Overflow	None
Plutonium	Distillation-alpha assay	Overflow	None
Uranium	Distillation-fluorometric	Overflow	None
Iodine	Dissolution-radiochemical	Overflow	None
Radioactivity	Dissolution-gamma spectroscopic	Overflow	None
Tritium	Dissolution-beta assay	Overflow	None
B. Cover Gas Samples			
Radioactivity	Gamma spectroscopic	Flowthrough	None
Tritium	Beta assay	Flowthrough	None
H_2, N_2, CO, CO_2, CH_4	Gas chromatography	Flowthrough	None
Oxygen	Continuous oxygen analyzer	Flowthrough	None

metals in sodium because it appeared to have potential application for (1) determining metals for which atomic-absorption or flame-emission methods are not yet available, and (2) assaying metallic impurities more rapidly than the other two methods. To assess these potential applications, a sample of EBR-II primary sodium was analyzed spectrographically by determining the trace-metals content of a distillation residue.

From the tests, it was concluded that the overall analysis time by the emission spectrographic methods is not significantly shorter than the analysis time by atomic-absorption or flame-emission methods. Accordingly, the methods manual specifies the use of emission spectrography only for those metals that cannot be readily determined in sodium by atomic-absorption or flame-emission methods.

Particulate analysis. As a part of the Analytical Standards Program, ANL must specify a method of particulate analysis for use in sodium technology programs. From work at other laboratories, a procedure has evolved that is well established in all aspects but those involving (a) the recovery of particulates in an unchanged form from filter devices and (b) the examination of particles in inert-atmosphere enclosures.

In the past, polar solvents such as alcohol or water have been used to dissolve sodium from particulates on a filter. This procedure is not satisfactory because of the possibility that some or part of the particulate may be soluble in the solvent. More attractive techniques are distillation of excess sodium away from the filter or dissolution of the residual sodium in an inert solvent followed by filtration of the solution. Of these two approaches, distillation has been selected for test as a sodium-removal and particle-recovery procedure. This procedure involves (1) forcing the excess sodium from the filter housing by heating to 125°C and establishing a helium pressure of about 4 psi on the entrance tube, (2) evacuating the housing and heating to 300°C for 24 hr to distill the residual sodium and collect it in the cold end tubes, (3) opening the filter housing, removing the filter, and separating and weighing the residue, and (4) mounting portions of the residue for microscopic or X-ray examination.

Testing of this procedure has begun using a filter removed from the Mechanical Properties and Corrosion Loop of the EBR-II Project. Microscopic observation of the filter showed that sodium removal had not been complete. The residue consisted of metallic sodium and a white polycrystalline material. This material, which was quite soft, appeared in the form of white plates that were agglomerates of particles generally less than 10 μm on an edge, and reacted with normal immersion oils and mounting materials. Particles of the material are being examined by X-ray diffraction.

Attention is also being given to the design of filters for large sodium systems. For this purpose, information is

needed on the sodium flow restriction offered by a filter of various porosities and areas. In this connection, a compact filter unit, consisting of a small-diameter, cup-shaped filter cartridge, has been installed in a bypass sampling location in the Sodium Analytical Loop (SAL). The nominal pore size is 7 μm and the area is about 10 cm^2. The performance of the filter will be evaluated when it is removed from the loop.

2. Analytical Development (M. H. Barsky, H. S. Edwards, A. F. Panek, M. F. Roche, L. E. Ross)

As discussed above, the standards program requires research activities so that it may meet its ultimate objective. None of the methods presently specified for use are true standard methods. For most of the impurities found in sodium, reliable, accurate standard methods must still be developed. Consequently, ANL has undertaken their development within its own research program and plans to utilize other laboratories in the national program in this endeavor.

ANL's recent developmental effort has been directed toward the investigation of the following methods: (1) high-temperature gas chromatography as a means of separating radioactive species in reactor cover gas prior to radioactivity assays, (2) proton activation as a basis for a reference method for determining total oxygen, carbon, and nitrogen in sodium, and (3) emission spectrographic analysis of a sodium aerosol, which is generated ultrasonically and excited by an induction-coupled plasma, as a means of determining trace metals in sodium.

a. Sampling and Analysis of Cover Gas for Fission Products

The objective of this work is the technical capability for determining the types and levels of radioactive fission products in the cover gas of EBR-II and FFTF and in future LMFBRs. The primary incentive for developing this capability is its potential applicability in the detection and characterization of fuel failures.

A fuel failure in an operating reactor will result in the release of fission products from the cladding. In almost all types of failures, the gaseous fission products (xenon and krypton) will be released and will appear in the cover gas. In a few types of failures the volatile fission products (cesium and rubidium) will be released and will also appear in the cover gas. Radioassay of cover gas, therefore, offers a convenient method for detection (via xenon and krypton) of a failure and for characterization of the type of failure (via cesium and rubidium). However, the radioassay is complicated by the high level of ^{24}Na (due to vapor and aerosol) normally encountered in cover gas. This complication is overcome at EBR-II by passing a sample of cover gas through vapor and aerosol traps to remove the ^{24}Na, but in the process, most of the volatile fission products are also trapped and only gaseous fission products (^{133}Xe, ^{135}Xe, ^{85m}Kr, and ^{88}Kr) are assayed. If the full potential of cover-gas analysis for fuel-failure characterization is to be realized, separation and assay of all fission products present in the cover gas are required. We believe that the technique of high-temperature gas chromatography will provide a simple approach for the requisite separations. Chromatographic columns, either of the solid-adsorption or liquid-partition type, can be operated at a temperature near or above that of the reactor cover gas. Under these conditions, it is expected that the volatile elements (e.g., sodium, rubidium, cesium) will be retained, and perhaps chromatographically separated, while the gaseous elements pass through. Further separation of the gases could be readily performed by use of a second column operated at or near room temperature. A high-temperature sampling system and gas chromatograph have been designed and constructed. Initial experiments are being carried out to demonstrate the separation of sodium vapor from hydrogen and inactive xenon and krypton.

b. Reference Method for Total Oxygen, Carbon, and Nitrogen in Sodium

Reference methods are needed for the determination of oxygen, carbon, and nitrogen in sodium to establish the accuracy of other analytical methods. The reference methods must be specific, accurate (±10%), and capable of determining concentrations of 0.1 ppm in sodium, and must provide samples free from contamination and segregation

Activation with charged particles has become an important tool for the specific and accurate assay of oxygen, carbon, and nitrogen in the subparts-per-million range [24]. Low-energy protons are of particular interest for our application because they do not appreciably activate sodium; thus, the need for separation chemistry is eliminated and the possibility of errors from contamination and segregation is reduced. Emphasis was, therefore, placed on the development of the proton-activation method.

The concept of determining oxygen, carbon, and nitrogen in sodium by proton activation is based on the following reactions: $^{18}O(p,n)^{18}F$, $^{13}C(p,n)^{13}N$ and $^{14}N(p,\alpha)^{11}C$. Preliminary investigations of the feasibility of this method were performed by bombarding nickel-foil-covered NaF pellets spiked with known amounts of Al_2O_3, C, and AlN. The results of these preliminary experiments gave the following projected sensitivities (in ppb): O, 50 ± 25; C, 20 ± 10; and N, 2 ± 1. Precision was determined only for the $^{18}O(p,n)^{18}F$ reaction. The specific $^{18}O(p,n)^{18}F$ production was constant to within 2%.

Two potential interfering reactions were observed. They were $^{16}O(p,\alpha)^{13}N$ and $^{11}B(p,n)^{11}C$. As noted above, the carbon determination is based on the assay of ^{13}N and the

nitrogen determination on the assay of ^{11}C. An experimental evaluation of the problems showed that the interference from ^{16}O will be serious only when the oxygen level is at least tenfold greater than the carbon level and that a correction for interference of ^{11}B can be made if the boron concentration does not exceed that of the nitrogen.

Deuterons and neutrons, if present in the proton beam, would also lead to interferences via the $^{23}Na(d,p)^{24}Na$ and $^{23}Na(n,\gamma)^{24}Na$ reactions. (Deuterons as D^+ are accelerated with the H_2^+ of the proton beam; neutrons arise from reactions of the beam with the beam tube and the collimators.) Deuterons were eliminated from the beam by employing a stripper foil (to change H_2^+ to H^+) and a magnet (to separate H^+ from D^+). Neutron production was minimized by focusing the proton beam through the center of the tube.

Having shown that adequate sensitivity could be achieved and that interferences from induced activities could be either circumvented or adequately controlled, a sampling/irradiation cell was designed. The cell permits irradiation of molten and well-stirred sodium and, thereby, circumvents the two major problems of proton activation, viz., surface activation rather than volume activation (due to the short range of the protons) and vaporization of sodium (caused by the heat generated in stopping the energetic proton beam). The cell consists basically of a nickel flow-through sampler. It is equipped with (1) non-contaminating valves that can be closed to isolate ~20 cm^3 of sodium and (2) a 6-mil nickel window that is coated on its inside surface with a thin (0.28 mg/cm^2) vapor-deposited layer of cobalt. (This coating, which is not activated by protons, was applied to prevent activities generated in the nickel from recoiling into the sodium.)

The experimental procedure involves the following steps: (1) by-pass sampling of a sodium system by means of the sampling/irradiation cell, (2) proton activation of the molten and well-stirred sodium in the same cell, (3) transfer of the sodium to a counting cell, and (4) assay of the induced activities.

Initial experiments with molten sodium were directed toward testing of the cell and evaluating the problems involved in the determination of oxygen in sodium. Accordingly, two samples obtained from a sodium loop were bombarded with protons. Findings from these experiments indicated that (1) determination of oxygen in sodium by proton activation of molten, well-stirred sodium is feasible, (2) the cell functioned satisfactorily, (3) a detection limit of 1 ppm oxygen is possible with this cell design, and (4) the induced activities other than ^{18}F were ^{24}Na, ^{56}Mn, and several copper isotopes.

The copper activities are believed to have been induced in the nickel window and to have recoiled into sodium via a breach in the thin cobalt layer that had been vapor-deposited on the window. The ^{56}Mn is believed to have been induced in the cobalt layer via the reaction $^{59}Co(n,\alpha)^{56}Mn$.

The production of the manganese and copper activities can be eliminated by the use of a window made from ^{58}Ni. A cell has been designed that incorporated such a window and also holds smaller samples. The smaller sample size (10 g rather than 70 g) should allow the detection limit to be lowered to 0.1 ppm of oxygen.

The work performed to date indicates that the proton-activation method for determining very low levels of oxygen, as required by the reference method, shows great promise. However, further development of this analytical method has been deferred because of budgetary limitations.

c. Analytical Method for Determining Metallic and Halide Impurities in Sodium

Knowledge of the metallic and halide impurity content of sodium is needed, not only for monitoring the purity of sodium systems, but also for estimating corrosion effects. Currently, individual determinations of metallic impurities are made by flame-absorption, flame-emission, or spectrographic analyses of either distillation residues or aqueous solutions of sodium. These analyses are time-consuming and are justifiable only when a high level of accuracy for a limited number of impurities is required; normally, this condition does not prevail. Hence, a rapid survey method is needed that can (a) monitor a large number of impurities simultaneously and (b) indicate when a significant change in impurity level has occurred.

A number of possible analytical approaches were evaluated for suitability in this connection. These included X-ray fluorescence, emission spectroscopy, and spark-source mass spectroscopy for (1) direct examination of metallic sodium, (2) examination of aqueous sodium solutions, and (3) examination of residues formed by distilling the sodium from a sample. The method selected for initial evaluation was one that involves emission spectroscopy of a sodium aerosol. In this method, the aerosol is generated by ultrasonic nebulization of molten sodium and excited by an induction-coupled plasma torch. This method was selected because it has the potential for (a) overcoming segregation problems in sampling, (b) direct on-line application, and (c) rapid monitoring of a large number of impurities with a high sensitivity.

Initial effort was directed toward procurement of equipment, including a 30-MH_3 induction generator, a half-meter scanning spectrometer, and a quartz plasma torch. Aerosol generation with a nebulizer system was tested using a low-melting alloy (tin-bismuth eutectic, mp 138.5°C) as a stand-in for sodium. Further work on testing of components and assembly of the integrated equipment was deferred because of budgetary limitations.

C. MONITORING OF SODIUM PURITY AND SODIUM PURIFICATION (J. T. Holmes, P. A. Nelson)

1. *National Meter Program* (P. A. Nelson, J. M. McKee, J. T. Holmes)

Argonne National Laboratory (ANL) has been given the responsibility of administering a National Meter Program involving the major sodium technology contractors in the United States. This program for development and application of sodium-purity monitoring stations is designed to (1) characterize the performance capabilities of present meters, (2) standardize the design and operational procedures and establish commercial availability for these characterized meters, (3) determine the requirements for meters on a continuing basis as LMFBRs are advanced to a commercial status, and (4) upgrade performance or develop new meters, as required, to meet long-range performance goals.

Sodium technology contractors will participate in a coordinated test plan to determine the capabilities of existing impurity meters that have been developed for continuous monitoring of LMFBR sodium. Completion of this plan will result in the needed characterization of the meters in the shortest possible time by taking advantage of existing facilities. Impurity monitors in this program include oxygen, hydrogen, and carbon meters, and steam-generator leak detectors.

At present, the foremost goal of the program is meeting the needs of FFTF for commercially available oxygen and carbon meters by July 1, 1971. An additional goal is to have commercial hydrogen meters available by that date, or shortly thereafter, although this has not been listed as an FFTF requirement.

In addition to the meters themselves, prototype meter modules that include the individual meters and provide temperature and flow control are being designed for FFTF. A module is also being developed for equilibrating metal specimens with sodium to obtain measurements of the chemical activities of impurities for calibration of the meters. Both the meter modules and the calibration modules will have general utility in LMFBR systems. Commercial suppliers will be sought for these modules, as well as for the meters themselves.

ANL has organized an advisory group, consisting of representatives of the sodium technology contractors and the Division of Reactor Development and Technology of the AEC, to review the meter characterization program. This group will meet several times in FY 1971 and FY 1972 to discuss the meter selection and the test plan. Changes in the plan will probably be required to adjust to capabilities of contractors and to reflect needs exposed by results of the testing. The advisory group will consider such changes as they are suggested and make recommendations.

The first meeting of the advisory group was held in late August 1970 at ANL. As a result of that meeting, a national program for characterization of the oxygen and carbon meters was initiated. The characterization program is designed to ensure that the meters selected for standardization will perform satisfactorily under specified conditions. In addition, data on the performance of the meters will be accumulated in a field-test program to begin late in FY 1971 and to continue during FY 1972. This more extensive program is required to obtain data on the life of the meters in terms of temperature and sodium impurity content. The field-test program will be developed by ANL with the consultation of the advisory committee.

2. *Direct Measurement of Chemical Activities of Impurities* (J. T. Holmes, R. J. Meyer)

The objective of this work is the development of methods for calibrating impurity meters for carbon, oxygen, hydrogen, and, possibly, nitrogen by independent chemical determinations of the activities of impurities. Application of such methods in on-line meter calibration devices is sought. The type of method under development generally involves equilibration of thin wires of a suitable metal in sodium. The equilibrium concentration of the impurity being determined is a measure of its chemical activity in sodium. These methods are being developed in a cooperative program between the Chemical Engineering and Materials Science Divisions.

Laboratory development of the method for determining oxygen activity is essentially complete. Measurements of the distribution coefficients for oxygen in the V-O-Na system for temperatures between 500 and 750°C, in 50-degree intervals, have been reported [25]. Chemical activities of oxygen in sodium of up to 0.1 ppm at 500°C and up to 16 ppm at 750°C can be determined from measurements of the equilibrium concentration of oxygen in vanadium. The method will be used for calibration of electrochemical oxygen meters and for measurements of oxygen activities in operating sodium systems, including reactor systems.

Niobium is being investigated as a possible detector metal for measuring higher oxygen activities in sodium at lower temperatures than is possible with vanadium. Present data on the Nb-O-Na system indicate that oxygen activities in sodium above 10 ppm can be measured at 650°C.

A technology is also required for measuring hydrogen, carbon, and nitrogen activities in sodium by the equilibration method. Vanadium is also being considered as a detector metal for measuring hydrogen activity in sodium, and some distribution coefficient data have been obtained. Vanadium, iron, and iron alloys are being considered for carbon detectors. The wire-equilibration method may be applied to nitrogen activity measurements; however, a

suitable detector metal has not yet been found.

A significant effort is also being mounted to establish reliable, routine analytical procedures for the determination of the oxygen, carbon, nitrogen, and hydrogen in the equilibrated metal specimens.

To use these methods for periodic on-line calibration of the various impurity meters, suitable equipment for specimen equilibration must be designed and incorporated into a modularized package with the necessary devices for controlling sodium temperature and flow. The module must be designed for rapid access to the specimens after equilibration. For radioactive sodium systems, this can be most easily accomplished by providing for complete drainage of the radioactive sodium. The conceptual design of the module is shown in Fig. II-5. Since the module heats sodium to 750°C, it will also be used as the carbon meter module (see Section II.C.4, below) by replacing the wire holder with the carbon meter membrane system. The module consists of (1) the sodium system, which includes a magnetic flow meter, regenerative heat exchanger, heater, isothermal test section, sodium flow-control valve, and associated inlet and outlet piping that provides for drainage of the sodium for radioactive operations, and (2) an associated instrument package, which includes the power supplied and controllers for the heater, the flow-meter readout, and a number of safety alarms.

3. Oxygen Meter (V. M. Kolba, L. J. Marek, R. R. Schlueter)

The objective of this work is to develop and prooftest an on-line oxygen meter module for monitoring oxygen activity in the primary and secondary sodium systems of LMFBRs. Electrochemical oxygen meters will be evaluated and improved, where necessary, to provide (1) reliable and reproducible measurement of the oxygen activity in sodium and (2) continuous operation of the meter at temperatures up to 900°F. Testing and development of the meter module

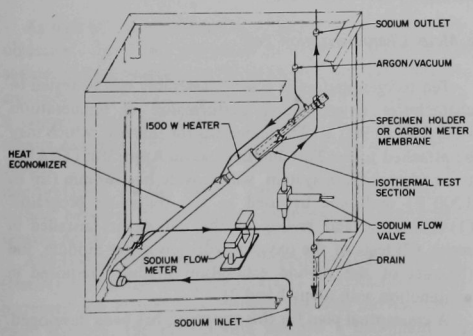

Fig. II-5. Specimen Equilibration-Carbon Meter Module. ANL Neg. No. 308-2382.

components will be carried out at the Illinois site of ANL. Characterization of the meter will be through the national program, which will involve major LMFBR sodium technology contractors. Prooftesting of the module will be done on the Radioactive Sodium Chemistry Loop (RSCL), which is being installed at EBR-II on the primary sodium system. Operating experience gained at EBR-II and in the meter-characterization program will be useful in the qualification of oxygen-meter modules for the Fast Flux Test Facility (FFTF) and for general LMFBR use.

a. Electrochemical Oxygen Meters

A new program being set up between ANL, Brookhaven National Laboratory (BNL), WADCO Corp., and the Zirconium Company of America (Zircoa) is expected to result in the commercial availability of oxygen meters by July 1971. The meters will have gas reference electrodes and improved thoria-7.5 wt % yttria solid electrolytes produced by an isostatic pressing process. The improved electrolyte tubes should be commercially available by early 1971, which will allow a few months for characterization studies to be conducted by ANL and Westinghouse Advanced Reactor Division (WARD) before the meter-commercialization target date of July 1971. The electrolyte tubes will be of the size (1/4-in. diameter) that is currently used in the Westinghouse version of the oxygen meter.

Until the improved electrolyte material becomes available from Zircoa, meters equipped with electrolyte tubes specially produced at WADCO by isostatic pressing will be obtained from BNL and Westinghouse. One of these meters will be installed at EBR-II for evaluating the effects of radiation from the activated primary sodium.

b. Apparatus for Oxygen-Meter Calibration

In this phase of the work, a system that can be used to test oxygen meters, evaluate electrolyte tubes and various reference electrode gases, provide a calibration facility, and permit evaluation of electronic equipment for readout of meter emfs will be established. A small (~2 gal) pumped sodium apparatus will be used. The apparatus, shown schematically in Fig. II-6, provides for testing up to four oxygen meters and determining their stability as a function of operating life in a sodium system having sodium flow rates of 0 to 0.5 gpm at temperatures up to 900°F. A cold trap is provided for controlling the oxygen level of the system.

Construction of the apparatus is complete and most of the instrumentation has been received and installed. Two United Nuclear Corporation (UNC) housings of the BNL type are presently installed on the apparatus. Six Westinghouse meters equipped with the electrolyte tubes specially produced by WADCO are on order; however, the

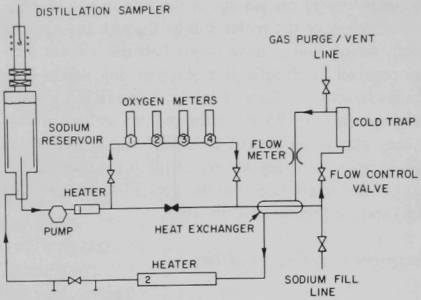

Fig. II-6. Apparatus for Oxygen-Meter Calibration. ANL Neg. No. 308-2545.

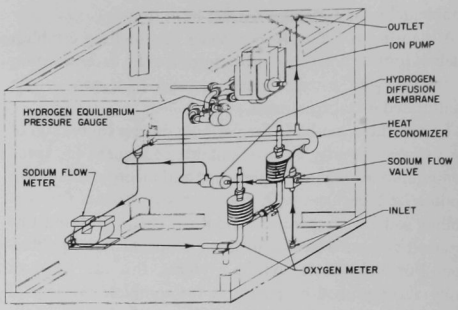

Fig. II-7. Oxygen-Hydrogen Meter Module. ANL Neg. No. 308-2383.

date of delivery to ANL is dependent upon receipt of the WADCO electrolyte tubes by Westinghouse.

Six BNL electrode assemblies, which fit into the UNC housings, have been received and will be used in the shakedown operations of the test apparatus.

c. Radiation Test at EBR-II

A test of the effect of radiation on the oxygen meter will be conducted by installing one oxygen meter on an existing sampling line in EBR-II. The meter will be operated prior to reactor start-up to obtain base-line data for comparison with data obtained during reactor operation. The test will thus permit a rapid evaluation of the effects of direct beta and gamma radiation on the operation of the oxygen meter. The results of this test are required to uncover possible detrimental effects of the radiation on cell output, stability, and life. The test is scheduled to being in early 1971.

Drawings have been prepared and fabrication of the piping needed to install the meter on EBR-II has been started. One of the Westinghouse oxygen meters now on order will be used in the test.

d. Oxygen-Hydrogen Meter Module

This work involves developing, prooftesting, and establishing commercial availability of an on-line equipment and instrument module for monitoring oxygen and hydrogen activity in sodium systems. A preliminary layout of a module containing two oxygen meters and one hydrogen meter in a stepped array has been completed (see Fig. II-7). A hydrogen meter (see Section II.C.5, below) has been included in the module with the oxygen meters since both types of meters operate at the same conditions of sodium flow and temperature. As a result, a considerable savings can be made by sharing accessory equipment. The module was designed to meet the requirements of FFTF. Comments on the preliminary design have been received from EBR-II and WADCO (FFTF), and these are being considered in the detailed design.

In addition to the oxygen and hydrogen meters, the module also provides the following components: (1) a cooler to accommodate FFTF inlet-sodium temperatures up to 1200°F, (2) a regenerative heat exchanger and line heaters to meet temperature-control requirements, (3) a control valve and flow meter to regulate and monitor sodium flow, and (4) an ion pump, vacuum valve, and ionization-type pressure gauge for the hydrogen meter.

Designs of the heat exchanger and hydrogen-meter housing are complete. Oxygen meters for the modules have been ordered from Westinghouse. Preliminary layouts of the electrical and instrumentation packages for the modules have been made and reviewed.

A prototype module will be pretested at ANL-Illinois prior to prooftesting at EBR-II. A detailed schedule and job-assignment chart have been developed for installation of the module at EBR-II on the Radioactive Sodium Chemistry Loop (RSCL), Cell B.

e. Meter-Characterization Test

Ten oxygen meters in a series assembly will be tested to characterize oxygen-meter performance at temperatures from 700 to 900°F. The apparatus for this test, which may be attached to the Test and Evaluation Apparatus (TEA) or to another sodium system, will provide hot sodium (up to 1200°F) and will be used in the following programs: (1) calibration and testing of the ten meters installed in series, (2) tests of the oxygen-hydrogen meter module, and (3) tests of the on-line calibration module (required in conjunction with items 1 and 2).

A conceptual plan for this apparatus has been developed. A design layout to determine space requirements and the preliminary design of a regenerative heat exchanger, heater, and cooler have been started.

4. Carbon Meter (C. Luner, D. J. Raue, P. J. Mach)

This work involves the development and prooftesting of an on-line carbon meter module for monitoring carbon activity in the primary and secondary sodium systems of LMFBRs. The meter housing and equipment for control of sodium temperature and flow are of the same design as those of the on-line calibration module (see Section II.C.2). Carbon-diffusion meters of the best available state-of-the-art design will be evaluated for the meter component of the module. Testing and development of the module components will be done at the Illinois site of ANL. The module will be prooftested on the Radioactive Sodium Chemistry Loop (RSCL) of EBR-II. Operating experience at EBR-II will be used to provide recommendations for carbon-monitoring stations for FFTF and general LMFBR use.

A carbon meter developed by the United Nuclear Corporation (UNC) is being given primary consideration as the on-line meter component of the carbon-monitoring station. This meter is based on measuring the rate of diffusion of carbon through an iron membrane at 1200 to 1400°F. The carbon reaching the reverse side of the membrane reacts with a flowing, moist, hydrogen-argon gas mixture to form CO. The CO is catalytically converted to CH_4, and the CH_4 concentration in the gas stream is continually measured by a flame-ionization detector.

The ultimate objective of this work is a reliable on-line carbon meter that will indicate whether or not detrimental carburization or decarburization of the materials of construction can occur in the LMFBR. The more immediate objectives are (1) an understanding of the basic relationship of the carbon-meter response to various carbon species, (2) a prooftest of the carbon meter in flowing sodium, and (3) improvement of the present diffusion-type carbon meter.

a. Carbon-Meter Response to Various Materials

As part of the experimental program to realize the first objective, the UNC diffusion probe was immersed in sodium and its response to the addition of various materials and carbon species was tested. The sodium was contained in a copper vessel and stirred with a copper agitator. All-copper equipment (except for the probe) was used because copper is inert to carbon. Thus, complications in the interpretation of the results, caused by competition for carbon between constructional materials and the carbon-sensing probe, were avoided.

Addition of trace amounts (<1 ppm) of sodium cyanide (NaCN) or sodium acetylide (Na_2C_2) to sodium at 630°C increased the carbon flux through the iron membrane. In each instance, the carbon flux reached a maximum and then remained constant for a number of hours. (Since the probe removes carbon, the carbon flux does eventually slowly decrease.) Figure II-8 shows the relationship

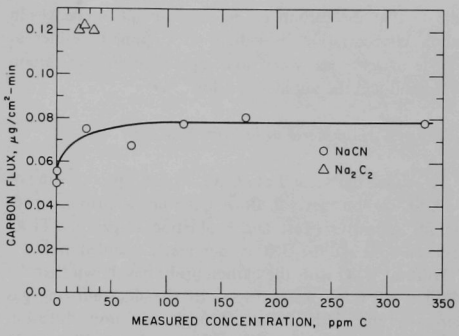

Fig. II-8. Carbon-Meter response to NaCN and Na_2C_2 in Stirred Sodium at 630°C. ANL Neg. No. 308-2384.

obtained between carbon flux and the measured concentration of NaCN in the sodium at 630°C. Initially, the carbon flux increased rapidly on the addition of 1 ppm or less of carbon (as NaCN), but above 10–20 ppm C the flux did not change. The addition of trace quantities of Na_2C_2 also increased the carbon flux, the initial increase being about twice that for cyanide. At the temperature of the experiment, acetylide decomposes rather slowly (see Section II.A.2.a) so that the variation of carbon flux as a function of acetylide concentration could not be readily measured. The further addition of sodium acetylide led to the formation of particulate carbon without noticeable increase in the analyzed acetylide content of the sodium (see Fig. II-8).

The response of the carbon meter was also tested by inserting a rod (5 in. by 1/4-in. OD) of low carbon (1020) steel into the sodium at 630°C. A few minutes after the rod was inserted, the carbon flux increased. After the rod was removed, the carbon flux reached a maximum and remained constant for 12 hr. When a Type 304 stainless steel rod was inserted, the flux decreased. The UNC meter housing, in which the probe is located and the sodium is heated, is itself made of stainless steel and can act as a getter to remove carbon from the sodium. Consequently, an inert liner for the meter housing is considered a possible improvement.

Selection of a material suitable for this service was based on the response of the probe to the addition of various materials to the crucible of stirred sodium at 630°C. Neither molybdenum nor a molybdenum-30 wt % tungsten alloy caused a noticeable change in the carbon flux, whereas a nickel rod increased the flux. Copper, although inert to carbon, was not considered a suitable liner material because of its relatively high solubility in sodium. Molybdenum has, therefore, been selected as a potential liner for the high-temperature sections in the meter housing.

The results of the experiments with carbon sources

indicate that the carbon probe can respond to changes in carbon concentration in sodium of < ppm C, either as cyanide or acetylide, when no competing sources of carbon are present and the initial flux is low.

b. Test of Carbon Meter in Flowing Sodium

To realize the second objective, namely, prooftesting of the UNC carbon meter in flowing sodium, a small pumped-sodium apparatus (Test and Evaluation Apparatus, TEA) has been built and the UNC carbon meter installed in it.

Work at UNC with the carbon probe has shown that the addition of 0.5% water vapor to the decarburizing gas increased the carbon flux through the iron diffusion membrane, but that a further increase to 1.5% did not increase the carbon flux. On the other hand, Hudson [26] has reported that the maximum rate of decarburization of low-carbon steel was obtained with >2.5% water vapor in the decarburizing gas. Because of this discrepancy, the effect on the carbon flux of water vapor in the decarburizing gas was investigated over a wider range of water concentrations than those reported by UNC. For these experiments 10% H_2-90% Ar, instead of the usual 5% H_2-95% Ar, was used as the decarburizing gas to ensure that the mixture, when combined with varying amounts of water, would prevent oxidation of the iron membrane at the temperature employed; that is, the experimental ratios of $p(H_2)/p(H_2O)$ in all cases exceeded the equilibrium constant $k = p(H_2)/p(H_2O)$ for the reaction $Fe + H_2O = FeO + H_2$. Figure II-9 shows the results obtained for experiments performed on TEA, using the UNC housing, a sodium temperature of 370°C, and probe temperatures of 625 and 750°C.

The data show about a fivefold increase in the carbon flux for a change of 0.77 to 2.38% in the water vapor content of the decarburizing gas. These data also indicate that there is little effect of temperature on the carbon flux over the range 625 to 750°C. Therefore, considerations are being given to decreasing the operating temperature of the meter below the recommended 760°C, which was based on static pot tests performed by the meter's developer, UNC; the decrease may be to a temperature as low as 650°C. For a given carbon concentration, the increase in diffusivity with increasing temperature tends to increase the flux; however, the decrease in the activity of carbon, even though the solubility increases with increasing temperature [27], tends to decrease the flux.

Increasing the flow of sodium past the probe from 0.08 to 0.17 gal/min increased the carbon flux by only 10%.

Additional tests have been performed on TEA to obtain the response of the UNC carbon meter to carbon species added to the flowing sodium. The temperature of the main loop in these tests was 500°C, and that of the side loop, where the probe is located, was 750°C. Preliminary testing

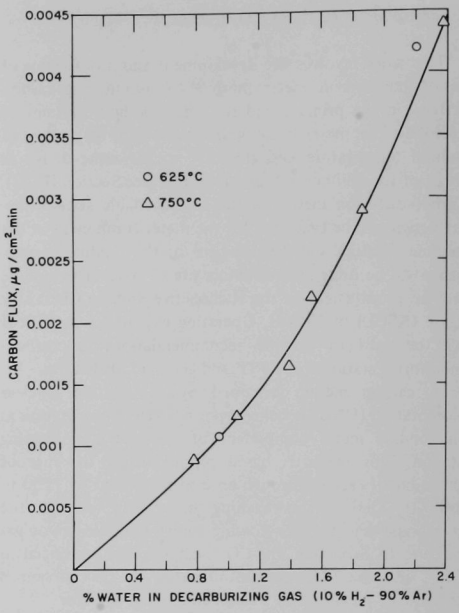

Fig. II-9. Effect of Water Vapor in the Decarburizing Gas on Carbon-Meter Response. ANL Neg. No. 308-2385.

of the UNC carbon probe in flowing sodium indicated no significant response of the carbon meter on the addition of 1 ppm C as Na_2C_2.

One possible reason for the lack of response of the probe was that, at the elevated temperature of the side loop, the added Na_2C_2 may have been removed by the stainless steel before it reached the carbon probe. To test this hypothesis, another probe housed in a molybdenum-lined, heated section (which would not be expected to remove significant amounts of carbon from the flowing sodium) has been installed on TEA in a parallel side loop. The response to carbon additives of the two meters will be compared, and, if the flux in the meter with the molybdenum-lined housing is significantly higher, a molybdenum lining may be incorporated in future housing designs.

A molybdenum-lined chamber for exposing iron or Fe-Ni alloys to flowing sodium has been installed. Startup of these new additions to TEA are now in progress. Work will proceed to establish (1) a standard probe and housing design, and (2) recommended operating temperature, decarburizing gas compositions, and sodium flow rate. Attempts will be made to correlate carbon meter readings with activities determined from metal specimens equilibrated with the carbon contained in the sodium in TEA.

5. Hydrogen Meter (D. R. Vissers, L. G. Bartholme)

The goals of this program are the design, development, and prooftesting of an on-line hydrogen meter for measuring the hydrogen activity in primary and secondary LMFBR sodium systems. The diffusion-type hydrogen activity meter under development at ANL is being evaluated for the on-line hydrogen meter component of the oxygen-hydrogen meter module (see Section II.C.3). Appropriate response-test procedures and on-line calibration procedures are being developed for the meter when required. Development and testing of the hydrogen meter will be carried out at the Illinois site of ANL. Prooftesting of the entire module will be made on the radioactive primary sodium system of EBR-II. Operating experience at EBR-II will be used to provide recommendations for hydrogen-monitoring for FFTF and general LMFBR use.

The hydrogen-activity meter being developed at ANL is an equilibrium diffusion-type monitor with a direct pressure readout of the activity of hydrogen in sodium. This direct readout is possible because the partial pressure of hydrogen in equilibrium with sodium is related by Sievert's law [28] to the hydrogen concentration in the sodium. The principal components of the meter (see Fig. II-10) are a high-surface-area nickel membrane that is immersed in the sodium, a pressure-measuring device such as a hot cathode-triode ion gauge, and an ion-pump vacuum system for periodic pumpdown. The nickel membrane operates at temperatures of 370 to 500°C.

A prototype of the ANL hydrogen-activity meter has been fabricated and is being evaluated in a newly constructed gas-flow test apparatus. The equilibrium hydrogen pressure of standard hydrogen-argon gas mixtures, equivalent to hydrogen concentrations in sodium of 0.5 to 4 ppm, were measured with a Varian Millitorr (hot cathode-triode) ionization gauge. The hydrogen-argon gas mixtures were prepared by blending ultrahigh-purity argon with analyzed standards of hydrogen-argon. Samples of the flowing gas were taken at the inlet and outlet of the chamber containing the nickel membrane; simultaneously, pressure measurements were made with the ionization gauge. Pressures indicated by the Varian Millitorr ionization gauge were approximately 25% less than the values calculated from gas-chromatographic analyses for hydrogen. The Millitorr gauges are originally calibrated with nitrogen, and a calibration factor must be applied to the pressure readout when the gauge is used to measure hydrogen (ion gauges are less sensitive to hydrogen). The apparently low results were obtained with the factor that Varian recommends, which is based on the data of Dushman [29]. However, recent studies [30] on the relative sensitivities of the ion gauge toward hydrogen and nitrogen have resulted in a revision of the calibration factor. With the revised factor, we find excellent agreement between the measured hydrogen pressure, as indicated by the Millitorr gauge, and that determined by gas chromatography. These data, which are shown in Fig. II-11, indicate that the Millitorr gauge, when calibrated for hydrogen, possesses the potential to serve as the sensor component of the hydrogen-activity meter.

Other studies were directed toward determining the time required to reach equilibrium from higher and lower initial hydrogen pressures. The hydrogen concentration in the flowing gas was changed at intervals of 60 min, and the concentration during the first and fourth hours was the same. The times required to reach the approximate equilibrium concentration after a step change in the hydrogen level was about 10 to 20 min. A representative plot of the experimental data is given in Fig. II-12.

The hydrogen-activity meter is being tested on the

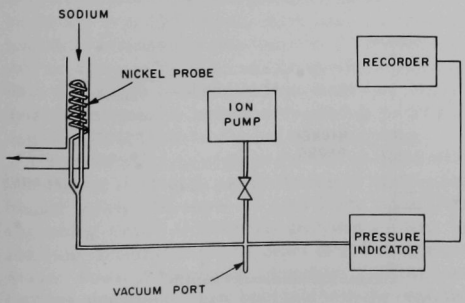

Fig. II-10. Hydrogen Activity Meter. ANL Neg. No. 308-2422.

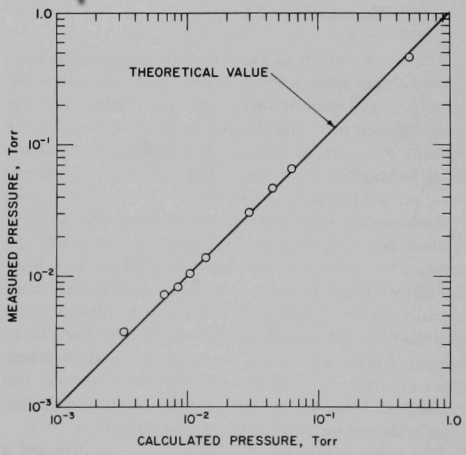

Fig. II-11. Hydrogen Activity Meter Calibration. ANL Neg. No. 308-2421.

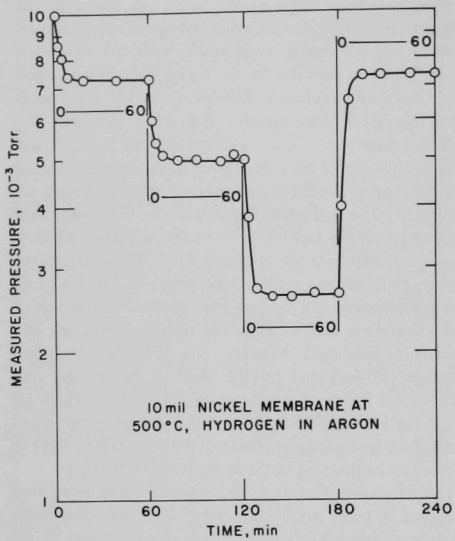

Fig. II-12. Time to Reach Equilibrium for Hydrogen-Activity Meter. ANL Neg. No. 308-2546.

Sodium Analytical Loop (SAL). Prooftesting of the meter in the oxygen-hydrogen meter module is scheduled for mid-1971 at EBR-II.

6. Detection of Leaks in Steam Generators (D. R. Vissers, C. C. McPheeters, L. G. Bartholme)

This work consists of evaluating the requirements for a leak-detection system for LMFBR steam generators and developing and prooftesting a detection system to meet these requirements. The detection system will use on-line impurity monitors for detecting the products of a sodium-water reaction; however, other means of detection are not being excluded from consideration.

First consideration is being given to hydrogen monitors for leak detection because they appear to be durable and sensitive to small changes in the hydrogen level of sodium. For this service, diffusion-type hydrogen monitors are being specially developed; a UNC electrochemical hydrogen meter may also be evaluated. Consideration will be given to an integrated detection system for large multimodular steam-generator units. A signla-interpretation and alarm unit will be developed that accommodates normal hydrogen fluctuations in the sodium without giving false alarms.

The requirements for the leak-detection system and a description of the ANL detector are presented in detail elsewhere [31]. The principal requirements of a steam generator leak detector are that it be sensitive, rapid, and precise. The sensitivity required to detect leaks that would lead to rapid perforation of adjacent tubes in a large generator (~10^6 lb sodium/hr) is the capability of detecting a change of ~4% in the hydrogen level at a concentration of 0.1 ppm hydrogen in sodium.

The in-sodium hydrogen monitor being developed for leak detection is based on the diffusion rate of hydrogen through a nickel membrane operated under a dynamic vacuum. A vacuum (10^{-6} to 10^{-8} Torr) is drawn at a steady rate by an ion pump; thus, a hydrogen-activity gradient develops from the sodium side to the vacuum side of the membrane and results in the diffusion of hydrogen through the membrane. The rate of hydrogen diffusion through the membrane, a direct measure of the hydrogen concentration in the sodium, will be determined by monitoring the current to the ion pump. This leak detector is shown schematically in Fig. II-13.

A prototype leak detector of the type described above has been installed on a pumped sodium system (Sodium Analytical Loop, SAL). Tests of this unit have indicated that the detector readout signal is quite stable when the ion-pump power supply is operated off a noise-free, 110-V, ac line. Further tests have shown, however, that the stability of the detector readout signal is strongly affected when other appliances are being operated off the same 110-V line. Typical ion-pump current readings, taken at 1-sec intervals, showed that the noise level was about 2.3% of the recorded signal of 17 μA, a current reading equivalent to ~0.1 ppm hydrogen in sodium. (An ion pump is normally operated at 3,000–5,000 V dc; consequently, in the conversion from ac to dc, any fluctuations in the input line voltage are greatly magnified in the output voltage.)

To improve the signal-to-noise ratio, a Sorensen ac line regulator (ACR, ±0.1%) was installed between the ion-pump power supply and the 110-V ac line. The conditions under which the regulator was tested were the same as those described above—an irregular 110-V line voltage and an ion-pump current corresponding to ~0.1 ppm hydrogen in sodium. The results showed the line regulator decreased

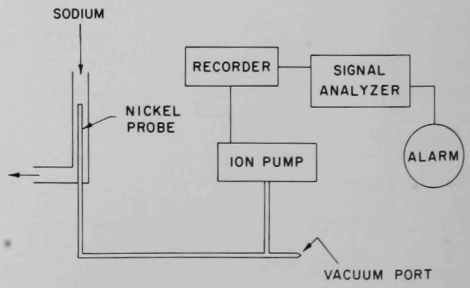

Fig. II-13. On-Line Ion Pump Hydrogen Detector. ANL Neg. No. 308-2420.

the noise level from 2.3% of the recorded signal to 0.06% and increased the sensitivity to the extent that a 4% change in the hydrogen level at a concentration of 0.1 ppm hydrogen dissolved in sodium could be detected.

In-sodium calibration tests of the leak detector were also conducted in SAL. The ion-pump current was related to the concentration of hydrogen dissolved in the sodium by determining the equilibrium-vapor pressure of hydrogen above the sodium. Equilibrium samples of hydrogen were collected on the vacuum side of the in-sodium nickel membrane after equilibration times of 1, 2, and 3 hr and analyzed for hydrogen with a gas chromatograph. The results of the analyses indicated that the equilibrium hydrogen pressure over the sodium was $1.9 \pm 0.05 \times 10^{-2}$ Torr, which corresponds to a dissolved hydrogen content in the sodium of 0.67 ppm. The value for the hydrogen content of the sodium was calculated using data on the equilibrium relationship between the dissolved hydrogen in sodium and the hydrogen pressure above it [32].

From this hydrogen concentration, the theoretical ion-pump current was calculated for the leak detector. In this calculation, the ion-pump pumping speed was assumed to be 7.5 liters/sec. (Earlier calibration studies on this type of pump with standard hydrogen leaks had indicated a pumping speed of 6–9 liters/sec.) The hydrogen permeability assumed for the nickel membrane was based on the work of Ebisuzaki *et al.* [33]. The results indicated a theoretical ion-pump current of 84 μA, a value that is in reasonable agreement with the measured ion-pump current of 101 μA.

The sodium in this system was next cold-trapped at temperatures of 190 and 156°C, and the effect of this cold-trapping noted on the ion-pump current, which varies directly with the hydrogen activity of the sodium. If the hydrogen activity of a sodium system that has been cold-trapped to a particular temperature is assumed to be the hydrogen solubility at that temperature, then the values of hydrogen activity found in this study and those reported by Birault *et al.* [34] should agree with the hydrogen solubilities determined by Meacham *et al.* [32]. All of these data are shown in Fig. II-14, and the agreement among the three sets of data is excellent. These studies indicate that hydrogen activities in sodium corresponding to 0.1 ppm dissolved hydrogen can be obtained by cold-trapping.

The presentation of a paper on the ANL hydrogen-meter leak detector at the 16th Annual Meeting of the American Nuclear Society [35] and to the staff of the Liquid Metal Engineering Center (LMEC) has generated requests for additional information on the meter from Westinghouse, Atomic Power Development Associates (APDA), and LMEC, and discussions have been held with the respective organizations during the past months. Westinghouse has decided, from these discussions, to install a hydrogen-meter leak detector on their Fission Product Loop Number Two.

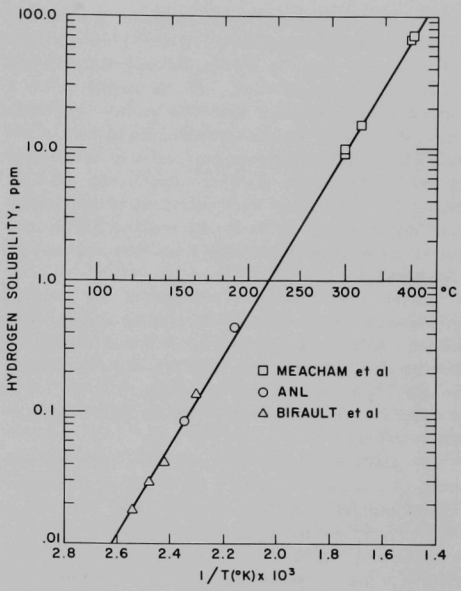

Fig. II-14. The Solubility of Hydrogen in Sodium. ANL Neg. No. 308-2547.

This loop is used to study the behavior of fission products in sodium-stainless steel systems. The long-range plans at Westinghouse call for evaporators, reheaters, and superheaters to be constructed of Incoloy 800; therefore, their requirements for a leak detector are much less stringent because the wastage rates of Incoloy 800 are much less than those of Croloy-2 1/4 or Type 304 stainless steel, which are commonly used in other systems. Consequently, the Westinghouse leak detector will be operated under conditions that require less rapid response times. Nickel membranes are currently being fabricated at ANL for Westinghouse.

Plans are being made to supply an ANL hydrogen-meter leak detector for the Sodium Component Test Installation (SCTI) at LMEC for use in their test of the Atomics International "hockey stick" steam generator, which is scheduled for spring or summer of 1971.

Work is also under way to develop a leak-detection system for the secondary sodium system at EBR-II.

7. Characterization of Cold-Trapped Sodium
(C. C. McPheeters)

The primary goals of this work are the determination of nonmetallic impurity levels in cold-trapped sodium (as a function of cold-trap operating parameters and procedures)

and interpretation of the experimental results. The methods for determining the impurities (O, C, H, N) in the sodium will be on-line impurity monitoring, and sampling and analysis. Experimental work will be carried on in a pumped-sodium apparatus that will provide stable but adjustable impurity levels in the sodium fed to the test cold trap. The EBR-II primary-coolant cold trap will also be equipped with on-line impurity monitors on the inlet and outlet sides. Data for both transient and steady-state operation of the test trap and the EBR-II trap will be correlated with cold-trap parameters and the feed composition.

Current work involves (1) design of the pumped-sodium system (Apparatus for Monitoring and Purifying Sodium, AMPS) for conducting definitive studies on the character of cold-trapped sodium and (2) planning for the in-line oxygen and hydrogen monitors to be provided on the inlet and outlet of the EBR-II primary-system cold trap.

The AMPS is a small, pumped-sodium apparatus consisting of a sodium reservoir, a purification leg, an experimental manifold, and an expansion tank. The sodium reservoir contains the bulk of the sodium used in the apparatus and is designed to enhance mixing. The purification leg provides a means of controlling the impurity level in the system by the forced circulation of sodium through an air-cooled cold trap and a hydrogen-getter trap. The experimental manifold provides a means of circulating sodium from the sodium reservoir to the test cold trap, which is instrumented with on-line oxygen-hydrogen meter modules and a calibration module. The expansion tank is used for level control. Above the expansion tank is a distillation sampler, which is used to obtain samples for analysis of the impurities in the sodium reservoir.

AMPS is designed for continuous operation at steady-state conditions. Impurity concentrations will be controlled by varying the temperatures in the purification-leg cold trap and hydrogen-getter trap. The control, which will be automatic, is based on the outputs of the oxygen and hydrogen meters.

The conceptual system design description has received AEC approval, and detailed design of components and systems has been started. AMPS construction is scheduled for completion late in 1971.

Oxygen and hydrogen meters will be installed on the effluent sodium line from the EBR-II primary cold trap. These meters will be used in conjunction with similar meters on the Radioactive Sodium Chemistry Loop (RSCL) to characterize the EBR-II cold-trapped sodium for normal and abnormal operations. An EBR-II plant modification proposal has been accepted, and the engineering package for the installation is being prepared.

D. FISSION PRODUCT AND COVER GAS TECHNOLOGY (W. E. Miller, P. A. Nelson)

1. Failed Element Detection and Location (FEDAL) Systems

a. Requirements for Detection Systems (W. E. Miller, W. J. Mecham)

Fuel failures in nonvented fast-reactor oxide fuel elements in sodium cooled reactors may be characterized as follows:

Type 1. Cracks or pinholes in the cladding, which allow fission gases to escape either intermittently or continuously.

Type 2. Failures in which sodium coolant enters the fuel element through a cladding defect. The sodium can subsequently be expelled or, if the defect is large enough, the sodium can continuously wash the oxide, carrying with it fission products that have leached from the fuel.

Type 3. Failures that allow particles of fuel oxide to escape to the coolant. This type of failure is not likely to occur spontaneously but would probably result from a failure that started with sodium-oxide contact and progressed because of a combination of chemical attack and flow erosion of the oxide.

Type 4. Fuel meltdown, which would occur when coolant flow is diminished and power output is maintained.

The present mode of operation of sodium-cooled reactors is to shut down and correct Type 1 failures. A charged-wire detector (called Fission Gas Monitor at EBR-II), based on the detection of gamma emitting daughters of ^{88}Kr, ^{89}Kr, and ^{138}Xe, has been the major instrument used to detect Type 1 failures. There has been no routinely used location system, although "tagging" by incorporating mixtures of stable isotopes of xenon inside the fuel-element jacket is being used for experimental fuels in EBR-II.

Commercial LMFBRs may continue to operate with Type 1 failures; in fact, some reactor concepts include the use of vented fuel, from which fission gases escape continuously. Unscheduled shutdowns of commercial plants would result from more serious types of fuel failures: propagation of failure from pin to pin, blocking of coolant flow channels, and washout of oxide fuel from the cladding. For less serious failures, adequate information is not available on how much dispersion of radioactive fission products, activated corrosion products, or fuel is tolerable in operating fast reactor systems. In light-water reactor plants, ~1% of the fuel pins develop leaks, and no serious failure progression occurs if the pin is left in until the normal discharge time. The level of radioactivity of the water coolant is kept low by venting volatile fission

products and by ion-exchange treatment of recycled water. However, in the different chemistry of an LMFBR system, the consequences of operating a reactor with 1% failures are not known. Moreover, the much higher "normal" radioactivity level in an LMFBR from activated sodium (principally 15-hr ^{24}Na), tends to obscure detection of failure progression.

One of the urgent needs in the overall LMFBR program is to test oxide fuels to failure and beyond, i.e., beyond the appearance of a pin hole or crack that allows escape of gas. For these tests, which might be conducted either in EBR-II or FFTF, a detection system is needed to monitor the failure while it is progressing. Data from a FEDAL system with diagnostic capability is necessary to evaluate the failure experiences and to build up fuel-reliability information under conditions where fuel elements are run beyond failure. Lack of such a system could jeopardize the test reactor. A FEDAL system is, therefore, required for this stage of LMFBR development, regardless of whether FEDAL is included in commercial LMFBRs.

Certain types of fuel failures (for example, gas blanketing, which might cause fuel pin meltdown) will require fast-response instrumentation for recognition. A number of fast-response devices are in various stages of development in the LMFBR program (from concept to testing in loops to reactor installations). Some of these devices are conductivity probes, flowmeters, microphones, tuning forks, and accelerometers. The principle of most of these devices is the detection of gas bubbles moving through a fuel assembly, and thus they have a potential for locating as well as detecting gas leaks. However, a fuel-failure detection system is needed that will distinguish between cladding defects that release only gas and serious failures that could lead to restricted coolant flow and, thus, could propagate failure to adjacent elements. Delayed-neutron monitors should detect extensive washout of oxide particles from the cladding, but these devices, which are designed to protect the reactor, provide little capability for determining the extent of leaching of the fuel by sodium prior to extensive washout.

The feasibility of continued operation of a sodium-cooled reactor containing fuel failures hinges on whether the failure progresses after contact of the fuel with sodium. If a completely passive fuel is developed—that is, one that continues to operate without difficulty after sodium enters the element through a cladding defect—then a FEDAL system with diagnostic capabilities may not be required in the long run. If fuels operate passively for only a short time, however, a FEDAL system will be required, even though the frequency of cladding failure is minimized by quality assurance programs. Results of tests and reactor experience to date lead to two important conclusions: (1) conditions have not been determined for preparing a passive fuel; and (2) prolonged exposure of bare fuel to high-velocity sodium will result in some leaching, disintegration, and removal of the oxide.

For a reactor fuel pin in which sodium is contacting the oxide, a logical point to cease operation is just before the release of a significant amount of oxide to the coolant. It is important, therefore, to define this fuel-failure condition more precisely. The results of tests [36] with the delayed-neutron detector at EBR-II indicate that this device will not be adequate for detecting this condition. When a 13-in.-long, bare metal fuel pin was exposed in the reactor, the signal-to-noise ratio (the noise is the background coming from fissions that regularly occur outside the cladding) of the device was only 3.9. It was concluded that the signal source of the delayed-neutron precursors was the surface recoils off the bare pin. The same phenomenon is expected with oxide fuel; that is, the only available source of delayed-neutron precursors for the signal will be surface recoils. (The short half-lives, maximum about 1 min, preclude the diffusion of neutron precursors from the interior of the fuel to the surface.)

Exposed fuel areas $<2\ cm^2$ are likely to escape detection by a delayed-neutron detector [37] because of its low signal-to-noise ratio. A defective area of $2\ cm^2$, which is greater than the cladding area adjacent to one oxide fuel pellet, is likely to lead to a gross failure, either from pellet washout or excessive fuel leaching by sodium, and such a defect would not be detected until the gross failure occurred.

Before particles are released, some leaching of fuel and consequent release of soluble fission products and gases to the coolant would have occurred. These should be recognizable to a detection system. A satisfactory approach to failure diagnostics would be as follows: (1) pick candidate fission-product elements for failure-progression monitoring, (2) develop monitors for measuring the concentration of these candidate indicators, and (3) correlate concentration of indicators to severity of failure and coolant contamination in reactor tests. The choice of fission product elements for failure diagnostics has been discussed elsewhere [38]. Cesium, rubidium, iodine, and tellurium appear to be the elements that will be readily leached out of oxide fuel by sodium. Varying amounts of isotopes of these elements should appear in the coolant before oxide particles are extensively washed out of the cladding. The questions of what specific isotopes to look for and what amounts must be detected to characterize a leak are very complex. The amount of a particular isotope that transfers from the oxide matrix to the sodium flowing outside one pin is controlled by two major considerations: (1) complex mass transfer processes governing the rate of transfer from the solid oxide matrix to the sodium inside the pin and (2) diffusion of the fission product isotope through this sodium, which then

mixes at some rate with the high-velocity sodium outside the cladding. These two processes are involved in the determination of the escape fraction, f, which, for the case of short-lived activity, is the fraction of the equilibrium yield in the pin that appears in the coolant sodium.

When a monitor measures the amount of a specific isotope in the coolant, it is measuring a "noise" component as well as a signal component. The noise for any specific isotope comes from two sources: (1) fissions occurring outside the cladding (from tramp uranium) and (2) residual amounts of the isotope left from a previous failure. The signal comes from activity injected into the coolant from the failure. For short-lived activity, the noise component from extraneous fissions quickly comes to an equilibrium level, which must be significantly less than the signal. For very long-lived isotopes (especially ^{137}Cs), residual activity from earlier failures becomes significant if the coolant is not treated to remove the activity from previous failures.

The signal-to-noise problem for short-lived activity (i.e., where the noise level from tramp uranium is at equilibrium and the activity level from a previous failure has attenuated appreciably) can be put in perspective by considering the following. The maximum amount of activity of a single isotope that can appear in the coolant from any one fuel pin failure is the equilibrium yield of that isotope in the pin. The actual amount will be less by a factor of f, the escape fraction. If S is the signal activity of an isotope being injected into the coolant from a failure and N is the activity of that same isotope from tramp uranium, then

$$S/N = Pf/p \qquad (1)$$

where P is the power generation in one fuel pin and p is the power generation from fissioning of tramp uranium.

In EBR-II, the power generation from tramp uranium, p, is about 10 W at a reactor-power level of 50 MW [39]. For oxide fuel elements 1 ft long operating at 20 kW/ft, $S/N = 2000f$. This means that the escape fraction, f, of a failed element must be greater than 5×10^{-4} to make the signal greater than the noise. For the same chemical species, the escape fraction decreases with decreasing half-life; thus, there will be a lower limit for the half-life of an isotope suitable for fuel-failure diagnostic work (a half-life of 1 min is not long enough, as demonstrated by experience with delayed neutron detectors). Cesium, rubidium, iodine, and tellurium isotopes being considered for failure diagnostics have a broad range of half-lives: cesium–30 yr, 32 min, 9.5 min; rubidium–15.4 min, 2.74 min; iodine–8.05 days, 20.8 hr, 6.68 hr, 52.5 min; tellurium–33 day, 72 hr, 30 hr, 50 min, 12.5 min. Experience with fuel failures in a reactor will show which isotope or group of isotopes is suitable for characterizing fuel failures.

b. Development of In-Sodium Monitors for Fuel-Failure Detection (N. R. Chellew, C. C. Honesty, R. C. Paul)

The on-line application of gamma spectrometry for analysis of fission-product isotopes in primary sodium is hampered by the interference from sodium-activation products, mainly ^{24}Na. Therefore, the major problem to be solved is the development of separations methods that are adaptable to on-line monitoring equipment.

Three approaches to the sodium-radioisotope separations problem have been considered: (1) Elements more volatile than sodium, including cesium and rubidium, could be separated from sodium by an in-line, multistage vacuum-distillation column that greatly increases the ratio of cesium and rubidium to ^{24}Na in the vaporized product. (2) Fission and corrosion products could be extracted into a second liquid phase, e.g., lithium, that is circulated and counted; this second phase accumulates the nonvolatiles when the volatiles, including sodium, are distilled from it. (3) Iodine in sodium could be determined from the rate of generation of its daughter xenon, a gas that could be sparged out of the sodium and counted. Current effort is being directed toward developing the iodine-monitoring concept into an on-line monitoring device.

The steps involved in monitoring iodine in the sodium are as follows: (1) sampling of the reactor sodium in a flow-through sampling-sparging vessel, (2) sparging the sample with helium (containing a small amount of inactive xenon as a carrier) in a gas recirculation loop to strip the sodium of the xenon that was present at the time of sampling, (3) trapping and discarding the xenon stripped in step 2, (4) allowing iodine in the sample to decay for a predetermined time to allow buildup of xenon daughters, (5) restripping the sodium of xenon gas with recirculating helium containing added inactive xenon, and (6) trapping and assaying the xenon produced from iodine decay. Assuming that the transfer of xenon from the sodium to the xenon trap is essentially complete, the concentration of iodine in the sodium phase is calculable from the measured xenon activity, decay constants of the isotopes in the mass chain selected, and the times involved in the various steps.

Of the xenon activities considered for assay in reactor application of the iodine-monitor concept, the 15.6-min ^{135m}Xe isotope is of primary interest. Its precursor, ^{135}I (6.7 hr), has a long enough half-life that its escape fraction to the coolant through a cladding leak should be significantly greater than that of delayed-neutron precursors, but its half-life is not so long that buildup of activity in the coolant would interfere with the detection of subsequent fuel failures. In addition, the half-lives of the ^{135}I precursors, 1.9-sec Sb and 29-sec Te, are short enough that they will not complicate the ^{135m}Xe assay. Calculations have shown that for assay of ^{135}I in EBR-II sodium (from tramp uranium only), two 5-min decay periods

(step 4, above) and two 5-min counting periods (step 6, above) are sufficient.

Current development work on this concept is concerned with (1) design of the sampling-sparging vessel, (2) design of a xenon counting trap, and (3) measurement of the rate of removal of xenon from sodium by the sparging technique.

c. Location Systems (W. J. Mecham, W. E. Miller)

It is appropriate to review the role of failed-element location in the overall system for dealing with fuel element failures. The overall sequence of operations involved in detection and replacement of failed fuel may be considered as consisting of four major steps: (1) detection of failure, (2) fuel-failure diagnostics, (3) adoption of a reactor operating strategy, and (4) removal of failed element. Note that location of the failed element may be a part of any of the four steps or it may be absent entirely. The reason that it may be absent is that all elements are replaced, eventually, whether or not they have failed. In one sense, then, the question that a diagnostic system should answer is not, necessarily, where a failed fuel is, but rather when it should be replaced.

The above comments should not be taken to indicate that location is not important for fuel-failure diagnosis and operation strategy. Location is very important in saving time in failed-element removal and replacement, if serious failures are frequent. Therefore, the need for a location system will depend on the overall fuel performance. If the fuel performance is reliable and failures do not propagate to adjacent elements or cause blockage of coolant channels, existing methods, such as flux tilting, may suffice for locating failures.

A number of concepts of locating failed fuel have been devised. Xenon tagging, which is presently being used for experimental fuels in EBR-II, will probably not be applicable in future reactors operating with vented and/or defective fuel. Several other concepts, which were evaluated for FFTF application, involved the disengagement of fission-gas bubbles from sodium. In these concepts, a stream of sodium is withdrawn from each fuel assembly and processed to release gas bubbles. Thus, it is theoretically possible to locate the fuel assembly containing the leaking fuel pin by detecting fission gases coming from that assembly. These concepts have proven to be difficult to implement because of the complexities arising from the presence of a line extending from the top of each fuel assembly to the processing equipment.

Part of the difficulty arises from the assumption that the locator method must be on-line. On-line location is not a necessity for an LMFBR power plant. If all the leaks that are detected by the detection method during an operating period are simply gas leaks, reactor operation would be expected to continue until a scheduled shutdown for fuel shuffling. At that time, a search would be made for the leaking elements. If a more serious failure occurred, and was detected and characterized as serious failure by the detection method, then plant shutdown would be required and a search would be made for the serious leaker after shutdown. If the above philosophy, which is followed in LWRs, were adopted for LMFBRs, then the following approach might be taken.

A small gas trap could be built into each fuel assembly. In its simplest form, this trap would be a closed dome placed over the outlet of each fuel assembly, but attached to it. The dome would have a smaller cross section than the fuel assembly to allow sodium flow out of each of the close-packed hexagonal arrays of fuel assemblies into the reactor vessel above the core. The gas trap would be designed to be inefficient at normal sodium velocities, since collecting bubbles from a stream of high-velocity sodium is difficult and the pressure drop would be very high. Instead, the trap would be designed to function at very low sodium velocities, such as those existing at reactor shutdown.

Two factors contribute to a gas release during reactor shutdown: (1) The pressure outside the pin is reduced when the sodium velocity is reduced, and, as a result, gas is released either from a fuel defect or from the vent as pressure balance is achieved. (2) Experience with oxide fuel indicates that a burst of gas is also released from the oxide matrix when the fuel cools.

If cladding leaks (either small, continuous gas leaks or large, serious leaks) are present at the end of the reactor operating cycle, the fuel-assembly gas trap should contain quantities of isotopes such as ^{88}Kr (2.77 hr), ^{85m}Kr (4.36 hr) and ^{135}Xe (9.3 hr). The gas trapped in each dome would be sampled with a "sipping" tool attached to the already existing refueling mechanism, and only one line would be used to route the gas samples, in turn, from the sipping tool to a shielded-detector site. Other ways of utilizing the sipping technique are under consideration.

2. Radioactive Repair Engineering (W. J. Mecham, W. E. Miller)

The primary system of an LMFBR becomes radioactive from activation of structural materials and sodium and from fuel sources, and the spread of this radioactivity throughout the primary system is expected to cause serious maintenance problems. Plans for the research and development work required to evaluate these maintenance problems are being formulated; the program emphasizes the use of EBR-II. The plans include work in the following categories: monitoring and surveillance, activity-level prediction, decontamination and maintenance procedures, and activity-level control methods.

There are two trends in design and proposed mode of operation of future LMFBRs that will lead to primary system contamination levels greater than those presently existing in EBR-II. (1) The temperature levels will be

higher, which will increase transport rates of activated corrosion products. (2) Reactors will continue to operate with fuel elements that have lost hermetic seals; thus, some fission products normally contained within the cladding could distribute throughout the primary system. The higher levels of radiation are expected to cause increased difficulties in maintenance, and the severity of these maintenance problems is related to the specific radiation levels in existence in the area of maintenance work.

At present, the radiation levels that will be encountered in future reactors cannot be predicted with any degree of certainty because the transport and deposition processes are very complex and complete theories for prediction do not exist. This information can be gained only by reactor experience, in which the radiation levels are monitored as temperatures are increased and the reactor is operated with some failed fuel in the core. Valuable insight into some of the problems could be gained by conducting experiments to study the spread of radioactivity in EBR-II. The proposed studies, some of which (items 2 and 6) would require plant changes, are as follows: (1) develop and implement standard methods of analysis for examination of contaminated surfaces taken from the reactor (these surfaces may be those of tabs inserted for this purpose or of components taken from the primary system or from the analytical cold trap); (2) gain access to the shell side of the intermediate heat exchanger for deposition measurements; (3) develop and execute a plan for use of tabs as a tool for measuring system contamination during periods of operation with failed fuel; (4) conduct experiments using reactor sodium to investigate the transport of activated corrosion products; (5) remove and analyze circulating particulates or measure their effects indirectly; and (6) use the cold trap or the analytical cold trap to investigate methods for removing activity from primary sodium.

3. Nature and Control of Sodium Aerosol (R. W. Kessie, W. E. Miller, L. J. Marek)

The presence of sodium aerosol in reactor cover gas can interfere with the movement of control-rod drive units, shafts, and other mechanical parts of the reactor, clog the gap between moving parts, and transport fission products and other impurities from the sodium phase to the cover-gas phase.

In sodium-cooled reactors of the pool design, the upper region of the primary containment vessel is filled with an inert cover gas of argon or helium, which promotes the isolation of the cooler primary containment cover from the thermally hot sodium. For reactors presently operating with a temperature of 400°C or less at the sodium-cover gas interface, no problems of sodium transport in the cover gas have been encountered. However, proposed LMFBR designs that extend the interface temperature to 650°C are expected to produce a large increase in the transport of sodium in the cover gas.

At temperatures above ~300°C, most of the sodium transported in the cover gas will leave the sodium pool as sodium vapor. If the interface temperature exceeds the cover-gas temperature by more than 50°C, most of the sodium vapor will be condensed to aerosol within a few millimeters of the interface. Convective recirculation of cooled aerosol from the cover gas back to the hot sodium surface will promote continued transport of sodium vapor from the pool surface to the aerosol particles. At the higher sodium-pool temperatures (>400°C), it is expected that processes of agglomeration and gravitational settling will control the concentration and size of the aerosol. Both experimental and calculational studies have been carried out to determine aerosol properties, to investigate the mechanism of sodium aerosol formation, and to study methods of aerosol control.

a. Experimental Studies

Initial experimental studies were directed toward measurements of sodium-aerosol concentrations in argon cover gas over a sodium pool at various temperatures. The experiments were conducted in a closed cylindrical vessel having inlet and outlet tubes for passing gas through the system; the apparatus is described in detail elsewhere [40]. The data from these experiments are presented in Table II-3. Because of experimental difficulties with loss of aerosol in the sample lines, the values obtained are considered to be only lower limits. In addition, the values for Runs NAF3 and NAF4 are estimated to have an accuracy of about ±20% due to a short collection time (1 min) and transient effects in the collection equipment at startup. The calculated vapor concentrations, obtained from the properties of saturated sodium vapor, are also given in Table II-3. Both the calculated vapor and the measured aerosol concentrations are based on the volume of cover gas at 1 atm and 25°C. In spite of the experimental difficulties, the results indicate that the sodium aerosol concentration can exceed the concentration resulting from the vapor pressure by a factor greater than 9. An extremely high aerosol concentration, 35 g/m^3, was measured above the sodium at 500°C.

Preliminary measurements of the particle-size distribution

TABLE II-3. Sodium Aerosol Concentration in Argon Cover Gas

Run	Sodium Temp (°C)	Measured Aerosol Conc. (g/m^3)	Calculated Vapor Conc. (g/m^3)
NAF1	200	0.00022	0.000168
NAF2	300	0.0048	0.0174
NAF3	403	4.6	0.490
NAF4	500	35	5.06
NAF5	600	plugged line	33.4

of sodium aerosol in argon over sodium at 400°C were made with a Casalla jet impactor. The experimental equipment was essentially the same as that used in the experiments described above, except that larger inlet and outlet tubes (1/4-in. OD, rather than 3/16-in. OD) were used.

The amounts of sodium collected in the individual stages of the jet impactor are given in Table II-4 for two experiments at 400°C. For Run NAJ5 (collection time, 6 min), some of the material was lost from the first stage, and this was visually apparent from the irregularity of the deposit. The final filter collected sodium aerosol that had passed through the four impactor stages in both runs. Also presented in Table II-4 are the results of an experiment (Run NAF8) in which all of the aerosol was collected on a single filter. The close agreement of this total aerosol concentration with the average total from the jet impactor runs indicates that aerosol collection in the body of the impactor is not significant. The fact that these values are about 20% higher than a previous value obtained at 400°C (Run NAF3) indicates the improvement effected by the larger-diameter outlet line.

The calculated stage particle size for 50% collection (and 50% penetration) is given in Table II-5 along with averaged aerosol data from Table II-4. The data are also plotted in Fig. II-15, where it can be seen that the mass mean diameter was ~4 μm, i.e., 50 wt % of the sodium aerosol was present as particles having diameters less than 4 μm. The plot in Fig. II-15 assumes a logarithmic normal distribution and a sharp cutoff of particle-size collection in the jet impactor stages, whereas the line actually has a steeper slope due to real width of the stage cut-off.

TABLE II-5. Particle-Size Distribution of Sodium Aerosol at 400°C

	Stage 1	Stage 2	Stage 3	Stage 4	Final Filter
Calibration constant[a] (μm)	15.4	6.5	3.3	2.2	
Avg. sodium concentration (g/m^3)	0.3	0.8	2.1	1.5	0.7
Cumulative wt % less than stated diameter	94	80	41	13	

[a]Calculated stage particle size for 10 liter/min flow rate from Report UR-129, "The Modified Cascade Impactor" by Sidney Laskin (1960).

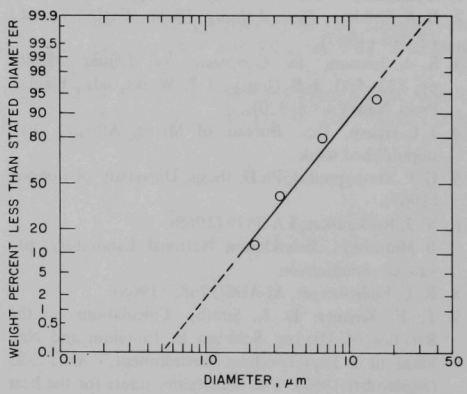

Fig. II-15. Particle-Size Distribution of Sodium Aerosol above Sodium at 400°C. ANL Neg. No. 308-2548.

b. Calculational Studies

The sodium aerosol characteristics in the cover gas over the sodium pool will be principally controlled by the following process mechanisms: (1) heat transport, (2) mass transport, (3) nucleation, (4) agglomeration, and (5) gravitational settling. The development of models based on combining these process mechanisms is needed to determine the value of small-scale laboratory experiments and the need for full-scale tests.

Heat transport calculations [41] have indicated that most of the condensation to aerosol will occur close to the sodium surface.

Sodium vapor that has evaporated from the sodium pool

TABLE II-4. Sodium Aerosol Concentrations in Argon Cover Gas

Sodium temperature: 400°C
Aerosol flow rate: 100 ml/min (25°C)
Impactor flow rate: 10 liters/min (25°C)

Run	Stage	Collection Time (min)	Sodium (mg)	Concentration (g/m^3)
NAJ5	1	6	Partially Lost	
NAJ5	2	6	0.425	0.71
NAJ5	3	6	1.150	1.92
NAJ5	4	6	1.025	1.71
NAJ6	1	1	0.30	0.30
NAJ6	2	1	0.0875	0.88
NAJ6	3	1	0.230	2.30
NAJ6	4	1	0.1275	1.28
NAJ5+6	Final Filter	7	0.475	0.68
NAJ5+6	Average Total			5.4
NAF8	Filter	40	21.25	5.31

surface will be cooled by natural convection in the cover gas. Most of the sodium vapor will condense on existing aerosol particles and cause them to grow. As these particles are removed either by gravitational settling or cover gas circulation new particles will be created by nucleation processes. Three processes are possible: nucleation on foreign particles, nucleation on ions, and spontaneous nucleation. Since no experimental data were found for nucleation processes of metal vapors, a calculational study [42] was made to examine these three processes as applied to sodium aerosols, and a comparison was made with experimental data for water vapor.

Further work on both the experimental and calculational studies of sodium aerosols has been deferred because of budgetary limitations.

REFERENCES AND FOOTNOTES

1. A summary of this section is given on pp. 5 to 8.
2. B. A. Shikhov, *Russ. J. Inorg. Chem. (English Transl.) 12*, 545 (1967).
3. S. A. Jansson, in *Corrosion by Liquid Metals*, pp. 523–560, J. E. Draley, J. R. Weeks, eds., Plenum Press, New York (1970).
4. J. L. Henry, U.S. Bureau of Mines, Albany, Ore., unpublished work.
5. G. P. Stavropoulos, Ph.D. thesis, University of London (1967).
6. V. J. Rutkauskas, LA-3879 (1968).
7. B. Minushkin, Brookhaven National Laboratory, private communication.
8. R. L. Eichelberger, AI-AEC-12685 (1968).
9. T. F. Kassner, D. L. Smith, "Calculations on the Kinetics of Oxygen Solution in Tantalum and Niobium in a Liquid-Sodium Environment," ANL-7335 (September 1967). The uncertainty limits for the heat of solution (±0.3 kcal/mol) were not reported by Kassner and Smith; they were determined as part of the present study.
10. J. D. Noden, K. A. Bagley, UKAEA report TN-80 (1958).
11. In EBR-II, tin from the seal troughs was inadvertently introduced into the coolant circuit several years ago. Reduction of the tin level in the primary coolant to <5 ppm has not been possible by cold-trapping. However, no deleterious effects or serious operational problems have arisen as a direct consequence of its presence in the system.
12. C. Luner, H. M. Feder, F. A. Cafasso, in *Proceedings of the International Conference on Sodium Technology and Large Fast Reactor Design, Argonne, Nov. 7–9, 1968,* ANL-7520, Part I, p. 455 (1969).
13. C. C. Addison, B. M. Davies, *J. Chem. Soc.* (A), 1827 (1969).
14. E. Veleckis, G. Redding, "Solubility of Helium in Liquid Sodium," in ANL-7675, p. 64 (1969).
15. E. Veleckis, R. Blomquist, R. Yonco, M. Perin, "Solubility of Argon in Liquid Sodium," in ANL-7325. p. 128 (1967).
16. S. K. Dhar, "Solubility of Krypton in Liquid Sodium," in ANL-6900, p. 125 (1964).
17. W. R. Grimes, N. W. Smith, G. M. Watson, *J. Phys. Chem 62*, 862 (1958).
18. These limits can be interpreted as follows. If repeated determinations of x_{Xe} are made at the same value of P, the probability that the average value of x_{Xe} will fall between these limits is 0.95. See, e.g., N. R. Draper, H. Smith, *Applied Regression Analysis,* John Wiley & Sons, Inc. (1966), p. 23.
19. This correction, which involved rounding to the temperatures shown in Table II-1, was never greater than ±3°C.
20. J. P. Stone *et al.*, NRL-6241, Naval Research Laboratory (Sept. 24, 1965); G. H. Golden, J. V. Tokar, ANL-7323 (August 1967).
21. The heat of solution calculated from the slope of a plot of log λ vs. $1/T$ corresponds to $H_{Xe}(\text{soln},T,P) - H_{Xe}(\text{g},T,P^{\circ})$, where the standard state is defined to be that of 1 mol of ideal gas at temperature T in a volume equal to the molar volume of sodium, V_{Na}.
22. E. L. Reed, J. J. Droher, LMEC-69-36, Liquid Metal Engineering Center (January 1970).
23. C. Mitra, Eng. Sc. dissertation, Columbia University (1959).
24. *Proceedings of the 2nd Conference on Practical Aspects of Activation Analysis with Charged Particles*, Liege, Belgium (EUR-3896 d-f-e), H. G. Ebert, ed. (1968).
25. D. L. Smith, "Investigation of the Thermodynamics of V-O Solid Solutions by Distribution Coefficient Measurements in the V-O-Na System," *Met. Trans. 2*, 579 (1971).
26. R. M. Hudson, *Trans. Met. Soc. AIME 227*, 695 (1963).
27. K. Natesan, T. F. Kassner, "Calculations of the Thermodynamic Driving Force for Carbon Transport in Sodium-Steel Systems," ANL-7646 (December 1969).
28. The concentration of hydrogen in sodium is given by $S = KP^{1/2}$, where K = Sievert's constant and P = hydrogen pressure.
29. S. Dushman, J. M. Lafferty, *Scientific Foundations of Vacuum Technique,* John Wiley & Sons, Inc., New York, N. Y. (1962).
30. K. B. Das, Boeing Development Center, Seattle, Wash., personal communication, September 1970.
31. "Sodium Technology Quarterly Report, January,

February, March 1970," ANL/ST-2, Argonne National Laboratory (July 1970).
32. S. A. Meacham, E. F. Hill, A. A. Gordus, "Quarterly Technical Progress Report on AEC-Sponsored Activities," APDA-228 (1968).
33. Y. Ebisuzaki, W. J. Kass, M. O'Keeffe, *J. Chem. Phys. 46*, 1378 (1967).
34. J. Birault, A. Bracket, E. Cambillard, J. Coron, L. Lannou, C. Rault, "Detection of Small Leaks by Hydrogen Measurements in a Sodium-heated Steam Generator," *Proceedings of the International Conference on Sodium Technology and Large Fast Reactor Design, Argonne, Ill., Nov. 7–9, 1968*, ANL-7520, Part I, p. 345 (1969).
35. D. R. Vissers, J. T. Holmes, P. A. Nelson, *Trans. Amer. Nucl. Soc. 13*(1), 96 (1970).
36. R. R. Smith *et al.*, "Exposed-Fuel Calibration Study in EBR-II, Second Series," ANL-7558, p. 30 (January 1970).
37. R. R. Smith *et al.*, "Locating and Identifying the Source of the May 24, 1967 Fission Product Release in EBR-II," ANL-7543, p. 28 (April 1969).
38. "Sodium Technology Quarterly Report, January, February, March 1970," ANL/ST-2, pp. 3-4 to 3-7, Argonne National Laboratory (July 1970).
39. Calculated from data for the equilibrium activity of ^{131}I in the coolant, given by R. R. Smith *et al.*, in "Exposed-Fuel Calibration Study in EBR-II, Second Series," ANL-7558, p. 34 (January 1970).
40. "Sodium Technology Quarterly Report, January, February, March 1970," ANL/ST-2, p. 3-14 (July 1970).
41. "Sodium Technology Quarterly Report, January, February, March 1970," ANL/ST-2, pp. 3-15, 3-16 (July 1970).
42. "Sodium Technology Quarterly Report, July, August, September 1970," ANL/ST-4, pp. 36–39 (December 1970).

III. MATERIALS CHEMISTRY AND THERMODYNAMICS [1]

(A. D. Tevebaugh)

A. HIGH-TEMPERATURE THERMODYNAMIC STUDIES (P. E. Blackburn)

The objective of this program is to obtain phase-diagram, thermodynamic, and chemical data that can be used to interpret and evaluate performance of fast-breeder-reactor fuels. This information will aid in understanding and in selecting methods for control of sodium-fuel interactions, fission product distribution in the fuel, cladding attack by corrosive fission products, plutonium segregation, and fuel swelling. In addition, these data will help to identify phases formed in fuel under operating conditions and to choose additives for controlling the chemical potentials of fuel anions and those fission products which are deleterious to prolonged fuel-pin lifetimes.

The high-temperature investigations of U-Pu-O, U-Pu-O-Na, U-Pu-O-Cs, U-C, and U-C-O fuel-fission product-sodium systems include mass-spectrometric vapor pressure measurements, phase-diagram studies, and activity measurements by transpiration experiments.

One series of mass-spectrometric studies of U-Pu-O is complete and studies of U-Pu-O-Na have been initiated. Phase diagram studies of $(U,Pu)O_{2-x}$ and $(U,Pu)O_{2+x}$ are partially completed and phase and reaction studies for the sodium-fuel reaction are under way. Equipment was built and tested for the mass-spectrometric study of the chemistry of U-Pu-O fuel and fission product cesium, Activities of the elements in U-C and U-C-O were measured by a gas-equilibration and transpiration technique.

1. Volatilization Studies of Uranium-Plutonium Oxides by Mass Spectrometry (J. E. Battles, W. A. Shinn)

As part of a continuing investigation of the high-temperature thermodynamic properties of potential nuclear reactor fuel materials, a mass-spectrometric study of the volatilization behavior of the U-Pu-O system is being conducted to determine the parent vapor species in equilibrium with the condensed phase(s), partial pressures of the vapor species as a function of temperature, and thermodynamic properties. In particular, attention has been focused on the volatilization behavior of single-phase $(U_{0.8}Pu_{0.2})O_{2-x}$ material for oxygen-to-metal (O/M) ratios from 1.92 to 2.00. Preliminary results of this study were previously reported (ANL-7675, p. 75). The investigation of single-phase $(U_{0.8}Pu_{0.2})O_{2-x}$ material was completed, and a paper entitled "A Mass Spectrometric Investigation of the Volatilization Behavior of $(U_{0.8}Pu_{0.2})O_{2-x}$" [2] was published. A summary of this study follows.

a. Uranium-Plutonium-Oxygen System

Because uranium-plutonium oxide reacts with tungsten and rhenium (ANL-7675, pp. 75–77), this study was conducted using nonreactive iridium effusion cells. The variations of the ion intensities of UO^+, UO_2^+, UO_3^+, PuO^+, and PuO_2^+ (the only species detected) as functions of temperature were determined with an ionizing electron energy of 15 eV for UO_3^+ and PuO_2^+ and 11 eV for PuO^+, UO^+, UO_2^+. The experimental procedures and treatment of data were the same as employed in previous studies [3,4]. The partial enthalpies of sublimation for the vapor species were determined from the data by the second-law method. The partial enthalpies, obtained in the range $1.92 \leqslant O/M \leqslant 2.00$, were averaged to give partial enthalpies of sublimation: 123.43 ± 1.69, 139.41 ± 1.81, 146.25 ± 1.67, and 158.47 ± 1.98 kcal/mol for the vapor species PuO, PuO_2, UO_2, and UO_3, respectively. Since UO^+ appears to result primarily from fragmentation of other vapor species, data for it did not enter into these calculations.

From the rate of mass effusion determined at 2241°K and for $1.92 \leqslant O/M \leqslant 2.00$, partial vapor pressures can be calculated from the equation for molecular effusion

$$P_i(\text{atm}) = 2.256 \times 10^{-2} \frac{WF_i}{AtK} \left(\frac{T}{M_i}\right)^{1/2} \qquad (1)$$

where W/At is the rate of effusion [in g/(cm^2)(sec)], F_i is the weight fraction of total vapor, K is the Clausing correction factor for molecular flow through short channels, T is the absolute temperature, and M_i is the molecular weight of species i. The ion intensities of the vapor species were determined during the effusion measurements. These values, when reduced to a fraction-of-total basis, give the vapor-phase composition in mole fractions if the ionization cross sections and multiplier efficiencies are assumed equal [4]. For the partial pressure calculations, the ion intensities of each species were "smoothed" by drawing a curve through the data plotted as a function of the O/M ratio. From these curves, values for the mole fraction of each vapor species were obtained for O/M ratios 1.92, 1.93, ..., and 2.00. The mole fractions were then converted to weight fractions, and the partial pressures calculated. The partial pressures derived from the experimental data at 2241°K are shown in Fig. III-1 as a function of the O/M ratio for the solid phase. Equations for the partial pressures as a function of temperature at any given O/M ratio may be calculated from the partial enthalpies and partial pressures (Fig. III-1).

From the partial pressures shown in Fig. III-1, it is

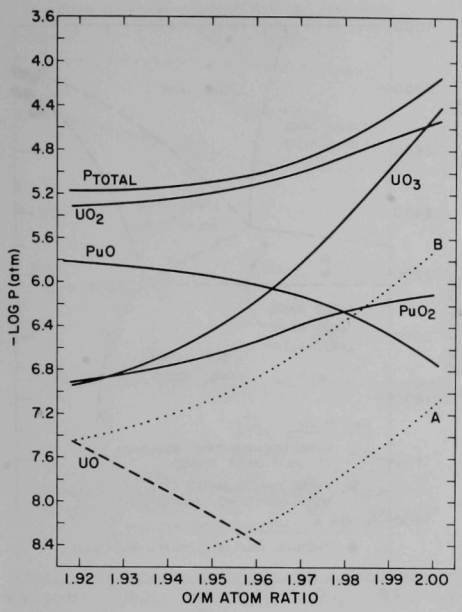

Fig. III-1. Partial Pressures of the Vapor Species over $(U_{0.8}Pu_{0.2})O_{2-x}$ at 2241°K. ANL Neg. No. 308-2240.

apparent that the vapor phase is predominantly U-bearing at the higher O/M ratios, whereas, at the lower O/M ratios, the vapor-phase composition more nearly approximates that of the solid phase. The ratio of Pu/(U + Pu) in the solid phase was 0.20 in the starting materials and 0.22 at the conclusion of the two series of experiments, which confirms that the vapor phase was generally richer in U than was the solid phase. Also, Fig. III-1 shows that the total vapor pressure decreased by approximately a factor of 10 as the O/M ratio decreased from 2.00 to 1.92. The data indicate that a broad minimum in the total vapor pressure is approached at an O/M ratio of about 1.92 or 1.93.

The oxygen partial pressures, $P(O)$, over the mixed oxide at 2241°K have been calculated from the free energies of formation for $UO_2(g)$ and $UO_3(g)$, given by Rand and Markin [5] via the reaction

$$UO_2(g) + O(g) \rightleftharpoons UO_3(g) \qquad (2)$$

along with the partial pressures of $UO_2(g)$ and $UO_3(g)$ determined in this study. The partial pressures of oxygen as a function of the O/M ratio are shown in Fig. III-1 and designated Curve A. Similarly, $P(O)$ have been calculated via the reaction

$$PuO(g) + O(g) \rightleftharpoons PuO_2(g) \qquad (3)$$

and the free energies of formation for $PuO(g)$ and $PuO_2(g)$ (Curve B). The large difference between Curves A and B results in part from uncertainties in relative ion cross sections and fragmentation of molecules such as UO_3 (ANL-7375, p. 101).

Further vaporization studies of the uranium-plutonium-oxygen system have been temporarily discontinued.

b. U-O-Na and U-Pu-O-Na Systems

Current efforts in the volatilization studies are being directed toward the sodium-fuel reaction. In particular, the studies are concerned with determination of the oxygen and sodium partial pressures (activities) in equilibrium with products of reaction between liquid sodium and $(U,Pu)O_2$ [e.g., Na_3UO_4, Na_3PuO_4, or $Na_3(U,Pu)O_4$]. Knowledge of the sodium and oxygen partial pressures will permit us to calculate the free energy of formation of these compounds. With these data and the oxygen partial pressures of the uranium-plutonium oxides, the O/M ratio for nonreactivity (or degree of reaction) of liquid sodium with the oxide fuel can be reliably predicted.

Survey experiments have been conducted on the vaporization of Na_3UO_4 (initially ~90% Na_3UO_4, 10% UO_2) using iridium effusion cells which are contained in a tungsten cell. These experiments, which covered the temperature range of 200–1350°C and required several days to complete, revealed that Na(g) was the predominant vapor species at all temperatures at which vapor species were detected. Sodium vapor was first detected at about 750°C and increased with temperature, but decreased with time at constant temperature. The vaporization of oxygen (O_2) became significant after an appreciable quantity of sodium had been lost at temperatures greater than 1000°C. At the higher temperatures, the oxygen partial pressure approaches that of Na(g). Other vapor species detected were $Na_2O(g)$ (very low at $T > 1075°C$) and UO_3 (low at $T > 1200°C$). Vapor species of the type Na_xUO_y were not detected. X-ray diffraction analysis of the sample material after heating to ~1350°C showed the presence of three solid phases: (1) a face-centered cubic phase with lattice parameter $a = 5.401$Å, (2) $NaUO_3$, and (3) $Na_2U_2O_7$. The fcc phase has not been identified. After additional heating, UO_{2+x} was the only phase detected.

In a series of experiments being conducted currently, the vapor pressures of sodium over material initially Na_3UO_4-10% UO_2 were determined at 903 and 927°C. In the first measurement at 903°C, the vapor pressure decreased by a factor of 15 as the Na_3UO_4 dissociated, i.e., $P(Na) = 2 \times 10^{-4}$ atm at the start and 1.3×10^{-5} atm at the conclusion. At 927°C, the vapor pressure was 1.9×10^{-5} atm, which agrees well with 1.3×10^{-5} atm

when the temperature difference is considered. The condensed phases present after the second measurement were $NaUO_3$, Na_4UO_5, and Na_3UO_4. Temperature-dependency measurements were not entirely satisfactory because of a 50 to 75% decrease in the Na^+ intensity with time. The solid phases present at the end of this run were $NaUO_3$ and Na_4UO_5.

As shown in the previous series of experiments, the dissociation of Na_3UO_4 eventually yields UO_{2+x} as the only solid phase. Between the initial and final components are three phase regions which are favorable for measuring the Na and O_2 partial pressures. The current experimental series (partial results presented above) should locate a suitable three-phase region for these measurements and also yield some information on the Na-U-O phase diagram. The sodium and oxygen partial pressures obtained in this three-phase region, together with sodium pressures in other regions, can then be used, through the appropriate thermodynamic cycle, to obtain oxygen partial pressures within the three-phase region Na_3UO_4-Na-$UO_{2\pm x}$. This oxygen pressure can be used to calculate the oxygen concentration in $UO_{2\pm x}$. A similar procedure will be followed with Na and $(U,Pu)O_2$ to establish the O/M ratio below which sodium-fuel interactions will not occur.

2. *U-Pu-O and Na-U-Pu-O Phase Studies* (A. E. Martin, F. C. Mrazek)

a. U-Pu-O Phase Diagram

The investigation of the hypostoichiometric region of the uranium-plutonium-oxygen phase diagram at elevated temperatures has continued. Data were obtained at Pu/(U + Pu) compositions of 0.198 and 0.441 by the equilibration of uranium-plutonium alloys with sintered crucibles made from coprecipitated mixed-oxide powders. The need for two stages in these equilibration experiments was previously discussed in ANL-7675, p. 78. The product crucibles from the equilibrations were analyzed for oxygen. The data thus obtained represent compositions on the hypostoichiometric boundary of the fluorite, mixed-oxide phase. Data for the Pu/(U + Pu) section of 0.198 are given in Fig. III-2. When attempts were made to measure the phase boundary of this section at 2247 and 2207°C, a third phase, a liquid oxide, apparently formed in addition to the solid oxide and liquid alloy. This conclusion was based on metallographic examination of the products at room temperature. Consequently, in this figure, data points representing the overall charge compositions of these experiments are located in the three-phase region consisting of liquid oxide, liquid alloy, and solid oxide.

Included in the figure are thermal analysis data by Aitken and Evans [6] for the O/M composition region from 1.92 to 2.00. The dashed lines in the figure are estimates. For example, the point O/M = 1.25 at 2350°C, where four

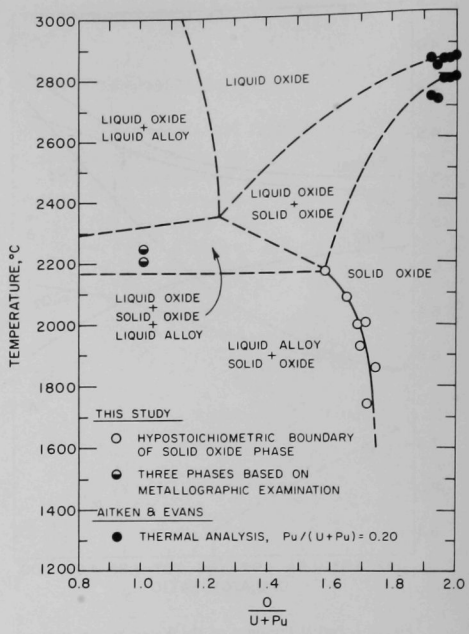

Fig. III-2. The Uranium-Plutonium-Oxygen Phase Diagram for the Section at Pu/(U + Pu) = 0.198. ANL Neg. No. 308-2528A.

lines converge, is an average of the monotectic compositions and temperatures from the U-UO_2 [7] and Pu-Pu_2O_3 [8] phase diagrams.

Two points on the hypostoichiometric boundary of the fluorite phase were obtained at the Pu/(U + Pu) section of 0.441. The oxygen-metal ratios are 1.60 and 1.51 at 1740 and 1920°C, respectively. These values are appreciably more hypostoichiometric than the phase-boundary line shown in Fig. III-2.

It was previously reported in ANL-7675, pp. 77–79, that the tie lines in the two-phase field, solid oxide plus liquid alloy, were tilted. Furthermore, the angle of tilt for an oxide with a Pu/(U + Pu) composition of about 0.2 was found to be essentially independent of temperature in the range from 1800 to 2200°C. The effect of composition on the tie-line directions has since been established at a temperature of about 1900°C. These tie-line data are given in Fig. III-3 in the form of an isothermal section through a portion of the uranium-plutonium-oxygen phase diagram at 1900°C.

A few experiments were conducted in the hyperstoichiometric region of the phase diagram. Sintered pellets of four Pu/(U + Pu) compositions, namely, 0.198, 0.441, 0.643,

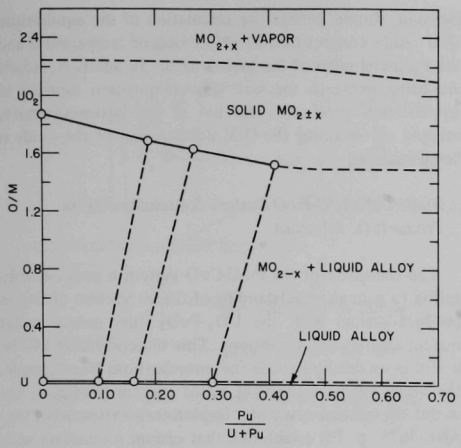

Fig. III-3. Uranium-Plutonium-Oxygen Phase Diagram; Isothermal Section at 1900°C Showing Tie Lines Established in the Two-Phase Field: Solid MO_{2-x} Plus Liquid Alloy. ANL Neg. No. 308-2549.

and 0.804, were oxidized at temperatures of 200, 300, 400, 600, 800, 1000, and 1200°C in air flowing at 20 cm^3/min. The O/M compositions of the products, calculated from the weight increases of the pellets, are plotted in Fig. III-4 as a function of the temperature of the oxidation. At 800°C and above, the data probably represent the compositions of the oxide phase(s) in equilibrium with oxygen at 0.21 atmosphere partial pressure of the air. Literature data [9] indicate that, for the pellets of Pu/(U + Pu) compositions

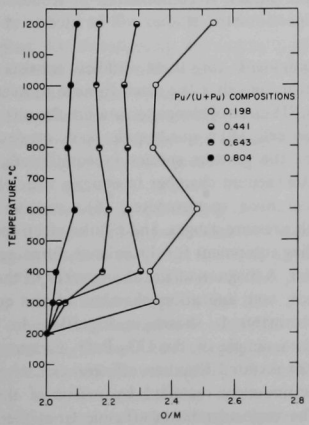

Fig. III-4. O/M Compositions of Products of Oxidation of Sintered Mixed-Oxide Pellets Based on Weight Increases. ANL Neg. No. 308-2550.

0.441, 0.643, and 0.804, the equilibrium oxide is the MO_{2+x} fluorite phase. On the other hand, for the Pu/(U + Pu) composition of 0.198, two oxide phases, M_3O_8 and MO_{2+x}, are in equilibrium with the air. The latter oxides form by disproportionation. The Pu/(U + Pu) composition of the M_3O_8 phase is less than, whereas that of the MO_{2+x} phase is greater than, that of the original MO_2 phase.

The oxidation below 800°C is mainly of interest from a reaction rate point of view. For example, it was surprising that at 200°C there was essentially no weight increase of any of the pellets after six days of oxidation in flowing air.

Of the 28 pellets oxidized in these tests, only two disintegrated during the oxidations. These were the pellets of Pu/(U + Pu) composition 0.198 that had been oxidized at 400 and 600°C.

Further work on both the hypostoichiometric and hyperstoichiometric regions of the phase diagram has been suspended temporarily to devote a greater effort to the study of the reaction of sodium with oxides. When the work is resumed, studies will include work on oxides with Pu/(U + Pu) compositions of 0.10 and 0.30, which are now available.

b. The Reaction of Liquid Sodium with Uranium-Plutonium Mixed Oxides

This problem is of great importance because of the possible interaction of sodium coolant with reactor fuel. Such a reaction could cause fuel swelling and cladding rupture in the event of a breach in the cladding. The severity of the problem may determine how long failed fuel elements can be left in the reactor core and also whether or not failed fuel elements can be stored in the reactor sodium coolant.

The study of this reaction in the Chemical Engineering Division, which is part of a coordinated program between the Chemical Engineering and Materials Science Divisions and the EBR-II project, can be thought of as a study of certain portions of the Na-U-Pu-O phase diagram at temperatures below 1000°C. The initial four objectives of the study and the progress which has been achieved thus far in meeting them are as follows.

(1) The Establishment of the Identity of the Na-O-M Phase Which Can Exist in Equilibrium with Sodium and the Mixed-Oxide Phase as a Function of the O/M Composition of the Mixed Oxide and Temperature. Before working with mixed oxides, confirmation was sought of the literature [10] evidence that Na_3UO_4 [X-ray data: face-centered cubic (fcc) structure, a_0 = 4.79–4.80Å] is the Na-U-O phase that can exist in equilibrium with sodium and UO_2 in the temperature range 600 to 1000°C. This confirmation was obtained when a fcc phase, a_0 = 4.78–4.79Å, was detected with sodium and UO_2 in products of reactions at 750 and 800°C.

Experiments were then conducted with mixed oxides with a Pu/(U + Pu) composition of 0.198. A fcc phase, a_0 = 4.78Å, was found to have formed in the presence of sodium and the MO_{2-x} phase in reactions at 800, 905, and 950°C. The similarity of these X-ray data to those for Na_3UO_4 indicates that the phase is Na_3MO_4, where M stands for uranium and plutonium. The Pu/(U + Pu) ratio of the Na_3MO_4 phase has not yet been established.

(2) The Preparation of Na_3UO_4 and Na_3MO_4 for Miscellaneous Purposes. Preparations of Na_3UO_4 are needed in quantities sufficient to establish their thermodynamic properties by calorimetry and mass spectrometry and for other purposes. Single-phase preparations of Na_3UO_4 have been made on a two-gram scale by reacting Na_2O and $UO_{2.14}$ (sometimes with excess sodium) at 800°C in nickel capsules that are welded shut. Attempts are currently being made to duplicate the process on a 70-g scale. When successful, attempts will be made to produce Na_3MO_4 on a similar scale.

In an attempt to establish the melting point of Na_3UO_4, a sample of single-phase Na_3UO_4 was heated for 10 min at 1425°C in a nickel capsule. Metallographic examination of the product showed that the Na_3UO_4 had merely sintered; it had not melted.

(3) The Establishment of the Mechanism of the Reaction of Liquid Sodium with Sintered Mixed Oxides. Synthetic mixtures of sintered Na_3UO_4 and UO_2 were prepared and examined metallographically after polishing. It was found that the two phases could be readily distinguished from each other visually. The same situation would probably hold for the Na_3MO_4 phase and the mixed-oxide phase, MO_2.

Thus, if experimental conditions are found for the reaction of liquid sodium with sintered mixed-oxide pellets such that Na_3MO_4 forms as a separate phase, it may be possible to detect the presence and location of this phase in the product pellet. Then, it should be possible to modify the experimental conditions in order to explore and perhaps establish the mechanism of the reaction. This is the initial approach being used on this problem. Thus far, the desired experimental conditions have not been established.

(4) The Establishment of the O/M Composition of the Mixed-Oxide Phase Which Can Exist in Equilibrium with Liquid Sodium and Na_3MO_4 as a Function of Temperature and the Pu/M Composition of the Mixed Oxide. This is a most important objective. Oxide of this composition could not react with sodium that contains less than the equilibrium concentration of oxygen required for the reaction

$$MO_2 + 3Na(\ell) + O_2 = Na_3MO_4$$

Thermodynamic data on the Na_3MO_4 phase, which are being sought by calorimetric and mass spectrometric studies in the Chemical Engineering Division and which may be obtained by proposed cell studies in the Materials Science Division, should permit the calculation of the equilibrium O/M oxide composition as a function of temperature and the Pu/metal ratio of the mixed oxide. In addition, efforts are being made to measure this composition directly in equilibration products. The use of the lattice-parameter method of obtaining the O/M composition of the oxide is being explored.

3. Studies of the U-Pu-O System Containing Fission Products (I. Johnson)

The chemistry of the Pu-U-Cs-O system is under investigation to gain an understanding of the interaction of fission product cesium with the UO_2-PuO_2 fuel matrix under reactor operational conditions. This understanding will be useful in establishing oxide-fuel specifications (for example, the initial value of the O/M ratio) and for predicting the useful life of fuel elements. Exploratory experiments (see ANL-7675, p. 79) established that cesium interaction with the fuel matrix will be important in the control of cladding attack. Theoretical calculations of solid-fuel swelling indicate that the extent that cesium interacts with the fuel matrix will have a significant effect on the magnitude of the solid swelling.

In the present investigation, the activity of cesium in a mixed UO_2-PuO_2 matrix will be determined as a function of the composition and the temperature. The cesium activity is expected to be significantly dependent on the oxygen potential of the system (O/M ratio), the cesium content of the solid phase, the nature (structure) of the solid phases, and the temperature. The cesium activity will be determined by the measurement of the partial pressure of cesium species in the vapor phase in equilibrium with known solid phases. A combination of Knudsen effusion and mass spectrometric studies will be used to obtain these data.

The equipment for these studies consists of (1) a Knudsen effusion cell, (2) a small furnace to heat the cell, (3) a Cahn RH electrobalance to measure the rate of weight loss of the cell, (4) a quadrupole mass spectrometer to characterize the gaseous species in equilibrium with the system, (5) a vacuum chamber to contain the cell, furnace, balance, and mass spectrometer, (6) a vacuum pumping system with pressure gauges, and (7) the electronic control and recording equipment for the balance, furnace, and mass spectrometer. A diagram of the arrangement of the effusion cell, furnace, and ionization chamber of the quadrupole mass spectrometer is shown in Fig. III-5. In a typical experiment, a sample of the UO_2-PuO_2-Cs system will be placed in the inverted Knudsen effusion cell, whose weight will be continuously recorded by means of the electrobalance. The molecular beam effusing from the orifice of the Knudsen cell will be collimated by an orifice plate and shutter placed just above the ionization chamber of the mass spectrometer. A fraction of the molecular beam that

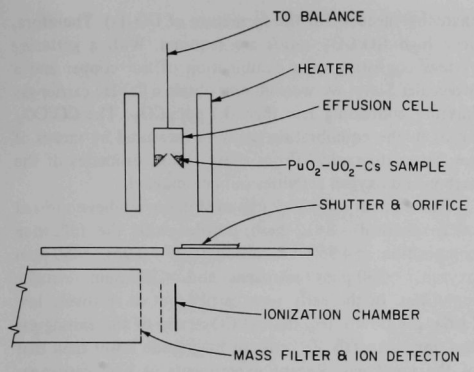

Fig. III-5. Diagram of Experimental Apparatus for Studies of Pu-U-Cs-O System. ANL Neg. No. 308-2551.

enters the ionization chamber will be ionized by electron impact. The positive ions so produced will be drawn into the quadrupole mass filter. Ions of a given mass-to-charge ratio will traverse the mass filter and be converted to an electron current using an electron multiplier.

The apparatus for this study has been constructed, and testing is now under way. It is anticipated that the complete experimental setup will be tested and the scope of the problem established using the UO_2-Cs system to avoid contamination of the apparatus with plutonium so that necessary modifications can be made more easily.

4. *Thermodynamics of Carbide Fuels: Transpiration Studies of U-Pu-C System* (M. Tetenbaum, P. D. Hunt)

A program for investigating the carbon potentials and total pressures of the U-Pu-C system is in progress. Total pressure of actinide metal species as well as carbon activity are being measured by a transpiration technique. Activity measurements over a wide range of temperature and with well-defined composition are needed to establish reliable thermodynamic quantities as well as to define phase-boundary composition. In particular, carbon-activity data are important in predicting possible carbon embrittlement of cladding by carbide fuel, the chemical state of fission products, and effects of additives on the properties of fast-reactor fuels. Current emphasis has been placed on the effects of oxygen contamination in uranium carbide on the system's uranium, carbon, and oxygen potentials. These studies are important in establishing allowable levels of impurity in carbide fuels. Little is known about the stability of the uranium-carbon-oxygen system [11–14]. The oxycarbide phase has mostly been investigated in the presence of other phases such as U, UO_2, U_2C_3, and UC_2.

a. Thermodynamic Consequences of Carbon-Acrivity Measurements Over UC_x

Estimates of the activity of uranium at various UC_x compositions can be made from free energy ($\Delta\bar{G}_U$) values derived from our carbon activity measurements (see Annual Report for 1969, ANL-7675, pp. 84–86) and the application of the Gibbs-Duhem equation in the form

$$\Delta\bar{G}_U(UC_x) - \Delta\bar{G}_U(UC_{1.00}) = -\int_{\Delta\bar{G}_C(UC_{1.00})}^{\Delta\bar{G}_C(UC_x)} \frac{N_C}{N_U} d\Delta\bar{G}_C$$

The standard free energy of formation of $UC_{1.00}$ was estimated from the heat of formation of $UC_{1.00}$ and the appropriate free energy functions. For $\Delta H^\circ_{298}(UC_{1.00})$, we used the value of -23.2 ± 1 kcal/mol obtained by Storms and Huber [15] by means of combustion calorimetry. The results are summarized in Fig. III-6. In general, the calculated uranium activity values are in good agreement with values based on Storms [16] adjusted vapor pressure values for UC_x and 126.3 kcal/mol as the heat of vaporization of uranium [17].

It should be noted that the shape of the calculated curves shown in Fig. III-6 are consistent with expectations, namely, a sharp increase in uranium activity near the stoichiometric composition as the composition of the condensed phase is reduced toward the lower phase boundary, U(ℓ) + UC(s), in the hypostoichiometric region.

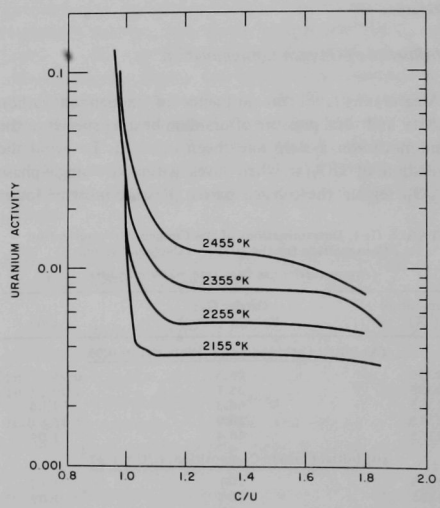

Fig. III-6. Uranium Activities Derived from Gibbs-Duhem Integration of Carbon Activity. ANL Neg. No. 121-6463.

b. Congruent Vaporizing Composition of Uranium Carbide

Attempts were made to establish the congruent vaporizing composition of uranium carbide by flowing an inert gas over uranium carbide at high temperature using the transpiration technique. These data provide a method for corroborating the carbon and uranium activities measured in the U-C system at the congruent vaporizing composition. The argon carrier-gas flow rate was approximately 200 ml/min. At various intervals (after cooling to room temperature), small portions of the uranium carbide residue were removed from the transpiration apparatus for analysis.

The results are summarized in Table III-1. It should be noted that the congruent composition was approached from both hypostoichiometric and hyperstoichiometric compositions relative to carbon. From the results, one can conclude that the congruent composition lies near C/U = 1.05 ± 0.01. In the temperature range 2255–2455°K, the congruent composition appears to be insensitive to temperature. For comparison, between 2200 and 2500°K, a congruently vaporizing composition of C/U = 1.07 ± 0.05 was obtained by Leitnaker and Witteman [18] from Langmuir vaporization experiments; Vozzella *et al.* [19] obtained C/U = 1.09 ± 0.003, and Bowman and Krupka [20] obtained C/U = 1.065 by the same technique. It is apparent that the congruent composition derived from our studies is in reasonable agreement with those obtained by means of Langmuir vaporization. The calculations also agree with those calculated from our uranium and carbon activities and literature data for uranium and carbon pressures.

c. Influence of Oxygen Contamination

Measurements of the influence of oxygen on carbon activity and total pressure of uranium-bearing species in the uranium-carbon system have been initiated. To avoid the formation of $UO_2(s)$ when investigating the single-phase UC_xO_y region, the oxygen partial pressure must be lower than that needed for the formation of $UO_2(s)$. Therefore, very high CO/CO_2 ratios are required. With a gettering system consisting of a combination of hot copper and a Molecular Sieve, we were able to obtain a CO-He carrier-gas mixture containing less than 0.1 ppm CO_2. The CO/CO_2 ratios in the equilibrating gas were measured by means of gas chromatography. From these ratios, estimates of the carbon and oxygen activities can be obtained.

TABLE III-1. Determinations of the Congruent Vaporization Composition for the Uranium Carbide System

(Argon carrier-gas flow rate ~200 ml/min)

Temperature (°K)	Carrier Gas Volume (liters)	C/U
(A) Initial Carbide Composition, C/U = 0.95		
2355	26.3	0.95 ± 0.02
2355	35.1	1.00 ± 0.01
2355	66.3	1.04
2355	28.0	1.05 ± 0.01
2355	40.4	1.05
(B) Initial Carbide Composition, C/U = 1.37		
2255	104	1.15
2255	104	1.09
2255	134	1.06
2255	91	1.04
2355	72	1.05
2455	67	1.06

The uranium carbide charge used in our studies consisted of a spherical −8+12 mesh powder with the following composition: ~4.55 wt % carbon (C/U = 0.96), ~150 ppm oxygen, ~350 ppm nitrogen, and <200 ppm metallic impurities. In the early runs carried out at relatively low carrier-gas flow rates, the CO/CO_2 ratio of the exiting gas was approximately an order of magnitude lower than that of the input gas. Recent experiments at high carrier-gas flow rates have minimized the discrepancy between input and output CO/CO_2 ratios. The results are summarized in Table III-2. It should be noted that metallographic examination of the residues did not show the presence of $UO_2(s)$ in the matrix or on the surface of the particles in any of the experiments.

From these data, we calculate carbon activities to be approximately 1.5×10^{-3} at 2355°K. For comparison, the carbon-activity values based on our measurements with the H_2-CH_4 mixtures over "oxygen-free" UC_x compositions ranging from C/U = 0.99 to C/U = 1.00 yielded $a_C \simeq 0.15$ at 2355°K. The effect of a small addition of oxygen, e.g., 1.5–2.0 at. %, results in a significant reduction in the activity of carbon. This can have important implications in the potential transfer of carbon from fuel to cladding materials.

The total pressure of uranium-bearing species at 2020, 2155, 2255, and 2355°K is shown in Fig. III-7. The total pressure of uranium-bearing species over uranium oxycarbide composition is considerably higher than those obtained with ' 'oxygen-free" material. These higher pressures may reflect in part the enhancement in uranium activity as a consequence of the significant reduction of carbon activity in the oxycarbide, as well as the vaporization of an oxygen-containing uranium species from the oxycarbide composition.

The free energy of formation of the oxycarbide compositions given in Table III-2 was roughly estimated from oxygen and carbon activity values derived from our measurements. In the absence of species information, the uranium activity was roughly estimated based on the total pressure of uranium-bearing species, the assumption that the vapor is uranium gas, and the sublimation pressure of pure uranium. From the expression $\Delta G_f^\circ = R'T \log N_i \Sigma a_i$, a tentative value of $\Delta G_f^\circ \simeq -40$ kcal/mol was obtained at 2355°K. The free energy of formation of "oxygen-free" $UC_{1.00}$ calculated from our carbon-activity measurements and Storms' adjusted vapor pressure measurements was $\Delta G_f^\circ \simeq -24.8$ kcal/mol at 2355°K.

TABLE III-2. Tentative Values of Carbon Activity and Oxygen Partial Pressure for U-C-O System

	Run 100-1	Run 101-1	Run 101-2
Temperature, °K	2355	2355	2355
Time of run, hr	5.5	2.9	6.7
Carrier gas	CO-He	CO-He	CO-He
Flow rate, ml/min	1100	1100	1100
Partial pressure CO in carrier gas, Torr	~10	~4	~4
CO/CO_2, input gas	3.2×10^4	5.4×10^4	5.7×10^4
CO/CO_2, output gas	2.2×10^4	4.6×10^4	4.7×10^4
$-\log p(O_2)$ (based on input)	12.52	12.98	12.94
$-\log p(O_2)$ (based on output)	12.20	12.72	12.78
Carbon activity (based on input)	2.0×10^{-3}	1.3×10^{-3}	1.4×10^{-3}
Carbon activity (based on output)	1.4×10^{-3}	1.0×10^{-3}	1.1×10^{-3}
Composition	$UC_{1.00}O_{0.04}$	$UC_{1.00}O_{0.02}$	$UC_{1.00}O_{0.02}$
Nitrogen content, ppm	710	-	-
Metallographic examination	UO_2 not detected	UO_2 not detected	UO_2 not detected

d. Relative Effects of Nitrogen and Oxygen Contamination on the Vaporization Behavior of Uranium Carbide

The vaporization behavior of uranium carbide containing oxygen and nitrogen as contaminants was also investigated. Oxygen and nitrogen contamination usually occur during preparation and fabrication procedures involving carbide fuels. The total pressure of uranium-bearing species was measured by means of the transpiration technique at 2255°K with helium as the carrier gas. At a number of intervals after starting transpiration, the condenser tube was cooled to room temperature and removed from the transpiration apparatus. The uranium-bearing sublimate inside the condenser tube was dissolved by repeated washing with hot concentrated nitric acid, and the washings were assayed for uranium. The results are summarized in Table III-3.

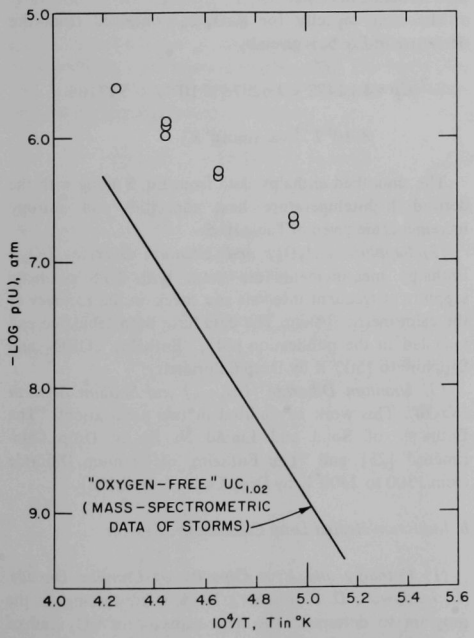

Fig. III-7. Preliminary Values for Total Pressure of Uranium-bearing Species over Uranium Oxycarbides Containing 1.5–2.0 at. % Oxygen. ANL Neg. No. 308-2552.

It is apparent from Table III-3 that, as transpiration proceeds through the various intervals, the total pressure of uranium-bearing species decreases with decrease in oxygen content in uranium carbide. For comparison, from Storms' measurements, the total pressure of uranium-bearing species (essentially uranium vapor) over "oxygen-free" $UC_{0.98}$ was found to be $\log p(U) = -6.64$. The total pressure of uranium-bearing species derived from our measurements over oxygen-depleted uranium carbide, but containing approximately 2000 ppm N (1.8 at. %), was found to be $\log p(U) = -6.56$ atm. We may conclude, therefore, that nitrogen contamination on the order of 2000 ppm does not significantly affect the activity of uranium over uranium carbides.

B. REACTOR SAFETY AND PHYSICAL PROPERTY STUDIES (M. G. Chasanov)

The primary objective of these studies is to provide physical property data for use in evaluating the safety of various fast-breeder reactor materials. The property data obtained experimentally at temperatures above normal operating conditions of LMFBRs will also be extrapolated to the much higher temperatures involved in accident situations. In addition, reactor material-fuel phase studies at high temperatures are under way to provide chemical information needed on fission-product distribution between molten fuel and other reactor materials for use in post-accident heat-removal calculations.

TABLE III-3. Total Pressure of Uranium-Bearing Species Over Uranium Carbides Contaminated With Oxygen and Nitrogen (transpiration technique at 2255°K, He carrier gas)

Run	Carrier Gas Flow Rate (ml/min)	Carrier Gas Volume (liters)	-log p(U) (atm)
Initial Composition: $UC_{1.00}O_{0.021}N_{0.024}$			
97-1	180	68	5.54
97-2	370	50	5.72
97-3	180	30	6.80
97-4	180	61	6.90
97-5	180	56	6.56
Final Composition: $UC_{0.98}O_{0.006}N_{0.036}$			

1. *Enthalpies and Heat Capacities by Drop Calorimetry*

Three complementary calorimetric systems for the measurement of high-temperature enthalpy increments are available for our use. Depending on the material to be studied and the temperature range to be covered, one may choose (1) the resistance-heated drop calorimetric system [21] (600–1600°K), (2) the electron-beam-heated drop calorimetric system [22] (1300–2500°K) or (3) the induction-heated drop calorimetric system [23] (2500–3600°K). During this period, systems (1) and (3) have been used for making measurements.

a. Resistance-heated Drop Calorimetric System
(D. R. Fredrickson)

(1) Ruthenium Dioxide ($RuO_{1.98}$). Thermodynamic data are needed on fission-product oxides for help in evaluation of the oxidizing potentials in reactor fuel pins. With this in mind, a survey of the literature was conducted on 22 fission-product elements that form various oxides. No high-temperature enthalpy data were found for RuO_2; high-temperature enthalpy measurements have since been completed by us on this compound. Other fission-product oxides will be studied later.

Ruthenium dioxide (obtained from Alfa Inorganics, Beverly, Massachusetts) was submitted for X-ray diffraction and spectrochemical analysis. These analyses showed no significant impurities present. A ruthenium analysis was performed by reducing the RuO_2 in a stream of hydrogen gas. The residue was assumed to be pure ruthenium metal since the spectrographic analysis did not indicate any appreciable metallic impurity except 0.05% platinum. The average percentage of ruthenium found was 76.16% (theoretical 75.95%); based on this analysis, the O/Ru molar ratio is 1.98 ($RuO_{1.98}$).

For the work reported below, the $RuO_{1.98}$ samples were sealed under vacuum in cylindrical platinum capsules with a 10-mil wall thickness, 1/2-in. diameter, internal volume of 5 cm^3, and a length of 2 in. These capsules had a filling tube, which was also used for evacuation, with dimensions 0.180-in. OD, 0.005-in. wall thickness, and 1.25-in. length.

The experimental enthalpy data (relative to 298.15°K) obtained for $RuO_{1.98}$, summarized in Table III-4, yield the equation

$$(H_T^\circ - H_{298.15}^\circ) = 18.2472T + 1.31489 \times 10^{-3} T^2 + 5.77166 \times 10^5 T^{-1} - 7493.1 \text{ cal/mol}$$

The standard deviation for Eq. 5 is 34 cal/mol or 0.27%. The constraint that $(H_T - H_{298}) = 0$ at 298.15°K has been used in fitting the data.

The heat capacity for $RuO_{1.98}$ obtained from the derivative of Eq. 5, is given by

$$C_P^\circ = 18.2472 + 2.62978 \times 10^{-3} T - 5.77166 \times 10^5 T^{-2} \text{ cal/(mol)(°K)}$$

The smoothed enthalpy data from Eq. 5 along with the derived high-temperature heat capacities and entropy increments are given in Table III-5.

(2) Sapphire (Al_3O_3) and Uranium Dioxide (UO_2). Enthalpy measurements are made with NBS synthetic sapphire at frequent intervals as a check on the accuracy of the calorimetric system. The data have been tabulated and included in the publication [24], "Enthalpy of UO_2 and Sapphire to 1500°K by Drop Calorimetry."

(3) Uranium Diboride ($UB_{1.98}$) and Sodium Bismuth (Na_3Bi). This work is reported in two publications, "The Enthalpy of Solid and Liquid Na_3Bi by Drop Calorimetry" [25] and "The Enthalpy of Uranium Diboride from 1300 to 2300°K by Drop Calorimetry" [26].

b. Induction-Heated Drop Calorimetric System

(1) Enthalpy and Heat Capacity of Uranium Dioxide (L. Leibowitz, D. F. Fischer). Work is continuing on the program to determine the heat capacity of UO_2 and of $(U,Pu)O_2$ to high temperatures. Accurate values for heat capacity and heat of fusion will facilitate estimation of the total energy released and the temperatures attained in a

TABLE III-4. Enthalpy of Ruthenium Dioxide ($RuO_{1.98}$)

Temperature (°K)	$(H_T - H_{298})$ Observed (cal/sample)[a]	$(H_T - H_{298})$ Observed (cal/mol)	$(H_T - H_{298})$ Calc. Eq. 5 (cal/mol)[b]	% Dev. (Obs. – Eq. 5)
619.4	470.18	5242.92	5245.48	-0.05
699.6	604.32	6738.70	6741.17	-0.04
704.7	611.63	6820.21	6837.68	-0.26
777.7	738.55	8235.48	8235.14	+0.01
778.0	738.60	8236.04	8240.94	-0.06
803.3	783.50	8736.72	8731.83	+0.06
803.6	781.82	8717.98	8737.67	-0.23
871.8	907.15	10115.52	10076.18	+0.39
872.0	906.25	10105.49	10080.14	+0.25
872.0	893.32[c]	10104.85	10080.44	+0.25
1074.0	1172.84[d]	14125.16	14158.45	-0.24
1074.1	1170.43[d]	14096.13	14160.41	-0.46
1174.6	1352.98[d]	16294.68	16245.53	+0.30

[a]0.089679 moles $RuO_{1.98}$ in a platinum capsule except as noted.
[b]$(H^\circ_T - H^\circ_{298.15}) = 18.2472T + 1.31489 \times 10^{-3} T^2 + 5.77166 \times 10^5 T^{-1} - 7493.11$ cal/mol.
[c]0.088405 moles $RuO_{1.98}$ in a platinum capsule.
[d]0.083032 moles $RuO_{1.98}$ in a platinum capsule.

reactor core during hypothetical destructive nuclear excursions. Induction heating is being used in conjunction with normal drop calorimetry procedures. The experimental procedure has been described previously [27].

We have now completed work on UO_2. The enthalpy increments measured for liquid UO_2 (relative to room temperature) are given in Table III-6. The temperatures reported are based on IPTS-48. In Fig. III-8 these data are given along with a few of our previous solid points and the liquid UO_2 data of Hein and Flagella [28]. The liquid UO_2 data can be represented by the following equation, obtained by the method of least squares

$$H^\circ_T - H^\circ_{298} = 32.457T - 11153.4 \qquad (7)$$

The enthalpy is given in calories per mole and T is in °K (see Table III-6). The estimate of the standard error for Eq. 7 is 544 cal/mol. Moderate extrapolations using this linear relation should be satisfactory.

TABLE III-5. Thermodynamic Functions of $RuO_{1.98}$

Temperature (°K)	$(H^\circ_T - H^\circ_{298})$ (cal/mol)	C°_p [cal/(mol)(°K)]	$S^\circ_T - S^\circ_{298}$ [cal/(mol)(°K)]
298.15	0	12.54	0
300.00	23.27	12.62	0.08
350.0	703.53	14.46	2.17
400.0	1459.06	15.69	4.19
450.0	2266.98	16.58	6.09
500.0	3113.54	17.25	7.87
550.0	3989.99	17.79	9.54
600.0	4890.50	18.22	11.11
650.0	5811.05	18.59	12.58
700.0	6748.74	18.91	13.97
750.0	7701.46	19.19	15.29
800.0	8667.62	19.45	16.54
850.0	9646.02	19.68	17.72
900.0	10635.71	19.90	18.85
950.0	11635.94	20.11	19.93
1000.0	12646.12	20.30	20.97
1050.0	13665.78	20.49	21.97
1100.0	14694.50	20.66	22.92
1150.0	15731.97	20.84	23.84
1200.0	16777.92	21.00	24.74

The heat of fusion of uranium dioxide found from our studies is 17.7 kcal/mol, in good agreement with the value of 18.2 kcal/mol reported by Hein and Flagella [28].

After a sample of UO_2 was heated in a tungsten capsule for ten minutes at 3610°K, analysis of the sample showed the presence of 0.22 wt % W. Ceramographic examination of this sample showed no serious tungsten contamination of the oxide. No corrections, thus, were made in our calculations for the heat of solution of tungsten in UO_2. The oxygen-to-uranium ratio in starting material for these studies was 2.015; after the experiment, this sample had an oxygen-to-uranium ratio of 1.98 (determined by vacuum fusion). Ceramographic analyses revealed small amounts of uranium metal deposited at grain boundaries; this indicates a slightly hypostoichiometric composition, in agreement with the chemical analyses.

Hein and Flagella [28] similarly found a very slight lowering in the O/U ratio in their enthalpy studies. They also reported that electron-microprobe analyses identified small particles of uranium metal throughout the UO_2. These findings are consistent with those of the present work. The effect of this slightly changed O/U ratio on the measured enthalpy of UO_2 is not clear at present.

To date, considerable effort has gone into preparation for measurements of the enthalpy of mixed-oxide fuel materials. A walk-in hood has been constructed around the

TABLE III-6. Enthalpy Relative to Room Temperature of Liquid UO_2[a]

Temperature (°K)	Observed $H^\circ_T - H^\circ_{298}$ (cal/mol)	Calculated (Eq. 7) $H^\circ_T - H^\circ_{298}$ (cal/mol)
3173	91699	91832
3257	95091	94558
3329	96277	96895
3404	99292	99329
3475	102244	101634
3523	102838	103192

[a]Gram formula weight of UO_2 assumed to be 270.03.

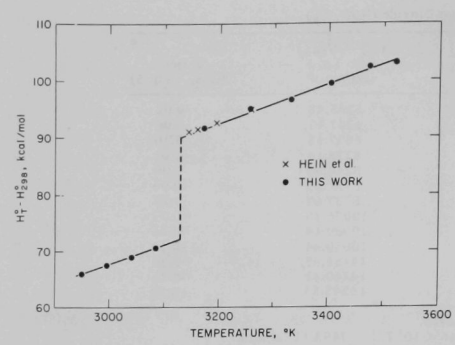

Fig. III-8. Enthalpy of Solid and Liquid UO_2 as a Function of Temperature. ANL Neg. No. 308-2175 Rev. 1.

induction-heated drop calorimetric system, which has been modified for operation from outside the hood. Once a sample capsule has been loaded into the furnace, the entire enthalpy determination can be performed without entering the hood. $(U_{0.8}Pu_{0.2})O_2$ pellets have been fabricated, as have suitable tungsten containers. Preparations are being made for loading and welding shut of these capsules, following which enthalpy measurements will begin.

2. *Vapor Pressure Over UO_2 at High Temperatures*
(M. G. Chasanov, G. T. Reedy)

Fuel vapor pressure is an important input parameter for equation-of-state calculations in fast-reactor safety analyses. The experimental data presently available must be extrapolated over many orders of magnitude to obtain vapor-pressure values at the temperatures of interest. We are carrying out studies to provide experimental vapor-pressure data over molten uranium oxide, thus providing a better basis for extrapolation to even higher temperatures. The data are being obtained by use of a transpiration apparatus described in ANL-7675, p. 90.

Much of the initial experimentation has involved measurements to evaluate such factors as inert carrier-gas flow rates, choice of operating techniques, hot-zone geometry, and the effect of vaporization on sample stoichiometry. These studies have utilized uranium oxide microspheres with an initial O/U ratio of 2.00. The carrier gas employed has been argon (99.999%). O/U ratios are determined by ignition of the solid to U_3O_8; uranium content of the condensate from the experiments is evaluated colorimetrically. The results of these initial studies are presented in Table III-7. These latter data include the highest-temperature pressure measurements yet reported for uranium oxide.

It was found that there was some reduction in the O/U ratio of the transpiration sample remaining after each

TABLE III-7. Total Pressure of Uranium-Bearing Species Over UO_2

Carrier gas: argon

Temperature (°K)	Initial O/U	Total Pressure (atm)	Condensed Phase
2615	2.00	4.45×10^{-4}	solid
2860	2.00	6.55×10^{-3}	solid
3175	2.00	7.1×10^{-2}	liquid
3390	2.00	0.18	liquid
3390	1.94	0.15	liquid

experiment. This was more pronounced at the higher temperatures. However, it is not yet clear whether this variation has a significant effect on the total pressure. This phenomenon will be studied later using a buffered carrier gas (probably H_2O-H_2 mixtures).

The data obtained for solid UO_2 (presented in Table III-7) are in excellent agreement with literature data, e.g., those of Tetenbaum and Hunt [29]. There are no other pressure data over the liquid available for comparison; however, one can make an extrapolation for the liquid based on the Tetenbaum and Hunt data for the solid and on Leibowitz's data for the heat of fusion of UO_2 (see Section III.B.1.b of this report) and by assuming a linear pressure-vs-$1/T$ relationship. Figure III-9 shows the extrapolated liquid pressure plot, Tetenbaum and Hunt's pressures

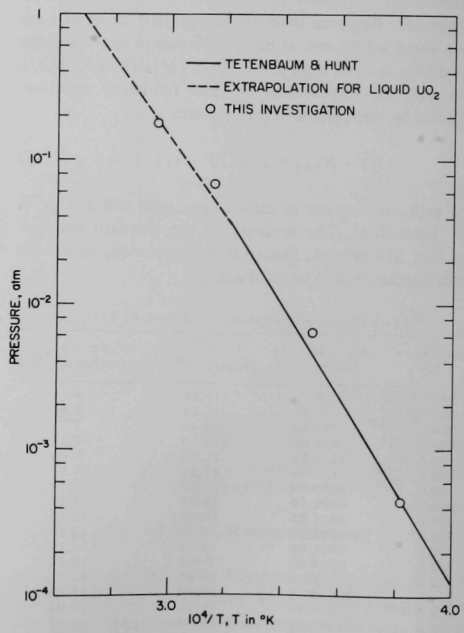

Fig. III-9. Total Uranium-Bearing Species Pressure over Near-Stoichiometric Uranium Oxide as a Function of Temperature. ANL Neg. No. 308-2419.

for the solid, and our experimental data. The agreement is quite good.

Future studies will involve utilizing buffered gas systems and trying to attain higher temperatures.

3. Matrix-Isolation Spectroscopy of UO_2 (S. D. Gabelnick)

The thermodynamic properties of the vapor species of fuel oxides are important in determining equation-of-state relationships used in projecting the results of certain fast-breeder-reactor design-basis accidents. Application of statistical mechanical techniques to spectroscopic data for these species presents a useful way of determining their thermodynamic properties at temperatures beyond the range of direct experimental measurements. The matrix isolation method, which consists of trapping molecules in frozen inert-gas lattices, allows low-temperature pseudo-gas phase studies to be carried out on molecules normally present in high gas-phase concentrations only at very high temperatures. Because the population of excited rotational quantum levels is eliminated under these low-temperature conditions, interpretation of the simplified infrared and visible spectra is greatly facilitated.

During the past year, construction and testing of the experimental apparatus were completed. A solid fuel sample of specific O/M ratio is heated by passing current through a small Knudsen cell. The molecular beam produced, together with a stream of inert gas, impinges on an infrared-transmitting window in a variable-temperature liquid helium cryostat. A diagram of the apparatus is shown in Fig. III-10. The variable-temperature feature allows one to select the optimum temperature for uniform crystallization of an inert gas and to study spectra of aggregates of the species of interest by controlled warming of the lattice

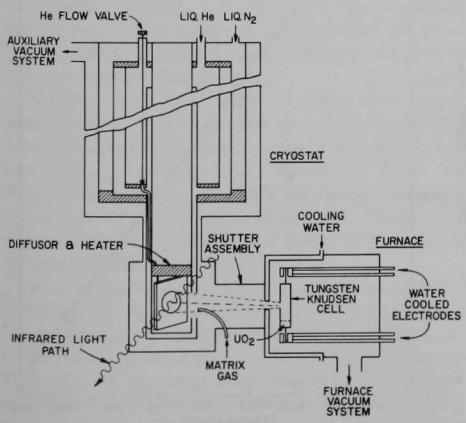

Fig. III-10. Matrix Isolation Apparatus. ANL Neg. No. 308-2553.

resulting in limited diffusion.

One of the important parameters in determining the thermodynamic properties of gaseous UO_2 is the O-U-O bond angle. It can be determined in principle by comparison of the asymmetric stretching frequencies of isotopically substituted molecules, using ^{18}O instead of ^{16}O. For molecules containing heavy central atoms, however, the bond angle effect is small and difficult to measure accurately. The Chemical Engineering Division has available a Fourier transform infrared system which has much greater sensitivity and precision and is much faster in making measurements than are conventional dispersive infrared spectrometers. Its use will greatly facilitate performing the above and other measurements to the required accuracy when the spectroscopic studies of the oxides of uranium begin in the immediate future.

4. Speed of Sound in Molten Reactor Materials (L. Leibowitz, M. G. Chasanov)

Experiments are in progress to measure the speed of sound in molten reactor materials with the initial efforts being directed to sodium. Compressibility data for molten fuel materials and coolant for use in conjunction with the Gruneisen equation of state will be available from these measurements. These speed-of-sound data will also be of value in assessing shock propagation through molten fuel and coolant, as well as in analyzing two-phase flow of coolant. The initial results on sodium to 1000°C, presented below, extend by about 200°C the temperature range of available data.

A cell, for use with the pulse-echo technique, shown in Fig. III-11, was fabricated from Type 304 stainless steel, and the buffer rod-to-reflector distance was carefully measured. The cell was then filled with mercury, and the speed of sound in mercury was measured using an X-cut 5-MHz quartz transducer. Arenberg Ultrasonic Laboratory, Inc. equipment was used in conjunction with a Tektronix Type 547 oscilloscope, which was calibrated against a Type 180A Tektronix time-mark generator. The transducer was bonded to the end of the buffer rod with epoxy cement. The speed of sound in mercury agreed with literature values [30] to within about 0.4%. This was considered satisfactory agreement. The mercury was then removed from the cell and, in a helium glovebox (1 ppm H_2O, 10 ppm O_2), the cell was loaded with high-purity sodium, capped, and TIG-welded shut. The sodium used contained, as principal impurities, 200 ppm potassium, <20 ppm oxygen, <10 ppm carbon, <8 ppm calcium, and <25 ppm halogen.

The cell was heated in a Marshall furnace and temperatures measured with a chromel-alumel thermocouple in contact with the outer wall of the cell. This thermocouple was calibrated against an NBS calibrated thermocouple (IPTS-48). Measurements of the speed of sound in sodium

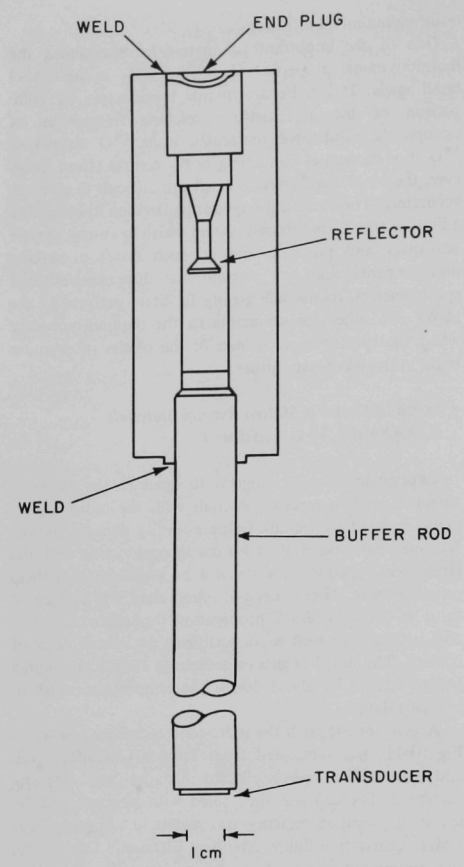

Fig. III-11. Schematic Drawing of Cell Used in Speed-of-Sound Measurements. ANL Neg. No. 308-2324.

were made from 182 to 1001°C. The data are presented in Table III-8 and in Fig. III-12. Multiple echoes were readily detectable in these experiments and each datum point given represents the average of two to four echoes, which gave closely agreeing values. The following equation can be used to represent the data

$$V = 2577.3 - 0.53607t \qquad (8)$$

where the velocity, V, is in meters sec^{-1} and the temperature, t, is in degrees, Centigrade. Moderate extrapolations to temperatures above 1000°C should be reasonably satisfactory. The estimate of the standard deviation for this equation is 3.92 meters sec^{-1}. Equation 8 may be compared

TABLE III-8. Speed of Sound in Sodium[a]

t (°C)	V (m/sec)	t (°C)	V (m/sec)
596	2260	742	2182
240	2446	792	2151
240	2446	843	2125
207	2467	895	2098
182	2478	446	2341
270	2429	774	2167
396	2364	373	2386
485	2321	335	2394
644	2239	536	2285
557	2281	949	2066
336	2391	1001	2035
693	2208	896	2094

[a]Data are tabulated in order measurements were performed.

with that given by Trelin *et al.* [31].

$$V = 2585.6 - 0.542t \qquad (9)$$

Values for the speed of sound in sodium at 250°C given by Pochapsky [32], Trelin *et al.* [31], and the present work are, respectively, 2446, 2450, and 2443 meters sec^{-1}. This agreement is considered satisfactory.

Table III-9 presents a summary of values for relevant thermodynamic properties of liquid sodium from 100 to 1000°C. In the calculation of these quantities, we employed, in addition to the speed-of-sound values from

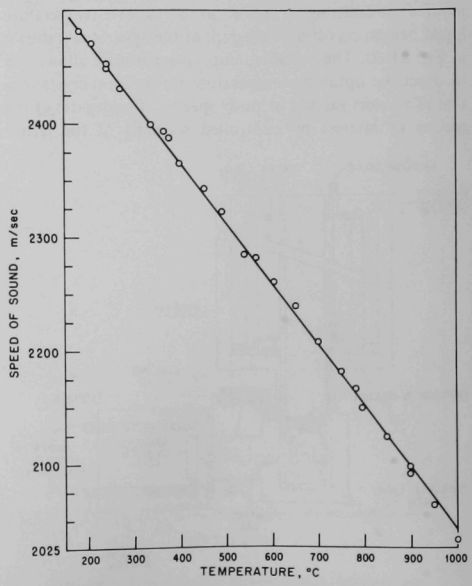

Fig. III-12. Speed of Sound in Liquid Sodium as a Function of Temperature. ANL Neg. No. 308-2326.

TABLE III-9. Computed Thermodynamic Properties of Liquid Sodium

t (°C)	V (m/sec)	ρ (g/cc)	α ($10^{-4}K^{-1}$)	β_S $\left(10^{-11}\frac{cm^2}{deg}\right)$	β_T $\left(10^{-11}\frac{cm^2}{deg}\right)$	C_p (J/gK)	C_v (J/gK)
100	2523.7	0.9270	2.5083	1.6936	1.8768	1.3833	1.2484
200	2470.1	0.9037	2.5999	1.8137	2.0780	1.3391	1.1688
300	2416.5	0.8801	2.6932	1.9459	2.3081	1.3042	1.0995
400	2362.9	0.8563	2.7884	2.0917	2.5698	1.2785	1.0406
500	2309.3	0.8323	2.8854	2.2530	2.8658	1.2621	0.99219
600	2255.7	0.8083	2.9844	2.4317	3.1985	1.2549	0.95402
700	2202.0	0.7841	3.0856	2.6301	3.5703	1.2569	0.92593
800	2148.4	0.7599	3.1890	2.8511	3.9836	1.2682	0.90766
900	2094.8	0.7356	3.2947	3.0976	4.4407	1.2888	0.89893
1000	2041.2	0.7114	3.4028	3.3736	4.9452	1.3185	0.89950

the present work, the liquid sodium densities correlated by Stone *et al.* [33] and the heat capacities for sodium reported by Ginnings *et al.* [34].

At present, it is planned to fabricate a new cell, of slightly modified design, from Ta-10% W alloy, which will allow extension of these measurements to higher temperatures (~1500°C).

5. Theoretical Extrapolation of Measured Physical Property Data to Higher Temperatures (S. D. Gabelnick, M. G. Chasanov)

A variational calculational method, based on thermodynamic considerations and mass constraints, has been used to determine the effects of burnup, void volume, and fuel starting composition on the phase composition and pressure of an oxide fuel-fission product system at 2500°K. The predicted vapor pressure is important in contributing to the understanding of certain design-basis accidents; knowledge of the phase composition of the system is necessary for post-accident heat-removal analyses. The algorithm and assumptions upon which the calculations are based have been presented in ANL-7675, pp. 90–92. The assumptions include temperature uniformity, immiscibility of fission product and fuel condensed phases, and free access of vapor species to void and plenum regions.

Revisions have been made to reflect that oxygen pressure, which is of central importance to the algorithm, is greater for hypostoichiometric mixed-oxide fuels than for pure UO_{2-x} systems. The theory of Rand and Markin [35], according to which the oxygen pressure is related to the plutonium and uranium valences, and experimental data of Markin and McIver [36] have been incorporated into the computations.

Some results for $(U_{0.8}Pu_{0.2})O_{2-x}$ fuels are presented in Table III-10. These indicate that, at least at the relatively low temperature for which the calculations were carried out (2500°K), the total pressure is independent of pre-burnup O/M ratio. At this temperature, nonoxides are the major contributors to the total vapor pressure. At higher temperatures, where this will not be the case, a greater sensitivity of the total pressure to pre-burnup O/M ratio is expected. The leveling off of the increase in post-burnup O/M with increased burnup results from conversion of the fission-product molybdenum from the metallic to the oxide phase at the equilibrium oxygen partial pressure 7.8×10^{-5} atm. The molybdenum acts as a sink for the oxygen released by the fissioning plutonium. Consequently, the ratio of oxygen bound with fuel and fission products in the fuel matrix will not significantly increase until all the molybdenum is converted to the oxide. Complete conversion is not expected to occur for the maximum burnups anticipated in normal reactor operation.

Programming modifications have been completed to account for the fact that fission-product oxides will be present in the fuel lattice rather than as separate phases. Similarly, the possibility of alloy formation between metallic fission-product species has been introduced. Ideal solution theory has been assumed. The decreased activities of the condensed fission-product species are expected to alter the calculated quantities significantly. In the future, attempts will also be made to consider the effects of coolant and cladding materials for the complete meltdown design-basis accident.

6. Thermal Diffusivity of Reactor Materials: Liquid UO_2 (J. Fischer, L. Leibowitz, J. Haley)

Values of the thermal diffusivity of UO_2 in the liquid state are of importance to the reactor safety program. This information is needed to evaluate means of safely cooling the core of an LMFBR in the event of a meltdown incident. Reliable experimental values of thermal diffusivity and thermal conductivity are available for solid UO_2 up to about 2300°K. There has been speculation that the thermal conductivity of UO_2 will increase above 2300°K and that a contributing factor to such an increase would be increased electronic conductivity. There is also considerable uncertainty about radiative heat transfer in UO_2. It is hoped that the present research will resolve these uncertainties.

We have selected a method of determining thermal diffusivity which was first proposed by Cowan [37]. In this method, thermal diffusivity is determined from the phase change in a thermal wave passing through a sample. This wave is produced by heating the sample with a sinusoidally modulated electron beam. Several experimental variations using this approach have been developed and applied to metals up to 3200°K and to oxides up to 2000°K [38].

We plan to obtain thermal diffusivity data for liquid UO_2 between its melting point and about 3500°K and for solid UO_2 from 2300°K to the melting point. Because tungsten will be used as a container material for the experiments with UO_2, thermal diffusivity data for tungsten are needed. The values of thermal diffusivity for tungsten will be checked against the literature values in the range of 2800 to 3200°K, and additional values for tungsten will be sought up to 3500°K.

These experiments will be performed in a dual-gun

TABLE III-10. Summary of Results for Mixed-Oxide Fuels at 2500°K

Pre-Burnup O/M:	1.95				1.98			
At. % Burnup	3	5	8	10	3	5	8	10
Post-Burnup O/M	1.974	1.991	2.015	2.021	2.004	2.018	2.021	2.021
O_2 Partial Pressure (atm)	2.29×10^{-8}	4.85×10^{-7}	3.01×10^{-5}	7.79×10^{-5}	9.84×10^{-6}	5.69×10^{-5}	7.79×10^{-5}	7.79×10^{-5}
Total Vapor Pressure (atm)	116	193	309	386	117	195	310	386

electron beam furnace, formerly used as a high-temperature tensile test furnace. Extensive electronic modifications to the system, needed for these diffusivity measurements, are currently being made. Cell design and temperature and phase-shift measuring procedures are also currently under test.

7. Reactor Materials-Fuel Phase Studies at High Temperatures: Distribution of Fission Products Among Molten Fuel and Reactor Material Phases (J. Fischer, J. Schilb)

Knowledge of the distribution of fission products to the phases produced in the event of a meltdown of the core of an LMFBR is required to predict the fission-product heat distribution after an incident and be able to assure that means are available for cooling the products of the meltdown. In the type of hypothetical incident being considered, simultaneous failure of multiple safeguards and loss of effective cooling could lead to melting of the oxide fuel, the stainless steel cladding, the core-support steel, and the concrete container. A discussion of safety engineering tasks and an evaluation of the meltdown problem can be found in the LMFBR Program Plan, Volume 10. In addition to the factors presented in that report, consideration must be given to the possible dissolution of concrete in the molten UO_2-PuO_2 layer, thereby forming a liquid less dense than molten steel.

To properly evaluate the capabilities of heat removal after a meltdown incident, it is necessary to know the physical distribution of the phases. It is also requisite to know the quantitative distribution of fission-product heat among the phases produced.

One phase of an experimental program is to determine the distribution of fission-product elements between molten UO_2 and molten stainless steel. The fission products to be studied (Nb, La, Mo, Zr, and Ru) are among those that contribute the major portion of the heat produced soon after shutdown of a fast reactor and that have properties suitable for the experimental method used.

We have performed experiments in an arc-melting furnace to determine how zirconium distributes between liquid phases of UO_2 and iron. The results of the experiments with zirconium are outlined in Table III-11. In Experiment 1, the iron-zirconium alloy was melted without contacting UO_2. In a 4-min melt time, only a small decrease in zirconium concentration was found. In Experiment 2, with a 2-min melt time, it was found that the UO_2-Fe-Zr system did not react completely and most of the zirconium remained in the metal phase. In Experiments 3 and 4, with 12-min melt times, only a trace of zirconium remained in the metal phase. In Experiments 5 and 6, zirconium oxide was added to the UO_2 phase before the melt. The metal phase was iron without zirconium. The zirconium concentration in the metal phase remained very low after a 6-min melt time.

Metallographic examination of cross sections of the resultant uranium oxide-iron buttons indicated that there was a clean separation of the oxide and metal phases. Microprobe analysis of a cross section of the button from Experiment 5 (Table III-11) indicated that the low concentration of zirconium, <0.04 wt %, in the iron phase was due to small localized inclusions of UO_2 containing zirconium in the iron phase. The experiments establish what one would predict thermodynamically: zirconium would be distributed to the oxide phase in the event of a core meltdown incident.

The distribution of fission-product elements between liquid UO_2-concrete and molten steel is under study because of the possible interaction of molten fuel components with the concrete which will lie below the core of a reactor such as FFTF. Molten UO_2 coming into contact with the concrete will cause it to melt. The liquidus point of a typical concrete mixture to be used in FFTF construction will be about 1400°C. Dissolution of SiO_2, CaO, and Al_2O_3 can further lower the liquidus to about 1100°C. At some point, the density of the magma will become less than that of the molten steel—then the liquid phase of UO_2-PuO_2-F.P. and concrete constituents will rise to the surface and the molten steel will sink to the bottom. A knowledge of the distribution of fission products between the steel and UO_2-concrete phases becomes important if one is to be able to estimate the heat distribution to the phases.

An effort was made to find a container material for this oxide-metal mixture. Experiments with a tantalum carbide crucible in the arc-melting furnace for a short duration showed little reaction with iron. In another experiment, a concrete-UO_2-iron mixture plus some inactive fission-product oxides, contained in a tantalum carbide crucible welded into a tantalum capsule, was melted in a resistance-heated furnace. The crucible proved unsatisfactory because of creep of the molten ceramic materials. A similar

TABLE III-11. Distribution of Zirconium Between Molten UO_2 and Iron

Experiment No.	Melt Time (min)	Zr Concentration in Metal Phase Before Melt (wt %)	Zr Concentration in Metal Phase After Melt (wt %)	Comments
1	4	0.51	0.49	No UO_2 in melt.
2	2	0.76	0.67	
3	12	0.78	0.12	
4	12	0.90	<0.03	
5	6	$<3 \times 10^{-3}$	<0.04	ZrO_2 was added to the UO_2 phase before melting. No Zr was added to the metal phase before melting.
6	6	$<3 \times 10^{-3}$	0.07	

experiment using a zircon crucible was satisfactory, and this will be used for future studies.

C. CALORIMETRY (W. N. Hubbard)

The calorimetric program is directed toward the experimental, empirical, or theoretical determination of thermodynamic properties of substances that are of interest in high-temperature chemistry and nuclear technology. Measurements are being made of standard enthalpies of formation (ΔHf°_{298}) of the substances. Complementary experimental determinations of high-temperature increments ($\Delta H^{\circ}_{T} - \Delta H^{\circ}_{298}$) are reported in Section III.B.1. Complementary low-temperature thermal measurements (of C°_{p}, ΔH°_{tr}, and S°) are being performed in the Chemistry Division and elsewhere.

The method of fluorine bomb calorimetry was developed for measurements on substances not amenable to more conventional calorimetric techniques and has now been used to determine the enthalpies of formation of 35 elemental fluorides and 21 other compounds. The more conventional oxygen bomb calorimetry has been used for studies of 15 reactions and solution calorimetry for measurements of 9 aqueous reactions.

Attempts at the determination of thermodynamic properties by empirical calculations (e.g., the correlation and estimation of enthalpies of formation for the rare earth trifluorides: ANL-7450, p. 64) and by theoretical calculations (e.g., extended Hückel molecular-orbital calculations for the chalcogen hexafluorides: ANL-7450, p. 66) now include ab initio calculations based on the Hartree-Fock-Roothaan approach for the following binary fluorides and their ions: OF, SF, SeF, NF, and PF.

The data and results presented in this report are to be considered preliminary; when published in their final form in a journal article, they may be slightly different owing to refinements in the calculations.

1. *Thermochemistry of Plutonium Compounds* (G. K. (G. K. Johnson, E. H. Van Deventer)

The elucidation of the basic thermodynamic properties of the plutonium carbides is important because of the interest in them as fast-breeder-reactor fuels.

a. *Enthalpy of Formation of Plutonium Monocarbide*

The determination of the enthalpy of formation of plutonium monocarbide (ANL-7675, p. 94) has been published in a paper with the title "The Enthalpy of Formation of Plutonium Monocarbide" [39]. The abstract of this paper is as follows:

> The energy of combustion in oxygen of a specimen of arc-melted plutonium monocarbide ($PuC_{0.878\pm0.003}$) was measured in a bomb calorimeter. The standard enthalpy of formation $\Delta H^{\circ}_{f,298.15}(PuC_{0.878\pm0.003}, c)$ was calculated to be 11.41 ± 0.61 kcal mol^{-1}.

b. *Enthalpy of Formation of Plutonium Sesquicarbide*

As part of the continuing program to provide accurate thermochemical data for plutonium compounds, the standard enthalpy of formation of plutonium sesquicarbide was determined by oxygen bomb calorimetry.

A sample of plutonium sesquicarbide was prepared [40] by arc melting an appropriate mixture of plutonium and graphite. Chemical and spectrochemical analyses showed the sample to contain the following impurities (in ppm): 0, 220; N, 125; W, 170; Mo, 30; Ni, 10; Fe, 10; Si, 15; and Ca, 7. The carbon content of the sample was determined to be 6.83% and the plutonium content, taken by difference, was 93.11%. The C/Pu atom ratio was calculated to be 1.466. The combustion technique used was similar to that described previously for plutonium monocarbide [39], except that several grams of plutonium metal were added to the sample in each experiment to serve as a combustion aid. Even with the addition of the plutonium metal, the combustions were not complete. Carbon analyses of the combustion residues showed that between 0.3 and 3.5% of the carbon content of the starting samples remained in the residues. Because of the uncertainty in the state of combination of the unreacted carbon, an empirical correction for the carbon was made as follows: The energy evolved in each experiment was divided by the mass of Pu_2C_3 charged to the bomb, and this quantity was plotted against the carbon content of the residues. Extrapolation of this line to zero carbon residue yields a value for the energy of combustion which is independent of any assumption about state of the carbon residue. Based on four

combustions, the least-squared result of the extrapolation yielded an energy of combustion of plutonium sesquicarbide of -1442.1 ± 0.7 cal g^{-1}. This result was used to derive a preliminary value for the standard enthalpy of formation of plutonium sesquicarbide, $\Delta Hf^{\circ}_{298}(PuC_{1.466}, c)$, of -19.4 ± 0.7 kcal mol^{-1}.

Several high-temperature vaporization studies have been conducted on the plutonium-carbon system from which values of $\Delta Hf^{\circ}_{298}(PuC_{1.5})$ have been calculated. These studies, which have been discussed in detail by Battles *et al.* [41], yield $\Delta Hf^{\circ}_{298}(PuC_{1.5})$ values in the range from -12.3 to -17.5 kcal mol^{-1}, all of which are considerably more positive than the result derived in our oxygen bomb study. In addition to the vaporization data, there have been several other oxygen bomb calorimetric studies [42–44] made on $PuC_{1.5}$. Unfortunately, none of these studies have been published in any detail, and, therefore, the accuracy of the studies is very difficult to assess. The reported values for $\Delta Hf^{\circ}(PuC_{1.5})$ from these calorimetric investigations are 0.85 [42], -21 ± 2 [43], and -24.5 [44] kcal mol^{-1}. The first result is a very preliminary result and is in serious disagreement with any of the other data. The remaining results are even more negative than the value derived herein. Thus, there would appear to be a polarization of data, with the calorimetric results being more negative than the vaporization results. The reason for such disagreement is not apparent at this time.

2. *Thermochemistry of Hydrogen Fluoride*

Much of the work of this laboratory with fluorine bomb calorimetry is related to the thermochemistry of hydrogen fluoride. The enthalpies of combustion in fluorine of Si and SiO_2 led to a paper on the enthalpy of formation of gaseous hydrogen fluoride [45]. Similarly, the combustions of boron, boron oxide, carbon, silicon, silicon dioxide, iodine, magnesium, uranium, and several other compounds in fluorine can be used to calculate values for the enthalpy of formation of aqueous HF. Most of the values so obtained for $\Delta Hf(HF, aq)$ indicate that the selected values tabulated by the National Bureau of Standards [46] and by the Soviet Academy of Sciences [47] are too positive by approximately 0.5 kcal. The basis for the tabulated values [46,47] for $\Delta Hf(HF, aq)$ is the derived value [45] for $\Delta Hf^{\circ}(HF, g)$, combined with the enthalpy of solution in water of *real* HF gas (measured at various dilutions by numerous investigators). Although corrections were attempted to account for the differences between real HF and the ideal gas, uncertainties in the thermodynamic properties of real HF gas led to considerable uncertainty in the results. To avoid the uncertainties associated with HF gas, we have measured (1) the enthalpy of formation of liquid HF directly from gaseous hydrogen and fluorine, (2) enthalpies of solution of liquid HF in water to form aqueous HF of various concentrations from $HF \cdot 2\,H_2O$ to $HF \cdot 5500\,H_2O$, and (3) the enthalpy of neutralization of liquid HF by dilute aqueous NaOH to arrive at the enthalpy of formation of HF at infinite dilution and the enthalpy of formation of the fluoride ion.

a. Enthalpy of Formation of Liquid Hydrogen Fluoride
(J. L. Settle)

The enthalpy of formation of liquid hydrogen fluoride was determined by measuring the energy released by the reaction of fluorine with hydrogen in a two-compartment calorimetric combustion bomb [48]. Even though the nickel metal of which the bomb is constructed is resistant to reaction with fluorine, it was found that the HF product caused extensive corrosion in the combustion compartment. Therefore, the combustion compartment was gold-plated to protect it from HF. However, the gold plating was slightly reactive with fluorine, and an empirical correction for the thermal effect of the reaction had to be made. Empirical corrections were also made for the vaporization of the liquid HF to saturate the bomb and for the energy of mixing of gaseous HF and F_2. The entire study required that the energies of the following four reactions be measured:

$$x\mathrm{Au(c)} + \frac{3x}{2}\mathrm{F_2(g)} \rightarrow x\mathrm{AuF_3(c)} \qquad (1)$$

$$x\mathrm{AuF_3(c)} + \frac{1-3x}{2}\mathrm{F_2(g)} + \frac{1+2y}{2}\mathrm{H_2(g)} \rightarrow$$

$$x\mathrm{Au(c)} + (1-z)\mathrm{HF(\ell)} + z\mathrm{HF(g)} \cdot y\mathrm{H_2(g)} \qquad (2)$$

$$(1-z)\mathrm{HF(\ell)} + z\mathrm{HF(g)} \cdot y\mathrm{H_2(g)} \rightarrow$$

$$(1-z)\mathrm{HF(\ell)} + z\mathrm{HF(g)} + y\mathrm{H_2(g)} \qquad (3)$$

$$(1-z)\mathrm{HF(\ell)} + z\mathrm{HF(g)} \rightarrow \mathrm{HF(\ell)} \qquad (4)$$

Reaction 1 is the spontaneous reaction that occurred when fluorine was put into the gold-plated combustion compartment in preparation for a combustion. Reaction 2 is the main combustion reaction that occurred when excess hydrogen was expanded from the storage compartment into the combustion compartment of the bomb. During Reaction 2, the gaseous fluorine reacted with hydrogen to form HF; part of the excess hydrogen reduced the AuF_3; the HF in excess of the quantity needed to saturate the combustion chamber condensed to the liquid state; and the HF(g) and the excess hydrogen in the combustion compartment mixed homogeneously. In Reactions 2 and 3 the symbolism $z\mathrm{HF(g)} \cdot y\mathrm{H_2(g)}$ is not intended to imply compound formation but to indicate a homogeneous mixture of the gases. Because there was no information on the energy of mixing of HF(g) and H_2(g), it was necessary

to perform the reverse of Reaction 3 in a calorimetric experiment in which hydrogen from the storage compartment was expanded into the combustion compartment, which had been presaturated with HF(g) by the introduction of excess HF(ℓ). The energy of Reaction 4, the reverse of the HF vaporization reaction, was measured by presaturating the storage compartment with HF(g) [by the introduction of excess HF(ℓ)], and then expanding the HF(g) into the evacuated combustion compartment. Summation of Reactions 1 through 4 yields the desired reaction

$$\frac{1}{2}H_2(g) + \frac{1}{2}F_2(g) \rightarrow HF(\ell) \qquad (5)$$

for which, with the reactants and product in their respective standard states, $\Delta E(5) = \Delta E(1) + \Delta E(2) + \Delta E(3) + \Delta E(4)$.

From these measurements, the standard enthalpy of formation of liquid HF, $\Delta Hf^{\circ}_{298}(HF,\ell)$, was calculated to be -72.57 ± 0.09 kcal mol^{-1}. This value for $\Delta Hf^{\circ}_{298}(HF,\ell)$ supersedes the previous, preliminary value from this laboratory [49,50].

b. The Enthalpy of Solution and Neutralization of Liquid Hydrogen Fluoride (G. K. Johnson)

The determination of the enthalpy of solution of liquid HF in water according to the reaction

$$HF(\ell) + nH_2O(\ell) \rightarrow HF \cdot nH_2O(\ell)$$

was discussed previously [51]. The data presented at that time have since been found to be in error due to a small leakage of HF vapor through the windows (3-mil Kel-F film) of the ampoules used to contain the HF(ℓ). This work has been repeated with 5-mil Kel-F film windows, which are impervious to HF at room temperature.

Previously [51], an attempt was made to extend the enthalpy of solution measurements to infinite dilution based on equilibrium constants and enthalpies for the equilibria

$$HF \rightleftharpoons H^+ + F^-$$

$$HF + F^- \rightleftharpoons HF_2^-$$

present in aqueous solutions of hydrogen fluoride. A better method to obtain the standard enthalpy of solution is through measurements of the enthalpy of neutralization of HF(ℓ). The simplified cycle, which ignores only some dilution terms, is as follows:

$$HF(\ell) + OH^- \cdot \infty H_2O \rightarrow (F^- + H_2O) \cdot \infty H_2O$$

$$H_2O \cdot \infty H_2O \rightarrow (H^+ + OH^-) \cdot \infty H_2O.$$

The sum of these two reactions yields the desired reaction

$$HF(\ell) + \infty H_2O \rightarrow (H^+ + F^-) \cdot \infty H_2O.$$

Six measurements of the enthalpy of neutralization of HF(ℓ) in 0.1*N* NaOH yielded an average value and standard deviation for $\Delta H_{neut.}$ of $-21{,}036 \pm 5$ cal mol^{-1}. This result, when combined with the enthalpy of ionization of water, $13{,}345 \pm 25$ cal mol^{-1} [52], yields the standard enthalpy of solution at 298°K, $\Delta H^{\circ}_{soln}(HF,\ell) = -7961 \pm 30$ cal mol^{-1}.

Due to physical limitations of the solution calorimeter, it was not possible to make enthalpy of solution measurements in the region of $HF \cdot 150\,H_2O$ to $HF \cdot 2\,H_2O$. This, however, is a region in which there are a number of enthalpy of dilution measurements available in the literature. Unfortunately, the literature values are not all in agreement. To aid in the selection of data in this region, a number of enthalpy of dilution experiments were performed using concentrated HF solutions.

The data obtained in this study have been summarized in Table III-12 at selected values of nH_2O. The tabulated quantities are the enthalpy of solution of HF(ℓ) in *n* moles of water; Φ_L, the relative apparent molal enthalpy which is equal to the negative of the enthalpy of dilution from $HF \cdot nH_2O$ to $HF \cdot \infty H_2O$; and the enthalpy of formation of aqueous HF according to the reaction

$$\frac{1}{2}H_2(g) + \frac{1}{2}F_2(g) + nH_2O(\ell) \rightarrow HF \cdot nH_2O(\ell)$$

This latter quantity is obtained by adding $\Delta Hf^{\circ}(HF,\ell) = -72.57 \pm 0.09$, the determination of which is discussed above, to $\Delta H_{soln}(HF,\ell)$.

Other quantities that are derivable from the work include (1) the standard enthalpy of formation of the fluoride ion, $\Delta Hf^{\circ}(F^-,aq) = -80.35 \pm 0.09$ kcal mol^{-1}, which is equal to $\Delta Hf^{\circ}(HF \cdot \infty H_2O)$ using the usual convention that $\Delta Hf^{\circ}(H^+ \cdot \infty H_2O) = 0$, and (2) the enthalpy of formation of NaF(c) of

TABLE III-12. Thermochemical Properties of Aqueous HF

n	$\Delta H_{soln}(Hf,\ell)$ (cal mol^{-1})	Φ_L (cal mol^{-1})	$\Delta Hf(HF \cdot nH_2O)$ (kcal mol^{-1})
∞	−7691	0	-80.25_9
5000	−5154.7	2536.3	-77.72_3
1000	−4679.7	3011.3	-77.24_8
500	−4586.1	3104.9	-77.15_4
200	−4514.0	3177.0	-77.08_2
100	−4498.0	3193.0	-77.06_6
50	−4482.6	3208.4	-77.05_1
20	−4454.0	3237.0	-77.02_2
10	−4417.8	3273.2	-76.98_6
5	−4330.0	3361.0	-76.89_8
2	−3981.5	3709.5	-76.55_0
1	−3393.7	4297.3	-75.96_2

-137.95 ± 0.10 kcal mol^{-1}. The latter quantity is obtained from the neutralization data using values of $\Delta Hf^{\circ}(NaOH,aq) = -112.439 \pm 0.015$ kcal mol^{-1} [53], and $\Delta H^{\circ}_{soln}(NaF,c) = 218 \pm 10$ cal mol^{-1} [52].

The results obtained for the enthalpy of formation of aqueous HF from combination of the hydrogen-fluorine reaction combustion work and the enthalpy of solution work are substantially ($\sim$0.75 kcal mol^{-1}) more negative than the values selected in NBS Technical Note 270-3 [46]. These results are, however, in excellent agreement with the results derived indirectly from the cycles involving HF(aq) and fluorides whose enthalpies of formation have been determined by fluorine bomb calorimetry. Thus, it appears that the thermochemistry of this very important reaction medium is now firmly established.

3. *Enthalpies of Formation of Disodium and Monosodium Acetylides* (G. K. Johnson, E. H. Van Deventer)

The thermodynamic and chemical properties of disodium acetylide, Na_2C_2, are currently of considerable interest because this material is thought to have a role in the transport of carbon in liquid-sodium reactor coolants [54]. Therefore, an investigation was undertaken to determine the standard enthalpy of formation, $\Delta Hf^{\circ}_{298.15}(Na_2C_2, c)$, from measurements of the enthalpy of reaction of Na_2C_2 with water. The enthalpy of formation of monosodium acetylide, $NaHC_2$, was also determined by the same technique because its chemistry is closely related to that of Na_2C_2.

The calorimeter employed in this study was an LKB-8700 solution and reaction calorimeter, modified for quartz-crystal thermometry. The samples of Na_2C_2 and $NaHC_2$ were obtained from Alfa Inorganics, Inc. The samples were handled in a helium-atmosphere glovebox or in sealed containers to avoid contamination by atmospheric moisture. The acetylide content of the samples was determined to within ±0.3% by hydrolysis and collection of the acetylene evolved. The $NaHC_2$ content of the Na_2C_2 sample was determined by heating to $\sim$150°C and collecting the evolved C_2H_2 with the assumption that the following reaction occurred:

$$2\,NaHC_2(c) \rightarrow Na_2C_2(c) + C_2H_2(g) \qquad (6)$$

Oxygen was determined by neutron activation and metal impurities by emission spectrography. The results of these analyses are as follows: 98.6% Na_2C_2, 0.35% $NaHC_2$, and 0.31% oxygen in the Na_2C_2 sample; 100.0% $NaHC_2$ and 0.19% oxygen in the $NaHC_2$ sample. Metal impurities in both samples were less than 50 ppm total. The oxygen in both samples is assumed to be present as a mixture of sodium carbonate and sodium hydroxide.

The calorimetric measurements were conducted in an acetylene-saturated NaOH solution instead of pure water for two reasons: (1) Aqueous sodium hydroxide was used so that the initial and final solutions would have a similar *p*H, thus minimizing complications from dissolved or atmospheric CO_2, and (2) the solution was saturated with C_2H_2 so that all of the product C_2H_2 would be evolved as a gas, thereby avoiding an uncertain correction for the solubility of C_2H_2 in aqueous solutions.

The samples of Na_2C_2 (0.084 g) and $NaHC_2$ (0.11 g) were loaded into small ampoules, which were weighed and sealed in helium and then placed in the calorimeter with 95 cc of 0.014*N* NaOH. The ampoules were constructed of Kel-F in order that contact with H_2O could be made very slowly through a pinhole puncture. Preliminary experiments with glass ampoules had shown that, when the ampoules were broken, the reaction between the acetylide and water was very violent and resulted in decomposition of some of the acetylene to form free carbon. None of the acceptable experiments showed free carbon in the product solution.

The enthalpies of reaction of the Na_2C_2 and $NaHC_2$ samples with water were determined to be -548.45 ± 1.09 and -269.03 ± 0.95 cal g^{-1}, respectively. Thermal corrections for the impurities in the Na_2C_2 and $NaHC_2$ samples were -3.76 ± 0.61 and -0.38 ± 0.45 cal g^{-1}, respectively. The corrected molar enthalpies of reaction were -38.65 ± 0.35 and -12.95 ± 0.19 kcal mol^{-1}, respectively, for the reactions

$$Na_2C_2(c) + 1.1\,NaOH \cdot 4400\,H_2O \rightarrow C_2H_2(g) + 3.1\,NaOH \cdot 4398\,H_2O \qquad (7)$$

and

$$NaHC_2(c) + 0.55\,NaOH \cdot 2200\,H_2O \rightarrow C_2H_2(g) + 1.55\,NaOH \cdot 2199\,H_2O \qquad (8)$$

To obtain the standard enthalpies of formation, the following auxiliary reactions are needed:

$$Na(c) + 0.55\,NaOH \cdot 2200\,H_2O \rightarrow 1.55\,NaOH \cdot 2199\,H_2O + 1/2\,H_2(g) \qquad (9)$$

$$2C(graph) + H_2(g) \rightarrow C_2H_2(g) \qquad (10)$$

A value of -44.035 ± 0.015 kcal mol^{-1} was calculated for $\Delta H(9)$ (the enthalpy change for Reaction 9) from the data of Gunn [55] and Parker [56]. The enthalpy of formation of C_2H_2, $\Delta H(10)$, was taken to be 54.19 ± 0.19 kcal mol^{-1} [57]. The standard enthalpy of formation of Na_2C_2 according to

$$2Na(c) + 2C(graph) \rightarrow Na_2C_2(c) \qquad (11)$$

is $\Delta Hf^{\circ}_{298} = \Delta H(11) = -\Delta H(7) + 2\Delta H(9) + \Delta H(10) =$

4.77 ± 0.40 kcal mol^{-1}. Similarly, the enthalpy of formation of $NaHC_2$ according to

$$Na(c) + 1/2\,H_2(g) + 2C(graph) \rightarrow NaHC_2(c) \qquad (12)$$

is $\Delta Hf^{\circ}_{298} = \Delta H(12) = -\Delta H(8) + \Delta H(9) + \Delta H(10) = 23.10 \pm 0.27$ kcal mol^{-1}.

The results obtained in this study, $\Delta Hf^{\circ}_{298}(Na_2C_2, c) = 4.77 \pm 0.40$ and $\Delta Hf^{\circ}_{298}(NaHC_2, c) = 23.10 \pm 0.27$ kcal mol^{-1}, are in surprisingly good agreement with some of the work done in the 1890's, which involved very impure samples. Matignon [58] studied the reaction of Na_2C_2 and $NaHC_2$ with HCl(aq). The results obtained, when combined with modern auxiliary data, yield $\Delta Hf^{\circ}(Na_2C_2) = 4.1$ and $\Delta Hf^{\circ}(NaHC_2, c) = 24.6$ kcal mol^{-1}. De Forcrand [59] measured the enthalpy of reaction of Na_2C_2 with H_2SO_4(aq), from which we calculate $\Delta Hf^{\circ}(Na_2C_2) = 4.2$ kcal mol^{-1}. Thus, it would seem that the enthalpies of formation of Na_2C_2 and $NaHC_2$ are well established.

The enthalpy of formation of Na_2C_2 at 25°C, in itself, does not predict the stability of Na_2C_2 at reactor temperatures; however, estimates of the entropy, $S^{\circ}_T(Na_2C_2)$, and enthalpy functions, $(H_T - H^{\circ}_{298})$, would indicate that the free energy of formation from either solid or liquid Na, ΔG_f, is positive for all temperatures above 25°C, and thus the substance is thermodynamically unstable relative to free sodium and graphite. Until experimental measurements of the entropy and enthalpy functions become available, the estimates on which these conclusions are based must be viewed as highly uncertain. It is also likely that the formation of Na_2C_2 would be enhanced by amorphous carbon in a highly active state, which is probably the case in a reactor.

4. The Thermochemistry of Na_3UO_4 and Na_2O (P. A. G. O'Hare)

It has been demonstrated that Na_3UO_4 is the compound likely to be in equilibrium with sodium and uranium dioxide in the presence of excess oxygen. Because there apparently exist no thermodynamic data for this compound, and because of its obvious significance to sodium-cooled, oxide-fueled reactors, the determination of the enthalpy of formation of Na_3UO_4 has been added to the program of the group. Preliminary measurements by solution calorimetry are under way, and a calorimetric-grade sample is being prepared by A. E. Martin and W. A. Shinn of the High Temperature Materials Group.

Because the enthalpy of formation of Na_2O is a necessary auxiliary datum for the study of Na_3UO_4 and the literature values are discordant, the determination of the enthalpy of formation of Na_2O has also been placed on the program.

5. Enthalpy of Formation of Molybdenum Disulfide (P. A. G. O'Hare, E. Benn, F. Y. Cheng, G. Kuzmycz)

The calorimetric investigation of MoS_2, described briefly earlier (ANL-7675, p. 98), has been concluded. The work is described in a recent publication, "A Fluorine Bomb Calorimetric Study of Molybdenum Disulfide: The Standard Enthalpies of Formation of MoS_2 and Mo_2S_3" [60]. The abstract of the paper is as follows:

> The energy of the reaction between fluorine and a well-characterized sample of natural molybdenite (MoS_2) to give gaseous MoF_6 and SF_6 was measured in a fluorine bomb calorimeter. The corresponding standard enthalpy of formation at 298.15K, $\Delta H^{\circ}_f(MoS_2, c, 298.15\ K)$ is $-(65.8 \pm 1.2)$ kcal mol^{-1}, in reasonable agreement with several modern high-temperature studies. A survey of thermochemical data in the literature leads to a consensus value of $-(97 \pm 3)$ kcal mol^{-1} for $\Delta H^{\circ}_f(Mo_2S_3, c, 298.15\ K)$.

6. Enthalpy of Formation of Xenon Hexafluoride (G. K. Johnson)

An investigation to determine the enthalpy of formation of xenon hexafluoride has been undertaken. A reliable value for the energy of the Xe-F bond in XeF_6 is of fundamental importance to chemists. Published values for $\Delta Hf^{\circ}(XeF_6)$ based on calorimetric [61,62] and equilibrium [63] results are discordant, varying between −70.4 [63] and −126 [62] kcal mol^{-1} depending on the auxiliary data used.

A sample of XeF_6 has been prepared [64] and will be reacted with PF_3(g) according to

$$XeF_6(c) + 3\,PF_3(g) \rightarrow Xe(g) + 3PF_5(g) \qquad (13)$$

This reaction proceeds spontaneously and will necessitate the use of a two-chambered reaction vessel. The necessary auxiliary data for the reaction

$$PF_3(g) + F_2(g) \rightarrow PF_5(g) \qquad (14)$$

have already been determined [65] in this laboratory. This work is in progress.

7. Quantum Chemical Investigations of Selected Nonmetal Monofluorides (P. A. G. O'Hare)

As part of a continuing effort to (1) rationalize previously observed [66,67] bond energy trends and (2) establish a scheme to predict reliable thermodynamic data for fluorine-containing molecules, free radicals, and ions, we have been involved for a considerable part of the present year in the calculation of accurate wave functions for gaseous diatomic fluoride molecules and ions. Although this

study is far from complete, a substantial amount of useful and informative data, outlined in the following paragraphs, has been obtained.

a. The Oxygen-Fluorine System

This phase of the investigation has been described in a recent publication [68]. The abstract of the paper is as follows:

Self-consistent-field wave functions near the Hartree-Fock limit have been calculated by the Roothaan expansion method for $OF(^2\pi)$ at several internuclear separations; the total energy at the Hartree-Fock minimum (1.321Å) was found to be −174.19502 hartree. Based on the assumption that the correlation energy was approximately the same as for O_2^-, and also by interpolating the correlation energy of OF across the CF, NF, OF, and F_2 sequence, the binding energy, D(OF), was deduced to be $3.0^{+0.3}_{-0.8}$ eV. A Dunham analysis of the potential energy curve gave values for the various spectroscopic constants.

In addition, the ionization potential and electron affinity for the vertical processes, and the dipole and quadrupole moments of $OF^+(^3\Sigma)$, $OF(^2\pi)$ and $OF^-(^1\Sigma)$ were also calculated.

The various properties reported in the above paper are summarized in Table III-13.

b. The Sulfur-Fluorine and the Selenium-Fluorine Systems

The results for these systems have been published [69,70]. The abstract of the paper is as follows:

Self-consistent-field wave functions, near the Hartree-Fock limit, have been computed by the Roothaan expansion method for $SF(^2\pi)$ and $SeF(^2\pi)$ at the experimental internuclear separations. The results from the present investigation, coupled with our previous calculations on OF, show that the Hartree-Fock binding energies of OF, SF, and SeF vary nonmonotonically, in harmony with the experimental dissociation enthalpies. Other properties reported herein for SF and SeF include the vertical ionization potentials and vertical electron affinities, and the dipole and quadrupole moments for the neutral and charged species. The computed ionization potential for SF suggests that the experimental appearance potentials for SF^+ are too large by approximately 2 eV. Thermodynamic calculations based on the electron affinities predict substantial stabilities for SF^- and SeF^- at moderate temperatures.

The various properties reported in the above paper are summarized in Table III-13.

c. The Nitrogen-Fluorine System

Wave functions were computed for the three low-lying states, viz., the $^3\Sigma$ ground state and the excited $^1\Sigma$ and $^1\Delta$ states of NF. Among the hitherto unreported data obtained in this part of the investigation are the electron affinity of $NF(^3\Sigma)$ and the dipole and quadrupole moments of the three low-lying states. The total Hartree-Fock energy for $NF(^3\Sigma)$ is approximately 13 eV more stable than that obtained in a previous molecular orbital study described by Sahni [71]. Derived dissociation energy and ionization potential values are in excellent agreement with results from experimental studies [72,73]. Based on thermochemical arguments, the NF^- ion is predicted to be only marginally stable at room temperature. In harmony with the latter observation, the NF^- ion has never been detected experimentally.

The various properties deduced for NF are summarized in Table III-13.

d. The Phosphorus-Fluorine System [70]

Among the more interesting aspects of this part of the investigation was the calculation of both the vertical and adiabatic ionization potentials, I(PF). The adiabatic ion, as one would anticipate, was found to be about 0.25 eV more stable than the vertical ion. Rather unexpectedly, however, the vertical ionization potential came out to be almost 4 eV lower than the value implicit in Wada's [74] mass spectrometric appearance potential measurements. Wada's data

TABLE III-13. Computed Properties of Diatomic Fluorides

Molecule	D_0° (eV)	I (eV)	E_a (eV)	μ(D)[a]	Q($\times 10^{-26}$ esu cm^2)[a]
$OF(^2\pi)$	$3.0^{+0.3}_{-0.8}$	13.1 ± 0.5	1.4 ± 0.5	−0.36	0.13
$SF(^2\pi)$	4.2 ± 0.2	10.0 ± 0.4	2.5 ± 0.5	−1.40	0.57
$SeF(^2\pi)$	4.0 ± 0.2	9.5 ± 0.4	≤2.8 ± 0.5	−2.21	−1.04
$NF(^3\Sigma^-)$	3.4 ± 0.2	13.2 ± 0.3	0.6 ± 0.3	−0.41	−0.75
$NF(^1\Sigma^+)$	3.5 ± 0.5[b]			0.08	−0.62
$NF(^1\Delta)$	1.8 ± 0.5[c]			−0.17	−0.68
$PF(^3\Sigma^-)$	4.5 ± 0.3	9.7 ± 0.2[d]	1.4 ± 0.3	−1.17	−0.90

[a]Values of μ and Q have also been computed for the positive and negative ion of each molecule.
[b]Excitation energy for the process $NF(^3\Sigma^-) \rightarrow NF(^1\Sigma^+)$.
[c]Excitation energy for the process $NF(^3\Sigma^-) \rightarrow NF(^1\Delta)$.
[d]Adiabatic ionization potential is 9.5 ± 0.2 eV.

yield an ionization potential almost 100% larger than that for the adjacent SiF and SF and imply, *inter alia*, that removal of an antibonding electron from PF results in a weakening of the bond. Our calculated ionization potential is much more plausible and is believed to be the most reliable value to date.

The desired bonding energy, D_0°(PF), is identical to that [75] deduced from a modified Birge-Sponer treatment of the spectroscopic data [76] (see Table III-13). In contrast with NF , the PF ion is predicted to be thermodynamically quite stable at moderate temperatures.

REFERENCES AND FOOTNOTES

1. A summary of this section is given on pp. 8 to 10.
2. J. E. Battles, W. A. Shinn, P. E. Blackburn, R. K. Edwards, in *Plutonium 1970: Proceedings of the Fourth International Conference on Plutonium and Other Actinides, Nuclear Metallurgy*, Vol. 17, Part II, pp. 733–742, The Metallurgical Society of AIME.
3. J. E. Battles, W. A. Shinn, P. E. Blackburn, R. K. Edwards, *High Temp. Sci. 2*, 80 (1970).
4. J. E. Battles, J. W. Reishus, W. A. Shinn, in "Argonne National Laboratory, Chemical Engineering Division Annual Report," ANL-7575, p. 77 (1968).
5. R. H. Rand, T. L. Markin, Atomic Energy Research Establishment Report AERE-R5560 (1967); the free energy values were derived from the data of R. J. Ackerman, P. W. Gillis, R. J. Thorn, *J. Chem. Phys. 25*, 1089 (1956), and J. Drowart, A. Pattoret, S. Smoes, *Proc. British Ceramic Soc.*, No. 8, 67 (1967).
6. E. A. Aitken, S. K. Evans, GEAP-5672 (1968).
7. R. K. Edwards, A. E. Martin, *Thermodynamics*, Vol. 2, pp. 423–429, Proc. Symp. Vienna, 1965, IAEA, Vienna (1966).
8. "Chemical Engineering Division Annual Report, 1968," ANL-7575, p. 85 (1969).
9. V. Benedict, C. Sani, "Studies on the Ternary System UO_2-U_3O_8-PuO_2," EUR 4136e (1970).
10. R. T. Pepper, J. R. Stubbles, C. R. Tottle, *Appl. Mater. Res. 3*, 203 (1964).
11. J. L. Henry *et al.*, U.S. Bureau of Mines Report 6968 (1963).
12. B. Ch. Steele *et al.*, *J. Nucl. Mater. 35*, 1 (1970).
13. R. F. Stoops, J. Hamme, *J. Amer. Ceram. Soc. 47*, 59 (1964).
14. J. Bazin, A. Accary, *Proc. Brit. Ceram. Soc. 8*, 175 (1967).
15. E. K. Storms, J. Huber, *Nucl. Materials 23*, 19 (1967).
16. E. K. Storms, *The Refractory Carbides*, Ch. XI, p. 205, Academic Press, New York (1967).
17. R. J. Ackerman, E. G. Rauh, *J. Phys. Chem. 73*, 769 (1969).
18. L. M. Leitnaker, J. Witteman, *J. Chem. Phys. 36*, 1445 (1962).
19. P. A. Vozzella, A. D. Miller, M. A. DeCrescente, *J. Chem. Phys. 49*, 876 (1968).
20. M. G. Bowman, M. C. Krupka, the "Fourth Uranium Carbide Conference," TID-7676, p. 128 (1963).
21. D. R. Fredrickson, R. D. Barnes, M. G. Chasanov, R. L. Nuttall, R. Kleb, W. N. Hubbard, *High Temp. Sci. 1*, 373 (1969).
22. D. R. Fredrickson, R. Kleb, R. L. Nuttall, W. N. Hubbard, *Rev. Sci. Instr. 40*, 1022 (1969).
23. L. Leibowitz, M. G. Chasanov, L. W. Mishler, *Trans. Met. Soc. AIME 245*, 981 (1969).
24. D. R. Fredrickson, M. G. Chasanov, *J. Chem. Thermodyn. 2*, 623 (1970).
25. D. R. Fredrickson, M. G. Chasanov, R. D. Barnes, S. G. Johnson, *High Temp. Sci. 2*, 259 (1970).
26. D. R. Fredrickson, R. D. Barnes, M. G. Chasanov, *High Temp. Sci. 2*, 299 (1970).
27. L. Leibowitz, L. W. Mishler, D. F. Fischer, "Chemical Engineering Division Annual Report, 1969," ANL-7675, p. 89 (1970).
28. R. A. Hein, P. N. Flagella, "Enthalpy Measurements of UO_2 and Tungsten to 3260°K," USAEC report GEMP-578 (1968).
29. M. Tetenbaum, P. D. Hunt, *J. Nucl. Mater. 34*, 86 (1970).
30. V. C. Hubbard, A. L. Loomis, *Phil. Mag. 5*, 1177 (1928).
31. Yu. S. Trelin, I. N. Vasil'ev, V. B. Proskurin, T. A. Tsyganova, *Teplofizika Vysokikh Temperatur 4*, 364 (1966); English translation: *High Temperature 4*, 352 (1966). Data previously reported by Trelin [Yu. S. Trelin, I. N. Vasil'ev, V. V. Roschchupkin, *Atomnaya Energiya 9*, 410 (1960); English translation: *Soviet Atomic Energy 9*, 955 (1960)] are in error by 2–2.5%.
32. T. E. Pochapsky, *Phys. Rev. 84*, 553 (1951).
33. J. P. Stone, C. T. Ewing, J. R. Spann, E. W. Steinkuller, D. D. Williams, R. R. Miller, *J. Chem. Eng. Data 11*, 320 (1966).
34. D. C. Ginnings, T. B. Douglas, A. F. Ball, *J. Res. Nat. Bur. Stand. 45*, 23 (1950).
35. M. H. Rand, T. L. Markin, in *Thermodynamics of Nuclear Materials*, IAEA, p. 637 (1968).
36. T. L. Markin, E. J. McIver, in *Plutonium 1965*, p. 845. A. E. Kay, M. B. Waldron (eds.), Chapman Hall, London (1967).
37. R. D. Cowan, *Proposed Method of Measuring Thermal Diffusivity at High Temperatures*, USAEC report LA-2460 (1960); also, *J. Appl. Phys. 32*, 1363 (1961).
38. J. B. Ainscough, M. J. Wheeler, *Brit. J. Appl. Phys.*

Ser. 2, *1*, 859 (1968); O. A. Kraev, A. A. Stel'makh, *High Temperature 1*(1), 5 (1963), M. Serizawa *et al., Proc. of Eighth Conf. on Thermal Conductivity (1968)*, Plenum Press, N.Y., p. 549 (1969); M. J. Wheeler, *Brit. J. Appl. Phys. 16*, 365 (1965).
39. G. K. Johnson, E. H. Van Deventer, O. L. Kruger, W. N. Hubbard, *J. Chem. Thermodyn. 2*, 617 (1970).
40. By J. A. Leary, Los Alamos Scientific Laboratory, Los Alamos, New Mexico.
41. J. E. Battles, W. A. Shinn, P. E. Blackburn, R. K. Edwards, *High Temp. Sci. 2*, 80 (1970).
42. E. J. Huber, C. E. Holley, Jr., *Thermodynamics of Nuclear Materials*, p. 581, IAEA, Vienna (1962).
43. R. Lapage, UKAEA, Aldermaston, Berkshire, England, private communication (1969).
44. J. P. Marcon, *J. Inorg. Nucl. Chem. 32*, 2581 (1970).
45. H. M. Feder, S. S. Wise, J. L. Margrave, W. N. Hubbard, *J. Phys. Chem. 67*, 1148 (1963).
46. D. D. Wagman, W. H. Evans, V. B. Parker, I. Halow, S. M. Bailey, R. H. Schumm, NBS Technical Note 270-3, U.S. Government Printing Office, Washington, D.C. (1968).
47. V. A. Medvedev *et al., Thermal Constants of Compounds*, Vol. 1, Academy of Sciences of the USSR, Moscow (1965).
48. J. L. Settle, E. Greenberg, W. N. Hubbard, *Rev. Sci. Instrum. 38*, 1805 (1967).
49. E. Greenberg, ANL-7675, p. 95 (1969).
50. E. Greenberg, H. M. Feder, W. N. Hubbard, presented at the First International Conference on Calorimetry and Thermodynamics, Warsaw, Poland, Aug. 31–Sept. 4, 1969.
51. ANL-7675, p. 95 (1969).
52. V. B. Parker, "Thermal Properties of Aqueous Uni-univalent Electrolytes," NSRDS-NBS 2, p. 19 (1965).
53. S. R. Gunn, *J. Phys. Chem. 71*, 1386 (1967).
54. ANL-7575, p. 120 (1969).
55. S. R. Gunn, *J. Phys. Chem. 71*, 1386 (1967).
56. V. B. Parker, "Thermal Properties of Aqueous Univalent Electrolytes," NSRDS-NBS 2, p. 55 (1965).
57. "The JANAF Thermochemical Tables," Dow Chemical Co., Midland, Mich.
58. C. Matignon, *Compt. rend. 124*, 1215 (1897).
59. De Forcrand, *Compt. rend. 120*, 1026 (1895).
60. P. A. G. O'Hare *et al., J. Chem. Thermodyn. 2*, 797 (1970).
61. L. Stein, P. Pluriem, "Noble-Gas Compounds," p. 144, The University of Chicago Press (1963).
62. C. C. Selph, thesis, Georgia Inst. of Tech. (1970).
63. B. Weinstock, E. E. Weaver, C. P. Knop, *Inorg. Chem. 5*, 2189 (1966).
64. By J. G. Malm of the Chemistry Division, ANL.
65. E. Rudzitis, E. H. Van Deventer, W. N. Hubbard, *J. Chem. Thermodyn. 2*, 221 (1970).
66. P. A. G. O'Hare, W. N. Hubbard, H. M. Feder, IUPAC Thermodynamk Symposium, Heidelberg, Germany, Sept. 1967, Paper No. II-5.
67. P. A. G. O'Hare, H. M. Feder, Amer. Chem. Soc. 152nd National Meeting, New York, N.Y., Sept. 1966, Abstracts of papers No. V-163.
68. P. A. G. O'Hare, A. C. Wahl, *J. Chem. Phys. 53*, 2469 (1970).
69. P. A. G. O'Hare, A. C. Wahl, *J. Chem. Phys. 53*, 2834 (1970).
70. Proceedings of the 3rd European Symposium on Fluorine Chemistry, Aix-en-Provence, France, Sept. 1970.
71. R. C. Sahni, *Trans. Faraday Soc. 63*, 801 (1967).
72. W. C. Price, T. R. Passmore, D. M. Roessler, *Discuss. Faraday Soc. 35*, 201 (1963).
73. (a) J. T. Hesson, V. H. Dibeler, *J. Chem. Phys. 32*, 1884 (1960).
(b) R. M. Reese, V. H. Dibeler, *J. Chem. Phys. 24*, 1175 (1956).
74. Y. Wada, Ph.D. thesis, Kansas State University (1965).
75. P. A. G. O'Hare, USAEC report ANL-7459 (1968).
76. A. E. Douglas, M. Frackowiak, *Can. J. Phys. 40*, 832 (1962).

IV. REACTOR AND ANALYTICAL CHEMISTRY [1]

(C. E. Crouthamel)

A. CHEMISTRY OF IRRADIATED FAST-REACTOR FUELS AND MATERIALS (C. E. Johnson)

The study of the chemical behavior of irradiated fast-reactor fuels has as its principal objective the collection of chemical data that will aid in the understanding of the complex chemical processes that take place in these fuels during irradiation. The current effort is directed toward the study of uranium-plutonium mixed-oxide fuels.

A method has been developed for determining the relative radial distribution of krypton in irradiated fuels. This method, which involves laser-beam sampling and subsequent beta-counting of ^{85}Kr, will provide useful information for the development of fuel-swelling models.

Studies of irradiated mixed-oxide fuel specimens by electron microprobe analysis has continued, with emphasis on uranium-plutonium redistribution, fission product distribution, and fuel-cladding interactions.

1. Fuel Analysis Techniques (C. E. Johnson, D. V. Steidl, C. G. Wach)

a. Determination of Fission-Product Krypton in Mixed-Oxide Fuels

Pressure from fission gases retained in ceramic fuels during irradiation may contribute to the swelling of fuel during irradiation. Generally, measurements of fission gases have been made only on the amount released from the fuel matrix during irradiation. This amount may vary from 30 to 80% of the total amount of gas calculated to be present, depending primarily on fuel density, power density, and thermal cycling. The distribution of the gas remaining in the fuel is thought to be a function of such parameters as temperature gradient and fuel porosity; that is, the central hotter regions would contain less gas per unit volume than the outer, cooler regions. However, because of greater porosity, small particle sizes, and cracking of the fuel in the cooler regions, gas may be released rapidly in local regions and, therefore, the data indicate wider scattering in gas concentration in the outer regions than in the inner regions.

Experimental data on the radial distribution of fission gases retained in irradiated fuels is needed in the development of fuel-swelling models. A method has therefore been developed for determining the relative distribution of ^{85}Kr in irradiated fuels as a function of radial position. The method utilizes laser-beam vaporization to release the krypton contained in a small sample of fuel. The experimental procedure is as follows: (1) the laser is focused on a selected area of the fuel sample held within a vacuum chamber, (2) the chamber is evacuated and inactive krypton carrier gas is added to prevent adsorption of ^{85}Kr on the walls of the system, (3) the laser is fired, and (4) the released ^{85}Kr and carrier gas are mixed and pumped cryogenically through a Millipore filter (to remove other fission-product activity) to a sample tube for subsequent beta counting. The craters produced by volatilization of the fuel samples are 60–80 μm in diameter. The volumes of the volatilized samples are determined from measurements of silicone rubber replicas of the specimen surface.

Preliminary experimental work was done on a cross section of a vibratorily compacted (vibrapacked) fuel of UO_2-20 wt % PuO_2. The sample, designated SOV-3, had an average density 83% of theoretical and had been irradiated to 3.7 at. % burnup at a maximum linear power rating of 21.4 kW/ft. Laser samples were taken from three regions of the fuel: (1) the inner and outer columnar-grain region (the innermost region of the fuel, which attained the highest temperature during irradiation), (2) the equiaxed-grain region (an intermediate temperature zone), and (3) the unrestructured region (the outermost, coolest region). The amount of ^{85}Kr in the columnar grains was greater than in the equiaxed region, and the largest amount was in the unrestructured region. The ^{85}Kr contents of various regions of SOV-3 are given in Table IV-1 in units of cpm/μm^3 of fuel. It should be emphasized that these values represent concentrations relative to each other and are not absolute values for the ^{85}Kr content.

Careful examination of the data indicated the importance of proper focusing of the laser beam on the sample surface. When the laser is properly focused, a crater is formed whose depth generally exceeds that of its radius; moreover, the crater walls appear smooth, thereby indicating that melting had taken place. (The latter feature is desirable because the melted material tends to restrict the gas evolution from material surrounding the crater.) When the laser beam is not properly focused, only the surface of the sample is heated and a significant amount of ^{85}Kr is released without any appreciable crater formation. This type of sampling results in an abnormally high ^{85}Kr

TABLE IV-1. Radial Distribution of ^{85}Kr in Irradiated UO_2-20 wt % PuO_2 Fuel (SOV-3)

Fuel Region	Distance from Fuel Center (mm)	^{85}Kr (10^3 cpm/μm^3)
Void edge[a]	1.10	-
Inner columnar grains	1.29	9.34
Middle columnar grains	1.95	17.2
Outer columnar grains	2.47	10.7
Equiaxed grains	2.76	5.40
Unrestructured region	3.02	38.2
Inner cladding wall	3.175	-

[a]Oxide fuels that have attained high burnups usually have a void space in the center of the fuel, which results from densification during irradiation.

content per unit volume of material vaporized and produces a distorted pattern of ^{85}Kr distribution. Therefore, a laser shot was considered successful only if the ratio of crater depth to crater radius was ≥0.8.

A more detailed examination was made of the radial distribution of ^{85}Kr in a specimen of pellet fuel of 95% theoretical density, irradiated to 6.5 at. % burnup at a maximum linear power rating of 16 kW/ft. This fuel sample (F2R) was obtained from the General Electric Laboratory at Vallecitos. The distribution of ^{85}Kr in F2R was determined in three separate experiments. Again, the crater replicas were examined carefully to eliminate from consideration the craters that did not fit the criteria described above. The data are given in Table IV-2 and also in Fig. IV-1, where cpm of $^{85}Kr/\mu m^3$ of fuel is plotted as a function of radial position.

The results from SOV-3 and F2R show major differences in the relative distribution of ^{85}Kr in the two types of fuel. However, the high-density pellet fuel sample (F2R) that was irradiated at lower maximum linear power is of greater interest because it is more representative of LMFBR prototype fuels than the low-density, vibrapacked SOV-3 fuel. The data from F2R show good reproducibility in the columnar-grain region. The greater variation in the data for the unrestructured region and equiaxed-grain region may reflect the heterogeneity of the gas distribution on a microscale or it may be a consequence of the more open fuel structure in this region, which would allow gas communication over larger fuel volumes. The high krypton concentration at the hot void edge suggests that pore migration toward the hotter end of the thermal gradient is occurring, with trapped bubbles of gas accumulating at the void edge. Pore migration at the cooler ends of the columnar grains does not appear to lower the gas concentration as effectively as in the mid-columnar grain region; moreover, substantial amounts of fission gas remain in the outer regions of the fuel.

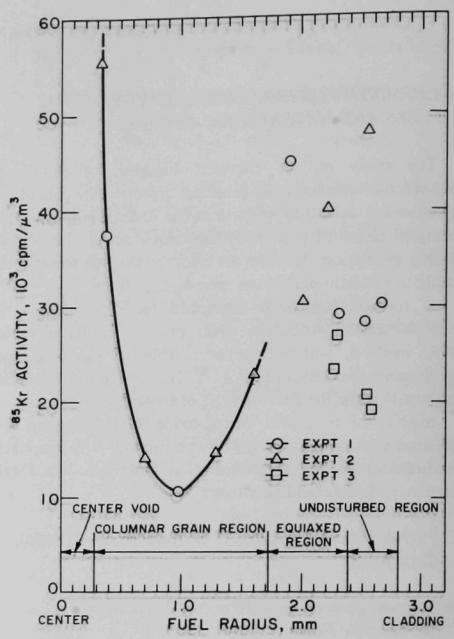

Fig. IV-1. Relative Radial Distribution of ^{85}Kr in Irradiated UO_2-20 wt % PuO_2 Fuel (F2R). ANL Neg. No. 308-2325 Rev. 2.

TABLE IV-2. Radial Distribution of ^{85}Kr in Irradiated UO_2-PuO_2 Fuel (F2R)

Fuel Region	Expt. No.	Distance from Fuel Center (mm)	^{85}Kr (10^3 cpm/μm^3)
Void edge	-	0.24	
Columnar grains	2	0.33	55.8
	1	0.39	37.6
	2	0.70	14.1
	1	0.98	10.6
	2	1.29	14.5
	2	1.61	22.8
Equiaxed grains	1	1.90	44.9
	2	2.01	30.2
	2	2.22	39.9
	3	2.26	23.2
	3	2.30	26.7
	1	2.31	28.9
Unrestructured region	1	2.52	28.2
	3	2.53	20.5
	2	2.55	48.6
	3	2.59	19.1
	1	2.66	30.1
Inner cladding wall	-	2.794	-

b. Application of Energy-Dispersion Devices to Electron Microprobe Analysis of Irradiated Fuels

In electron microprobe analysis, a focused electron beam is used to excite characteristic X-ray spectra, the intensity of the X-ray is a function of the elemental concentration. For analysis, the characteristic X-rays are identified by the use of crystal X-ray spectrometers. These spectrometers separate the X-ray emission according to wavelength, by diffraction from a crystal (wavelength dispersion). Detection and separation of X-ray spectra can also be achieved by the use of the energy-dispersion characteristics of certain solid-state materials, for example, lithium-drifted silicon crystals, in which the amplitude of the detector output signal is proportional to X-ray photon energy. Presently available detectors of this type have energy discrimination characteristics capable of distinguishing between photons with energy differences as small as 0.6 keV. This resolving power can be maintained even at high counting rates. The advantage of energy dispersion over wavelength dispersion is its ability to detect all lines in the emission spectrum simultaneously with great speed and high photon-counting efficiency.

A lithium-drifted silicon energy-dispersion detector has been installed on the electron microprobe. The output from the Si(Li) detector is fed into a multichannel analyzer, from which the resolved X-ray spectrum may be observed on an oscilloscope or in graphic form from a Calcomp plot of the tabulated data. Utilization of this device should provide increases in speed, resolution, and sensitivity in electron microprobe analysis. Counting times of 2 to 4 min are required to obtain adequate information for elemental identification in a sample. This may be compared with a time of about 1 hr to obtain the same information using wavelength-dispersion techniques. In certain cases—for example, the identification of palladium in a noble metal inclusion—overlapping lines of neighboring elements interfere with the palladium line. The Si(Li) detector offers the advantage of quickly shifting to an energy region where the spectrum of interest is sufficiently free from interference to allow ready identification.

To protect the detector from the large quantities of beta radiation accompanying each sample, a collimated lead shield covers the detector. Preliminary experiments have demonstrated the utility of this detector but have indicated the need for a thin (0.25–0.37 mm) beryllium filter to be permanently fixed in the entry port to remove low-energy electrons emitted from radioactive samples. When the detector is flooded with electrons, the crystal is essentially converted from a semiconductor to a conductor. Under such conditions the crystal loses its capabilities to act as an energy-dispersion device. Figure IV-2 shows the spectrum obtained for a 200-sec count of a metal inclusion in the fuel specimen SOV-1. The spectrum shows the presence of molybdenum, technetium, ruthenium, rhodium, uranium,

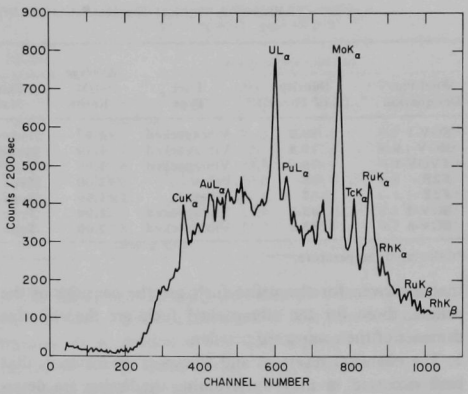

Fig. IV-2. Energy-Dispersion Spectrum of Metal Inclusion in Irradiated UO_2-20 wt % PuO_2 Fuel (SOV-1). ANL Neg. No. 308-2554.

plutonium, copper, and gold. The gold comes from the gold plating material covering the sample, and the copper comes from the mounting material. The uranium and plutonium are not part of the metal inclusion but were detected because of a larger-than-normal beam diameter, which overlapped the metal inclusion-fuel matrix boundary and excited the oxide phase. The presence of molybdenum, technetium, ruthenium, and rhodium in the inclusion was corroborated by wavelength-dispersion techniques.

2. Electron Microprobe Analysis of Irradiated Fuels
(C. E. Johnson, C. A. Seils, K. E. Anderson)

The electron probe microanalyzer, which accomplishes microsampling and microanalysis directly, is being used to study fuel-cladding interactions, distribution of fission products, and redistribution of fissile nuclides. The instruments used in these studies are Applied Research Laboratories EMX and EMX-SEM electron probe microanalyzers that are equipped with adequate shielding to handle fuel specimens having gamma activity as great as 1 R/hr at 1 ft.

During the past year, transverse cross sections from test fuel pins SOV-1, HOV-15, TVOV-1, F2R, and F2Z have been studied intensively. Table IV-3 summarizes the important data on the physical characteristics and irradiation conditions for these pins. Similar data are included in the table for two other fuel pins, SOV-3 and SOV-6, which were studied previously (see ANL-7575, p. 98, and ANL-7675, p. 102). All the fuels were fully enriched uranium oxide-plutonium oxide fuels with starting compositions of ~20 wt % plutonium oxide. The specimens F2R and F2Z were pellet fuels; the other specimens were vibrapacked fuels (i.e., the powdered fuel material was vibratorily compacted in the cladding). In Table IV-3, the densities

TABLE IV-3. Physical Characteristics and Irradiation Conditions of Mixed-Oxide Fuel Specimens

Fuel Pin Designation	Density (% of Theor.)	Fuel Type	Average O/M Ratio	Cladding Material	Burnup (at. %)	Max. Linear Power Rating (kW/ft)	Centerline Temp.[a] (°C)	Fuel Surface Temp.[a] (°C)	Cladding Temp.[a] (°C)
SOV-1	80.0	Vibrapacked	1.99	Type 304 SS	5.0	20.1			600
HOV-15	79.8	Vibrapacked	1.99	Hastelloy-X	3.5	21.4	2790	1060	550
TVOV-1	76.8	Vibrapacked	1.99	V-20% Ti	3.6	19.6			
F2R	95	Pellet	2.00	Type 347 SS	6.5	16.0	2600	870	550
F2Z	87	Pellet	1.99	Type 316 SS	4.7	13.0	2360	910	560
SOV-3	83.1	Vibrapacked	1.99	Type 304 SS	3.7	21.4	2500		550
SOV-6	83.5	Vibrapacked	2.00	Type 304 SS	2.7	17.0			

[a]Calculated temperature.

that are given for the pellet fuels are the densities of the pellets; those for the vibrapacked fuels are the effective densities of the compacted powder.

The chemical reactions and transport of materials that have occurred in these fuels during irradiation are determined, to a major extent, by the oxygen potentials and by the thermal gradients that are generated in each sample during irradiation. Data obtained by microprobe analysis on the distribution of many components in irradiated fuels have given major support to the hypothesis that vapor transport is the principal mechanism for movement of materials in the oxide fuel.

a. Fissile-Material Redistribution

Uranium and plutonium redistributions were determined for all fuel elements examined during the current period. These analyses were carried out on radial segments of each fuel, and the data are tabulated in Table IV-4 for the ratio $PuO_2/(PuO_2 + UO_2)$ as a function of radial distance. Uranium and plutonium redistribution varied considerably from sample to sample. TVOV-1 and HOV-15 showed the most extreme redistribution. In these specimens, the fuel material nearest the cladding was virtually free of plutonium, its general composition being largely a uranium oxide with small amounts of cladding-component oxides. About 0.2 mm from the cladding edge, within the unrestructured region, the plutonium concentration began to increase and reached a plateau that extended through the equiaxed-grain region and the cooler half of the long columnar-grain region. At this point, the ratio $PuO_2/(PuO_2 + UO_2)$ began to increase again and reached a maximum of about 0.40 at the central void edge. (Center melting occurred in these fuels and played a significant role in creating a large central void.) The most significant feature of these fuels is the presence of relatively pure uranium oxide in the cooler, peripheral areas, which indicates major vapor-phase transport of uranium oxide species. (Mass-spectrometric effusion studies have shown that UO_3 becomes the major vapor species even over the slightly hypostoichiometric UO_2-20 wt % PuO_2 fuel.)

Less extreme redistributions were found in the other fuels examined. In F2Z and SOV-6, the plutonium concentrations at the central void were about 7% higher than in the starting material and gradually decreased to a minimum in the central columnar-grain region. From this point to the outer edge, the plutonium concentrations were approximately those of the starting materials. The data for SOV-1 were quite similar except that the increase at the central void amounted to only 4%.

The variations in the plutonium concentration observed in the outer, cooler regions in SOV-1 and SOV-6 are indicative of the heterogeneity of these regions of the fuel. The temperatures over the columnar-grain and equiaxed-grain regions of the fuel are high enough for formation of UO_2-PuO_2 solid solution. However, little, if any, solid

TABLE IV-4. $PuO_2/(PuO_2 + UO_2)$ Ratio[a] for Irradiated Mixed-Oxide Fuels as a Function of Radial Position

Fuel Sample \ Radial Distance[b] (mm)	0.50	1.00	1.50	2.00	2.50	3.00									
SOV-1	← Void Edge →	0.244	0.212	0.187	0.170	0.143	0.132	0.168	0.190	0.020	0.425	0.192			
HOV-15	← Void Edge →	0.395	0.335	0.293	0.277	0.290	0.311	0.306	0.255	0.075	0.005				
TVOV-1	← Void Edge →	0.435	0.394	0.362	0.342	0.335	0.350	0.357	0.308	0.150	0.010				
F2R	← 0.248	0.242	0.239	0.238	0.237	0.237	0.237	0.238	0.239	0.240	0.241	0.242	0.244	0.245	
F2Z	← 0.227	0.202	0.178	0.169	0.167	0.171	0.174	0.175	0.174	0.182	0.183	0.172	0.180		
SOV-6	← Void Edge →	0.255	0.255	0.207	0.197	0.202	0.209	0.196	0.197	0.240	0.150	0.190			

[a]All $PuO_2/(PuO_2 + UO_2)$ ratios of as-fabricated fuel were reported to be 0.200. However, our analyses indicate that the ratio for F2R is about 0.245 and the ratio for F2Z is about 0.175.
[b]Fuel geometrical center is at 0.0 and fuel-cladding interface is at 3.17 mm.

solution occurs in the outer region of the fuel because of its lower temperature. Here, large discrete particles of UO_2 and PuO_2 can be found. Depending upon the sample volume examined, large variations in the plutonium concentration can occur in this region.

Of the fuels studied, F2R, a high-density pellet fuel, was unique in that very little redistribution occurred. The concentration of plutonium at the central void was only about 2% higher than the starting concentration, and the remainder of the fuel had a constant composition.

b. Microanalysis of Metallic Inclusion

A detailed examination has been made of metal inclusions found in the fuels HOV-15 and F2R. In each fuel, metal inclusions were examined along several different radial sectors. Each radial sector extended along a line roughly corresponding to a single columnar grain, from the void edge to the termination of the columnar grain and beyond to the cladding wall. The metal inclusions varied in size from 3 to 10 μm and were irregular in shape. All inclusions found in the columnar-grain region contained the noble metal fission products molybdenum, technetium, ruthenium, rhodium, and palladium, as well as iron, which is believed to have been transported into the fuel from the cladding. The metal inclusions varied in composition as a function of radial position but all were free of uranium and plutonium. In HOV-15, a group of inclusions found near the cladding contained a mixture of cladding and fission-product components: iron, molybdenum, palladium, nickel, copper, and cobalt. The data for radial sections of HOV-15 and F2R are given in Tables IV-5 and IV-6, respectively.

For HOV-15, the ratios of fission-product concentrations in the inclusions were compared with the ratios that would be expected on the basis of their fission yields. In the first seven inclusions listed in Table IV-5 (those from the fuel interior), the ratios of the three fission products Ru:Tc:Rh agree reasonably well with the calculated fission-yield ratios of 3.8:1.5:1.0; however, the observed concentrations of molybdenum are only one-half of those expected from the fission yields. The palladium content of inclusions in the high-temperature regions is also lower than expected. The high vapor pressure of palladium, along with the greatly increased concentrations observed in the three outermost inclusions, suggest that palladium is transported to the outer, cooler regions by vaporization. In the outer regions, the formation of iron-palladium alloys lowers the vapor pressures of both palladium and iron. It is seen from Table IV-5 that the three inclusions nearest the cladding contain appreciable amounts of both iron and palladium. These three inclusions were relatively large and, on a mass basis, it appears that a large percentage of the fission-product palladium has been transported to the outer regions of the fuel.

The three inclusions nearest the cladding also contained large concentrations of cladding constituents. The cladding material, Hastelloy X, has a nominal composition of 47% Ni, 9% Mo, 22% Cr, 18% Fe, and small amounts of cobalt, copper, and tungsten. The cladding components were homogeneously distributed throughout each inclusion, iron and nickel being the major constituents. The transport of iron from stainless steel to the oxide fuel by a

TABLE IV-6. Metal Inclusions in Irradiated UO_2-20 wt % PuO_2 Fuel (F2R)

Radial Distance (mm)	Concentration (wt %)					
	Mo	Tc	Ru	Rh	Pd	Fe
0.30	Void Edge					
0.38	55.4	12.7	21.5	5.0	5.0	0.5
0.84	51.3	8.6	23.0	7.3	9.2	0.6
1.16	47.9	12.6	29.4	9.9	0.1	0.2
1.45	48.0	14.2	29.0	8.2	0.4	0.2
1.69	43.2	15.9	31.5	9.1	0.1	0.1
1.91	30.5	19.5	39.0	11.0	0.1	0.1
2.21	45.5	14.8	31.3	8.1	0.1	0.1
3.17	Cladding Edge					

TABLE IV-5. Metal Inclusions in Irradiated UO_2-20 wt % PuO_2 Fuel (HOV-15)

Radial Distance (mm)	Concentration (wt %)								
	Fe	Mo	Tc	Ru	Rh	Pd	Ni	Co	Cu
1.19	Void Edge								
1.26	0.13	26.9	16.8	45.0	8.4	2.7	<0.01[a]	<0.01[a]	<0.01[a]
1.39	0.15	22.4	14.6	51.1	9.1	2.7	<0.01[a]	<0.01[a]	<0.01[a]
1.73	0.36	31.3	11.7	41.9	12.0	2.9	<0.01[a]	<0.01[a]	<0.01[a]
1.94	0.46	28.2	11.9	41.0	15.7	2.8	<0.01[a]	<0.01[a]	<0.01[a]
2.06	0.46	31.1	13.2	41.7	10.8	2.8	<0.01[a]	<0.01[a]	<0.01[a]
2.24	0.27	30.3	12.4	40.9	12.6	3.5	<0.01[a]	<0.01[a]	<0.01[a]
2.35	0.32	32.5	13.2	38.0	11.3	4.7	<0.01[a]	<0.01[a]	<0.01[a]
2.48	0.33	37.8	13.4	30.5	10.9	7.0	<0.01[a]	<0.01[a]	<0.01[a]
2.71	0.13	25.5	48.9	11.7	10.8	2.9	<0.01[a]	<0.01[a]	<0.01[a]
2.76	13.1	51.3	19.7	1.7	10.9	1.7	1.5	<0.01[a]	<0.01[a]
2.85	39.0	9.8	<0.04[a]	<0.04[a]	<0.04[a]	23.8	20.2	0.7	6.4
2.87	37.1	10.8	<0.04[a]	<0.04[a]	<0.04[a]	20.6	23.0	1.2	7.2
2.91	37.7	8.0	<0.04[a]	<0.04[a]	<0.04[a]	21.2	23.8	1.3	8.0
3.17	Cladding Edge								

[a]Minimum detection limits.

van Arkel-de Boer type of process has been previously discussed (ANL-7675, p. 104). This type of transport process, however, would not account for the large amounts of nickel found in the inclusions described above. Analysis of several inclusions in HOV-15 in the region near the cladding has shown evidence of the presence of chlorine. Chlorine in the fuel during irradiation could cause significant vapor-phase transport of cladding constituents, particularly nickel.

For the pellet fuel, F2R, the ratios of the concentrations of the three fission products Ru:Tc:Rh again show good agreement with ratios calculated from fission-yield data. However, we see a significant difference, as compared with HOV-15, in the distribution of iron and the metallic fission-product components that have appreciable vapor pressures, i.e., palladium and molybdenum. In the cooler regions of the high-density fuel, the concentrations of these components are smaller, and in the interior fuel regions, the concentrations are larger.

In F2R, the distribution of palladium, iron, and molybdenum throughout the columnar-grain region is expected to be governed by transport of elemental vapor species, since all three have significant elemental vapor pressures and would not be oxidized in the higher temperature regions. The metallic inclusions nearest the void edge show a sharp increase in molybdenum, palladium, and iron contents. This finding is somewhat unexpected; however, similar increases in concentration near the void edge have been observed for ^{85}Kr and cesium. This distribution is believed to be characteristic of gaseous components. Pore sweeping is known to occur in this region of the fuel and the thermal gradient diminishes at the void edge. Thus, this region is a potential location for the pile-up of gas-filled pores sweeping toward the void edge. Also, with cracks in the fuel providing a communication line to the central void, palladium, molybdenum, and iron vapor species trapped in the central void cavity may, upon slow cooling of the fuel, diffuse back into the fuel and condense as alloy inclusions near the void edge. The relatively small total amounts of molybdenum, iron, and palladium in the metal inclusions near the void edge indicate that the transport of vapor back into the fuel has not been extensive.

c. Microanalysis of Fuel-Cladding Reaction Zones

The fuels examined have shown varied fuel-cladding reactions, surface erosion, and grain-boundary attack. Depending upon specific fuel parameters and the type of cladding used, varying depths of attack have been noted in all fuels. It has been established with out-of-pile studies [2–4] on stainless steels that oxygen-containing cesium species such as Cs_2O and CsOH caused significant intergranular attack. Cesium metal or CsI did not appear to initiate any attack in the temperature region of interest (500–600°C). The three conditions necessary for intergranular attack are temperatures above 500°C, the presence of alkali metal, and oxygen potentials near stoichiometric fuel compositions. The rate of attack of the cladding is believed to rise with temperature and oxygen potential.

Detailed examination of fuel sample SOV-1 showed the most extreme intergranular attack of the cladding thus far observed, with general penetration up to 50% of the stainless steel cladding. Large quantities of cesium were found distributed in intergranular areas of the cladding. Studies of HOV-15 showed minimal attack of the Hasteloy-X cladding; however, cesium was found in all areas examined. Examination of TVOV-1 indicated that cesium had penetrated the V-20% Ti cladding to a depth of ~15%. This zone of attack also showed a depletion of titanium and migration of titanium back into the fuel. The band of cesium in TVOV-1, which was also associated with iodine, extended circumferentially around the fuel. Specimens F2R and F2Z did not show any intergranular attack of the stainless steel cladding; however, iron was transported from the inner cladding surface into the fuel and found alloyed (e.g., with a mixture of noble metal fission products or with palladium only) in metallic inclusions in the body of the fuel.

The X-ray scanning images of a reaction zone in SOV-1 are shown in Fig. IV-3. In Fig. IV-3a, it is seen that cesium completely fills the reaction zone and is also deposited along the fuel-cladding interface. Further, the iodine X-ray image (Fig. IV-3g) shows that only a small amount of the total cesium is associated with iodine. The major part of the cesium is associated with molybdenum (Fig. IV-3c), presumably as an oxide phase, deposited in the same zone. This is not to suggest that molybdenum participated in the fuel-cladding reaction, but that both cesium and molybdenum vapor species may transport oxygen to the reaction zone.

d. Microanalysis of Fuel Matrix

Studies have been made of the radial distribution of cesium and molybdenum in the mixed-oxide matrix of both pellet and vibrapack fuels. These data aid considerably in understanding the influence of these elements on fuel-cladding reactions, fuel-element swelling and fuel lifetimes. Analyses were made by scanning the electron beam and integrating the X-ray intensity over contiguous areas (80 by 80 μm) of the oxide matrix across the radius of each fuel. The fuels F2R, F2Z, and SOV-1 were analyzed for cesium, and these data are presented in Fig. IV-4, where cesium X-ray intensity is plotted against radial distance. Similar data were obtained for molybdenum in F2R and SOV-1 and these are presented in Fig. IV-5.

For each sample, the cesium concentration in the matrix increases sharply in regions near the cladding. The peak in the data for F2R at ~0.87 fractional radius coincides with a circumferential crack found in this particular sample.

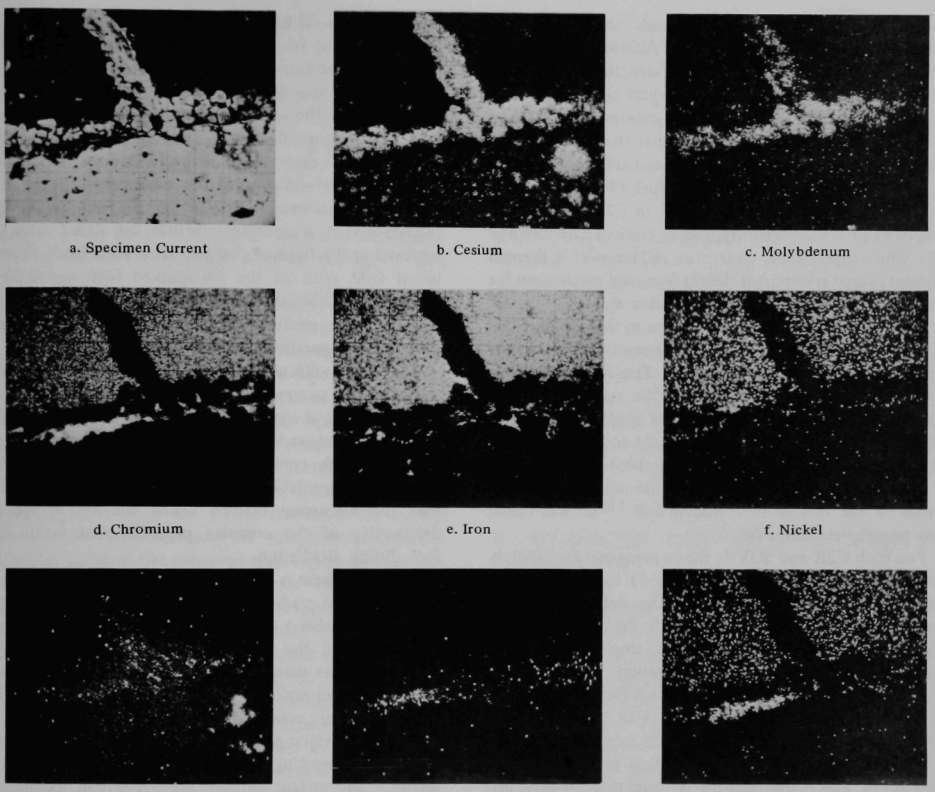

a. Specimen Current

b. Cesium

c. Molybdenum

d. Chromium

e. Iron

f. Nickel

g. Iodine

h. Tellurium

i. Manganese

Fig. IV-3. Electron Microprobe Scanning Images of Fuel-Cladding Reaction Zone in SOV-1 (all images are 160 by 200 μm). ANL Neg. No. 308-2304.

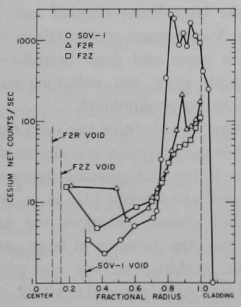

Fig. IV-4. Radial Distribution of Cesium in the Oxide Matrix of Irradiated UO_2-PuO_2 Fuels. ANL Neg. No. 308-2555.

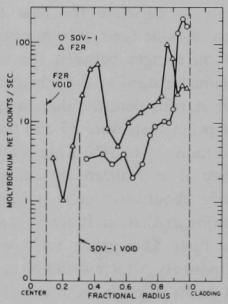

Fig. IV-5. Radial Distribution of Molybdenum in the Oxide Matrix of Irradiated UO_2-PuO_2 Fuels. ANL Neg. No. 308-2429.

Thorough examination of this crack showed that it contained large quantities of cesium. Although the data for F2Z do not show a maximum in this area, there is a plateau followed by a sharp increase in cesium concentration in locations nearer the cladding. X-ray scanning images taken of each location analyzed showed that the cesium is not uniformly distributed within the defined area but is located in the cracks and voids within the fuel. (This feature was also observed near the central void in F2R, where large quantities of cesium were trapped in cracks.) The distribution data suggest that, under the influence of a thermal gradient, vapor transport is the predominant mechanism for migration of cesium to the inner cladding wall.

Data on the distribution of cesium in the oxide matrix of F2R have also been obtained by a combination of laser sampling and gamma spectrometry. The most significant finding was that both ^{137}Cs and ^{134}Cs exhibit maximum concentrations about 1 mm from the cladding edge. This behavior for F2R is in marked contrast to that previously observed in SOV-6 (see ANL-7675, p. 106). In SOV-6, the ^{137}Cs concentration increased continuously from the center of the fuel to the cladding and ^{134}Cs was found only near the cladding edge.

For both F2R and SOV-1, the concentration of molybdenum in the oxide matrix (Fig. IV-5) increases sharply near the cladding. The peak in the data for F2R at 0.86 fractional radius coincides with the circumferential crack found in this sample and also duplicates a similar peak found in the cesium concentration. Attempts were made to exclude all metallic inclusions from analysis, but this was virtually impossible for F2R. The peak at 0.4 fractional radius is due to the large number of metallic inclusions found at this radial position in the fuel cross section. In SOV-1 the inclusions were more widely dispersed and, in general, could be excluded from analysis.

e. Discussion

In attempting to correlate the data that have been collected on mixed-oxide fuels, it is important to recognize two significant differences between the vibrapacked and pellet fuels. Characteristically, the vibrapacked fuels have somewhat lower starting densities than the pellet fuels. The densities of the pellet fuels were 87 and 95% and those of the vibrapacked fuels, 77 to 84%. This difference is of great importance when it is realized that changes in starting density will bring about changes in porosity and thermal conductivity during irradiation. Porosity is a measure of the openness in a fuel. The pellet fuels would have low interconnected porosity, which would be expected to block vapor-transport paths through the fuel and thereby reduce the potential for vapor phase redistribution by this mechanism. The vibrapacked fuels, on the other hand, would have high interconnected porosity, which can impose a low thermal conductivity, i.e., large thermal gradients can be set up in the fuel. Thus, in the fuels of low starting density, conditions exist for having an open structure that would allow vapor transport under large thermal gradients.

A second important difference between vibrapacked and pellet fuels is the specification of initial oxygen-to-metal (O/M) ratio upon fabrication. The initial O/M ratio sets the chemistry that takes place in the fuels during irradiation. The stated O/M ratio of all the vibrapacked fuels studied was ~1.98. However, because of the method of fuel preparation, it is doubtful whether the stated ratio was achieved in the finished fuel pins. It is more likely that the initial O/M ratio of the vibrapacked fuels was 2.00 or greater. The O/M ratio of the pellet fuels (1.99 and 2.00) can be more easily controlled during preparation and therefore the specified O/M ratio can be met.

The data collected thus far have been interpreted in terms of the parameters discussed above—interconnected porosity, thermal conductivity, and O/M ratio—and particularly their relation to vapor transport of materials in the fuel. Although complete information on these parameters is not available for the fuels studied, we believe that the discussion offered below will aid in the understanding of the complex processes that occur in a fuel during irradiation.

Although there is pore migration toward the hotter end of the thermal gradient during irradiation, it is very likely that there is also a counter flow of uranium-oxide vapor species toward the cooler end of the thermal gradient. These processes then result in transport of uranium from the central void region to the cooler unrestructured region leaving the inner zone enriched in plutonium. This is not to suggest that vapor-phase transport is the only transport mechanism operating during the life of the fuel: solid-state diffusion and surface diffusion are certainly in operation to some degree in the fuel interior. In the cooler temperature regions, vapor transport is believed to predominate; however, even in the higher-density, hotter regions of the fuel interior solid-state diffusion appears to be inadequate to account for the large heavy-element and fission-product redistributions. Vapor-phase condensation across the thermal gradient in pores and grain boundaries and surface diffusion in both pore and columnar-grain boundaries would be expected to predominate.

It is important to recognize the roles that cesium (and possibly molybdenum) species and the oxidizing potential of the fuel play in the intergranular attack of the cladding. It has been well established [3] in a thermal-gradient experiment, that cesium enhances the rate of oxygen transport. Further, the presence of large concentrations of oxygen at the cladding surface can promote internal oxidation and lead to intergranular attack of the cladding. During irradiation of hypostoichiometric fuel, the oxygen potential at the cladding wall is believed to approach stoichiometry (O/M = 2.00) with decreasing oxygen potential occurring in the hot fuel interior.

In the fuel samples examined, the extent of intergranular attack appears to be most strongly influenced by the starting densities of the fuels. Because of their more open structure (low starting density), vibrapacked fuels have exhibited severe intergranular cladding attack by cesium oxide as well as transport of cladding components back into the hot fuel matrix by metal-halogen vapor species. This is in contrast with the behavior in pellet fuels, in which intergranular attack has not been observed and vapor transport across the unrestructured region has been significantly reduced for both fission products and the cladding components.

Molybdenum has been found in a variety of states in the fuel specimens studied. Metallic molybdenum has been found alloyed with the noble metal fission products in the columnar-grain region. It has also been found alloyed with iron and other cladding components and with palladium in the equiaxed-grain and unrestructured regions. These regions also contain molybdenum in an essentially pure state (>95%). Moreover, if the oxidizing potential of the fuel is high enough, molybdenum is dissolved in the oxide matrix. In hyperstoichiometric fuel a large fraction of the molybdenum forms solid solutions of molybdenum-uranium-plutonium oxide in the columnar-grain region. In hypostoichiometric fuel, under the influence of the thermal gradient, molybdenum oxide inclusions appear in the outer, cooler regions as the oxidizing potential in this region is increased by burnup. The unique behavior of molybdenum is an important aid in interpreting the local oxidizing potentials that exist in the fuel during irradiation.

To assess the contributions that various molybdenum species might make to the transport of molybdenum throughout the fuel, the vapor pressures of these species were calculated using (1) oxygen-activity data for a fuel of 5 at. % burnup, derived from a model by Rand and Markin, and (2) data on the free energy of formation of the various molybdenum species [5]. The following reaction was considered:

$$Mo(s) + xO_2(g) \rightleftharpoons MoO_{2x}(g)$$

The calculations of vapor pressure were made at 3000 and 2300°K, the respective temperatures estimated for the hot and cold ends of the columnar-grain region. These data, given in Table IV-7, indicate that MoO_2 has the greatest vapor pressure at both temperatures, thus indicating the potential for vapor-phase transport of MoO_2 in the fuel.

The distribution of molybdenum in the oxide matrix (see Fig. IV-5) suggests a vapor-phase transport of molybdenum to the cladding. As stated previously, the sharp peak at 0.83 fractional radius for F2R coincides with a circumferential crack found at this location. The blocking of vapor transport through the unrestructured zone to the cladding is probably caused by the lesser interconnected porosity of this higher-density pellet fuel. The molybdenum distribution for the lower-density SOV-1 fuel is suggestive of increased interconnected porosity, which would account for molybdenum being found in large concentrations near the cladding wall.

TABLE IV-7. Vapor Pressure of Molybdenum Species

Molybdenum Species	Vapor Pressure (atm) at Indicated Temperature	
	3000°K	2300°K
Mo	1.00×10^{-4}	4.68×10^{-8}
MoO	2.25×10^{-5}	1.05×10^{-9}
MoO_2	2.28×10^{-4}	3.78×10^{-7}
MoO_3	6.41×10^{-6}	1.93×10^{-8}

The large increases in molybdenum concentration in the peripheral areas of the fuel may also indicate a corresponding change in the oxidizing potential in these fuels, which may reflect the nonequilibrium state that exists between the fuel center and the peripheral regions of the fuel. This nonequilibrium state would result from vapor transport that occurred predominantly toward the cooler end of the thermal gradient.

B. FAST-REACTOR CROSS-SECTION MEASUREMENTS

(N. D. Dudey)

An understanding of fast-neutron processes is essential to the design and development of fast breeder reactors. The objectives of the cross-sections program are (1) to provide data for defining the breeding characteristics of a fast reactor and for characterizing the irradiation environment of a fast reactor, (2) to measure spectrum-averaged cross sections and fast-neutron fission yields in various fast-reactor neutron spectra, and (3) to apply these data to problems of interest to the overall fast breeder reactor program. The emphasis of this program has historically involved measurements of cross sections and reaction rates in the EBR-II reactor. The more recent trend has been to carry out cooperative experiments with both the EBR-II Project and the Materials Science Division so that our expertise in foil-activation rate measurements, cross sections, and general nuclear chemistry may be combined with their expertise in irradiation-damage effects and reactor physics in an attempt to consider more multidisciplinary problems.

The work of the group during the past year has included the following: (1) measurements of capture-to-fission ratios (alpha) of the principal heavy elements that constitute both present and future fast reactor fuels, (2) some studies of helium production in EBR-II irradiated stainless steels and the possible relationship of helium production to irradiation damage effects, (3) a comprehensive program to measure the fast-neutron fission yields of tritium and other low-mass fission products, and (4) fast-neutron spectral characterization studies, with particular emphasis on the foil-activation studies conducted in the ZPR-3 mockup studies of EBR-II.

1. Spectrum-Averaged Measurements (N. D. Dudey, R. R. Heinrich, J. Williams)

a. Capture-to-Fission Ratios in EBR-II

The economics of a breeder reactor is largely dependent upon the reactor's capability for breeding, i.e., producing more fissile fuel than it consumes. For this reason it is very important to determine the breeding capability of a fast reactor. One measure of the breeding capability is the breeding potential, defined as the maximum number of neutrons available for breeding. This quantity can be calculated as follows:

$$B = \frac{(\nu - 1 - \alpha)}{(1 + \alpha)}$$

where ν is the number of neutrons emitted per fission event in the primary fuel and α is the ratio of the number of captures to the number of fissions taking place in the fuel. Each of these quantities is spectrum dependent, that is, each varies with neutron energy spectrum, hence with position in the reactor. Since $\nu(E)$ is a function that varies relatively slowly with neutron energy, the breeding potential is largely determined by the variation of α with neutron energy, i.e., with position within the reactor. Our program has involved measuring α for ^{233}U at 9 locations throughout EBR-II, ^{235}U at 11 locations, ^{238}U at 5 locations, ^{239}Pu at 15 locations, ^{240}Pu at 10 locations, and ^{242}Pu at 14 locations.

The measurements were performed by irradiating these 64 samples in EBR-II for periods of 0.5 to 1.6 yr. The number of fissions occurring in each sample was measured by radiochemically separating the fission product ^{137}Cs, assaying the activity by counting on Ge(Li) detectors relative to an absolute standard of ^{137}Cs, and computing the number of fissions from the measured number of ^{137}Cs atoms in the sample and the known fission yields of ^{137}Cs for each isotope. The number of captures was measured in the ^{233}U, ^{235}U, ^{239}Pu, and ^{240}Pu samples by radiochemically separating the uranium or plutonium from stainless steel encapsulation material and fission products, and determining the number of atoms of capture products by mass-spectrometric isotope-dilution techniques [6]. For ^{233}U, ^{235}U, ^{239}Pu, and ^{240}Pu, the number of atoms of the respective capture products, ^{234}U (2.5×10^5y), ^{236}U (2.4×10^7y), ^{240}Pu (6.8×10^3y) and ^{241}Pu (13y), could be determined directly because their half-lives are suitably long. However, for ^{238}U and ^{242}Pu, whose capture products have shorter half-lives, the number of captures was determined by measurement of a daughter of the capture product.

For ^{238}U, the following reactions are involved:

$$^{238}\mathrm{U} \xrightarrow{n} {}^{239}\mathrm{U(24m)} \xrightarrow{\beta} {}^{239}\mathrm{Np(2.4d)} \xrightarrow{\beta} {}^{239}\mathrm{Pu(2.4y)}$$

The number of captures in these samples was determined by radiochemically separating plutonium and determining the number of atoms of ^{239}Pu by high-resolution alpha counting.

For ^{242}Pu, the following reactions are involved:

$$^{242}\mathrm{Pu} \xrightarrow{n} {}^{243}\mathrm{Pu(5h)} \xrightarrow{\beta} {}^{243}\mathrm{Am(7.7y)} \xrightarrow{\alpha} {}^{239}\mathrm{Np(2.4d)}$$

The number of captures in the ^{242}Pu samples was determined by first radiochemically separating the americium and then determining the number of atoms of ^{243}Am. This was accomplished by allowing the ^{243}Am to reach equilibrium with its decay product ^{239}Np, separating the ^{239}Np, and counting the ^{239}Np on Ge(Li) detectors relative to an absolute standard of ^{243}Am-^{239}Np.

The results of these measurements are shown in Figs. IV-6 to IV-9. In these figures, the measured values of alpha are plotted against the axial or radial distance of the samples from the center of the core of EBR-II. Error estimates for the experimental measurements have been made on the basis of a propagation-of-error analysis. In general, the relative errors are about 2–3% except for the ^{242}Pu values. The results for ^{242}Pu shown in Figs. IV-4 and IV-5 have not yet been corrected for fissions resulting from ^{239}Pu and ^{241}Pu impurities in the samples; consequently, no error estimates have been made. The error estimates of 2–3% do not include any uncertainties in the assumed fission yield of ^{137}Cs, which is probably of the order of 5–15%. Table IV-8 summarizes the breeding potential, $(\nu - 1 - \alpha)/(1 + \alpha)$, for the fissile nuclides ^{233}U, ^{235}U, ^{239}Pu, and ^{240}Pu.

b. Helium Production in EBR-II Irradiated Stainless Steel

In cooperation with the Materials Science Division, a study was made of helium generation in sections of the control and safety-rod thimbles in EBR-II, and the results of the study have been published [7]. The helium concentrations were measured at selected sampling positions and, on the basis of cross-section data and dosimetry measurements on the samples, the helium concentrations were calculated. This study indicated that helium generation rates in stainless steels can be calculated for EBR-II irradiations with an accuracy of about 25–30%. The most significant finding in this study was the observation of helium and nitrogen concentration gradients along the thimbles; these concentration gradients were very strongly correlated with the temperature of the thimble during irradiation. This phenomenon is thought to result from transport of nitrogen by the sodium coolant from the cooler to the hotter regions of the reactor; in the hotter regions, the nitrogen diffuses into stainless steel, where it can undergo (n,α) reactions to produce helium. Because helium acts to stabilize voids in stainless steels irradiated at

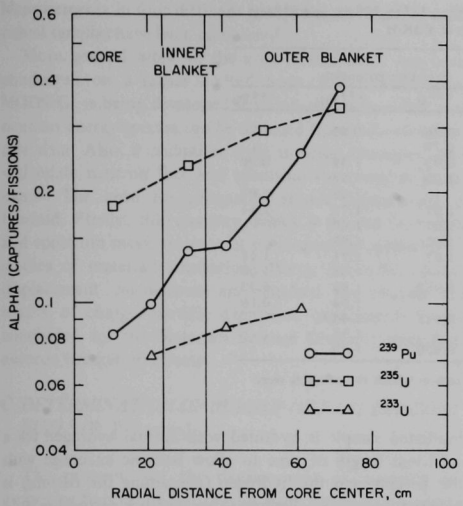

Fig. IV-6. Capture-to-Fission Ratios for ^{239}Pu, ^{235}U, and ^{233}U as Functions of Radial Position in EBR-II. ANL Neg. No. 308-2418.

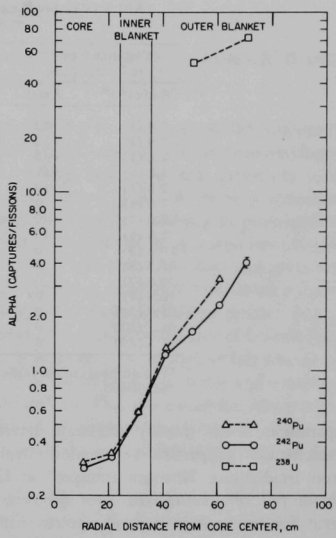

Fig. IV-8. Capture-to-Fission Ratios for ^{240}Pu, ^{242}Pu, and ^{238}U as Functions of Radial Position in EBR-II. ANL Neg. No. 308-2416.

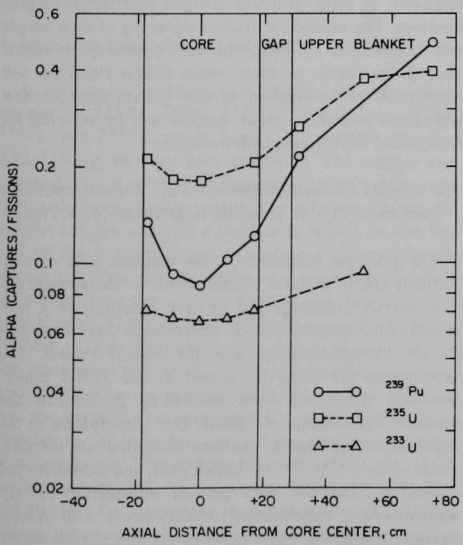

Fig. IV-7. Capture-to-Fission Ratios for ^{239}Pu, ^{235}U, and ^{233}U as Functions of Axial Position in EBR-II. ANL Neg. No. 308-2417.

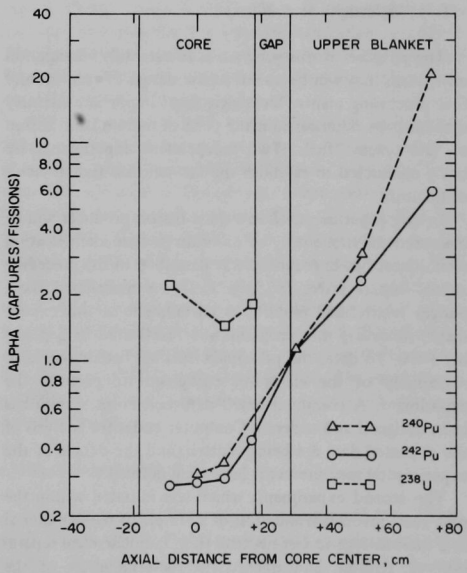

Fig. IV-9. Capture-to-Fission Ratios for ^{240}Pu, ^{242}Pu, and ^{238}U as Functions of Axial Position in EBR-II. ANL Neg. No. 308-2415.

TABLE IV-8. Breeding Potential for ^{233}U, ^{235}U, ^{239}Pu, and ^{240}Pu at Various Positions in EBR-II

Distance from Core Center (cm)		Breeding Potential			
Radial[a]	Axial	^{233}U	^{235}U	^{239}Pu	^{240}Pu
2.8 (1)	+73	-	0.76	0.96	-
2.8 (1)	+52	1.29	0.79	-	-
2.8 (1)	+30	-	0.93	1.39	0.30
2.8 (1)	+17	1.33	1.03	1.58	-
2.8 (1)	+9	1.34	-	1.65	1.05
2.8 (1)	0	1.35	1.07	1.72	1.11
2.8 (1)	−9	1.34	1.07	1.69	-
2.8 (1)	−17	1.33	1.02	1.57	-
10.2 (3)	0	-	1.07	1.71	1.11
21.3 (5)	0	1.33	-	1.65	1.04
30.6 (7)	0	-	0.989	1.55	0.73
40.8 (9)	0	1.30	-	1.54	0.18
51.0 (11)	0	-	0.895	1.44	-
61.2 (13)	0	1.28	-	1.31	-
71.5 (15)	0	-	0.830	1.09	-

[a]The numbers in parentheses indicate the row in which the samples were irradiated.

high temperatures, it can thereby accelerate deterioration of the mechanical properties of stainless steel under fast-neutron irradiations. Nitrogen transport in LMFBRs has the potential of creating the same problem in fast reactors that boron creates in thermal reactors, namely, an accelerated loss of ductility of steels under neutron irradiation.

2. Low-Mass Fast-Neutron Fission Yields (N. D. Dudey, R. L. Malewicki, M. J. Fluss)

The purpose of this program is to establish information on tritium that will be useful in the design of reactors and fuel processing plants. The single most important quantity that must be determined is the yield of tritium from fission of fast reactor fuels. Two independent experiments are being conducted to establish the fast-neutron fission yields of tritium.

In one experiment, all low-mass fission products will be measured simultaneously by on-beam particle identification techniques; this experiment was described in the preceding annual report (ANL-7675, p. 119). As mentioned then, budget restrictions required a curtailment of this experiment; however, this program was reactivated in September 1970. To date, the principal effort has been directed to reassembly of the electronic equipment to perform the experiment. A computer-based data collection system has been designed and ordered. Computer codes for analysis of the expected data are being written, and the details of the experimental measurements have been defined.

The second experiment, which was initiated within the past year, involves irradiation of a sample of fissile material in a monoenergetic fast-neutron flux, radiochemical separation of tritium, and quantitative determination of the tritium by means of low-level gas proportional counting. The equipment for the radiochemical separation has been assembled and checked out. In the separation scheme, the irradiated sample is hydrided with natural hydrogen for a sufficient length of time to allow isotopic exchange with the tritium, and the hydrogen (containing the tritium) is pumped through a palladium valve, which is permeable only to hydrogen isotopes, to effect separation from other sample constituents. At present the entire technique for the yield determination is being verified by performing tritium-yield measurements on thermal-neutron-irradiated ^{235}U, for which tritium yields have been reported in the literature. Samples of ^{239}Pu, ^{233}U, and ^{235}U were irradiated at three different energies with monoenergetic neutrons. The number of fissions occurring in each sample was determined by nondestructive gamma-spectrometric analysis for fission products whose fission yields are well known. After verification of the tritium radiochemical separation procedure, these samples will be analyzed for tritium and the tritium yields determined.

3. Dosimetry Characterization of a Fast-Neutron Irradiation Environment (R. R. Heinrich, N. D. Dudey, R. J. Popek)

The principal objective of this program is to develop methods and to perform measurements to characterize the flux intensity, fluence, and neutron spectrum of a fast-reactor environment. Several experiments have been performed in collaboration with the EBR-II Project. The experiments are being conducted in the ZPR-3 critical assembly, which has been mocked-up to simulate the irradiation conditions of EBR-II. Our participation in the experiments has been to perform activation-rate measurements using ^{235}U, ^{238}U, nickel, gold, and aluminum foil dosimeters. The foil data provide information for the comparison of experimental measurements with reactor physics calculations. These experiments thus provide dosimetry data that can be directly related to EBR-II measurements, and they also enable an evaluation and definition of the accuracy of the theoretical calculations to be made.

Measurements in four different assemblies on over 500 individual samples have been completed.

More general work in the area of dosimetry has been conducted on a rather limited basis. A computer code, MODSIG, is being developed with which neutron flux and neutron energy spectra can be deduced from foil-activation-rate data. Also, a computer code is being developed that will relate neutron flux and spectrum to atomic displacements. The need for computing atomic displacement is twofold. Firstly, this quantity, which is derived from flux and spectrum measurements, is more directly applicable to studies of materials irradiation effects. Secondly, atomic displacement calculations are required for relating the results of charged-particle simulation experiments (being conducted by the Materials Science Division) with fast-neutron irradiation effects.

C. DETERMINATION OF BURNUP OF FAST REACTOR FUELS (R. P. Larsen)

The program for the development of methods for measuring burnup of fast reactor fuels has as its objectives the establishment of accurate values for the fast fission yields of burnup monitors and the development of accurate analytical methods for determining the concentrations of these monitors in irradiated nuclear fuels. Recent work has been directed primarily toward the measurement of fast fission yields and the evaluation of changes in fission yields with neutron energy.

1. Long-Term Irradiation in EBR-II (R. P. Larsen)

A long-term irradiation in EBR-II of encapsulated samples of ^{232}Th, ^{233}U, ^{235}U, ^{238}U, ^{237}Np, ^{239}Pu, ^{240}Pu, and ^{241}Pu, which began in December 1966 (see ANL-7350, p. 94), has been completed. The samples were removed from the reactor in September 1970, nearly a year sooner than originally expected. The subassembly containing the samples occupied a position in Row 2 for the first half of the irradiation and a position in Row 4 for the second half. Two sets of samples were irradiated: one set in the core at about the vertical centerline and the other in the axial blanket. These samples will be chemically analyzed to establish (1) the fast fission yields of burnup monitors for fast reactors as well as the yields of other fission-product nuclides that are of interest to the fast-reactor program, e.g., the krypton and xenon isotopes, and (2) the isotopic abundances of nuclides formed by nonfission nuclear transformations. The estimated burnups of the fissile nuclides are 20–25% for the samples irradiated in the core and 10–15% for the samples irradiated in the axial blanket. Burnup values of these magnitudes will enable the number of fissions to be determined (from pre- and postirradiation actinide element analyses) with an accuracy of ±0.5%. Analysis of these samples is expected to be started about September 1971.

2. Determination of Fast Fission Yields (R. D. Oldham, R. J. Popek, R. J. Armani [8])

A new method for determining the number of fissions that occur in a fast-reactor fuel has been developed. By this method, which was described previously (ANL-7675, p. 122), the fission yields of burnup monitors can be determined without the necessity of prolonged irradiation of the type discussed above. A low-power (10 kW) irradiation of mica fission-track detectors and gram amounts of the fissile nuclide is conducted to establish a factor relating the activity of a particular fission product (e.g., ^{95}Zr) to the number of fissions. The number of fissions that occur in a longer irradiation (~3 months) at full reactor power can then be determined from this factor and a measurement of the ^{95}Zr activity. This determination, along with analyses for long-lived or stable fission products, would provide the necessary data for calculating the yields of these fission products.

Several low-power irradiations have been conducted in the EBR-II mockup experiments in ZPR-3. One of the major objectives of these irradiations was to provide ^{95}Zr-to-fissions factors for 3-month irradiations of ^{235}U, ^{238}U, and ^{239}Pu that were to be carried out in EBR-II. The completion of the 4-yr irradiations in EBR-II (discussed above) nearly a year sooner than anticipated has obviated the need for the 3-month irradiation in EBR-II. The fission yields obtained by the analysis of the long-term irradiations will be more accurate and the acquisition of the data will not be appreciably delayed.

The irradiations in ZPR-3 also offered the opportunity (1) to make direct measurements of the fission yields of short-lived, gamma-active fission products and (2) to determine the variation of fission yields with neutron energy. The latter determination was performed to establish the applicability of the fission-yield data obtained in the spectrum of the EBR-II core to other neutron spectra. This information is necessary because the neutron spectrum in which the 4-yr irradiation was conducted was somewhat harder than the spectra of most other EBR-II irradiations and also harder than the spectra expected in the Fast Flux Test Facility (FFTF) and other LMFBRs. The experiments in ZPR-3 and the acquisition of fission-yield data are described below.

a. Irradiations in ZPR-3

Low-power irradiations of gram samples of ^{235}U, ^{238}U, and ^{239}Pu and mica fission-track detectors were carried out in two EBR-II mockup experiments in ZPR-3 (Assemblies 60 and 61). The Assembly-60 mockup of EBR-II had a blanket of ^{238}U; in Assembly 61, the ^{238}U blanket was replaced by a nickel reflector. Three irradiation packages

were included in each assembly: in the core, interface, and blanket (or reflector) regions. The neutron spectra in which the Assembly 60 packages were irradiated corresponded to those of Rows 2, 7, and 12 of the present loading of EBR-II. The core and interface spectra for Assembly 61 were nearly similar to those of Rows 2 and 7 of EBR-II, but the spectrum for the nickel reflector region was highly degraded.

The samples were irradiated in ZPR-3 in packages of the type shown in Fig. IV-10. Each package contained eight fission-track detectors (strips of mica in contact with nanogram depositions of the fissile nuclide on platinum); these are represented by the circles in Fig. IV-10. Each row of detectors was backed by a metal foil strip of the same nuclide. The ^{235}U and ^{239}Pu foils were 1.75 by 0.25 by 0.030 in. and the ^{238}U foils were 1.75 by 0.25 by 0.060 in. The uranium and plutonium foils were wrapped with aluminum foil to prevent the loss of fission fragments by recoil.

The mounting of the fissile nuclides for the track detectors was accomplished by an electroplating technique similar to that reported by Handley and Cooper [9]. An appropriate amount of the nuclide (of high isotopic purity) in a small volume of dilute nitric acid was dissolved in dimethyl sulfoxide and the nuclide electroplated in a 0.25-in.-dia circle onto a platinum strip (2 by 0.375 by 0.005 in.). Four depositions were made on each platinum strip. Each set of fission-track detectors for a particular nuclide consisted of two platinum strips and two strips of mica. The platinum strips and mica were assembled in the irradiation package in such a way that there were eight track detectors uniformly spaced across the package.

b. Determination of Absolute Yields of Gamma-Active Fission Products

The irradiated samples were received at Argonne, Illinois within 24 hr of the completion of the irradiations in ZPR-3 (located at the National Reactor Testing Station in Idaho). Each metal strip was cut into sections corresponding to the positions of the fission-track detectors and each section was assayed by gamma spectrometry on a predetermined time

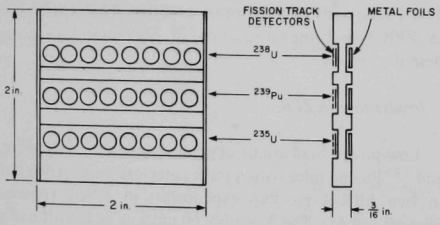

Fig. IV-10. Irradiation Packages for ZPR-3 Experiments. ANL Neg. No. 308-2414.

schedule covering a period of 128 days. The fission products of interest for yield determinations were those having half-lives between 1 and 100 days, fission yields greater than 1%, and high gamma-branching ratios. The counting schedule provided at least three good measurements of each of these fission products.

The nuclides measured were ^{95}Zr(65 d), ^{97}Zr(17 h), ^{103}Ru(42 d), ^{105}Rh(36 h), ^{131}I(8 d), ^{132}Te(78 h), ^{133}I(21 h), ^{140}Ba(13 d), and ^{143}Ce(33 h). One section of each of the ^{235}U, ^{238}U, and ^{239}Pu foils from each irradiation was also analyzed for ^{99}Mo(67 h) by beta counting after dissolution of the sample and radiochemical separation of the ^{99}Mo from other fission products [10]. Data for the nuclides with half-lives of less than 2 days (^{97}Zr, ^{105}Rh, ^{133}I, and ^{143}Ce) were obtained only for the Assembly 61 samples (an equipment malfunction occurred during early counting of Assembly 60 samples).

The gamma spectrometry was carried out with a lithium-drifted germanium diode detector coupled to a 4096-channel analyzer. The detector had been calibrated with respect to both energy and geometry by means of appropriate radioactive standards. The output of the analyzer was stored on magnetic tape and these data were processed by the computer code LIVER, which was developed by Gunnink and coworkers [11] and modified by N. D. Dudey and R. R. Heinrich of the Chemical Engineering Division. The input of the code included the calibration of the detector with respect to efficiency and geometry; the half-lives, gamma energies, and branching ratios of the fission-product nuclides; and the irradiation and out-pile times. The output of the computer is reported as "atoms-at-time-zero" for each fission-product nuclide.

The number of fissions per gram in each of the foil sections is established by means of the mica fission-track detectors. This is done by relating the number of fission tracks induced in a section of mica to the amount of fissile material on the corresponding section of platinum. The platinum and mica strips have been sectioned, and analyses are under way. The ^{239}Pu is being determined by alpha counting and the ^{235}U and ^{238}U by mass-spectrometric isotope-dilution analysis. The number of fissions is being determined by etching the mica with hydrofluoric acid and counting the fission tracks under a microscope [12].

c. Fission Yields as a Function of Neutron Energy

The fission yields of nuclides used to determine burnup of driver fuel and test fuels in EBR-II have been measured in a thermal neutron spectrum and in the relatively hard spectrum of EBR-I [13], but no reliable fission-yield information is available for neutron energies between these extremes. Therefore, the values of the fission yields used for EBR-II burnup analyses are either the EBR-I values or those obtained by a linear interpolation between thermal and EBR-I values. The lack of information on the

relationships between fission yields and neutron energy has raised the following questions: (1) Are the fission yields of the burnup monitors varying with changes in the neutron energy spectra that exist in EBR-II? (2) Are the fission yields to be measured on the samples irradiated in the core of EBR-II (see Section IV.C.1) adequate for accurate burnup determinations on fuels from FFTF and other fast-breeder reactors? The ZPR-3 data from Assembly 60 can be used to answer the first of these questions, since the neutron spectra in which the three packages were irradiated were the same as those in Rows 2, 7, and 12 of EBR-II. The ZPR-3 data from Assembly 61 can be used to answer the second question, since the neutron spectrum in which the core package was irradiated was very similar to the spectrum for the 4-yr irradiation in EBR-II, and the spectra of the interface and reflector packages bracketed the expected neutron spectra of FFTF.

One method of utilizing the ZPR-3 data to establish whether any changes in fission yields are occurring with changes in the neutron energies would be to compare the absolute fission yields for various reactor positions, however, the requisite data from the fission-track detectors are not yet available (see Subsection a, above). An alternative method, which utilizes available data, has, therefore, been devised; this method is described below.

The percent change in the fission yield of a particular nuclide can be calculated from the ZPR-3 data provided that the fission yield of one of the nuclides measured does not vary significantly with neutron energy. Barium-140 is such a nuclide. The ^{235}U fission yields [13] are 6.31 and 6.21% for thermal and fast (EBR-I) neutron spectra, respectively; the ^{239}Pu yields are 5.61 and 5.59% for thermal and fast neutron spectra, respectively. Barium-140 has, therefore, been used as the basis for calculating relative fission yields. The relative fission yield is defined as the ratio of atoms of a particular nuclide to the atoms of ^{140}Ba. Since the ^{140}Ba fission yield does not change appreciably with neutron energy, the percent change in the relative fission yield of a particular nuclide should be a reliable measure of the percent change in the absolute fission yield. All the samples from the ZPR-3 irradiations were dimensionally the same, and were assayed gamma-spectrometrically with the same equipment. The calculations were all made using the same fixed input data, e.g., detector calibration and nuclear constants. Therefore, the relative error in the atoms-at-time-zero due to errors in the fixed input data is a constant for each nuclide, and in the calculation of percent change in the relative fission yields, these errors cancel.

Of the fission-product nuclides assayed in the ZPR-3 irradiations ^{103}Ru and ^{131}I are, for ^{235}U fission, the most subject to changes in fission yield with neutron energy [13]. The fission yields of these two nuclides increase by 17 and 13%, respectively, in going from a thermal spectrum to that of EBR-I. For ^{239}Pu fission, the fission yield of ^{131}I shows the greatest increase, 13% (thermal to EBR-I spectrum).

The relative fission yields of ^{95}Zr, ^{103}Ru, and ^{131}I for ^{235}U and ^{239}Pu fission are summarized as a function of median fission energy in Tables IV-9 and IV-10. The ^{95}Zr relative fission yields are included in these tables for comparative purposes since it is known that the fission yield of ^{95}Zr, like that of ^{140}Ba, varies little with neutron energy for both ^{235}U and ^{239}Pu fission. Data from samples of ^{235}U and ^{239}Pu, irradiated in a thermal flux and counted with the same detector, are also given in the tables for comparison.

The relative fission yields of ^{95}Zr, ^{103}Ru, and ^{131}I for ^{238}U fission are given in Table IV-11. As expected, these yields showed no variation within the neutron energy range of the experiments, since fissioning of ^{238}U occurs only above the threshold energy of ~1 MeV.

From the Assembly 60 data in Tables IV-9 and IV-10, it is apparent that the ^{235}U relative fission yields of ^{103}Ru and ^{131}I and the ^{239}Pu relative yield of ^{131}I do not change from the core spectrum (Row 2 of EBR-II) to the blanket spectrum (Row 12 of EBR-II). It is, therefore, concluded that for irradiations carried out in EBR-II, the neutron spectrum does not affect the yields of fission products used to determine burnup.

From the Assembly 61 data in Table IV-10, it is apparent that the ^{239}Pu relative fission yield of ^{131}I does not change from the core, a spectrum much harder than that expected for FFTF, to the nickel reflector, a spectrum somewhat softer than that expected for FFTF. (In FFTF the principal source of fission will be ^{239}Pu.) It is, therefore, concluded that (1) the absolute yields of the fission products to be used to monitor burnup of FFTF fuel are independent of the neutron spectra in which they will be irradiated, and (2) the analysis of samples from the long-term irradiation in Rows 2 and 4 of EBR-II will provide ^{239}Pu fission-yield data of the accuracy required for FFTF irradiations.

TABLE IV-9. ^{235}U Fission Yields of ^{95}Zr, ^{103}Ru, and ^{131}I, Relative to ^{140}Ba, as a Function of Median Fission Energy

ZPR-3 Assembly and Sample Location[a]	^{95}Zr	^{103}Ru	^{131}I	Median Fission Energy, keV
60 Core (2)	1.006	0.498	0.505	446
61 Core	1.026	0.500	0.507	442
60 Interface (7)	0.992	0.496	0.496	315
61 Interface	1.000	0.486	0.512	293
60 Blanket (12)	1.009	0.493	0.493	132
61 Reflector	0.978	0.464	0.467	0.37
Thermal	1.010	0.438	0.399	2×10^{-5}
Std. Dev.	±0.015	±0.005	±0.010	

[a]The numbers in parentheses are the corresponding row numbers in EBR-II.

TABLE IV-10. ^{239}Pu Fission Yields of ^{95}Zr, ^{103}Ru, and ^{131}I, Relative to ^{140}Ba, as a Function of Median Fission Energy

ZPR-3 Assembly and Sample Location[a]	^{95}Zr	^{103}Ru	^{131}I	Median Fission Energy, keV
60 Core (2)	0.820	1.154	0.758	446
61 Core	0.803	1.145	0.754	442
60 Interface (7)	-	-	-	315
61 Interface	0.806	1.139	0.772	293
60 Blanket (12)	0.792	1.174	0.755	132
61 Reflector	0.792	1.161	0.754	0.37
Thermal	0.820	1.150	0.647	2×10^{-5}
Std. Dev.	±0.015	±0.010	±0.010	

[a]The numbers in parentheses are the corresponding row numbers in EBR-II.

TABLE IV-11. ^{238}U Fission Yields of ^{95}Zr, ^{103}Ru, and ^{131}I, Relative to ^{140}Ba, as a Function of Median Fission Energy

ZPR-3 Assembly and Sample Location[a,b]	^{95}Zr	^{103}Ru	^{131}I	Median Fission Energy, keV
60 Core (2)	0.805	0.920	0.508	466
61 Core	-	0.917	0.497	442
60 Interface (7)	0.811	0.903	0.505	315
61 Interface	-	0.914	0.500	293
Std. Dev.	±0.010	±0.010	±0.005	

[a]The numbers in parentheses are the corresponding row numbers in EBR-II.
[b]No blanket or reflector values are given because the neutron energies were too low to induce a significant number of fissions.

REFERENCES AND FOOTNOTES

1. A summary of this section is given on pp. 10 and 11.
2. P. Hoffman, F. Thümmler, H. Wedemeyr, "Compatibility Studies with Simulated Fission Products on Stainless Steel and Molybdenum," KFK-979 or EURFNR-685 (1969).
3. "Sodium Cooled Reactors, Fast Ceramic Reactor Development Program Quarterly Report, August–October 1969," GEAP-10028-32, Sect. 6–7 (1969).
4. "Reactor Development Program Progress Report, December 1969," ANL-7655, p. 123 (Jan. 29, 1970).
5. JANAF Thermochemical Tables, Dow Chemical Co., Midland, Michigan (1965).
6. The mass spectrometry was performed by M. Laug, Idaho Division.
7. N. D. Dudey, S. D. Harkness, H. Farrar IV, *Nucl. Appl. Technol. 9*, 700 (1970).
8. Applied Physics Division, ANL.
9. T. H. Handley, J. H. Cooper, *Anal. Chem. 41*, 381 (1969).
10. The ^{99}Mo analyses were performed in the Applied Physics Division.
11. R. Gunnink, H. B. Levy, J. B. Niday, UCID-15140, Lawrence Radiation Laboratory (1967).
12. The fission-track counting is being done in the Applied Physics Division.
13. F. L. Lisman, R. M. Abernathy, W. J. Maeck, J. E. Rein, *Nucl. Sci. Eng. 42*, 191–214 (1970).

V. CHEMISTRY OF LIQUID METALS AND MOLTEN SALTS [1]

(A. D. Tevebaugh)

Research, both theoretical and experimental, on liquid metals and molten salts has been in progress for several years in the areas of (1) investigating the behavior of liquid sodium as a coolant in nuclear reactors, (2) studying the thermodynamic and electrochemical properties of cells with liquid lithium and liquid sodium anodes, and (3) determining the thermodynamic properties and structure of various fused salts. This year an investigation of the thermodynamic properties of lithium-hydrogen-metal systems pertinent to controlled thermonuclear fusion was initiated.

The theoretical program was devoted to (1) refining a model for predicting gas solubilities in liquid metals, (2) showing that the existence of repulsive long-range interactions in liquid metals, first suggested by a sophisticated theory of metals, may also be deduced through simple bond-energy calculations, and (3) testing a mathematical analysis which makes possible the simultaneous determination of surface and volume diffusion coefficients from knowledge of the kinetics of grain-boundary groove-growth kinetics.

The experimental programs in liquid metals and molten salts can be divided into three main scientific categories. (1) The thermodynamic properties and phase relationships are being determined for lithium- and sodium-containing binary and ternary systems and for alkali-halide-containing binary and ternary systems. The experimental methods include thermal analysis, emf measurements, solubility determinations, vapor-liquid equilibria, and others. (2) The transport properties of alkali metal- and chalcogen-containing liquids are being investigated using conductivity methods and electron microprobe analyses. Concentration profiles of unsteady-state mass-transport experiments are determined by microsampling techniques. (3) The structure of fused salts is investigated primarily by laser-Raman spectroscopy.

The fundamental research on liquid metals and molten salts has led to the investigation of a number of electrochemical cells as power sources and energy-storage devices. Because these cells (which have liquid lithium anodes, molten alkali halide electrolytes, and molten chalcogen-containing cathodes) show promise of being developed into batteries having very high specific power (500 W/kg) and high specific energy (300 W-hr/kg), various government agencies are sponsoring three battery-development programs.

The battery-development programs represent possible applications in which either high specific energy or high specific power, or both, are important. The National Heart and Lung Institute is sponsoring work on a lithium/selenium secondary battery weighing about 1 kg and capable of delivering about 100 W-hr for ultimate use in a totally implantable heart-pump system. The U.S. Army at Fort Belvoir is supporting the development of high-specific-power lithium/selenium batteries for possible application in vehicular hybrid power systems using electric power to supplement the primary power source. Work on lithium/sulfur cells, which may prove to be suitable for use in family electrically driven automobiles, has been funded by the National Air Pollution Control Administration and will in the future be funded by the Environmental Protection Agency. This application requires high specific energy, high specific power, and low cost.

Various aspects of the investigations mentioned above have been reported in the open literature during the last year. Some of the papers are listed as Refs. 2–13.

A. LIQUID METAL STUDIES (E. J. Cairns, F. A. Cafasso)

Research is being conducted to increase the understanding of liquid metals and semi-metals. Particular emphasis is given to the study of sodium and lithium because of their projected use as coolants in nuclear fission and fusion reactors, respectively. The current experimental and theoretical programs include (1) determination of thermodynamic properties, including binary metallic phase equilibria, metal-metal-hydrogen ternary systems, gas solubilities, and calculation of liquid metal binding and (2) measurement of transport properties, such as electronic conductivity of sulfur and sulfur-containing mixtures, diffusion of reaction products in sulfur-containing cathodes of electrochemical cells, surface diffusivity in liquid sodium, and measurement of surface and volume diffusion coefficients.

1. Thermodynamics

a. Phase Equilibrium Studies of Binary Lithium-Chalcogen Systems (P. T. Cunningham, S. A. Johnson)

(1) The Lithium-Selenium System. Phase equilibrium studies of the lithium-selenium system were reported in part earlier (see ANL-7675, p. 129). Some of those data are included here for the sake of completeness. This system has been studied over the whole range of composition from pure lithium to pure selenium. The only intermediate phase found is Li_2Se; all other alloy compositions studied were prepared by mixing Li_2Se with either lithium or selenium. The Li_2Se was prepared by reacting selenium vapor with liquid lithium at 300°C.

Thermal analysis was used to determine thermal invariants in the system. Ordinary heating and cooling curves as well as differential thermal analysis (DTA) were employed. The results of these experiments are summarized in Table V-1. The only thermal effect noted on the

TABLE V-1. Summary of Thermal Analysis Data on the Lithium-Selenium System

Composition, at. % Li in Se	Method[a]	Container Material	Max Temp. (°C)	Temperature of Thermal Effects (°C)[a]		
100.0 (Li)	TA	Ta	220	180.5		
99.3	TA	Ta	210	180.5		
99.0	TA	Ta	220	180.6		
85.0	TA	347 SS[b]	1000	180.5		
66.6 (Li_2Se)	DTA	Nb[b]	1350			1302 ± 2
66.6 (Li_2Se)	Visual	Nb	1350			1303 ± 5
55.0	TA	Quartz	400		219.8	349.3
50.0	TA	Quartz	400		220.0	351.7
40.0	TA	Quartz	400		220.0	351.8
40.0	DTA	Al[b]	575		218.0	352.0
35.0	TA	Quartz[b]	615		220.3	347.0
35.0	DTA	Al[b]	500		218.0	352.0
31.9	DTA	Al[b]	415		219.0	354.0
31.5	DTA	Al[b]	480		219.0	352.0
20.0	TA	Quartz	430		220.0	349.4
10.0	TA	Quartz	400		221.0	334.0[c]
10.0	TA	Quartz	385		220.0	349.8
10.0	TA	Quartz	410		220.0	350.0
10.0	TA	Quartz[b]	706		196.0[c]	342.0[c]
10.0	DTA	Al[b]	400		219.0	352.0
7.5	TA	Quartz	410		219.8	350.5
5.0	TA	Quartz	380		210.0[c]	343.0[c]
5.0	TA	Quartz	370			350.7
4.0	TA	Quartz	390		220.0	347.0[c]
3.0	TA	Quartz	420		219.8	341.5[c]
3.0	TA	Quartz	400		220.3	346.6[c]
0.0 (Se)	TA	Quartz	400		220.2	
0.0 (Se)	DTA	Al[b]	395		218.0	

[a]The methods used were heating or cooling curves (TA), where reported temperatures are those of thermal arrests, and differential thermal analysis (DTA), where reported temperatures are those of the intersection.
[b]Sealed container.
[c]Temperature taken from a cooling curve that had clearly undercooled.

lithium-rich side of Li_2Se was at 180.5°C, the melting point of pure lithium. On the selenium-rich side of Li_2Se, thermal effects were noted at 220.0 and 350.1°C for all compositions from 55 to 3 at. % lithium. The 220°C effect is associated with selenium melting while the 350°C effect has been interpreted as the temperature of a monotectic reaction. Both of these effects displayed a strong tendency to undercool unless the sample was vigorously stirred.

The melting point of Li_2Se was determined by two methods. In the first method the sample was placed in a niobium crucible, which contained a black-body cavity, and then mounted in a molybdenum-wound resistance furnace. The crucible was then carefully heated in an argon atmosphere. The temperature was continuously monitored with a calibrated optical pyrometer. Fusion of the Li_2Se was observed to occur at 1303°C. The second method employed was high-temperature DTA with the sample again in a niobium capsule. Alumina served as the reference material. This technique yielded a melting point of 1302°C. This close agreement is considered to be somewhat fortuitous in view of the uncertainties of the measurement of high temperatures. From these two types of measurements, the melting point is concluded to be 1302 ± 5°C. There was no indication that the Li_2Se had reacted with the niobium crucibles.

The indications, based on the thermal analysis results, of a miscibility gap in the lithium-selenium system were confirmed by quenching samples containing from 2 to 26 at. % lithium from temperatures above 350°C. Since the thermal effects expected to be associated with a reaction of the type $L_2 \rightarrow L_1 + L_2$ could not be detected, the boundaries of the miscibility gap were determined by chemical analysis of quenched samples. Samples having compositions within the miscibility gap were held at temperature in sealed quartz vials for periods of up to several days to insure equilibrium and phase separation, and then quenched in liquid nitrogen. The two phases present, which are quite different in appearance, were then separated and analyzed for lithium and selenium. Lithium was determined using flame photometric techniques and selenium was determined using the standard potassium iodide method [14]. The results of these analyses are shown in Fig. V-1 by the square symbols. The region of immiscibility extends to a relatively high temperature, the consolute temperature being above 800°C.

Crossing of the upper liquidus also failed to produce detectable thermal effects (some DTA curves gave indications of a liquidus crossing, but the results were scattered and not reproducible). Microscopic study of quenched samples was used to locate the upper liquidus. Samples of various known compositions were heated to a temperature sufficiently high to insure that they were in the liquid region and then cooled to the temperature of interest, which was maintained for several hours prior to quenching

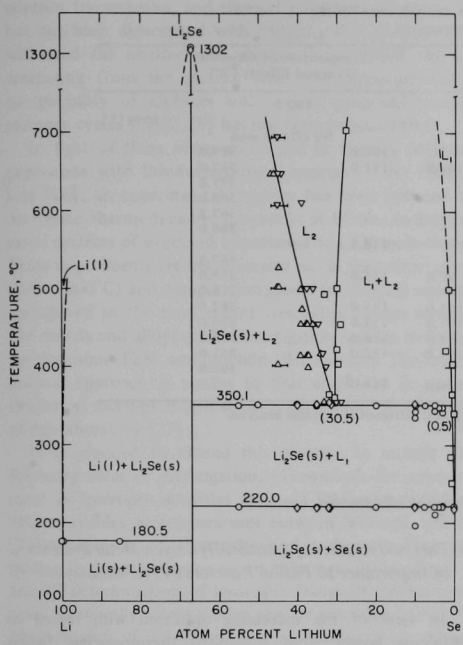

Fig. V-1. Phase Diagram of the Lithium-Selenium System. ANL Neg. No. 308-2327 Rev. 1.

in liquid nitrogen. Compositions which were below the liquidus at the holding temperature contained large, well-formed crystals of Li_2Se, while those above the liquidus prior to quenching contained only fine dendritic crystals of Li_2Se. The different structures were easily distinguishable at low magnification (about 14X) and allowed the liquidus temperature to be closely bracketed at several compositions. The results of these experiments are shown by triangles in Fig. V-1, where the base-down orientation indicates that the sample was quenched from below the liquidus and the apex-down orientation indicates quenching from above the liquidus.

X-ray diffraction patterns were obtained for a number of samples of various compositions and thermal histories. The only intermediate phase detected was Li_2Se, which has a simple antifluorite structure. Slight differences in the cell constant which occur, depending on whether the Li_2Se has been in contact with lithium or selenium, suggest the presence of a small homogeneous range for the Li_2Se phase.

The phase diagram shown in Fig. V-1 is entirely consistent with all experimental data. Previously noted discrepancies arising from emf measurements (ANL-7675, p. 129) have been resolved (see Subsection V.B.1.b of this report). The miscibility gap on the selenium-rich side of the diagram extends from 0.5 to 30.5 at. % lithium with a monotectic temperature of 350.1°C. The mutual solubility of the terminal phases at their melting points is very slight; no melting point depression is observed within the accuracy of these experiments (±0.2°C).

(2) The Lithium-Sulfur System. The lithium-sulfur system has proven to be a difficult system to study. Fewer data are available than for the lithium-selenium system discussed above. Qualitatively, however, the two systems appear to be very similar.

Thermal analysis, including ordinary heating and cooling curves and DTA, was used to determine the thermal invariants for the system. The results are shown in Table V-2 and in Fig. V-2 as circles. Previous thermal-analysis data by Pearson and Robinson [15] are shown in Fig. V-2 as squares. There is considerable scatter in the data primarily due to severe undercooling and the fact that the heats of transformation are relatively small. The thermal effects noted are at 100, 115, and 365°C. The low-temperature effect (100°C) is associated with the transformation from orthorhombic to monoclinic sulfur, whereas the effect at 115°C is associated with the melting of monoclinic sulfur. Neither of these effects is observed on cooling without extreme undercooling (40–60°C). The effect noted at 365°C is presumed to be due to a monotectic-type reaction, similar to that observed in the lithium-selenium system, since it is present over a wide range of compositions (5–60 at. % lithium). The failure of X-ray diffraction patterns to show any intermediate phase other than Li_2S would seem to rule out a eutectic reaction at 365°C. Furthermore, Li_2S does not appear to be polymorphic in this temperature range, and its simple antifluorite structure would not be expected to change with increasing temperature.

Efforts to determine accurately the extent of the miscibility gap and the position of the liquidus have been frustrated by difficulties in achieving good phase separation, making interpretation of chemical analysis impossible. Quenched samples have proven to be very difficult to polish; therefore meaningful microscopic examination of samples has been impossible.

The melting point of Li_2S was measured in a molybdenum-wound resistance furnace. The Li_2S was obtained from the Foote Mineral Co. and was reportedly of 97+% purity. Samples were contained in both niobium and vitreous-carbon crucibles. The temperature was measured using a calibrated optical pyrometer. The melting point was found to be 1372^{+10}_{-20} °C, which should represent a lower limit for the melting point of pure Li_2S. This value is

TABLE V-2. Summary of Thermal Analysis Data for the Lithium-Sulfur System

Composition, at. % Li in S	Method[a]	Container Material	Max. Temp. (°C)	Temperature of Observed Thermal Effects (°C)			
100 (Li)	CC	Ta	200		180.5		
66.6 (Li_2S)	Visual	Nb,C	1400				1372^{+10}_{-20}
66.6 (Li_2S)	DTA	Al	450		No effects seen		
60.0	DTA	Al	420		108.0	358.0	
51.0	DTA	Al	420	106.0	111.0	367.0	
50.0	HC	Al	405			371.0	
50.0	CC	Al	405			365.0	
23.1	HC	Al	390			367.2	
23.1	CC	Al	390			360.0	
15.0	HC	Pyrex			113.0		
15.0	CC	Pyrex	390			357.5	
13.0	HC	Pyrex		99.0	114.0	358.0	
13.0	CC	Pyrex	386			370.0	
10.0	DTA	Al	405	101.0	111.0	362.0	
9.0	DTA	Al	405	101.0	112.0	363.0	
9.0	HC	Pyrex[b]	510	101.0	115.0	364.0	
5.0	DTA	Al	405	101.0	112.0	361.0	
5.0	HC	Pyrex				361.0	
0.0 (S)	DTA	Al	405	101.0	116.0		

[a]The methods used were cooling curves (CC), heating curves (HC), and differential thermal analyses (DTA).
[b]Evacuated and sealed vial.

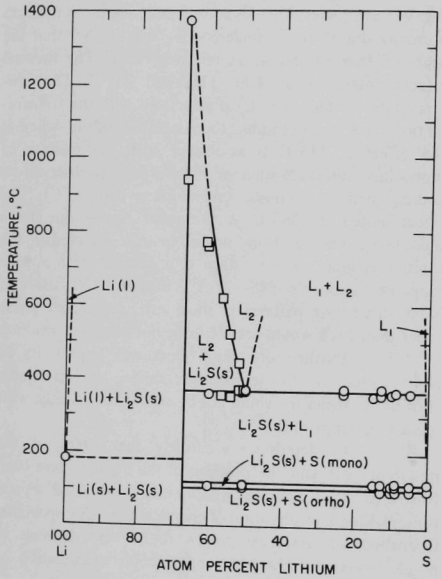

Fig. V-2. Proposed Phase Diagram for the Lithium-Sulfur System. ANL Neg. No. 308-2413.

considerably higher than that reported by Pearson and Robinson [15] (900–975°C) who observed rapid reaction between Li_2S and their porcelain container.

Work on the lithium-sulfur system will continue in order to establish the validity of the interpretation of the limited amount of data now available.

b. Thermodynamics of Lithium-Hydrogen-Metal Systems of Importance to Fusion Reactors (V. A. Maroni)

In view of the increasing optimism with regard to obtaining power from controlled thermonuclear fusion reactions [16–19], the program of experimental studies of liquid metals has been extended to include systems of potential importance to controlled thermonuclear reactors (CTR). In the past year, CTR conceptual designs advanced by other laboratories [17,20] for deuterium-tritium (D-T) type reactors have been reviewed in depth in order to ascertain insofar as possible the critical system-independent physicochemical parameters that must be known before fusion reactors can be built. The results of this comprehensive review have led to several conclusions: (1) It will be economically and ecologically very important to maintain a well-confined and well-controlled tritium inventory [21–23]. (2) Much of the basic physicochemical data necessary to make accurate estimates of the tritium inventory are not at hand. (3) A number of aspects of the recently advanced concepts for D-T fueled reactors are common to all designs. These system-independent aspects will prevail regardless of the size or shape of the reactor. In virtually all designs, the plasma is confined within a niobium envelope, operated between 800 and 1000°C, which is cooled with liquid lithium or molten lithium-beryllium fluoride. The tritium needed for refueling the reactor is bred from the lithium in the blanket and/or cooling fluid by means of the $^6Li(n,\alpha)^3H$ and $^7Li(n,\alpha n)^3H$ reactions [24].

Niobium has been selected as the wall material in most conceptual designs because of its favorable structural,

neutron transmission, and thermal properties. However, it has not been determined with certainty that niobium can withstand the neutron and photon fluxes which will be emanating from the plasma. Also, the physicochemical compatibility of niobium with various proposed tritium recovery cycles [22,23,25] has not been demonstrated.

In light of these observations and in view of previous experience with lithium-hydrogen systems in this laboratory [26], an experimental program has been initiated to determine thermodynamic properties of lithium-hydrogen-metal systems of expected importance to CTR technology. These experiments are being carried out in the temperature (600–1000°C) and composition (down to 10 ppm) regimes anticipated in the most recent conceptual design studies. The metals and alloys under investigation include niobium, molybdenum, TZM, and niobium-1% zirconium. The experimental approach is similar to that employed in earlier studies on metal-hydrogen systems conducted by members of this laboratory [27].

It is planned to extend this program to include the following areas of investigation: (1) methods for measurement of hydrogen activities in liquid lithium and molten lithium halides at temperatures between 600 and 100°C, (2) development of electrochemical techniques for promoting hydrogen transfer across thin metallic membranes, and (3) determination of hydrogen transport characterizations. Eventually, these studies may be extended to include measurements of the thermodynamic and transport properties of lithium hydride mixtures with various fused salts of interest for blanket and coolant applications.

Phase-equilibrium experiments, now in their early stages, are being conducted using hydrogen and deuterium; succeeding experiments will be carried out using tritium.

c. Theoretical Studies

(1) Gas Solubility in Liquid Metals (H. M. Feder, H. Schnyders). Liquid metals, when considered as solvents, behave in ways quite unlike normal, insulating liquids, and even the qualitative rules of solvency which apply tc insulating liquids are inapplicable. In order to unravel some of the many interrelated factors which control the behavior of liquid metals as solvents, we have chosen to study the simplest solutes, i.e., the noble gases. (Knowledge of the solubility of noble gas blanketing materials and fission products in liquid sodium is also of practical significance to the reactor technologist.) Elsewhere in this report (Section II.A.3) the experimental data are presented. In this section, we shall present the results of a continuing effort to develop a physically and calculationally realistic model of such solutions. In contrast to models previously proposed [28], the present model explicitly takes into account the effects of the large density of nearly free (unbound) electrons which are present within a liquid metal.

The excess molecular free energy of formation of a dilute solution, Δg^{xs}, may be set equal to the total reversible isothermal work done during three conceptual operations which are performed sequentially in order to transfer a solute molecule from its standard state in a gaseous phase into solution. These operations are as follows: (1) A solute molecule from the gas phase is confined to a small volume, δV, in which it exerts a pressure, P_h, equal to the internal pressure of the solvent, P_i; the work done during this compression is denoted by w_{comp}. (2) A spherical cavity of volume equal to δV is created in the solvent; the work done during the formation of this cavity is denoted by w_{cav}. (3) The solute molecule is inserted into the cavity; in so doing, an amount of work, denoted by w_{attr}, is done by the attractive forces acting between the solute molecule and the surrounding solvent. The excess molecular free energy, Δg^{xs}, may be set equal to $w_{comp} + w_{cav} + w_{attr}$. The following paragraphs describe a method for estimating each of these quantities.

(i) In the calculation of w_{comp}, we are concerned with only the entropic work of confinement of a molecule of finite dimensions in a volume of comparable size. For this purpose, hard-sphere theory [29] is applicable and the true atomic potential may be replaced by an effective hard-sphere potential which is characterized by one parameter, the effective hard-sphere diameter, a, of the solute molecule. To calculate the work, we require an appropriate equation of state for the hard-sphere gas; we have chosen to use the scaled particle [29] or Percus-Yevick [30,31] approximation

$$\frac{P_h \frac{\pi}{6} a^3}{k_B T} = \frac{y(1 + y + y^2)}{(1 - y)^3} \qquad (1)$$

where P_h is the pressure of a hard-sphere gas, k_B is Boltzmann's constant, T is the absolute temperature, and y, the packing fraction, is defined by $(\pi/6)a^3\rho$, ρ being the number density of the hard-sphere gas. The entropic work of compression is given by

$$w_{comp} = -\int_{k_B T}^{\delta V} P_h dV - k_B T \int_{\Omega}^{k_B T} \frac{dV}{V} \qquad (2)$$

where Ω is the atomic volume of the solvent (ρ^{-1}). The second term in Eq. 2 is included in order to refer the excess free energy of solution to a standard state appropriate to the definition of the Ostwald coefficient [32], i.e., the solute gas (considered to be ideal) at the molar volume of the liquid. On substitution of Eq. 1 into Eq. 2 one obtains

$$w_{comp} = k_B T \left[\ln \frac{\Omega}{\delta V (1 - y)} + \frac{3\, y(2 - y)}{2\,(1 - y)^2} \right] \qquad (3)$$

(ii) In order to calculate w_{cav} for a liquid metal, one must take into account the specific effects arising from the high density of mobile electrons in its conduction band. The simplest way to do so is to employ the

nearly-free-electron (NFE) model [33] of metals. All metals exhibiting NFE behavior will be considered as spatially uniform, immobile distributions of positive charge corresponding to N positive ions of valence z in a volume V, counterbalanced by a mobile distribution of conduction electrons having a uniform density $n_0 = zN/V = z\rho$. When one removes from the center of such a distribution a small spherical volume, δV, of positive charge, and distributes it uniformly over the surface of a large sphere, the net electronic work can be analyzed in terms of several effects. First, the excess negative charge ($en_0\delta V$) left in the cavity repels (by a screened coulombic potential) all the electrons in the conduction band and increases their potential energy. It can be readily shown that the work of repulsion is given by the following expression [34]

$$w_{\text{rep}} = \frac{n_0 \delta V}{\eta_{\text{F}}} \tag{4}$$

where η_{F} is the electronic density of states in the conduction band at the Fermi energy. (The Fermi energy, E_{F}, is the highest occupied energy level of the NFE in the conduction band of a metal.) Second, the expansion of the larger sphere reduces the average kinetic energy of the conduction electrons because they are free to explore a larger volume. For the most energetic electrons the reduction can be calculated because E_{F} varies as $V^{-2/3}$, hence $\delta E_{\text{F}}/E_{\text{F}} = -(2/3)(\delta V/V)$. If we denote by κ_{F} the ratio of the average kinetic energy per electron to its maximum, the total reduction for all electrons will be

$$w_{\text{kin}} = n_0 V \bar{\kappa}_{\text{F}} \delta E_{\text{F}} = -\frac{2}{3} \bar{\kappa}_{\text{F}} E_{\text{F}} n_0 \delta V \tag{5}$$

In the foregoing development we have implicity assumed that the electron gas remains spatially uniform at its density n_0 throughout, even in the cavity. However, it is well known that a uniform gas of conduction electrons will redistribute in the presence of an excess charge in such a way as to completely screen the potential due to the excess charge at large distances [35]. This redistribution takes the form of spatial oscillations (Friedel oscillations) [36] of the electron density about its mean value, n_0. The exact description of these oscillations depends upon the details of how the excess charge is distributed in the vicinity of the cavity. For simplicity, the model assumes a physically plausible (but not necessarily exact) distribution of the excess charge–a surface charge of magnitude $en_0\delta V$ uniformly distributed over the spherical cavity surface of radius $R = (3\delta V/4\pi)^{1/3}$. The work done by the electron gas as it responds to this charge distribution by spatial redistribution [35] has been found to be

$$w_{\text{osc}} = -(n_0 \delta V)^2 \frac{k_{\text{F}}^{\circ}}{2\pi} \int_0^{\infty} dx \frac{1}{\epsilon(x,0)} \left[\frac{1}{\epsilon(x,0)} - 1\right] \left[\frac{\sin bx}{bx}\right]^2 \tag{6}$$

where the parameter $b = (9\pi n_0 \delta V/4)^{1/3}$, the wave-number at the Fermi energy $k_{\text{F}}^{\circ} = (3\pi^2 n_0)^{1/3}$, $\epsilon(x,\omega)$ is the wave-number and frequency-dependent dielectric function for the electron gas, and $x = k/k_{\text{F}}^{\circ}$. Summing the contributions to w_{cav} we find

$$w_{\text{cav}} = (\eta_{\text{F}}^{-1} - \frac{2}{3} \kappa_{\text{F}} E_{\text{F}})\, n_0 \delta V + w_{\text{osc}} \tag{7}$$

(iii) The generalized potential due to dispersion forces, ϕ_{disp}, felt by a single molecule (B) near or within a macroscopic body (A) has been shown by Linder [37] to be given by the expression

$$\phi_{\text{disp}} = \frac{3}{4} \hbar \frac{\bar{\omega}_{\text{B}} \bar{\omega}_{\text{A}}}{\bar{\omega}_{\text{B}} + \bar{\omega}_{\text{A}}} a_{\text{B}}(0) g_{\text{A}}(0) \tag{8}$$

where $\hbar$ is Planck's constant divided by 2π, $a_{\text{B}}(0)$ is the static polarizability of the molecule in question, $g_{\text{A}}(0)$ is the static reaction field due to the macroscopic body, and $\bar{\omega}_{\text{B}}$ and $\bar{\omega}_{\text{A}}$ are the frequencies at which the corresponding frequency-dependent functions $a_{\text{B}}(\omega)$ and $g_{\text{A}}(\omega)$ have dominant resonances. The work done in bringing a molecule from a region of zero potential into the fluid is $w_{\text{attr}} \cong \phi_{\text{disp}}$. (The approximation is not important and only amounts to neglect of quadrupolar and higher-order multipolar forces.) For a situation in which the macroscopic body is represented by a solvent continuum having a cavity of radius R in which a solute molecule resides, the reaction field [37] is given by

$$g_{\text{A}}(\omega) = \left(\frac{2\epsilon_{\text{A}}(0,\omega) - 2}{2\epsilon_{\text{A}}(0,\omega) + 1}\right) \frac{1}{R^3} \tag{9}$$

In Eq. 9 the wave-number appropriate to the dielectric function is zero because only the long-wavelength limit is of interest in discussing dispersion forces. The long-wavelength limit of the dielectric function takes a particularly simple form for a metal [38]

$$\epsilon_{\text{A}}(0,\omega) = 1 - \frac{\omega_{\text{p}}^2}{\omega^2} \tag{10}$$

where ω_{p} is the plasmon frequency of the metal. Substituting Eq. 10 into Eq. 9, we obtain

$$g_{\text{A}}(\omega) = \left(\frac{-2\omega_{\text{p}}^2}{3\omega^2 - 2\omega_{\text{p}}^2}\right) \frac{1}{R^3}; g_{\text{A}}(0) = \frac{1}{R^3} \tag{11}$$

This function has an obvious resonance at

$$\bar{\omega}_{\text{A}} = \left(\frac{2}{3}\right)^{1/2} \omega_{\text{p}} \tag{12}$$

In the same long-wavelength limit, Langhoff and Karplus [39] have derived lowest-order Padé approximants to $a_{\text{B}}(\omega)$, which are, respectively, an upper bound

$$a_{\text{B}}^{(u)}(\omega) = \frac{Z}{(Z/a_0) - \omega^2} \tag{13}$$

and a lower bound

$$a_B^{(\ell)}(\omega) = \frac{a_0{}^2/a_1}{(a_0/a_1) - \omega^2} \tag{14}$$

In these equations, Z is the total number of electrons in the solute molecule; a_0 is not only the static polarizability of the solute molecule but also the first coefficient in a Cauchy series (representing the experimental frequency-dependent polarizability) [40] in which a_1 is the second coefficient. These functions have their principal resonances at effective frequencies

$$\bar{\omega}_B(u) = (Z/a_0)^{1/2} \tag{15}$$

and

$$\omega_B(\ell) = (a_0/a_1)^{1/2} \tag{16}$$

Substitution of Eqs. 11, 12, and 13 into Eq. 8 results in an upper-bound value

$$w_{attr}^{(u)} = -\frac{\pi\hbar(Za_0)^{1/2}}{\delta V} \cdot \frac{\omega_p}{\omega_p + \left(\frac{3}{2}\frac{Z}{a_0}\right)^{1/2}} \tag{17}$$

Similarly, substitution of Eqs. 11, 12, and 16 into Eq. 8 yields the lower-bound value

$$w_{attr}^{(\ell)} = -\frac{\pi\hbar a_0\left(\frac{a_0}{a_1}\right)^{1/2}}{\delta V} \cdot \frac{\omega_p}{\omega_p + \left(\frac{3a_0}{2a_1}\right)^{1/2}} \tag{18}$$

As one substitutes higher-order upper- and lower-bound Padé approximants for Eqs. 13 and 14, the bounds to w_{attr} tend to merge at a value near the arithmetic mean of Eqs. 17 and 18. To the expected accuracy of our model we may write

$$w_{attr} = \frac{1}{2} w_{attr}^{(u)} + w_{attr}^{(\ell)} \tag{19}$$

(iv) The total work, Δg^{xs}, done in the three steps of our conceptualization of the solution of an atom of gaseous solute in a liquid metal is the summation of Eqs. 3, 7, and 19; it is related to the molar excess free energy of solution and the Ostwald coefficient, λ, by

$$N_0 \Delta g^{xs} = \Delta G^{xs} = -RT\ln\lambda \tag{20}$$

where N_0 is Avogadro's number.

(v) Calculations have been carried out for the solution of noble gases in liquid sodium. The input data necessary for calculations of ΔG^{xs} and λ are available from a number of sources and are collected in Table V-3. The internal pressure of the metallic solvent was computed from its volume expansion coefficient β_T and its isothermal compressibility κ_T

TABLE V-3. Physical Properties of Liquid Sodium (500°C) and the Noble Gases

A. Liquid Sodium (500°C)

$P_i = 7650$ atm	$n_0 = 2.179 \times 10^{22}$ (cm^{-3})[a]
$\Omega = 27.64$ (cm^3 mol^{-1})[a]	$\beta_T = 2.86 \times 10^{-4}$ (°C^{-1})[a]
$\omega_p = 5.24$ eV[b]	$\kappa_T = 2.891 \times 10^{-5}$ (atm^{-1})[c]

B. Noble Gases

	He	Ar	Xe
(a_0)[d,e]	1.384	11.091	27.340
(a_1)[d,e]	1.550	28.16	116.2
(a)[f], Å	2.56	3.41	3.97
Z	2	18	54
δV,[g] Å^3/atom	38.5	63.9	86.8

[a]E. I. Goltsova, *High Temp. 4*, 348 (1966).
[b]ω_p (25°C) = 5.9 eV; J. L. Robins, P. E. Best, *Proc. Phys. Soc. London 79*, 110 (1962).
[c]Y. S. Trelin, J. N. Vasil'ev, V. B. Proskurin, T. A. Tsyganova, *High Temp. 4*, 352 (1966).
[d]P. W. Langhoff, M. Karplus, *J. Chem. Phys. 53*, 233 (1970).
[e]In atomic units, $\hbar = m = e = 1$.
[f]See H. Reiss, *Advan. Chem. Phys. 9*, 1 (1965); C. C. Lim, D. H. Bowman, R. A. Aziz, *Can. J. Chem. 46*, 3477 (1968); G. Boato, G. Casanova, *Physica 27*, 571 (1961).
[g]Calculated from Eqs. 1 and 2 using the data and parameters given in this table.

$$P_h = P_i \equiv T\frac{\beta_T}{\kappa_T} \tag{21}$$

Temperature-independent effective hard-sphere diameters, a, for the solute molecules were taken from the values determined by fitting experimental second virial coefficient data for the gases. With these values for P_i and a, the left-hand side of Eq. 1 is known and it may be solved for y. Then δV is determined from $y\delta V = 1/6\, a^3$. Because liquid sodium approximates very well to an ideal univalent free-electron metal, further simplications are possible, e.g., $\eta_F = (2/3\ E_F)^{-1}$, $E_f = h^2 k_F^2/2m_e$ where m_e = the electronic mass, $\bar{\kappa}_F = 3/5$, and $\epsilon(x,0)$ is given by the Lindhard formula [41].

The quantities needed for the computation of w_{attr} are the Cauchy coefficients, a_0 and a_1, derived from optical refractivity data [40], and the plasmon frequency, ω_p, derived from electron-loss experiments. The latter measurements are usually carried out at only one temperature. We have assumed that ω_F may be scaled to the temperature of interest by the known temperature dependence (ω_p° proportioned to $\rho^{1/2}$) of the ideal plasmon frequency of a free-electron gas. In the few cases where the temperature dependence of ω_p has been measured, this assumption appears to be valid.

Reliable experimental Ostwald coefficients for helium [42,43], argon [43,44], and xenon [45] in liquid sodium are presented in Fig. V-3 as the mean values of multiple determinations at each temperature. Calculated values of λ from Eq. 20 are indicated by the dashed and solid lines.

In Table V-4 are shown the contributions to the free

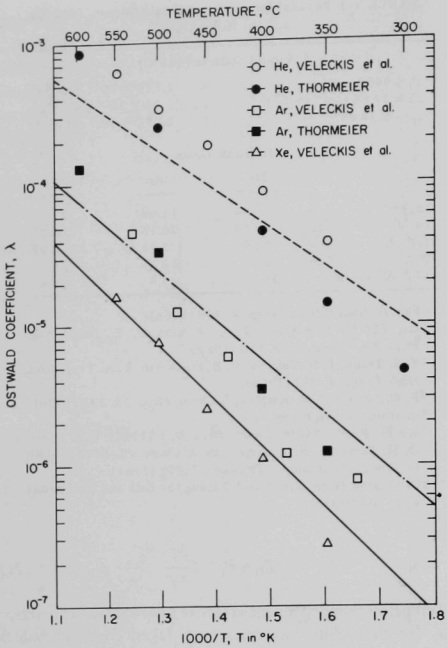

Fig. V-3. Ostwald Coefficients of Helium, Argon, and Xenon in Liquid Sodium. Open circles, squares, and triangles represent the experimental data of E. Veleckis et al. for helium,[42] argon,[44] and xenon[45] in sodium, respectively. Solid circles and squares represent the data of K. Thormeier[43] for helium and argon in liquid sodium. The dashed, dot-dashed, and solid lines, respectively, represent Eq. 20 for helium, argon, and xenon dissolved in sodium. ANL Neg. No. 308-2412.

TABLE V-4. Reversible Work Contributions to the Excess Free Energies of Solution for He, Ar, and Xe in Liquid Sodium at 500°C[a]

	He	Ar	Xe
$N_0 w_{comp}$	2.2	2.8	3.4
$N_0 w_{cav}$	12.6	20.2	26.8
$N_0 w_{attr}$	−1.5	−6.7	−12.0
$N_0 g^{xs}$ (calc)[b]	13.3	16.3	18.2
ΔG^{xs} (exp)	12.3[c] 12.7[f]	16.6[d] 15.8[f]	18.1[e]

[a]All values in kcal mol^{-1}.
[b]Data in Table V-3 substituted in Eq. 20.
[c]E. Veleckis, G. Redding, ANL-7675, p. 64 (1970).
[d]E. Veleckis, R. Blomquist, R. Yonco, M. Perin, ANL-7325, p. 128 (1967).
[e]E. Veleckis, W. Kremsner, ANL/ST-4 (1970).
[f]K. Thormeier, *Atomkernenerg. 14*, 449 (1969).

energies of solution at one temperature. Considering the relative magnitudes of these terms, their uncertainties, and the uncertainty in the experimental results, we conclude that the proposed model does indeed provide a fairly reliable calculation of the solubility of noble gases in a liquid metal.

According to the model we have presented, Δg^{xs} is dominated by the electronic cavity-making term, which strongly depends on the valence-electron density of the metal. It is then no surprise that, for all liquid metals other than the alkalis and some of the alkaline earths, the noble gas solubilities are predicted to be less than those measurable by current experimental techniques.

(2) Binding Calculations for Liquid Metals (J. G. Eberhart). The potential energy of a pair of rare gas atoms which experience a van der Waals interaction is quite familiar in its qualitative features. As the interatomic distance increases, the potential energy decreases, passes through a minimum, and then increases asymptotically to zero. The interaction is repulsive only at the very small interatomic distances where electron overlap is constrained according to the Pauli exclusion principle. At all larger separations, the interaction is attractive resulting from the induced dipoles of the atoms.

The situation for a crystalline or a liquid metal is quite different. According to pseudopotential theory [46], the potential for a pair of ions immersed in the sea of conduction electrons does not asymptotically approach zero at the larger interionic distances, but exhibits instead a damped oscillation about zero. Thus, instead of being attractive at all the larger separations, the interaction is alternately attractive and repulsive as distance increases. This long-range oscillatory behavior is a consequence of the dielectric screening of the ionic core by the surrounding conduction electrons. A potential of this form was first suggested by Friedel [47], and this behavior is often called Friedel oscillations.

It is the purpose of this study to show that simple calculations of bond energies also suggest the presence of repulsive interactions in liquid metals at longer ranges. The bond energy which characterizes the interaction between a particular pair of atoms in a metal is not related in any simple way to the ion-ion potential for metals which was discussed above. This long-range oscillatory potential characterizes the interaction between two ions immersed in the sea of conduction electrons. The depth of the first well is largest and provides an estimate of the work necessary to move the pair of ions from the separation at this first minimum to an infinite separation where the initial and final states are both metallic. The bond energy, by contrast, is defined in terms of the vaporization process, in a way which will be specified shortly. Here, the initial state is metallic, whereas the final state is an atomic vapor with localized electrons. Thus, bond energies can be expected to be considerably larger than the ion-ion potential energies in the region of oscillation. Both properties, however, can provide an indication of whether repulsive interactions exist

in the metallic state at the larger interionic distances.

Model and calculations. The calculation of covalent bond energies from the heat of atomization of various molecules is a familiar and straightforward task. In a similar fashion, the nearest-neighbor bond energy of a metal can be estimated by dividing the heat of vaporization, L, by one-half of the coordination number and will yield a bond energy which is positive in sign, i.e., an attractive interaction. To find evidence of repulsive interactions at larger distances, it is necessary to calculate at least the first and second nearest-neighbor bond energies, ϕ_1 and ϕ_2, and this requires at least one other thermodynamic property which is related to the breaking of metallic bonds. Such a property is the surface energy. The surface energy of metals has been characterized in recent years by the so-called broken-bond model by which the work required to create two new interfaces is related to the number of bonds broken in the process and the energy of each type of bond. Using a nearest-neighbor version of this model, Skapski [48] was able to calculate the surface energy of liquid metals from their heats of vaporization and the coordination number of interior and surface atoms. Taking first and second nearest-neighbor interactions into account, Mackenzie, Moore, and Nicholas [49] developed equations for the surface energies of different crystal faces of a given metal. Supplementing their surface-energy equations with analogous expressions for the heat of vaporization, it is possible to calculate ϕ_1 and ϕ_2 for a variety of metals.

Three assumptions are made in the bond-energy calculations. First, the liquid-metal cohesive energy is the result of pair-wise interactions between first and second nearest neighbors only, which can be characterized by bond energies ϕ_1 and ϕ_2. More distant neighbors are neglected, the calculations of Nicholas [50] suggest that this is a satisfactory approximation. Second, because of local order, the atoms in the liquid interior are assumed to have the same coordination as atoms in the solid lattice formed by the metal upon crystallization. This conclusion is based on the modest volume change experienced by most metals upon melting (2 to 4%) and is consistent with the few measurements which have been made of the coordination number of liquid metals. Metals which crystallize into bcc and fcc lattices will be considered here. Third, the atoms in the surface layer have the same coordination that would be expected from cleavage along the closest-packed plane with no relaxation or rearrangement in the surface. The closest-packed surface plane is selected because it has the lowest surface energy.

The heat of vaporization at absolute zero, L_0, is related to the bond energies ϕ_1 and ϕ_2 through the bulk coordination numbers. In a bcc lattice, the coordination numbers for the first and second nearest-neighbor atoms are 8 and 6. Thus, for every atom vaporized, four first and three second nearest-neighbor bonds are broken and

$$L_0 = 4\phi_1 + 3\phi_2 \text{ (bcc)} \tag{22}$$

Similarly, from the coordination numbers of 12 and 6 in a fcc lattice, it follows that

$$L_0 = 6\phi_1 + 3\phi_2 \text{ (fcc)} \tag{23}$$

The work required to cleave a liquid or solid to produce two new surfaces each of area A, is $2A\gamma$, where γ is the surface tension. For the (110) plane of a bcc lattice with a unit cell edge length of a_0 at absolute zero, the cleavage of an area $\sqrt{2}\,a_0^2$ requires the breaking of four first and four second nearest-neighbor bonds. Thus the work required to produce these two new surfaces is

$$2\sqrt{2}\,a_0{}^2\gamma_0 = 4\phi_1 + 4\phi_2 \text{ (bcc)} \tag{24}$$

where γ_0 is the surface energy, i.e., the surface tension at absolute zero. Similarly, for the (111) plane of a fcc lattice, the cleavage of an area $(\sqrt{3}/4)\,a_0^2$ requires the breaking of three first and three second nearest-neighbor bonds. Thus

$$(\sqrt{3}/2)a_0{}^2\gamma_0 = 3\phi_1 + 3\phi_2 \text{ (fcc)} \tag{25}$$

The density of the liquid at absolute zero, ρ_0, can be used to calculate a_0. Because the bcc unit cell contains two atoms

$$a_0{}^3 = 2\,\Omega_0 = 2M/N\rho_0 \text{ (bcc)} \tag{26}$$

where Ω_0 is the atomic volume at absolute zero, M is the molar mass, and N is Avogadro's number. Similarly, from the fcc unit cell with four atoms

$$a_0{}^3 = 4\Omega_0 = 4M/N\rho_0 \text{ (fcc)} \tag{27}$$

To calculate ϕ_1 and ϕ_2 for bcc metals, it is thus necessary to solve simultaneously Eqs. 22 and 24 with a_0 provided by Eq. 26. For the fcc metals, ϕ_1 and ϕ_2 are found from the simultaneous solution of Eqs. 23 and 25 with a_0 provided by Eq. 27.

Calculations of ϕ_1 and ϕ_2 were performed on all liquid metals where the L, γ, and ρ data were sufficiently reliable to extrapolate to absolute zero. At absolute zero, L, which is an enthalpy, and γ, which is a Helmholtz free energy, both become energies and yield energies for ϕ_1 and ϕ_2. Tables V-5 and V-6 show the data employed and the calculated bond energies. The results are that (1) ϕ_1 is positive, corresponding to an attractive first nearest-neighbor interaction, and (2) ϕ_2 is negative, which implies that the second nearest-neighbor interaction is repulsive. Thus, even from this extremely simple model, an indication is obtained of the existence of repulsive interactions at larger interionic distances in metals.

TABLE V-5. Bond Energies for BCC Metals

Metal	L_0 (eV/atom)	ρ_0 (g/cm^3)	γ_0 (erg/cm^2)	ϕ_1 (eV/bond)	ϕ_2 (eV/bond)
Li	1.624[a]	0.546[b]	470[b]	0.869	−0.618
Na	1.096[a]	1.02[b]	220[b]	0.579	−0.406
K	0.914[a]	0.9105[b]	125[b]	0.462	−0.311
Rb	0.840[a]	1.587[b]	95[b]	0.440	−0.307
Cs	0.804[a]	2.02[b]	80[b]	0.419	−0.291
Ca	1.747[a]	1.613[c]	472[c]	0.563	−0.168
Fe	4.135[a]	8.618[d]	2758[e]	1.310	−0.368

[a]R. Hultgren, R. L. Orr, P. D. Anderson, K. K. Kelley, *Selected Values of Thermodynamic Properties of Metals and Alloys,* John Wiley & Sons, Inc., New York (1963).
[b]J. Bohdansky, H. E. J. Schins, *J. Inorg. Nucl. Chem. 29*, 2173 (1967).
[c]J. Bohdansky, H. E. J. Schins, *J. Inorg. Nucl. Chem. 30*, 2331 (1968).
[d]A. V. Grosse, A. D. Kirshenbaum, *J. Inorg. Nucl. Chem. 25*, 331 (1963).
[e]C. T. Wang, R. A. Karassev, A. M. Samarin, *Izv. Akad. Nauk SSSR, Otd. Tekh. Nauk, Metall. i. Toplivo 1*, 30 (1960).

TABLE V-6. Bond Energies for FCC Metals

Metal	L_0 (eV/atom)	ρ_0 (g/cm^3)	γ_0 (erg/cm^2)	ϕ_1 (eV/bond)	ϕ_2 (eV/bond)
Ni	4.256[a]	9.908[b]	2348[c]	0.928	−0.437
Cu	3.359[d]	9.077[e]	1629[f]	0.740	−0.361
Ag	2.877[d]	10.53[g]	1136[h]	0.618	−0.277
Al	3.221[d]	2.626[g]	996[h]	0.602	−0.330
Pb	1.979[a]	11.41[g]	538[h]	0.423	−0.186

[a]R. Hultgren, R. L. Orr, P. D. Anderson, K. K. Kelley, "Supplement to Selected Values of Thermodynamic Properties of Metals and Alloys," Lawrence Radiation Laboratory, University of California, Berkeley, California (1969).
[b]A. V. Grosse, A. D. Kirshenbaum, *J. Inorg. Nucl. Chem. 25*, 331 (1963).
[c]V. N. Eremenko, V. I. Nizhenko, *Ukr. Khim. Zh. 30*, 125 (1964).
[d]R. Hultgren et al., *Selected Values of Thermodynamic Properties of Metals and Alloys*, John Wiley & Sons, Inc., New York (1963).
[e]J. A. Cahill, A. D. Kirshenbaum, *J. Phys. Chem. 66*, 1080 (1962).
[f]Yu. V. Naidich, V. N. Eremenko, *Phys. Met. and Metall. 6*, 62 (1961).
[g]H. E. J. Schins, EUR-3653 (1967).
[h]J. Bohdansky, H. E. J. Schins, *J. Inorg. Nucl. Chem. 30*, 3362 (1968).

2. *Transport Properties*

a. Conductivities of Sulfur and Sulfur-Containing Mixtures
(R. K. Steunenberg, C. Trapp [51], R. M. Yonco)

Much information has been published on the electrical conductivities of solid, crystalline semiconductors and the effects of temperature and dopants upon the conductivity. However, few data are available on the electronic conductivity of liquid elemental semiconductors and the effects on conductivity of temperature and dopants. Amorphous and liquid semiconductors are expected to be less sensitive to doping than crystalline semiconductors [52], but the magnitude of the effect cannot yet be predicted from theory. Although the mechanism of conduction in liquid semiconductors is not yet fully understood, it is believed to result primarily from the "hopping" of electrons between localized sites, rather than by excitation into a conduction band. The electrical conductivities of sulfur and sulfur-phosphorus mixtures are therefore of theoretical as well as practical interest, the latter deriving from the possible use of these materials as cathode reactants in secondary electrochemical cells.

Additional measurements of the conductivity of elemental sulfur and P_4S_3 have been made with both alternating and direct current. The ac measurements were made with an Electro Scientific Industries Model 290A impedance bridge and a Model 860A generator/detector at frequencies of 0.1, 1.0, and 10.0 kHz. The dc measurements were made with the same bridge, using a dry cell as the power supply and a Leeds and Northrup Model 9835B microvolt amplifier as a null detector. The conductivity cells consisted of two parallel 6.3-mm dia spectrographic graphite electrodes connected to metal leads that were sealed into the quartz or Pyrex container. The interelectrode distance was about 4 mm.

(1) Elemental Sulfur. The conductivity of elemental sulfur was determined with a quartz cell in which tungsten leads were used with the graphite electrodes. The cell constant, which was measured with the aid of standard KCl solutions, was 0.1235 cm^{-1} at 25.2°C. The sulfur was obtained from the American Smelting and Refining Co. with a purity specification of 99.999+%. No additional purification was attempted. When the experiment was completed, the sulfur showed very slight contamination with a black particulate material, which was tentatively identified as carbon.

The results of the sulfur conductivity measurements are

presented in Fig. V-4. These conductivities are nearly two orders of magnitude lower than those obtained previously (ANL-7675, pp. 135–136), and they are in reasonable agreement with an extrapolation of the lower-temperature data of Feher and Lutz [53], as well as the two values quoted by Meyer [54]. The present data show the expected linear relationship between $\log K$ and $1/T(^\circ K)$ over the temperature range of the measurements (about 300 to 400°C). The conductivities decreased with increasing frequency, and extrapolation of the ac data to zero frequency resulted in values that were in good agreement with the dc data. The temperature dependence of the dc conductivities corresponds to an activation energy of 37.2 kcal/g-atom, or 1.62 eV. The results of these measurements indicate that the electronic conductivity of sulfur decreases markedly with increasing purity, probably as a result of the doping effect of the impurities.

(2) Phosphorus-Sulfur Mixtures. The electrical conductivity of P_4S_3 was measured, using the same type of equipment and techniques that were employed in the sulfur measurements. The P_4S_3, which was procured from the Eastman Kodak Co. without a purity specification, appeared to be rather impure. This material was purified by extraction with CS_2, followed by sublimation. The Pyrex cell had molybdenum leads to the graphite electrodes. The cell constant, determined with the aid of KCl solutions at 25.4°C, was 0.1354 cm^{-1}.

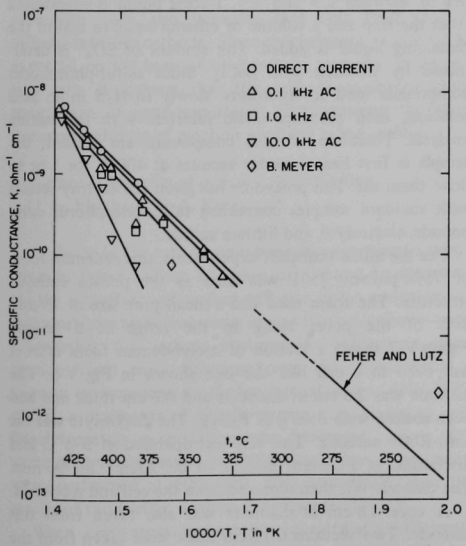

Fig. V-4. Specific Conductance of High-Purity Sulfur (cell material: quartz; leads: tungsten; electrodes: spectrographic graphite; atmosphere: helium, 1 atm). ANL Neg. No. 308-2411.

The results of the measurements are presented in Fig. V-5. These conductivities are somewhat lower than those obtained during a previous temperature cycle, possibly because of the volatilization of P_2O_5 that may have been present as an impurity. The data show the expected linear dependence of $\log K$ upon $1/T(^\circ K)$, and the slope of the line represents an activation energy of 10.8 kcal/mol or 0.47 eV. Although there is some scatter of the data, particularly at the lower temperatures, there appears to be no systematic dependence of the conductivity upon frequency.

The earlier conductivity data on phosphorus-sulfur mixtures (ANL-7675, pp. 135–136) were evaluated in the light of the newer results. The older data were corrected for the presence of probable impurities, assuming that conductivities are additive. The results are shown in Table V-7. It is clear that the conductivity of sulfur increases sharply upon the addition of small amounts of phosphorus up to about 10 at. %. Further additions of phosphorus appear to have only a minor effect on the conductivity of sulfur. As the phosphorus concentration is increased to 10 at. %, the activation energy of the conductivity decreases. This effect is attributed to a decreasing energy gap for the conduction mechanism. However, additional data are needed for an adequate interpretation of the conduction mechanism in this system.

b. Transport Studies in Sulfur-Containing Cathodes

(B. A. Feay, R. M. Yonco

An understanding of transport mechanisms is essential to

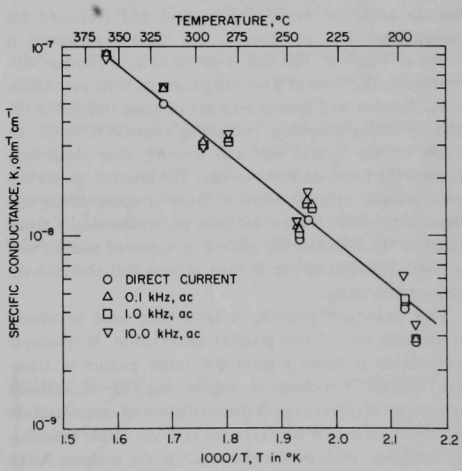

Fig. V-5. Specific Conductance of P_4S_3. ANL Neg. No. 308-2410.

TABLE V-7. Specific Conductance of Phosphorus-Sulfur Mixtures

Composition (at. % P)	Specific Conductance ($ohm^{-1} cm^{-1}$)		
	300°C	350°C	400°C
0	1.6×10^{-11}	2.0×10^{-10}	1.7×10^{-9}
2.2	1.3×10^{-8}	5.1×10^{-8}	1.7×10^{-7}
9.0	5.0×10^{-8}	1.4×10^{-7}	3.3×10^{-7}
57.0 (P_4S_3)	3.6×10^{-8}	8.2×10^{-8}	1.5×10^{-7}

total understanding of the chemical and electrochemical processes taking place in sulfur cathodes (which are used in lithium/sulfur secondary cells). To gain insight into these mechanisms in sulfur-containing systems, a study was undertaken of the transport of reaction products in cathodes containing sulfur and sulfur-phosphorus compounds. The experimental plan was to operate a Li/LiBr-RbBr/Li in S or /Li in P_4S_{10} cell so as to deposit a known amount of lithium at the cathode-electrolyte interface, and then examine the cathode by various analytical techniques to determine the concentration profiles of lithium-containing reaction products in the porous cathode structure. By studying these profiles as a function of temperature, deposition rate, and cathode structure, it was hoped that transport properties such as diffusion coefficients could be determined.

To carry out this plan, a suitable electrochemical cell was designed and appropriate analytical techniques were developed. It was necessary that the cell have a well-defined cathode-electrolyte interface and be capable of high current densities, thus permitting high lithium deposition rates. It was also necessary to minimize losses of cathode material during cell assembly and operation, and to insure that the cathode could be easily disassembled and sectioned for examination. The cell designed for these experiments is shown in Fig. V-6. The cell is operated in a furnace well attached to the floor of a helium glovebox. Brief evacuation of the furnace well insures removal of gases trapped in the cathode during assembly, permitting electrolyte to fill the inside of the quartz cap and insuring that electrolyte contacts the entire cathode surface. The inverted quartz cap helps prevent cathode material from escaping during the experiment. After lithium has been electrochemically transferred to the cathode, the cathode is removed and allowed to cool. The quartz cap is then broken and the cathode sectioned for analysis.

Two analytical procedures have been used to obtain information on reaction-product distribution. Microscopic examination provides a good qualitative picture of transport effects. Wet-chemical sulfide analysis of cathode sections allows quantitative determination of concentration profiles of lithium products in the cathode. Other quantitative methods, such as electron microprobe analysis, X-ray emission, and total sulfur analysis, cannot distinguish between reactants and products and thus are not suitable.

The wet-chemical sulfide analysis used is a modification

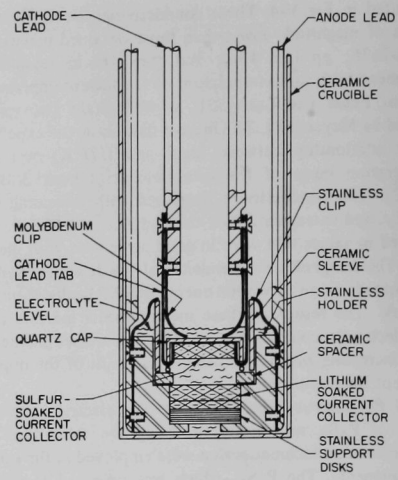

Fig. V-6. An Experimental Lithium/Sulfur Cell for Mass Transport Studies. ANL Neg. No. 308-2409.

of a standard sulfide analysis [55]. Acetic acid is added to the sample and the evolved H_2S is trapped as SO_4^{2-} in basic peroxide. The trap is heated and HCl is added to bring the pH to between 2.3 and 2.7. Excess liquid is evaporated from the trap and a volume of ethanol equal to that of the remaining liquid is added. The amount of SO_4^{2-} is determined by titration with $BaCl_2$. Since sulfur-phosphorus compounds tend to hydrolyze slowly to H_2S in an acid solution, their presence could interfere with the sulfide analysis. Therefore, if such compounds are present, the sample is first heated under vacuum at 400°C for 1 hr to drive them off. This procedure has given satisfactory results with standard samples containing sulfur-phosphorus compounds, electrolyte, and lithium sulfide.

For the initial transport experiments, molybdenum foam of 75% porosity [56] was used as the porous cathode structure. The foam used had a mean pore size of 19 μm, 80% of the pores being in the range of 8–36 μm. Figure V-7 shows a section of molybdenum foam after it had been in a cell like the one shown in Fig. V-6. The cathode was 2.5 cm in diameter and 0.6 cm thick and had been soaked with 3.46 g of P_4S_{10}. The electrolyte was the LiBr-RbBr eutectic. The cell was operated at 375°C and discharged at a current density of 0.1 A/cm^2 for 96 min. The cathode was then removed from the cell and sectioned.

A core 0.8 cm in diameter was also taken from this cathode. Two sections 0.13 cm thick were taken from the end of the core that had been in contact with electrolyte. Sulfide analysis as described above was performed on these core sections. The analysis showed less than 5 mg of sulfide in each section. This contrasts with approximately 50 mg of

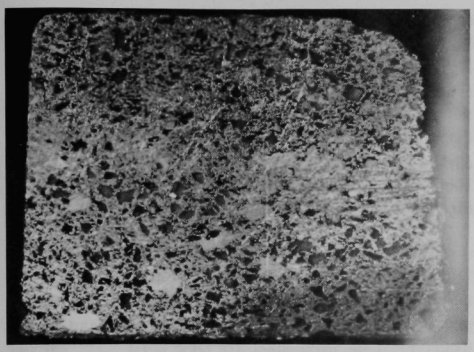

Fig. V-7. Photograph of a Section of Molybdenum-Foam Cell Cathode after an Experiment. ANL Neg. No. 308-2427 T-1.

sulfide that would be expected on the basis of the amount of lithium transferred.

The sulfide analysis of the core sections indicates that very little reaction product is transported into the porous molybdenum structure. The visual evidence based on the photograph in Fig. V-7 tends to support this conclusion since the reaction products appear to be concentrated in a very thin layer at the bottom edge, which was the edge in contact with the electrolyte. The charge-discharge behavior of similar cells also indicates that very little product diffuses into the cathode. Since this behavior would not be expected on the basis of temperature, viscosity, or deposition rate, it appears that the cathode current-collector structure is of great importance in determining the mass-transport behavior of reaction products in the cathode.

c. Surface Diffusivity of Iron in Liquid Sodium
(J. G. Eberhart, W. A. Kremsner)

A study of the rate of grain-boundary grooving of α-iron (bcc) in liquid sodium has been carried out to determine (1) the importance of surface diffusion in the corrosion and transport processes that occur in a sodium environment and (2) whether the sodium environment enhances surface-tension-driven mass transport over that observed in a vacuum environment. In the last annual report (ANL-7675, p. 66), a discussion of sample preparation, annealing, and interferometric examination was presented, along with some preliminary results at 800°C. Since then, experiments were performed at 600, 700, 800, and 880°C, and the results of this further analysis are presented here.

When a polycrystalline metal is annealed at a sufficiently high temperature, grain-boundary grooves are produced at the intersection of the grain boundaries with the metal surface. The grooves are formed by surface-tension-driven mass transport and have a profile as indicated schematically in Fig. V-8. With the development by Mullins [57,58] of a theory of grain-boundary grooving, it has been possible to distinguish between the mass-transport mechanisms of surface and volume diffusion and to determine the diffusion coefficient.

One technique available for elucidating the mechanism of grain-boundary grooving is the examination of individual groove profiles. According to Mullins' theory, the profile of a grain-boundary groove formed by surface diffusion is different from one formed by volume diffusion. Allen [59] has characterized this difference with the relative ridge height of the groove, h/d, where h is the ridge height and d is the groove depth (both shown in Fig. V-8). The ratios are

$$h/d = 0.199 \text{ for surface diffusion} \tag{28}$$

$$h/d = 0.149 \text{ for volume diffusion} \tag{29}$$

Relative ridge-height measurements were made of many grooves on each of the specimens annealed at 700, 800, and 880°C (grooves produced at 600°C were too small for accurate measurement). The distributions were not significantly different at the three temperatures, and a histogram for the combined data is shown in Fig. V-9. The mode of the distribution is in good agreement with the value of $h/d = 0.199$ expected for surface diffusion.

A more common method of distinguishing between surface and volume diffusion is through the kinetics of grain growth. Mullins has shown that

$$w = 4.6\,(Bt)^{1/4} \text{ for surface diffusion} \tag{30}$$

$$w = 5.0\,(At)^{1/3} \text{ for volume diffusion} \tag{31}$$

where w is the groove width (shown in Fig. V-8), t is the annealing time, and B and A are constants at a given temperature.

Examination of many grooves on each α-iron surface showed a variability in groove width. To facilitate comparison of grooves on different specimens, the widest groove observed on each specimen was selected for the kinetic analysis. The results are shown in Fig. V-10 in a log-log plot of w versus t. The data at 880, 800, and 700°C were fitted to a straight line by the method of least squares, with the

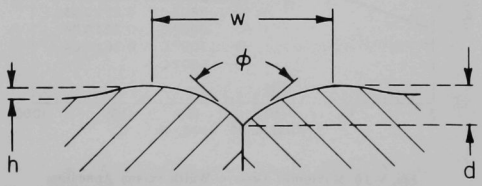

Fig. V-8. Schematic Cross Section of a Grain-Boundary Groove. ANL Neg. No. 308-2517.

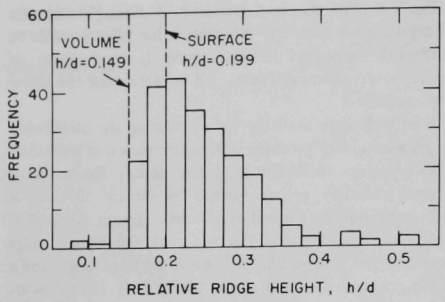

Fig. V-9. Relative Ridge Heights of Grain-Boundary Groove for α-Iron in Liquid Sodium, All Temperatures Combined. ANL Neg. No. 308-2518.

resulting slopes and their standard deviations shown. At 600°C, only the longest-annealed specimen has sufficiently well-developed grooves for width measurement. Within experimental error, the slopes agree with the exponent of 1/4 in Eq. 30. Thus, the groove-growth kinetics also suggest a surface-diffusion mechanism for α-iron in a liquid sodium environment.

From the intercepts at 880, 800, and 700°C, as well as from the maximum groove width on the single 600°C specimen, the parameter B was calculated using Eq. 30. Mullins' analysis of grain-boundary grooving showed that

$$B = D_{SL}\nu\gamma_{SL}\Omega^2/kT \qquad (32)$$

where D_{SL} is the diffusion coefficient for transport of solid atoms along the solid-liquid interface, ν is the surface atom concentration of the solid, γ_{SL} is the solid-liquid interfacial tension, Ω is the atomic volume of the solid, k is the Boltzmann constant, and T is the absolute temperature. Equation 32 was used to calculate D_{SL} from B. Here it was assumed that the iron surface atom concentration is that of the closest-packed (110) plane with $\nu = 2^{-1/6}\Omega^{-2/3}$. At the temperature of the experiments, $\Omega = 7.8 \times 10^{-24}$ cm³/atom. The interfacial tension is taken to be γ_{SL} = 2000 erg/cm². The resulting values of D_{SL} are shown in Fig. V-11. They are fit to an Arrhenius equation

$$D_{SL} = D^{\circ}_{SL}\exp(-Q_{SL}/kT) \qquad (33)$$

where D°_{SL} is a pre-exponential factor and Q_{SL} is the activation enthalpy for surface diffusion. The least-squares values of these parameters are $D^{\circ}_{SL} = 10^{1.5\pm0.7}$ cm²/sec and $Q_{SL} = 1.6 \pm 0.1$ eV/atom. Any error that may be present in the assigned value of γ_{SL} will affect D°_{SL} but not Q_{SL}.

Blakely and Mykura [60] measured the surface-diffusion coefficient of α-iron in vacuum, D_{SV}. Their results, shown for comparison in Fig. V-11, were characterized by $D^{\circ}_{SV} = 10^5$ cm²/sec and $Q_{SV} = 2.5 \pm 0.2$ eV/atom, based on γ_{SV} = 2000 erg/cm² and the same values of ν and Ω. It can be seen that over nearly all the α-iron range (up to 911°C) surface diffusion is more rapid in a liquid sodium environment than in vacuum. Furthermore, surface diffusion in sodium is found to occur with a lower activation enthalpy than in vacuum.

According to the terrace, ledge, and kink model of a crystal surface [61], the activation enthalpy for surface diffusion is the sum of the enthalpy of formation of an adsorbed atom and the enthalpy of activation for movement of the atom. In a vacuum this process involves the

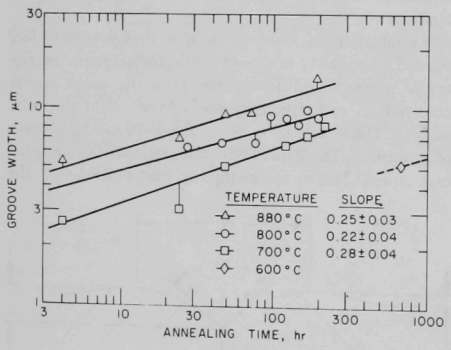

Fig. V-10. Maximum Groove Width versus Annealing Time for α-Iron in Liquid Sodium. ANL Neg. No. 308-2408.

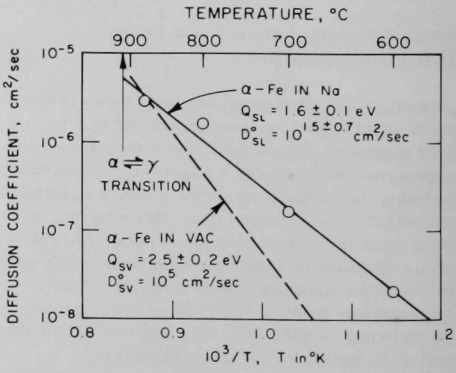

Fig. V-11. Surface Diffusion Coefficient versus Reciprocal Temperature for α-Iron in Liquid Sodium (dashed line is for α-iron in vacuum, from ref. 60). ANL Neg. No. 308-2407.

breaking of certain Fe-Fe bonds. In liquid sodium the same Fe-Fe bonds are probably broken, but, in addition, interactions occur between the diffusing iron atom and the neighboring sodium atoms. Thus bonding considerations provide a possible explanation of the lower activation enthalpy in liquid sodium.

d. The Simultaneous Determination of Surface and Volume Diffusion Coefficients (J. G. Eberhart, H. M. Feder)

The growth of a grain-boundary groove often occurs by the combined action of surface and volume diffusion. A technique is presented here for separating the two contributions without previous knowledge of the volume diffusion coefficient, making grain-boundary grooving a more powerful tool for diffusion study.

Mullins has shown that the time dependence of the width of a grain-boundary groove, w, is $t^{1/4}$ for surface diffusion [62] and $t^{1/3}$ for volume diffusion [63]. In many studies an empirical law of the form $w \propto t^{1/n}$, where n is a constant and $3 < n < 4$, has been demonstrated, implying the combined action of surface and volume diffusion. Mullins and Shewmon [64] developed a theoretical equation for groove growth under the combined mechanisms. Their result has been applied in a number of investigations [65–67] of metals whose volume self-diffusion coefficient, D_V, was previously known from independent measurements. The value of D_V is used in an iterative procedure with the groove-width measurements to calculate the surface diffusion coefficient, D_S. This procedure is not suitable in situations where D_V is unknown. For this case an alternative method of analysis, first suggested by Chang [68] and further developed here, is capable of yielding values of D_S and D_V simultaneously. It is based on a combination of the Mullins and Shewmon equation and the empirical $w \propto t^{1/n}$ growth law.

According to the theory of Mullins [62,63], the development of a grain-boundary groove proceeds at the rate $dw/dt = \beta_S/w^3$ for surface diffusion only and $dw/dt = \beta_V/w^2$ for volume diffusion only. If integrated, these equations become $w^4 = 4\beta_S t$ and $w^3 = 3\beta_V t$ or, in their more familiar forms, $w = 4.6\ (Bt)^{1/4}$ and $w = 5.0\ (Ct)^{1/3}$. Mullins has shown that the parameters B and C are functions of temperature given by $B = D_S\gamma\Omega^2\nu/kT$ and $C = D_V\gamma\Omega/kT$, where γ is the surface tension, Ω is the atomic volume, and ν is the surface atom concentration. According to Mullins and Shewmon, the groove-growth rate for the combined action of surface and volume diffusion is the sum of the rates by each mechanism and thus

$$dw/dt = (\beta_S/w^3) + (\beta_V/w^2) \tag{34}$$

On the other hand, the empirical growth law referred to previously, which is deduced from the generally observed linearity of log-log plots of w versus t, yields a growth rate of $d \log w/d \log t = 1/n$, or

$$dw/dt = w/nt \tag{35}$$

Equating the right-hand members of Eqs. 34 and 35 then yields, after rearrangement

$$w^4/t = n\beta_S + n\beta_V w \tag{36}$$

Equation 36 is thus a hybrid of the existing theoretical and empirical equations for groove growth. The result implies that a plot of w^4/t versus w should be linear with a slope of $n\beta_V$ and an intercept of $n\beta_S$. To calculate β_V and β_S, it is then only necessary to obtain $1/n$ from the slope of a log-log plot of w versus t.

To test this method of analysis of grooving kinetics, it is necessary to employ data for a metal for which D_V is known from independent measurements. Suitable groove-width data were kindly provided by N. A. Gjostein [69] from his study of the groove development of copper in a hydrogen atmosphere [65]. Figure V-12 shows a log-log plot for Gjostein's copper specimen annealed at 1020°C. From a linear-regression analysis, a slope of $1/n = 0.307 \pm 0.003$ is obtained. In Fig. V-13, a plot of w^4/t versus w is shown, and a linear-regression analysis provides a slope of $n\beta_V = 210 \pm 7\ \mu m^3/hr$ and an intercept of $n\beta_S = 870 \pm 140\ \mu m^4/hr$. From the value of $1/n$, it is found that $\beta_V = 64.5 \pm 2.2\ \mu m^3/hr$ and $\beta_S = 267 \pm 44\ \mu m^4/hr$. Thus $C = 3\beta_V/(5.0)^3 = (4.30 \pm 0.15) \times 10^{-16}\ cm^3/sec$. Finally, using Gjostein's [65] values of $\gamma = 1670\ erg/cm^2$ and $\Omega = 1.18 \times 10^{-23}\ cm^3/atom$, a volume self-diffusion coefficient of $D_V = CkT/\gamma\Omega = (3.89 \pm 0.13) \times 10^{-9}\ cm^2/sec$ is obtained. Considering the uncertainty in γ, this result compares favorably with existing values (primarily from tracer sectioning experiments) for copper [70–74], which range from 2.7×10^{-9} to $4.0 \times 10^{-9}\ cm^2/sec$ at 1020°C after correction for correlation effects [75].

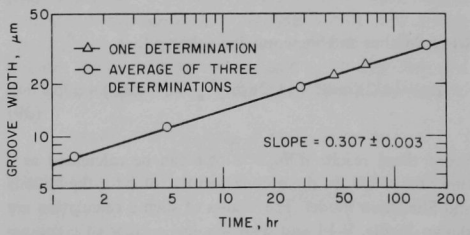

Fig. V-12. Log-Log Plot of Groove Width versus Annealing Time for Copper at 1020°C (data of Gjostein[65]). ANL Neg. No. 308-2406.

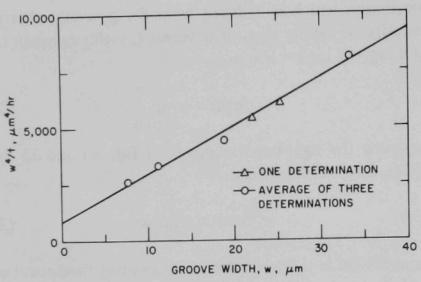

Fig. V-13. Linear Analysis for Simultaneous Determination of Surface and Volume Diffusion Coefficients for Copper at 1020°C (data of Gjostein[65]). ANL Neg. No. 308-2405.

From these results it is possible to calculate the fraction of grooving produced by volume diffusion, ϕ, at any stage of groove development. From the rate of growth by each mechanism

$$\phi = \frac{(\beta_V/w^2)}{(\beta_S/w^3) + (\beta_V/w^2)} = \frac{aw}{1 + aw} \tag{37}$$

where $a = \beta_V/\beta_S$. From the slope-to-intercept ratio in Fig. V-13, $a = 0.241 \pm 0.040\ \mu m^{-1}$. The measured groove widths in Gjostein's data range from 7.4 to 34.9 μm. Thus during his observations ϕ varied from 0.64 to 0.89 and the groove growth was dominated by volume diffusion.

Because of the generally observed linearity of log-log plots of groove-growth data, it is of interest to compare this empirical growth law, embodied in Eq. 35, with the theoretical growth law of Mullins and Shewmon, stated in Eq. 34. A convenient means of comparison is the tangent of a log-log plot, $d \log w/d \log t$. For the empirical Eq. 35, it was shown that $d \log w/d \log t = 1/n$, which is a constant. On the other hand, for the theoretical Eq. 34

$$d \log w/d \log t = (t/w)/(dw/dt) = a^4 \beta_S t\,[(aw)^{-4} + (aw)^{-3}] \tag{38}$$

where Mullins and Shewmon have shown that

$$aw - (1/2)(aw)^2 + (1/3)(aw)^3 - \ln(1 + aw) = a^4 \beta_S t \tag{39}$$

From these results $d \log w/d \log t$ can be calculated as a function of aw or, more conveniently, of ϕ for the Mullins and Shewmon model. The results of such a calculation are shown in Fig. V-14 and span the entire range of combinations of the two mechanisms from pure surface diffusion ($\phi = 0$) to pure volume diffusion ($\phi = 1$). The previously determined range of ϕ values for Gjostein's copper measurements at 1020°C corresponds to $d \log w/d \log t$ values between 0.292 and 0.318. Thus the Mullins and Shewmon model shows little variation in $d \log w/d \log t$ for a typical range of w values.

B. MOLTEN SALT STUDIES (E. J. Cairns)

Understanding the thermodynamic, physicochemical, and structural properties of molten salts continues to be of importance to many AEC programs. Emphasis in this program has shifted slightly to include the study of binary and ternary systems in which one component is a metal or semi-metal. The extent to which molten-salt electrolytes interact with and influence the behavior of electrochemical systems has been investigated. The use of spectroscopic methods to elucidate the structure of molten salts and species existing in molten salt media continued to be an important area of research.

1. Thermodynamics

a. Phase Equilibria by Solubility Methods (V. A. Maroni, E. J. Hathaway)

(1) Solubilities in Selenium-Containing Systems. Measurements of the solubility of Li_2Se in molten alkali halides have been extended to include the LiF-LiCl-LiI and the LiBr-RbBr eutectics. In these experiments samples of Li_2Se were equilibrated at various temperatures with the selected halide eutectic, and filtered samples were taken. The newly measured solubilities of Li_2Se, determined by chemical analysis of the filtered samples, are plotted in Fig. V-15 together with previously reported results (ANL-7675, p. 130). Results for the all-lithium eutectics lie on a reasonably straight line with a slope corresponding to a heat of solution of 13.3 kcal/mol. The points for the LiBr-RbBr eutectic lie on a line of nearly the same slope but displaced significantly to lower solubility values. The presence of a large cation like rubibium apparently suppresses the solubility of selenide ion.

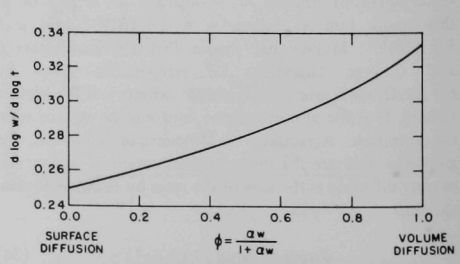

Fig. V-14. Tangent of a Log-Log Groove-Growth Plot versus the Fraction of Grooving Which Occurs by Volume Diffusion. ANL Neg. No. 308-2556.

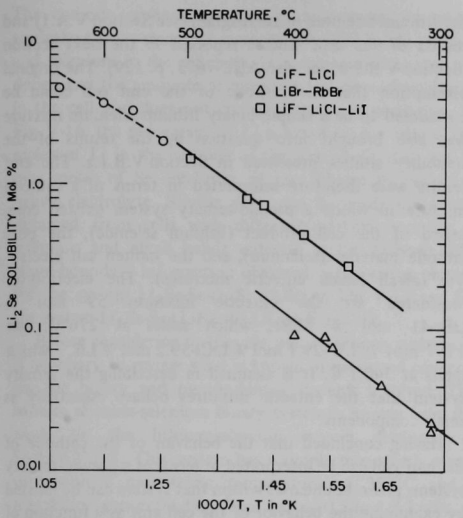

Fig. V-15. Solubilities of Li_2Se in Various Eutectics Containing Lithium Halide. ANL Neg. No. 308-2404.

Measurements of the solubility of selenium in molten LiF-LiCl-LiI (ANL-7675, p. 130) indicated that very little selenium dissolves in molten lithium halides in the 350–500°C range. A study has been conducted to determine the effect of the presence of Li_2Se on the solubility of selenium in molten alkali halides. Saturated solutions of Li_2Se, Se, and an 80 mol % Se-Li_2Se mixture were prepared in the LiBr-RbBr eutectic at 365 ± 1°C. After each sample was equilibrated, a portion of the salt phase was filtered off and analyzed for selenium. The results of these measurements are given in Table V-8, along with the results of an experiment conducted with the same Li_2Se mixture dissolved in the LiCl-CsCl eutectic. A substantial increase is noted in the solubility of selenium from Li_2Se mixtures compared with the cases in which Li_2Se alone and Se alone were the solutes. This is believed to be due to the formation of soluble polyselenides, Se_x^{-n}, where the values of n and x have not been clearly determined. The solubility of polyselenide ion appears to increase with increasing size of the added cation.

Solubility measurements of two lithium halide eutectics in liquid selenium have also been made. The solubilities of LiCl-CsCl and LiBr-RbBr in selenium were determined as a function of the amount of Li_2Se present. After saturation of the selenium with a sample of each salt at 395 ± 10°C, a portion of the selenium phase was filtered off and analyzed for the constituent elements of the salt. These experiments were then repeated with Li_2Se added to the salt-selenium mixture prior to equilibration. The results of these measurements are summarized in Table V-9.

The combined solubility results presented in this section and in a previous report (ANL-7675, p. 130) for the constituent binary systems of the Li_2Se-Se-alkali halide pseudo-ternary systems allow a semi-quantitative determination of several phase boundaries to be made. In the absence of Li_2Se, the mutual solubilities of alkali halides in selenium and selenium in alkali halides are very low, usually less than 0.1 mol % at temperatures between 350 and 400°C. Also, the solubility of Li_2Se in alkali halides in the absence of elemental selenium is found to be less than 0.5 mol % at temperatures below 400°C. Solubilities in the Li_2Se-Se binary system are discussed in detail in Section V.A.1 of this report. The total dissolved selenium in the alkali halide-rich phase is increased markedly by the presence of Li_2Se as well as by the addition of large cations such as Cs^{1+} to the Li_2Se-Se-alkali halide ternary mixtures. The solubility of alkali halide in selenium is very low (<0.1 mol % at 400°C) and is not appreciably enhanced by the presence of Li_2Se. The large amounts of lithium and cesium in the selenium sample saturated with the LiCl-CsCl-Li_2Se mixture (see Table V-9) probably entered the selenium as Li_2Se and Cs_2Se since the halide content of this sample was extremely low.

(2) Solubilities in Sulfur-Containing Systems. Solubility experiments similar to those described above were also conducted on the constituent binary systems of the Li_2S-S-alkali halide pseudo-ternary system. The solubility of Li_2S in the LiF-LiCl-LiI eutectic as a function of temperature has already been reported (ANL-7675, p. 130). The solubilities of sulfur in other alkali halide mixtures have not been measured extensively owing to the high vapor pressure of sulfur in the temperature region of interest. However, they are assumed to be very low, and preliminary experimental results from other sources tend to

TABLE V-8. Solubilities of Several Selenium-Containing Solutes in Molten Lithium Halides

Solvent Eutectic[a]	Solute	Temp (°C)	Total Selenium Dissolved in the Eutectic
LiBr-RbBr	Se	365.5	0.03_0 mol % Se
LiBr-RbBr	Li_2Se	364	0.02_6 mol % Se
LiBr-RbBr	Li_2Se + Se[b]	365	1.45 mol % Se
LiCl-CsCl	Li_2Se + Se[b]	365	7.3 mol % Se

[a]Eutectic compositions: 59 mol % LiBr-41 mol % RbBr; 60 mol % LiCl-40 mol % CsCl. [b]Se/Li_2Se mole ratio ≈4.0.

TABLE V-9. Solubilities of Various Solute Salt Mixtures in Selenium

Solute	Temp (°C)	Composition (mol %) Li	Rb	Cs	Cl	Br
LiBr-RbBr	384–404	0.007	0.001	-	-	0.03
LiBr-RbBr	391–411	0.003	0.001	-	-	0.02
LiBr-RbBr+Li_2Se	385–405	0.003	0.016	-	-	0.02
LiCl-CsCl	385–405	0.007	-	0.01	0.13	-
LiCl-CsCl+Li_2Se	387–407	6.2	-	5.0	<0.02	-

support this assumption [76]. The solubility of alkali halides in sulfur also remains to be measured.

A series of experiments has been conducted to determine the relative solubilities of S, Li_2S, and 80 mol % S-Li_2S mixture in LiBr-RbBr in the 360–370°C range. An experiment to determine the solubility of 80 mol % P_4S_{10}-Li_2S was also conducted. Results of these studies are presented in Table V-10. As in the case of the Li_2Se-Se mixtures, the solubility of the chalcogen is increased markedly by the presence of the lithium chalcogenide. The sulfur-sulfide solubilities are generally higher than those of the selenium-selenide mixtures. Some problems were encountered in completely separating immiscible phases, which may have influenced the sulfur and sulfide results in Table V-10. In any case the effect of the difficulty of phase separation was not considered to be significant.

The solubility of P_4S_{10} in alkali halides in the presence of Li_2S was significantly lower than the solubility of the Li_2S-S mixture, and the phosphorus and sulfur were observed to dissolve nearly stoichiometrically. Apparently sulfide ions, S^{2-}, have more difficulty attaching themselves to the compact P_4S_{10} cages than to the long sulfur chains in elemental molten sulfur.

The general features of the Li_2S-S-alkali halide pseudo-ternary phase diagram inferred from these studies appear to be much the same as those inferred for the Li_2Se-Se-alkali halide diagram. Mutual solubilities of sulfur in the alkali halide mixture and alkali halides in sulfur appear to be low, although the latter measurements have not been made. The solubility of Li_2S in alkali halides is generally lower than that of Li_2Se in the corresponding eutectics. Solubility results for the Li_2S binary system are given in Section V.A.1 of this report. The addition of Li_2S to sulfur-alkali halide mixtures significantly increases the dissolved sulfur content of the salt-rich phase probably because of the formation of polysulfide ions. More detailed presentations of these results in terms of the Li_2S-S-LiX pseudo-ternary phase diagram will be presented in future reports.

b. Phase Diagrams of Pseudo-Ternary Lithium Selenide-Selenium-Alkali Halide Systems (P. T. Cunningham, E. J. Cairns, V. A. Maroni, S. A. Johnson, G. H. Kucera, E. J. Hathaway)

Investigation of these pseudo-ternary systems was undertaken in order to resolve apparent discrepancies between the lithium-selenium phase diagram (see Section V.A.1) and results of the emf studies reported in the next section (Section V.B.1.c; see also ANL-7675, p. 129). The original assumption that the cathode of the emf cell could be considered to be a simple binary lithium-selenium mixture was also brought into question by the results of the solubility studies presented in Section V.B.1.a. The emf results were therefore interpreted in terms of a cathode mixture in which a pseudo-ternary system existed comprised of the cell product (lithium selenide), the pure cathode material (selenium), and the molten salt electrolyte (alkali halide eutectic mixtures). The electrolytes considered are the eutectic mixtures 59 mol % LiBr-41 mol % RbBr, which melts at 276°C, an 11.7 mol % LiF-29.1 mol % LiCl-59.2 mol % LiI, which melts at 340.1°C. It is assumed in describing the ternary system that the eutectic mixtures behave essentially as single components.

Having concluded that the behavior of the cathode of the emf cell can be interpreted in terms of a pseudo-ternary system, phase boundaries within that system can be located by examining the behavior of the cell emf as a function of composition and temperature. For example, if the temperature is held constant and the cathode composition is varied while remaining within a two-phase region, then the compositions of the two phases can be expected to change (unless the changing overall composition happens to move along a tie line) and hence the cell emf will change. If, on the other hand, the overall composition lies in a three-phase region, changing the composition at constant temperature will merely alter the relative amounts of the three phases present, but will not alter their compositions, and the emf must remain constant. Thus, in a constant-temperature plot of emf versus cathode composition, phase boundaries are identified with discontinuities in slope. Such a plot is shown in Fig. V-16. Details of the emf measurements are presented in Section V.B.1.c. It can be seen that discontinuities in slope occur at 18.8, 28, and 32 at. % lithium.

TABLE V-10. Solubilities of Various Sulfur-Containing Solutes in the LiBr-RbBr Eutectic

Solute	Temp. (°C)	Concentration in LiBr-RbBr (mol %) S	P
Li_2S	360	1.5	-
S	371	0.3	-
Li_2S + S	371	11	-
P_4S_{10} + Li_2S	373	2.5	0.8

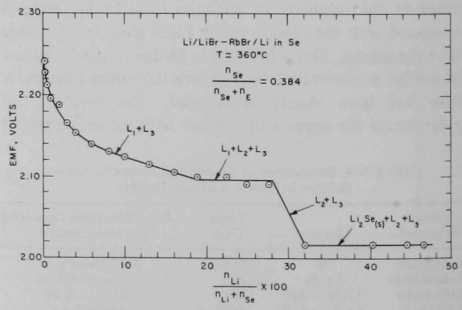

Fig. V-16. Emf as a Function of Temperature for Li/LiBr-RbBr/Li in Se Cell. ANL Neg. No. 308-2403.

The cathode composition can be represented in several equivalent ways since the quantity of alkali halide eutectic and selenium in the cell cathode is determined by the cell design and the amounts of selenium and electrolyte placed in the cell and does not change during cell operation. In Fig. V-16, the percentage of Li is based on the ratio of the moles of Li in the cathode to the sum of the moles of Li plus moles of Se, exclusive of the lithium in the alkali halide electrolyte. Similar plots can be made using data obtained from cells with different relative amounts of selenium and alkali halide eutectic in the cathode. The phase-boundary information obtained in this way is plotted for the system Li_2Se-Se-(LiBr-RbBr) in Fig. V-17 and for the system Li_2Se-Se-(LiF-LiCl-LiI) in Fig. V-18.

Before considering further the pseudo ternary systems, it is necessary to review what is known or presumed concerning the binary and pseudo-binary systems involved. The lithium selenide-selenium binary system is known from the work on the lithium-selenium system discussed in Section V.A.1. This system has a simple monotectic structure with a monotectic temperature of 350°C and a miscibility gap extending from below 0.5 mol % Li_2Se to 22 mol % Li_2Se. The selenium-rich liquid L_1 freezes at 220°C, the freezing point of pure selenium. The relatively lithium-rich liquid, L_2, exists between the upper liquidus and the immiscibility boundary, both of which rise steeply. Less is known about the selenium-alkali halide systems. Presumably they have no intermediate phases [although rubidium-selenium compounds may present complications for the Se-(LiBr-RbBr) system]. The solubility studies discussed in the preceding subsection indicate that the mutual solubilities in these systems are quite low. The thermal analysis discussed below shows that the presence of selenium does not alter the melting points of the alkali halide eutectics and vice versa.

On the basis of the data obtained from emf studies and what is known about the binary systems, the pseudo-ternary isothermal sections shown in Figs. V-17 and V-18 were proposed. The two liquid phases present in the lithium

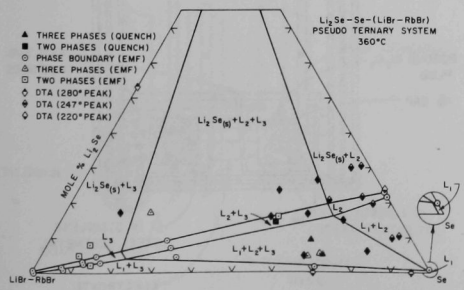

Fig. V-17. Li_2Se-Se-(LiBr-RbBr) Pseudo-Ternary System at 360°C. ANL Neg. No. 308-2402.

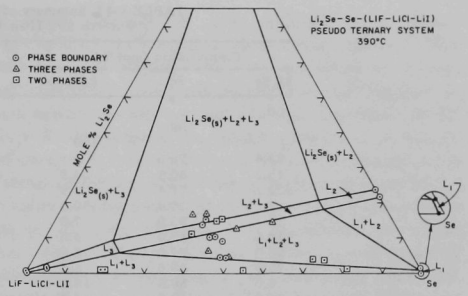

Fig. V-18. Li_2Se-Se-(LiF-LiCl-LiI) seudo-Ternary System at 390°C. ANL Neg. No. 308-2401.

selenide-selenium binary are seen to extend into the ternary phase diagram at the temperatures of these sections, and the designations L_1 and L_2 are retained. The alkali-halide-rich liquid, L_3, also extends into the ternary diagram. The region of three-liquid equilibrium is a particularly interesting feature of this system.

To further characterize these systems, a series of differential thermal analysis (DTA) curves was obtained for the pseudo-ternary system containing LiBr-RbBr. The results are given in Table V-11; the compositions of the samples are also indicated in Fig. V-17. All of the DTA samples weighed about 0.08 g and were contained in aluminum capsules sealed with press-fit caps. Curves were obtained using a du Pont Model 900 Differential Thermal Analyzer with a heating rate of 5°C per minute; alumina served as the reference material. It can be seen in Table V-8 that there are three thermal peaks observed at about 280, 247, and 220°C. These are associated with the disappearance of L_3, L_2, and L_1, respectively. Under this interpretation there would be four four-phase equilibria or thermal invariants, two of which occur very close to pure LiBr-RbBr and are essentially isothermal. These thermal data are entirely consistent with the proposed pseudo-ternary system. The thermal data can provide a qualitative idea as to the range of compositions covered by L_2 and L_3. For compositions lying near the lithium selenide-selenium binary, the peak associated with the disappearance of L_3 is not observed. This would seem to indicate that L_2 extends far enough into the phase diagram to prevent formation of L_3 from these compositions.

An effort has been made to determine the degree to which L_2 and L_3 extend into the phase diagram by equilibration of samples having compositions lying within the three-liquid region followed by separation of the phases for chemical analyses after quenching. To date these efforts have failed since, despite rapid separation of L_1, L_2 and L_3 do not separate completely. Microscopic examination of the quenched samples shows that there are indeed two phases present in addition to L_1, but their densities are

TABLE V-11. Summary of DTA Data on Se, Li_2Se, LiBr-RbBr Eutectic and Their Binary and Ternary Mixtures

Composition (mol %)			Peak Temperatures of Endothermic Effects Noted (°C)[a]			
Li_2Se	Se	Eutectic				
100						1302[b]
	100		221			
		100			280	
23.4	76.6		223			358[c]
16.2	60.3	23.5	221[d]	247	275	
22.1	71.4	6.5	221	245	(267)	350[e]
	70.0	30.0	221		283	
	93.0	7.0	221		284	
10.0	85.0	5.0	222	247	(270)	
20.0	75.0	5.0	222	246	(270)	
30.0	65.0	5.0	221	244	(260)	
6.0	80.5	13.5	222	247	277	
14.9	69.8	15.3	221[d]	247	280	
21.2	63.8	15.0	225[d]	246	(263)	
26.2	58.7	15.1	221[d]	247	282	
4.7	65.8	29.5	222	247	277	
16.0	51.8	32.2	222	247	276	
22.8	50.1	27.1	228 (?)	247	272	
52.4		47.6			278	
10.7	86.8	2.4	222	248	(274)	350[e]
30.4	67.5	2.1	223	246		
17.4	14.2	68.4		245	274	

[a]The exact temperature of a reaction is difficult to determine using DTA. Here we consistently report peak temperature. Uncertainties of ±2°C due to changing peak size might be expected. Values in ( ) are shoulders (not peaks) and may be associated with a liquidus crossing.
[b]The only effect seen is the mp of Li_2Se at 1302°C. This value is confirmed by other methods.
[c]The Li-Se Binary has a monotectic reaction at 350°C.
[d]Peak shows doubling.
[e]Seen on first heating only.

apparently quite similar. Other quenched samples having compositions in the two-liquid region between L_2 and L_3 were examined and were found to contain two phases, as expected. It seems likely that the consolute temperature of the miscibility gap between L_2 and L_3 is not very high, probably below 500°C.

Fewer supplemental supporting data are available for the pseudo-ternary system involving LiF-LiCl-LiI eutectic. Qualitatively, at least, it does not seem to differ greatly from the systems involving the LiBr-RbBr eutectic since the emf data show very similar behavior.

c. *Thermodynamics of Pseudo-Ternary Lithium Selenide-Selenium-Alkali Halide Systems by Emf Methods*
(E. J. Cairns, G. H. Kucera)

As explained in Section V.B.1.b, it has been found that fused lithium halide-containing electrolytes and lithium-selenium mixtures of certain compositions show significant solubilities in each other. This makes it necessary to include the influence of the electrolyte on the behavior of emf (and other) cells using these combinations of electrolytes and cathodes. This influence has been taken into account by considering the electrolyte mixture to be a single component in the pseudo-ternary lithium selenide-selenium-electrolyte system.

The experiments were performed in two ways, using two types of emf cells. The Type I cell, shown in Fig. V-19, consisted of a lithium reference electrode and a lithium-selenium alloy electrode immersed in the molten-salt

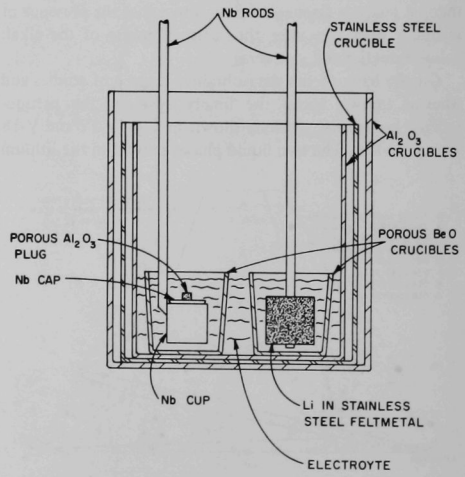

Fig. V-19. Type I Emf Cell for Studying the Effect of Temperature on Emf. ANL Neg. No. 308-2557.

electrolyte, each electrode being located in a separate compartment. The lithium electrode was prepared by impregnating a porous stainless steel cylinder (~1 cm high, ~1 cm in diameter) with molten lithium (99.97% pure, Foote Mineral Co.), which was retained in the porous metal by surface-tension forces. The lithium-selenium alloy electrode was prepared by mixing selenium (99.999+% pure, American Smelting and Refining Co.) with Li_2Se (prepared from Li and Se by vapor-phase transfer of Se) in the desired proportions. The mixture was placed in a cylindrical niobium cup (~0.7 cm^3), which had a tightfitting niobium cap containing a porous Al_2O_3 plug passing through it (for electrolyte contact). The electrolytes were prepared from salts purified by Anderson Physics Laboratory and were lithium-contacted before use to remove any traces of moisture and heavy metal ions. Two electrolytes were used: 59 mol % LiBr-41 mol % RbBr (mp = 278°C) and 11.7 mol % LiF-29.1 mol % LiCl-59.2 mol % Li (mp = 340.9°C). The Type I cell was operated in a helium atmosphere (<2 ppm H_2O, <5 ppm O_2, <5 ppm N_2) in an electric furnace and was primarily used to study the effect of temperature (280–525°C) on emf for various cathode alloy compositions.

The Type II cell, shown in Fig. V-20, was a three-compartment H-cell, which was loaded with weighed amounts of Li, Se, and electrolyte, assembled and sealed in a helium atmosphere, and operated in a molten $NaNO_3$-KNO_3 bath for good temperature uniformity. This cell was used primarily to study the effect of lithium-selenium alloy composition on emf, although the effect of temperature on emf was also studied. Operation of the Type II cell was usually started with pure selenium; changes of composition were performed by electrochemical transference of lithium into the selenium, keeping count of the number of coulombs involved. The ratio of selenium to electrolyte in the selenium compartment was varied from one cell to another in order to cover a wide range of selenium-to-electrolyte ratios in connection with the pseudo-ternary phase diagram. The rate of achievement of equilibrium varied from a few hours to a day or longer; this was enhanced by stirring the alloy with the spiral niobium current collector, which could be moved with the aid of a rubber coupling.

The emf measurements were made with high-input-impedance (10^{10} to 10^{13} ohms) differential dc voltmeters (Keighley Model 630 and Hewlett-Packard Model 3420B). The output of the voltmeters and the cell temperature were recorded by a strip-chart recorder in order to provide an easy means for identifying the equilibrium point. The emf readings for a given temperature and composition with the same cell were reproducible within 3 mV; readings from cell to cell were reproducible within about 5 mV. The current used for changing the composition of the lithium-selenium alloy (usually <50 mA) was supplied by a Wenking Model 61RS potentiostat connected as a galvanostat.

Typical results for emf as a function of temperature for various lithium-to-selenium mole ratios are shown in Fig. V-21. The data points for the lines marked 10.0 to 27.62 are too numerous and too closely spaced to be shown. Note that all of the data in this figure were taken from a cell using the LiBr-RbBr eutectic electrolyte, with a given selenium-to-electrolyte ratio in the selenium compartment $[n^0_{Se}/(n^0_{Se} + n) = 0.384]$. Three general types of

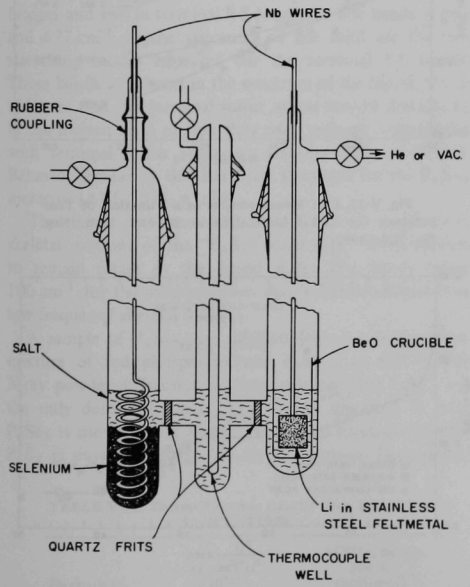

Fig. V-20. Type II Emf Cell for Studying the Effect of Alloy Composition on Emf. ANL Neg. No. 308-2558.

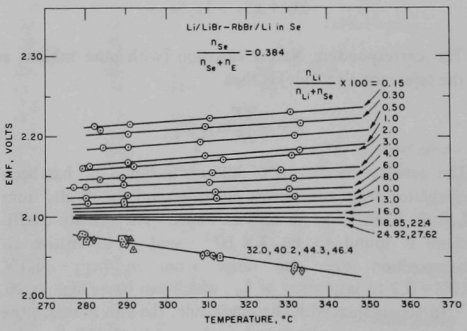

Fig. V-21. Emf Measurements of the Li/LiBr-RbBr/Li in Se Cell. ANL Neg. No. 308-2400.

behavior can be noted in the figure: (1) For lithium contents below about 19 mol %, i.e., $[n_{Li}/(n_{Li} + n_{Se})] \times 100 < 19.0$, $(\partial E/\partial T)$ is positive and $\partial E/\partial \ln x_{Li} = RT/2F$. (2) In the range ~19 to ~28 mol % Li, $(\partial E/\partial T) \approx 0$ and $\partial E/\partial \ln x_{Li} \approx 0$. (3) For lithium contents of 32 to at least 46.4 mol %, $(\partial E/\partial T)$ is negative and $(\partial E/\partial \ln x_{Li}) = 0$. Figure V-16 shows these three regions in terms of an emf-vs-composition plot for a temperature of 360°C, and introduces a fourth region between 28 and 32 mol % Li in Se. These four regions can be understood on the basis of the pseudo-ternary phase diagram shown in Fig. V-17.

The results shown in Fig. V-16 for $n^{\circ}_{Se}/(n^{\circ}_{Se} + n_E) = 0.384$ correspond to a line in Fig. V-17 drawn parallel to the Li_2Se-Se side of the diagram, but located at 38.4% of the distance between the LiBr-RbBr corner and the Li_2Se-Se side. The discontinuous change of slope at 18.8% Li in Fig. V-16 corresponds to the point located at 4.4% Li_2Se, 33.9% Se, and 61.7% LiBr-RbBr in Fig. V-17. This is the location of the phase boundary between the regions labeled $L_1 + L_3$ and $L_1 + L_2 + L_3$ on the two figures. In this manner, the phase boundaries shown in Fig. V-17 were located from the emf results and were found to be consistent with the results of the thermal analyses and other results discussed in Section V.B.1.b.

It can be seen from Fig. V-17 that liquid L_1 is selenium containing small concentrations of salt (<0.02 mol %) and lithium (<0.5 mol %); liquid L_2 is a lithium-selenium-salt mixture containing (at 360°C) the equivalent of 16–23 mol % Li_2Se and up to several percent salt; liquid L_3 is the salt-rich phase containing up to about 6 mol % Li_2Se and up to about 21 mol % Se (at 360°C). In all two-phase regions, the emf is a function of composition (except along tie-lines).

In the case of the $Li_1 + L_3$ region, it is found from data such as those in Fig. V-16 that $\partial E/\partial \ln x_{Li} = RT/2F$, indicating that two electrons and two lithium atoms are involved in the overall cell reaction, which may be written

$$2Li + xSe \rightarrow Li_2Se_x$$

The corresponding Nernst equation (with pure lithium as the reference electrode) is then

$$E = -\frac{RT}{2F}\ln\gamma_{Li}x_{Li}$$

The activity coefficient of lithium in liquid L_1 has been calculated from the Nernst equation and the results from Li/LiBr-RbBr/Li in Se cells at 360°C. The activity coefficient is found to be 3×10^{-15} and is insensitive to composition over the range from $n_{Li}/(n_{Li} + n^{\circ}_{Se}) \times 100 = 0.2$ to saturation of L_1, which can be as high as 20.

In accordance with the phase rule, the emf is insensitive to composition in the $L_1 + L_2 + L_3$ and $Li_2Se(s) + L_2 + L_3$ regions. As the lithium (or electrolyte) content of the selenium compartment changes, the relative amounts of the three phases change accordingly, but the activities of the three components remain fixed as long as the overall composition remains in a three-phase region.

From the emf in the $Li_2Se(s) + L_2 + L_3$ region, and the knowledge that the lithium activity in L_1 saturated with L_2 (and L_3) is equal to the lithium activity in L_2 saturated with L_1 (and L_3), it was possible to apply the Gibbs-Duhem equation (assuming that the activity coefficient of salt in L_2 and L_3 was constant) in correcting the free energy of formation of Li_2Se to unit activities of lithium and selenium. At 360°C, $\Delta Gf^{\circ}(Li_2Se) = -94.0$ kcal/mol.

The same kinds of experiments as those described above were also performed with the LiF-LiCl-LiI eutectic as the electrolyte. Typical emf-vs-temperature and emf-vs-composition curves are shown in Figs. V-22 and V-23. The resemblances to the corresponding figures with the bromide electrolyte are clear. The pseudo-ternary phase diagram, constructed from the emf data for 390°C, is shown in Fig. V-18 and is similar to that of Fig. V-17. The activity coefficient of lithium in liquid L_1 and the free energy of

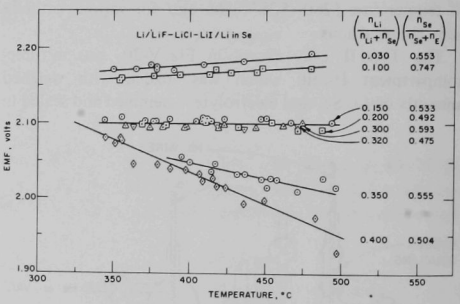

Fig. V-22. Emf Measurements as a Function of Temperature for Li/LiF-LiCl-LiI/Li in Se Cell. ANL Neg. No. 308-2399.

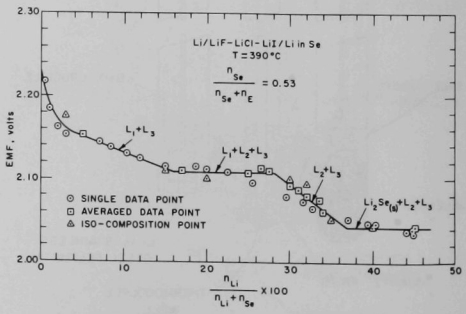

Fig. V-23. Emf Measurements as a Function of Composition for Li/LiF-LiCl-LiI/Li in Se Cell. ANL Neg. No. 308-2398.

formation of $Li_2Se(s)$, which were calculated from the emf results, are presented in Table V-12 together with the values from the bromide electrolyte cell.

2. *Structure Investigations by Spectroscopic Methods*
(V. A. Maroni, E. J. Hathaway)

a. Phosphorus-Chalcogen Compounds

Two phosphorus-chalcogen compounds, P_4S_7 and P_4Se_3, under investigation as cathode materials for electrochemical cells have been investigated by Raman spectroscopy. Raman spectra of the solid compounds were obtained at room temperature; the Raman spectrum of liquid P_4S_7 was obtained just above its melting point, 310°C. Raman spectra for solid and liquid P_4S_3, P_4S_{10} and liquid 85 at. % P-15 at. % S were reported previously (ANL-7675, pp. 138–140).

The spectra of liquid and solid P_4S_7 are shown in Fig. V-24 (a and b), and the vibrational frequencies and relative intensities determined from these spectra are listed in Table V-13. The bands in the liquid spectrum are broad and poorly resolved compared with those in the solid spectrum, however, frequencies of the principal bands and their relative intensities are nearly the same for the two spectra in the frequency range 450–100 cm^{-1}

In P_4S_7, five of the sulfur atoms are present in P-S-P bridges and two in terminal P-S locations. The bands at 663 and 677 cm^{-1} in the spectrum of the solid are the two stretching modes expected for the terminal P-S bonds. These bands are absent in the spectrum of the liquid, which indicates that the terminal sulfur atoms may be dissociated in the molten state or that they may undergo cross-linking with terminal sulfur atoms on adjacent P_4S_7 molecules. Behavior similar to this has been proposed for the P_4S_{10} molecule (ANL-7675, p. 139).

The bands between 475 and 100 cm^{-1} result from skeletal motions of the "P_4S_5" inner cage, which appears to remain intact in the liquid state. The bands below 100 cm^{-1} for the solid are either due to lattice vibrations or low frequency skeletal modes.

A sample of P_4Se_3 was distilled from a stoichiometric mixture of red phosphorus and P_4Se_{10} at 400°C. The X-ray powder diffraction pattern indicated that P_4Se_3 was the only detectable phase. The Raman spectrum of solid P_4Se_3 is shown in Fig. V-24c; the Raman spectrum of solid P_4S_3 is shown in Fig. V-24d for comparison. The spectral

TABLE V-12. Thermodynamic Results from Li/LiX/Li in Se Emf Cells

Electrolyte	γ_{Li} in L_1, 360°C	$\Delta Gf(Li_2Se, s)$, 360°C (kcal/mol)
LiBr-RbBr	3×10^{-15}	−94.0
LiF-LiCl-LiI	3×10^{-15}	−94.5

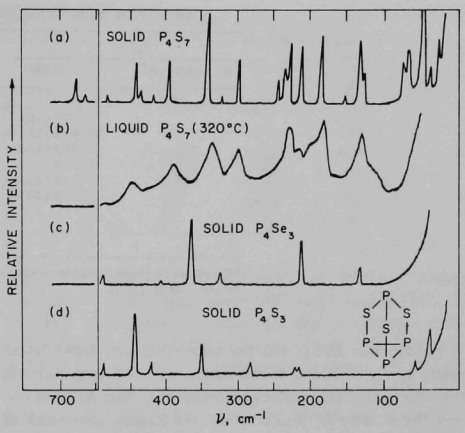

Fig. V-24. Raman Spectra of (a) solid P_4S_7, (b) liquid P_4S_7, (C) solid P_4se_3 and (d) solid P_4S_3. ANL Neg. No. 308-2397.

frequencies and relative intensities are listed in Table V-14 along with the results of a previous Raman study of P_4Se_3 in CS_2 solution by Irgolic *et al.* [77]. The band observed at 601 cm^{-1} in the CS_2 solution of Irgolic *et al.* was probably due to unreacted phosphorus in their sample (ν_1 for P_4 is reported by Pistorius [78] to be at 606 cm^{-1}). The Raman data for solid P_4S_3 are in good agreement with the previously reported results of Gerding, Maarsen, and Nobel [79].

TABLE V-13. Vibrational Frequencies (ν) and Relative Intensities[a] for Solid and Liquid P_4S_7

Solid		Liquid		
ν (cm^{-1})	Intensity	ν (cm^{-1})	Intensity[b]	Assignment
22	10			
34	10			
44	>100			Lattice modes
66	45			
74	45			
124	35	114	Sh	
131	80	129	70	
151	10			
185	85	183	90	
214	65	218	Sh	
227	80			P-S-P skeletal modes
232	40	229	80	
241	27			
297	55	297	40	
318	10			
340	100	334	50	
392	55	386	30	
413	10			
428	15			
436	55	439	20	
475	10			
663	10			P-S terminal modes
677	25			

[a]Relative intensities in arbitrary units.
[b]Sh = shoulder.

TABLE V-14. Raman Frequencies (cm^{-1}) for P_4X_3 (X = Se, S)[a]

P_4Se_3		P_4S_3	
CS_2 Solutions[b]	Solid[c]	Solid	Assignment
601	-	-	P_4
	481 (10)	484 (19)	P_4X_3
	405 (2)	-	P_4X_3 (?)
363	363 (100)	441 (100)	P_4X_3
317	322 (14)	418 (20)	P_4X_3
214	215 (53)	342 (60)	P_4X_3
	133 (24)	285 (21)	P_4X_3
	-	227,220 (9)	P_4X_3
	-	57 (13)	Lattice mode
	-	34 (47)	Lattice mode

[a]Numbers in parentheses indicate relative intensities.
[b]Irgolic et al. [77].
[c]This work.

P_4Se_3, like P_4S_3, has the cage structure shown as an insert in Fig. V-24d. For this structure with C_{3v} symmetry, ten vibrational frequencies are expected: four A_1, one A_2, and five E. The A_1 and E modes are Raman active and all ten modes are infrared active. Five of the Raman-active fundamentals for P_4Se_3 and possibly a sixth, if the weak band at 405 cm^{-1} is indeed a genuine vibration of P_4Se_3, are observed. The remaining unobserved Raman bands may be coincident with some of the observed fundamentals, too weak in intensity to be detected or at frequencies close to the exciting line.

The band at 481 cm^{-1} is attributed to the symmetric stretching motion of the P_3 base. This band occurs at 484 cm^{-1} for P_4S_3, indicating that there is little coupling of the bridging chalcogen motions with the symmetric motion of the P_3 base. Irgolic *et al.* have assigned the most intense band in the spectrum, 363 cm^{-1}, to the symmetric stretch of the apex phosphorus atom. The corresponding vibration in P_4S_3 is shifted to higher frequency (441 cm^{-1}), as expected, due to the fact that the sulfur atoms are lighter than selenium atoms. An attempt is made in Table V-14 to correlate the remaining P_4Se_3 bands with P_4S_3 bands on the basis of relative intensities, but specific assignments for these vibrations must await a complete normal coordinate analysis.

b. The Iodate Ion in Molten Nitrates

An investigation of the Raman spectrum of the iodate ion, IO_3^{1-}, dissolved in molten nitrates has been carried out as part of a program to study reactions of elemental iodine and iodine-containing species with fused nitrates. The reaction of elemental iodine with silver nitrate at 200°C is of particular interest because of its role in the silver nitrate scrubber towers used to remove ^{131}I from the gases released during the reprocessing of nuclear fuels [80]. The iodate ion was selected for investigation because it is one of the major reaction products formed when I_2 is contacted with a molten nitrate. We have also found that I_2O_5 reacts with molten nitrates to produce IO_3^{1-}.

Melts containing iodate dissolved in molten nitrate were prepared by heating 15 mol % I_2O_5-85 mol % MNO_3 mixtures (M = Li, Na, K, Rb, Cs, Ag, and Tl) for several hours at or near the melting point of the nitrate. Raman spectra of one of the iodate-nitrate mixtures in the 200–900 cm^{-1} region is shown in Fig. V-25, and the results for the entire series of experiments are summarized in Table V-15. The frequencies of the nitrate peaks for the various cations are in good agreement with previously published spectra [81]. Three Raman bands were observed which could be assigned to IO_3^{1-} in all of the mixtures. The strong band in the 770–810 cm^{-1} region was polarized in all cases, and the lowest-frequency band in the 290–340 cm^{-1} region was depolarized in all cases. The shoulder in the 340–380 cm^{-1} region appeared to be partially polarized in some of the spectra. For the cations Cs^{1+}, Ag^{1+}, and Tl^{1+}, a weak depolarized band was observed near 820 cm^{-1} which may also be due to IO_3^{1-}. However, the normally Raman-inactive A_2 mode of NO_3^{1-} has been observed in Raman spectra of molten $AgNO_3$ and $TlNO_3$ near 820 cm^{-1}.

The observed spectra for IO_3^{1-} are most consistent with a

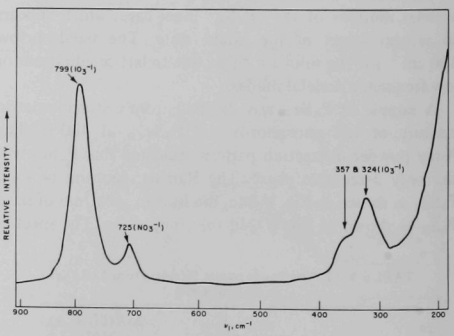

Fig. V-25. Raman Spectrum of KIO_3-KNO_3 ($IO_3^{1-}/NO_3^{1-} \approx 0.5$) in the 200–900 cm^{-1} Region at 450°C. ANL Neg. No. 308-2144.

TABLE V-15. Raman Data for Molten MIO_3-MNO_3 Mixtures

Composition	Temp. (°C)	Iodate Vibrations (cm^{-1})				Nitrate Vibrations (cm^{-1})	
		ν_3	ν_1	ν_2	ν_4	ν_1	ν_4
15 mol % I_2O_5-$LiNO_3$	280	-	807	344	290	1061	719
15 mol % I_2O_5-$NaNO_3$	300 340	-	795	366	323	1053	718
15 mol % I_2O_5-KNO_3	450	-	793	351	318	1046	717
15 mol % I_2O_5-$RbNO_3$	470	-	793	361	315	1045	712
15 mol % I_2O_5-$CsNO_3$	455	822	786	350	308	1042	712
12 mol % I_2O_5-$AgNO_3$	175	822	776	383	342	1039	729
18 mol % I_2O_5-$TlNO_3$	300	817	773	348	308	1033	708

pyramidal structure having C_{3v} symmetry. We believe that for most of the cations the antisymmetric stretching mode $\nu_3(E)$ is buried under the symmetric stretching mode, ν_1 (A_1) at 770–810 cm^{-1}. This observation is not unprecedented for iodates. Durig, Bonner, and Breazeale [82] were able to resolve ν_1 and ν_3 in solid $NaIO_3$ but found that in concentrated aqueous solutions of $NaIO_3$ the two vibrations merged into one symmetrical band.

The effect of changing the cation on the frequency of the symmetric stretching vibration of the iodate and nitrate ions is similar. Both ν_1 frequencies are observed to shift steadily to lower frequency with the cation sequence Li, Na, K, Rb, Cs, Ag, and Tl, which indicates in a qualitative way that the cation polarization effects on IO_3^{1-} and NO_3^{1-} are similar. Janz and coworkers have proposed a correlation [83] of the symmetric stretching mode of NO_3^{1-} with cation polarizing power, P, as defined by the equation $P = (5z^{1.27}/r^{0.5}I)(z/r)$, where z = ionic charge, r = ionic radius of the cation in Angstroms, and I = ionization potential in volts. Although a smooth curve results from such a plot for the alkali cations, Ag^{1+} and Tl^{1+}, there is reason to doubt the validity of the polarization expression above. Generally speaking, Janz *et al.* have made a correction to the normally defined polarizing power, z/r, by multiplying z/r by the shielding efficiency as given by Ahrens [84] $(5z^{1.27}/r^{0.5}I)$. Since one expects the polarizing power to decrease with increasing shielding efficiency, it probably would be more correct to divide z/r by the Ahrens' shielding efficiency term rather than take the product. If one constructs a plot of $P = (r^{0.5}I/5z^{1.27})(z/r)$ versus ν_1 for either NO_3^{1-} or IO_3^{1-}, the results for Ag^{1+} and Tl^{1+} do not fall on a smooth curve with the alkali metal points. This is reasonable if the mode of interaction of Ag^{1+} and Tl^{1+} with the oxyanions is significantly different from that of the alkali cations with the oxyanions. Evidence [85] has been presented to support this view for the case of molten $AgNO_3$.

c. Group II Halides

Raman studies of divalent metal ions in molten-halide media have continued with investigations of the ZnI_2-LiCl-KCl system and a reinvestigation of the $MgCl_2$-KCl system. Raman spectra of molten samples containing 5 mol % ZnI_2 in LiCl-KCl and 5 mol % $ZnCl_2$ in LiCl-KCl were identical, indicating that in chloride melts containing Zn^{2+} and low concentrations of iodide, the Zn^{2+} exists almost exclusively in the form of chloride complexes. The spectra are most consistent with the presence of $ZnCl_4^{2-}$. However, due to the low concentrations of Zn^{2+}, all of the expected vibrations for $ZnCl_4^{2-}$ were not observed. These studies have helped to develop an understanding of the high ZnI_2-removal efficiency of the LiCl-KCl cover salt used in the liquid zinc decladding process (see Section I.A). The fact that very little if any of the ZnI_2 dissolving in the cover salt remains intact explains the low vapor pressure of ZnI_2 in the system even at temperatures near the melting point of liquid zinc. (Raman spectra of ZnI_2-LiCl-KCl samples taken from the decladding process have been identical to samples of the same composition prepared by the addition of ZnI_2 to LiCl-KCl.)

The complete Raman spectrum of $MgCl_4^{2-}$ has been obtained using the 5145Å line of a Coherent Radiation Laboratories MG-52 mixed-gas (argon-krypton) ion laser for excitation. This spectrum is shown in Fig. V-26. Bands are observed at 325 ± 5 cm^{-1} (depolarized), 250 ± 2 cm^{-1} (polarized), 130 ± 5 cm^{-1} (depolarized), and 94 ± 5 cm^{-1}

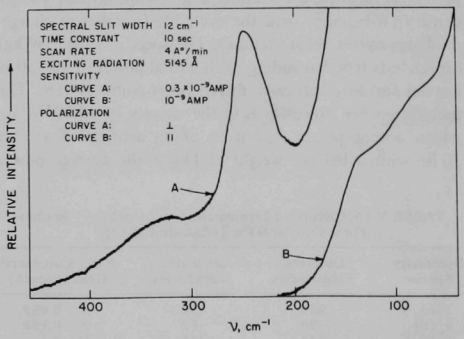

Fig. V-26. Raman Spectrum of Molten $MgCl^2$-KCl(Cl^{1-}/Mg^{2+} = 4.0) at 450?C. ANL Neg. No. 308-2559.

(depolarized). The four-band Raman spectrum, one band polarized and three bands depolarized, is characteristic of a five-atom tetrahedral species. The following assignments for $MgCl_4^{2-}$ under the point group Td can now be made: $\nu_1(A_1) = 250\ cm^{-1}$, $\nu_2(E) = 94\ cm^{-1}$, $\nu_3(T_2) = 325\ cm^{-1}$, and $\nu_4(T_2) = 130\ cm^{-1}$. This study confirms our earlier conclusion that the principal monomeric species in $MgCl_2$-KCl melts is $MgCl_4^{2-}$ (ANL-7675, p. 141).

The above Raman data for $MgCl_4^{2-}$ have been used to carry out a complete normal coordinate analysis. Wilson F and G matrices were constructed for a tetrahedral species according to the tabulated elements given by Nakamoto [86]. A Urey-Bradley type force field [87] was used, and it was assumed that $F' = -1/10F$ and that the molecular tension was zero. The observed and calculated frequencies and the computed force constants are given in Table V-16.

No significant improvement was observed by allowing H to vary; therefore, it was set equal to zero. The values of K and F are quite reasonable. They indicate that the Mg-Cl bond is a weak one, and that a modest repulsive interaction exists between the chloride atoms.

C. ENERGY CONVERSION (E. J. Cairns, R. K. Steunenberg, W. J. Walsh)

1. High-Specific-Energy Lithium/Selenium Batteries for Implantation

A program has been undertaken by the Chemical Engineering Division of Argonne National Laboratory under the Medical Devices Applications Program of the National Heart and Lung Institute to develop a lithium/selenium battery suitable for use as an implantable, rechargeable power source for an artificial heart or heart-assist device. For this application, the critical criteria of performance are the specific energy (W-hr/kg), the energy density (W-hr/cm^2), and the cycle life (number of charge-discharge cycles before failure). The specific power (W/kg) objective is less demanding, with a total power of 10–30 W needed for an electrically driven heart-pump system. The specific energy objective is in the vicinity of 100 W-hr/kg, which would permit operation of an artificial heart for 10 hr with a battery weight of 1 kg if the average power demand were 10 W. The battery is to be recharged by transmitting electromagnetic energy into the body by using a skin transformer system.

TABLE V-16. Calculated Frequencies (cm^{-1}) and Urey-Bradley Force Constants for Tetrahedral $MgCl_4^{2-}$

Symmetry Species	Observed Frequencies	Calculated Frequencies	Force Constants[a] (Millidynes/Å)
$\nu_1(A_1)$	250	250	$K = 0.669$
$\nu_2(E)$	94	92	$F = 0.158$
$\nu_3(T_2)$	325	325	$H = 0$
$\nu_4(T_2)$	130	132	

[a]K = Mg-Cl stretching constant.
F = Cl ··· Cl non-bonded repulsion constant.
H = Cl-Mg-Cl bending constant.

In the first year's effort on this program, the major emphasis was on cell design, including the development of suitable paste electrolytes, sealants, insulators, current collectors, and housings for the anode and cathode. Eighteen 7.5-cm dia cells were constructed, subjected to electrical performance tests, and examined after disassembly. Two batteries of 7.5-cm dia cells were built and tested. The first battery was unsealed and contained five cells. The second one contained six cells and was hermetically sealed from the environment.

a. Single-Cell Studies (H. Shimotake, A. A. Chilenskas, W. J. Walsh, J. C. Cassulo)

The development of reliable single cells is an essential step in achieving a successful battery. Consequently, much of the effort has been directed toward the construction and testing of experimental cells. Eighteen single cells, approximately 7.5 cm in diameter with an active electrode area of about 32 cm^2, were built and subjected to electrical performance tests.

Two types of tests were employed in the single-cell studies to evaluate cell performance with respect to current density, capacity density, and cycle life. Short-time tests were made to determine the current density as a function of voltage, which is normally a linear relationship, with the slope of the line representing the internal resistance of the cell. Other tests consisted of determining the voltage-capacity density relationship by discharging the cell at a constant current density while recording the voltage as a function of time. The cell was then recharged and the voltage again recorded as a function of time. Integration of the area under the voltage-capacity density curve over the time of charge or discharge yields the energy density (W-hr/cm^2). In some instances, the internal-resistance-free voltage (IR-free voltage) was determined as a function of capacity density. Since there is an inverse relationship between current density and capacity density [88], the cells were ordinarily discharged at a constant current density of 0.04 A/cm^2, which would be typical of a 10-W battery of five 7.5-cm dia cells. The cycle life of a cell was determined by the number of charge-discharge cycles that it had undergone prior to failure.

(1) Cell Design. Several cell design improvements were adopted during the eighteen single-cell tests. A schematic diagram of a recent cell design is given in Fig. V-27. The anode and cathode cups, which were about 7.5 cm OD with a depth of about 0.5 cm, were fabricated either by machining solid stock or by forming from sheet metal. The anode cups, which must be resistant to attack by molten lithium, were made of tantalum, stainless steel, hot-rolled steel, or Kovar [89]. The cathode cups must be resistant to

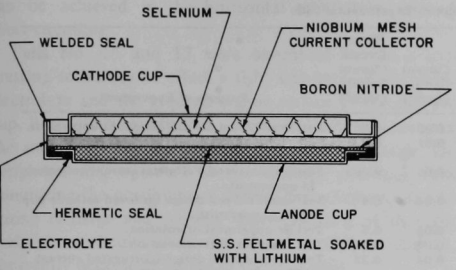

Fig. V-27. Single-Cell Design for an Implantable Battery. ANL Neg. No. 308-2220.

attack by selenium and lithium-selenium mixtures and were thus limited to tantalum, beryllium, and niobium. In some of the cells, concentric grooves were machined in the lip of the cathode cup, where it bears against the paste-electrolyte disk, to effect a seal. This technique proved especially useful in sealing the liquid selenium within the cathode cup.

Most of the paste-electrolyte disks consisted of 60 wt % LiF-LiCl-LiI electrolyte (a eutectic mixture of 11.7 mol % LiF, 29.1 mol % LiCl, and 59.2 mol % LiI; mp, 340.9°C) and 40 wt % α-$LiAlO_2$ filler. They were pressed at temperatures ranging from room temperature to 200°C with a force of about 54,500 kg (1,200 kg/cm^2). Some of the disks were coated with a low-melting salt mixture in an effort to decrease or eliminate permeation by selenium.

The cells were assembled by the following general procedure. Liquid lithium metal was soaked into the stainless steel Feltmetal [90] anode current collector at 500–600°C, this temperature being required to achieve satisfactory wetting. In some of the cells, a small amount of the molten-salt electrolyte was added to the lithium to promote wetting of the paste electrolyte. The cathode was prepared by melting selenium (mp, 220°C) into a corrugated niobium expanded-mesh current collector within the cathode cup. This cathode design was used to obtain a light-weight, relatively open structure that would promote convection and diffusion within the cathode. The cell components were then assembled and held under a compressive force by clamping or by tack-welding the peripheral ring to the cathode cup.

(2) Electrical Performance Results. The results of the cell performance tests are summarized in Table V-17. The first two cells were operated primarily to gain experience in the assembly and testing of full-size (7.5-cm diameter) cells. In Cell No. 3, Type 430 stainless-steel Feltmetal was used as the cathode current collector, and a significant improvement in performance over Cells No. 1 and 2 was observed. However, stainless steel was found to be attacked by lithium-selenium mixtures and hence is not a practical material for the cathode current collector.

Cell No. 4 involved a design modification for sealing the cathode cup to the paste-electrolyte disk by machining concentric grooves into the lip of the cathode cup where it bears against the paste electrolyte. The grooved area was pressed into the disk at a temperature above the melting point of the electrolyte. The electrical performance test of Cell No. 4 resulted in a short-circuit current density of 0.4 A/cm^2, a substantial improvement over values obtained with previous cells. The higher current density is attributed to better wetting of the paste electrolyte by lithium. No significant loss in weight was observed, and examination of the grooved surface where it had been in contact with the paste electrolyte showed that a satisfactory seal had been maintained. Consequently, grooved cathode-cup lips were used in most of the subsequent cells.

Cells No. 5 and 6 were similar to Cell No. 4, except that they were operated in a horizontal position with the selenium cathode uppermost. The open-circuit voltage (2.12 V) and the short-circuit current density (0.5 A/cm^2) did not differ significantly from those of Cell No. 4, but the capacity density was improved.

A new cell design incorporating a corrugated niobium metal mesh cathode current collector was tested in Cell No. 7. There were two other differences between Cell No. 7 and the previous ones: (1) The paste-electrolyte disk was coated with a low-melting salt (LiCl-LiI-KI, mp, 260.5°C), and (2) the cell was oriented vertically [91] during the test. The voltage-capacity density curve is shown in Fig. V-28. The initial open-circuit voltage was 2.3 V, and the short-circuit current density was 0.25 A/cm^2. The capacity density, 0.64 A-hr/cm^2, was the highest observed in any of the single-cell tests. The electrical performance of Cell No. 7 on one discharge was sufficient to meet the requirements of a 120 W-hr, 10-W battery of five 7.5-cm dia cells. However, approximately 16 g of selenium was lost from the cell, apparently through leakage caused by an increase in pressure resulting from the heating of helium trapped in the

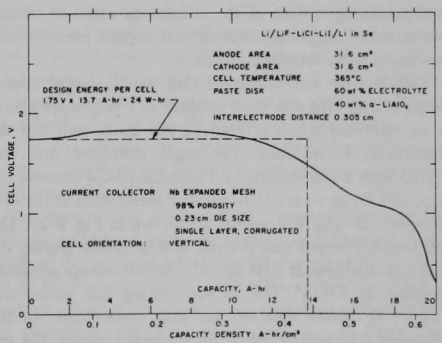

Fig. V-28. Voltage-Capacity Density Characteristics for Cell No. 7. ANL Neg. No. 308-2218.

TABLE V-17. Electrical Performance of Experimental Cells

Cell No.	Operating Temp. (°C)	Total Duration of Test (hr)	Theoretical Capacity Density (A-hr/cm²)	Maximum Capacity Density Achieved (A-hr/cm²)	Initial Open-Circuit Voltage (V)	Average Voltage (V)	Current Density (A/cm²)	Short-Circuit Current Density (A/cm²)	Purpose of Experiment
1	375–400	~2	0.64	0.002	2.3	0.6	0.02	0.032	Test first 7.5-cm dia cell design; Li uppermost.
2	385	24	0.64	0.098	2.1	0.6	0.01	0.021	Test modified Nb mesh current collector; Li uppermost.
3	385	43	1.32	0.23	2.16	1.5	0.02	0.095	Test stainless steel Feltmetal current collector; Li uppermost.
4	385	48	0.71	0.13	2.16	1.0	0.04	0.4	Test modified cell design (grooved cathode cup lip); Li uppermost.
5	375	20	0.65	0.32	2.12	1.7	0.04	0.5	Test Se-uppermost orientation.
6	350	138[a]	0.65	0.30	2.12	1.8	0.04	0.5	Test Se-uppermost orientation.
7	~365	72	1.04	0.64	2.3	1.6	0.04	0.25	Test modified cell design (corrugated current collector); vertical orientation.
8	~375	~16	0.51	0.08	1.9	0.94	0.04	0.05	Test modified cell design (polyimide composite insulator); Se uppermost.
9	~375	~16	0.50	0.08	2.1	1.2	0.04	0.76	Test modified cell design (polyimide composite insulator); Se uppermost.
10	380	24	1.04	0.25	2.25	1.8	0.04	0.25	Test cell with BN insulator and coated paste; vertical.
11	375	7	0.58	0.29	1.9	1.5	0.04	0.35	Test cell with cast-in-place electrolyte; Se uppermost.
12	365	7	1.04	0.29	2.25	1.75	0.04	0.45	Test modified cell design; vertical.
13	370	14	1.04	0.25	2.30	1.82	0.04	0.5	Test modified cell design; Se uppermost.
14	370	24	1.04	0.025	2.2	1.98	0.004	0.04	Test 50 wt % electrolyte-50 wt % filler paste; vertical.
15	375	3	1.04	0	1.1	0	0	0	Test sealed cell; vertical.
16	360	2	0.97	0.082	2.1	1.4	0.04	0.32	Test modified cell design; vertical.
17	380	2	0.97	0.082	2.2	1.7	0.04	0.13	Test modified cell design; vertical.
18	380	35	0.53	0.37	2.2	1.5	0.036	0.32	Test modified cell design with BN insulator; vertical.

[a]Includes 105 hr on open circuit.

cathode cup during assembly of the cell.

Cells No. 8, 9, and 11 employed a polyimide-$LiAlO_2$ composite insulator in the anode cup. The performance of Cell No. 8 was relatively poor, about 2.5 A-hr being obtained on an overnight discharge. Cell No. 9 performed somewhat better. It was discharged (2.5 A-hr) at an average voltage of 1.9 V, partially recharged (0.94 A-hr) at 2.1 to 2.4 V, discharged overnight (2.6 A-hr) at low current density (~0.007 A/cm²), recharged (3.5 A-hr) and discharged again (0.4 A-hr). The highest short-circuit current density, 0.76 A/cm², was achieved with Cell No. 9. Cell No. 11 was the only one tested in which the paste electrolyte was cast in place within the cell. A relatively high percentage (50%) of the theoretical capacity density was achieved, suggesting that the cast-in-place paste electrolyte might be investigated further.

Cell No. 10 was similar to Cell No. 7, except that a boron nitride ring was used in place of a polyimide gasket as an electrical insulator between the anode cup and the electrolyte. In addition, the paste-electrolyte disk was coated with a low-melting LiCl-LiBr-LiI-KI-CsI eutectic salt (mp, 184°C) in an effort to prevent permeation of the disk by selenium. The test results are shown in Fig. V-29. The cell was discharged and charged in 6-hr cycles. During the first 6-hr discharge at 0.04 A/cm², the cell voltage remained constant at 1.92 V. The IR loss during this period was 0.16 V, or about 47% of the total overvoltage. In the following 6-hr period, while on automatic charge, the cell became overcharged, with resulting electrolysis of the electrolyte. During the second discharge period, the voltage decreased from 1.9 to 1.5 V, and in the following charge period, the cell developed a short circuit after about 2 hr. These results indicate that recharging without short-circuiting is possible when a suitable material is used as an insulator, but that the current density must be limited to avoid increasing the IR-free voltage above the decomposition potential of the electrolyte.

A new cathode cup design was used in Cells No. 12 to 15 but did not result in a significant improvement in cell performance. Cell No. 13 showed that a smooth recharge

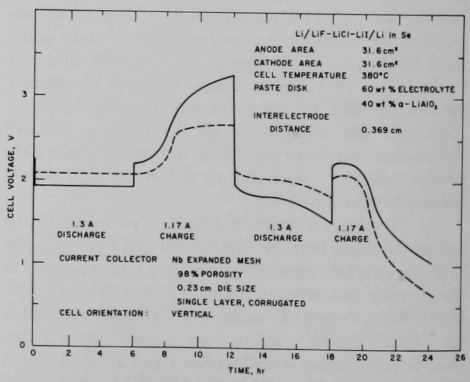

Fig. V-29. Discharge-Charge Characteristics of Cell No. 10. ANL Neg. No. 308-2221 Rev. 1.

can be achieved in the horizontal orientation without short-circuiting.

Cells No. 16 and 17 were assembled to test a hot-pressing technique to effect a tight seal between the paste electrolyte and the grooved sealing surface of the cathode cup. Both of these cells had a glass insulating seal between the anode cup and the peripheral ring. In this design, the peripheral ring operated at the cathode potential, thus minimizing the possibility of lithium deposition on the ring during recharge and possible short-circuiting of the cell. Early short circuits were experienced in Cells 16 and 17, apparently because of failure of the glass seals.

Cell No. 18 was of a similar design, except that a boron nitride ring was used as the insulator between the anode cup and peripheral ring, and another boron nitride ring was placed between the anode cup and the paste electrolyte. The maximum open-circuit voltage was 2.2 V, but a high internal resistance of 0.64 ohm was observed. The cell was discharged about 10 hr at a current density of 0.036 A/cm^2. During the first 2 hr, the voltage was about 1.5 V; it then increased to about 1.75 V where it remained for 8 hr, producing approximately 2 W and 12 A-hr. The cell was then recharged for 6 hr at 0.02 A/cm^2. During this period, the open-circuit voltage increased rapidly to 2.05 V, where it remained constant. Data on the first discharge-charge cycle are presented in Fig. V-30. The cell was then discharged again and recharged for 6 hr with the open-circuit voltage increasing steadily from 2.08 to 2.1 V, followed by a discharge at 0.035 A/cm^2 for 1 hr, with an average terminal voltage of 1.5 V. The test was terminated after 35 hr of operation when a short circuit developed. The performance of this cell was better than that of the previous 17 cells. On the first discharge, 72% of the theoretical capacity density was obtained. The design and cell assembly techniques used for Cell No. 18 were selected for the six cells that were used in the sealed-battery test (Section V.C.1.b of this report).

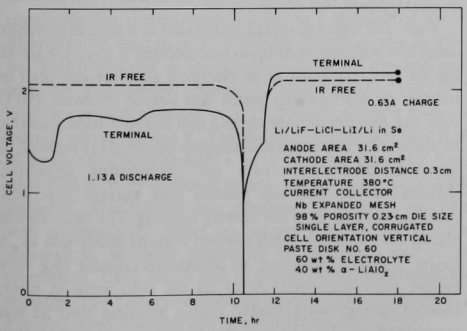

Fig. V-30. Electrical Performance of Cell No. 18. ANL Neg. No. 308-2396.

In several of the cells, Li_2Se was observed in large amounts at the interface between the anode and the paste-electrolyte disk. This was attributed either to leakage of selenium past the paste electrolyte, where there was evidence of paste cracking or a poor seal, or to permeation of the electrolyte by selenium. The short cell lifetimes experienced in these tests are attributed to the transport of selenium from cathode to anode. A study to determine the conditions required to avoid selenium permeation of the electrolyte is under way.

(3) Conclusions from Single-Cell Studies.

a) The electrical performance studies have indicated that a battery of five 7.5-cm dia lithium/selenium cells will be capable of meeting the goals of 10 W of power and an energy-storage capacity of 120 W-hr. Calculations indicate that such a battery will fall within the design limits of weight (1.1 kg) and size (10-cm dia, 8.4-cm high cylinder).

b) A substantial improvement is needed in the cycle life and longevity of the cells. This problem is believed to be related to the transport of selenium to the anode by gross leakage, permeation of the electrolyte, or solubility of selenium-bearing species in the electrolyte. A concerted effort has been undertaken to investigate means of avoiding selenium transport by these mechanisms.

c) Further work is needed to improve cell recharge characteristics. This is closely related to the preceding conclusion.

d) It appears that the cells can be operated in any orientation.

e) Suitable materials appear to be available for the cell components. However, longer-term life tests are needed, and additional development work is required on sealants, insulators, and cell-assembly techniques.

b. Battery Studies (H. Shimotake, A. A. Chilenskas, J. C. Cassulo)

Unsealed and hermetically sealed 10-W batteries were tested to (1) elucidate battery assembly problems, (2) determine electrical performance, (3) study cell interactions, and (4) determine the performance of materials of construction under operating conditions. Future work will be directed toward increasing the power level to 30 W, and the cylindrical shape may be modified for implantation.

(1) Unsealed Battery Test. For the unsealed, five-cell battery (Figs. V-31 and V-32), the cell design was similar to that used in Cells 12 to 15.

The battery was assembled in a bipolar configuration with the cathode of each cell electrically connected to the anode of the adjacent cell except for the cell at the positive end of the battery. The cells and battery were assembled in a helium glovebox to prevent contamination of the lithium and electrolyte disks by nitrogen, oxygen and water. The battery was operated with the selenium uppermost in each cell. During the test, the total battery voltage, the voltage

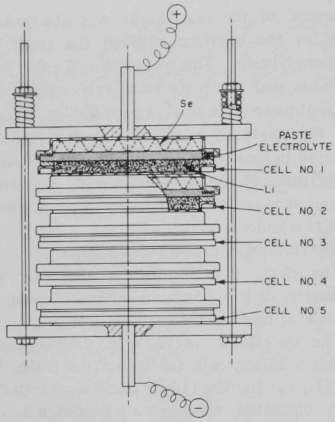

Fig. V-31. Schematic Diagram of Unsealed, Five-Cell Battery, ANL Neg. No. 308-2395.

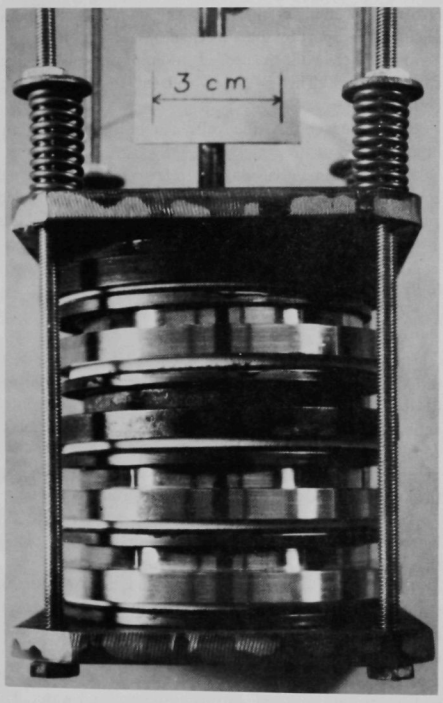

Fig. V-32. Photograph of Unsealed Five-Cell Battery. ANL Neg. No. 308-2140.

of each cell, and the current were continuously monitored and recorded.

A maximum open-circuit voltage of 10.45 V was obtained for the battery. Upon discharge at 1.3 A (0.04 A/cm^2), a terminal voltage of over 9.0 V (or the equivalent of about 12 W) was maintained for about 1 hr. After about 1.5 hr of operation, the two cells located at the lower end of the battery shorted, resulting in a three-cell battery instead of the original five-cell battery. The short circuit was attributed to softening of the paste disks, which resulted in a decrease in thickness of the paste below that required for separation of the anode and cathode. The discharge was terminated after 4 hr when the three-cell battery reached a potential of 4 V. After the battery had been held on open circuit for 1 hr, a charge of 1 A-hr was carried out. The battery was then discharged as a two-cell battery at a current of 1.3 A. This discharge was terminated when the battery reached a potential of 2.2 V after about 1 hr. Operation of the battery was finally terminated when a general short circuit occurred. Examination of the disassembled battery revealed deformation of the paste disks and resulting leakage of selenium from the cells.

This was the first attempt to build and operate a 10-W battery. The operation of the battery at 12 W for 1.5 hr demonstrated that the lightweight design employed was capable of achieving the specified power level. The early failure of the battery illustrated the need for sealed single cells which are free from deformation of the paste electrolyte and leakage of selenium.

(2) Sealed Battery Test. A six-cell experimental battery (shown in Fig. V-33) was developed which would allow (a) loading the hot cells into the battery housing (both cells and housing at about 350°C), (b) welding the loaded battery at temperature, hermetically sealing the battery from the environment, (c) leak-testing the sealed battery, (d) transferring the battery at operating temperature from the helium glovebox to a hood in an air environment, (e) good temperature monitoring, and (f) shunting any inoperable cells out of the circuit.

Each cell was assembled and sealed in a helium glovebox using hot-pressing techniques (see Section V.C.1.a). Each of the six cells exhibited good electrical performance prior to transfer to the housing, which was heated to about 350°C with the bottom aluminum ring and boron nitride insulator in place. The cell-transfer operation involved (a) removal of the individual cells from the hot-pressing apparatus, (b) removal of the top heaters and current tap, and (c) rapid transfer into the battery housing. The first cell was placed on a niobium mesh contact with its anode side up. A Lavite insulator ring and an aluminum contact ring were loaded after each cell. After all six cells were in place, Inconel springs were loaded and a stainless steel lid was arc-welded in place to seal the battery from the environment. A pressure test was performed to check leak-tightness. The battery was originally operated with

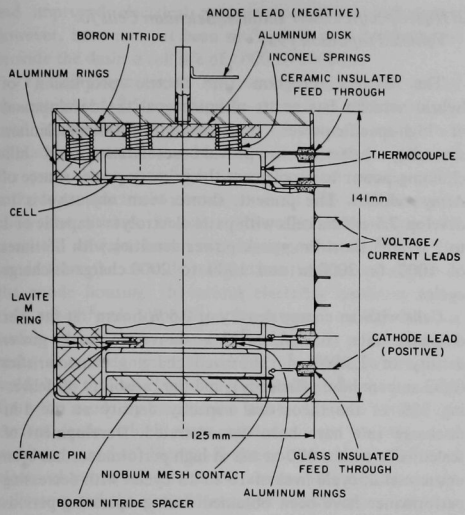

Fig. V-33. Schematic Diagram of Sealed Battery. ANL Neg. No. 308-2394.

selenium uppermost in each cell. An attempt was made to determine the effect of various orientations and mild motion on the electrical performance of the battery. During the test, the battery voltage, the voltage of each cell, and the current were continuously monitored and recorded.

A maximum open-circuit voltage of 6.8 V was obtained for the battery with Cells No. 3, 4, and 6 functioning normally, and Cells No. 1, 2, and 5 developing less than 0.5 V each. It is suspected that Cells No. 1, 2, and 5 experienced excessive temperature cycling during the transfer operations, which resulted in cracking of the paste electrolytes. These cells were shunted out of the electrical circuit and the system was operated as a three-cell battery. After 1 hr of operation in a helium glovebox, the battery was transferred out of the glovebox to an air environment with no appreciable change in performance. The first discharge was conducted at 1.25 A (0.04 A/cm^2) with an average voltage of 4.6 V. The battery produced about 6 W of power for over 4 hr with a total discharge time of 5.5 hr. About 33 W-hr of electrical energy was obtained in the first discharge. The battery was operated in various positions with no significant effect on battery voltage. The battery appeared to be fairly insensitive to motion as well as to orientation. Cells No. 3 and 4 failed during an attempted recharge. The battery voltage decreased very rapidly during a second discharge, and the test was terminated.

The early failure of Cells No. 1, 2, and 5 was attributed to excessive cooling during the cell-transfer operation. It appears that this problem can be avoided in future battery tests by either (a) development of isothermal cell-loading techniques or (b) development of single cells which can be assembled into a battery at room temperature.

c. Thermal Insulation Studies (A. A. Chilenskas)

A containment shell incorporating lightweight, high-efficiency thermal insulation is being developed to permit implantable batteries to sustain internal operating temperatures of about 370°C with an external surface temperature of 37°C. Two types of multifoil insulation have been tested for thermal efficiency in a test assembly. One type, using aluminized Kapton [92] film, was fabricated in our laboratory, whereas a second type, using glass paper and aluminum foil, was supplied by the Linde Division of Union Carbide.

Figure V-34 is a sketch of the thermal-insulation test assembly. Each of the annular blankets consisted of 11 layers of the insulating material wrapped in a spiral resulting in a total of 33 "radiation shields" in the annulus. The top and bottom insulator plugs consisted of 33 disks of the foil cut into three different diameters and arranged in a step geometry. The inner can was supported on three ceramic pins of 1.6-mm diameter. These pins were cemented to the inner can using Pyre ML [93]. After assembly, the Lavite plugs and the outer can lid were sealed to the outer can using self-curing silicone rubber.

The insulation was tested by measuring the amount of power input to the resistance-heated block that was

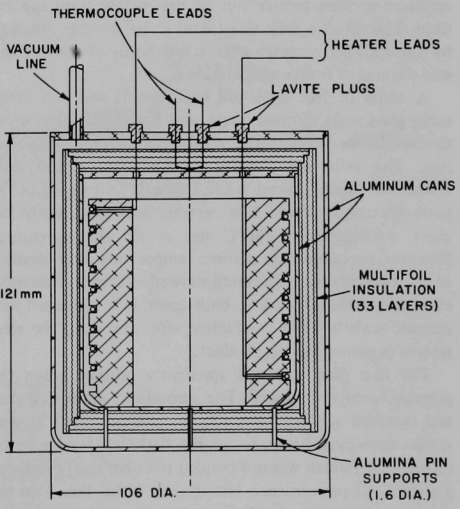

Fig. V-34. Thermal Insulation Test Assembly. ANL Neg. No. 308-2560.

required to maintain the temperature in the inner can at 370°C with the external surface temperature at about 37°C. This test was performed under dynamic vacuum conditions, whereas the implantable battery will require a vacuum of 10^{-4} Torr or better under static conditions.

The power input required for the aluminized polyimide was about 7.1 W, whereas about 3.7 W was required for the Linde insulation. Both values are very encouraging since the goal of achieving operating temperature with a heat loss of less than 3 W seems achievable with existing materials and fabrication capability. However, these tests did not permit an evaluation of the life of the insulators in a battery environment.

d. Sealants and Insulators (A. A. Chilenskas)

Hermetically sealing and insulating materials that are stable against chemical, thermal, electrical, and mechanical degradation are required for long-term battery operation under implantation conditions. Preliminary tests were conducted on a polyimide [93] and a silicone [94] resin as possible binders with powdered $LiAlO_2$ filler to form composite materials that possess both sealing and insulating properties. The polyimide was found to be an excellent sealant but exhibited low corrosion resistance toward lithium, selenium, and the eutectic salt. This material appears to be an adequate sealant for use in short-term testing of cells, but its sensitivity to attack by lithium and selenium appears to rule out its use in long-term applications. The silicone resin was found to be severely attacked by LiF-LiCl-LiI eutectic after a few hours of contact and was eliminated from consideration.

A series of five single-cell experiments was performed using glass seals, ceramic seals, and boron nitride rings as the insulators between the anode cup and the peripheral ring. The cells were similar to Cell No. 16 and were assembled with 60 wt % LiF-LiCl-LiI, 40 wt % $LiAlO_2$ paste-electrolyte disks. The ceramic seals apparently became conductive at 360°C and caused short-circuiting. However, reexamination at room temperature after cleaning of the two ceramic seals tested showed electrical resistances exceeding 100,000 ohms in both cases. It is suspected that ceramic seals become conductive after absorbing the electrolyte or some reaction products.

The first glass seal was apparently crushed when the pressing force was applied. The second cell test with a glass seal involved a lower force (25 kg) and produced a more stable open-circuit voltage. In the fifth cell test, a boron nitride ring (which was not bonded to either cup) produced a stable cell performance lasting over 20 hr. Based on the above results, boron nitride was selected as the ring material for use in the sealed battery test.

2. High-Specific-Power Lithium/Selenium Cells for Vehicle Propulsion [95]

The battery program for electric propulsion of hybrid vehicles has as its ultimate goal the development of high-specific-power, multikilowatt, lithium/selenium secondary batteries to provide acceleration and hill-climbing power to supplement the primary power source of Army vehicles. The present, shorter-term objective is to develop 7.5-cm dia cells with paste electrolytes capable of 1 to 3 W/cm^2 short-time peak power densities with lifetimes of 1000 to 2000 hr and 1000 to 2000 charge-discharge cycles.

Cells with an energy density of 0.5 W-hr/cm^2 at the 1-hr discharge rate (0.27 A/cm^2), a short-time peak power density of 2.3 W/cm^2, improved charging characteristics (0.92 ampere-hour efficiency), and the capability of delivering 52% of the theoretical capacity density at the 1-hr discharge rate have been demonstrated. Development of sealed cells with a 100-hr life at high performance has been unsuccessful; cycle lives of 10 to 13 cycles with decreasing performance have been obtained during operating periods of 120 hr. The life-limiting factor has been the transference of selenium through the paste electrolyte to the lithium electrode, causing an increase of internal resistance and a loss of capacity. Changes in cell design, construction, and operating procedure have been made which are expected to result in the development of long-lived sealed cells having the desired performance capabilities.

a. Single-Cell Studies (E. C. Gay, J. E. Kincinas, V. M. Kolba, J. D. Arntzen)

The electrical performance of single cells is evaluated in terms of voltage-current density and voltage-time behavior during constant-current discharge as a function of cell structure and number of charge-discharge cycles. The effects of various paste electrolyte treatments, structural configurations of the cathode current collector, and changes of other cell parameters are being studied to identify the cell design that yields the highest capacity density (with efficient selenium utilization).

The primary objective of the changes in cell design and operating techniques employed in the work described here was to maintain the best electrical performance achieved previously, 0.22 A-hr/cm^2 at 0.52 A/cm^2, for longer periods of time. The major life-limiting factor is the formation of Li_2Se at the lithium-paste electrolyte interface. It is believed that selenium passes around the paste electrolyte or through pores in the paste electrolyte forming Li_2Se at the lithium electrode. This accumulation of Li_2Se results in a considerable increase in the cell resistance and decrease in capacity. Techniques have been developed which result in improved charging characteristics

and improved electrical performance. These techniques, however, have not yet been sufficiently well developed to provide the desired cell life of 1000 to 2000 hr.

(1) Cell Components. A cross-sectional view of one of the assembled 7.5-cm dia paste-electrolyte cells presently used is shown in Fig. V-35. All of the cells tested had similar configurations and were operated with the plane of the paste electrolyte disk in the vertical position. The cathode compartment contained about 50% void volume to allow for lithium transfer. The other cell components consisted of (a) a boron nitride ring, which insulated the anode from the cathode compartment and served as part of the anode housing, (b) various electrical insulating materials, which were applied to the grooved cathode-housing sealing surface to avoid product formation at the cathode seal, (c) cathode voltage and current leads, which were welded to the cell clamping plate (this plate was insulated from the anode by an alumina disk), (d) anode voltage and current leads, which were welded to the stainless steel anode cup, and (e) Inconel-X springs, which provided good electrical contact between the anode and cathode current collectors and the paste electrolyte and also provided force at the grooved sealing surface between the paste electrolyte and the cathode housing.

The anode consisted of stainless steel Feltmetal (Huyck Metal Co.; 302 SS, 1.6 or 3.2 mm thick, 90% porosity, 67-μm mean pore size) that had been soaked in lithium at 550°C. The cathode consisted of niobium expanded mesh of approximately 63% porosity (0.23-cm die size). Sheets of the niobium mesh were welded together and welded to the inner surface of the niobium cathode cup. A description of the paste electrolytes and the quantities of lithium and selenium loaded into the various cells are given in Table V-18. The paste electrolytes were prepared using lithium aluminate and/or boron nitride filler (of approximately 46 and 7 m^2/g specific surface area, respectively) and LiF-LiCl-LiI eutectic. This eutectic has a composition (in mole percent) of 11.7% LiF-29.1% LiCl-59.2% LiI and has a melting point of 340.9°C. The resistivity of 380°C, the operating temperature for most of the cells in this report, is 0.41 ohm-cm. Some paste electrolyte disks listed in Table V-18 were coated with a lower-melting eutectic, LiCl-LiBr-LiI-KI-CsI, in an attempt to eliminate the permeability of the past electrolyte to selenium. This eutectic has a composition (in mole percent) of 3.7% LiCl-9.1% LiBr-52.3% LiI-15.7% KI-19.2% CsI and has a melting point of 184°C.

The features of the cell design which are required for good electrical performance are as follows:

1) The stainless steel Feltmetal containing lithium

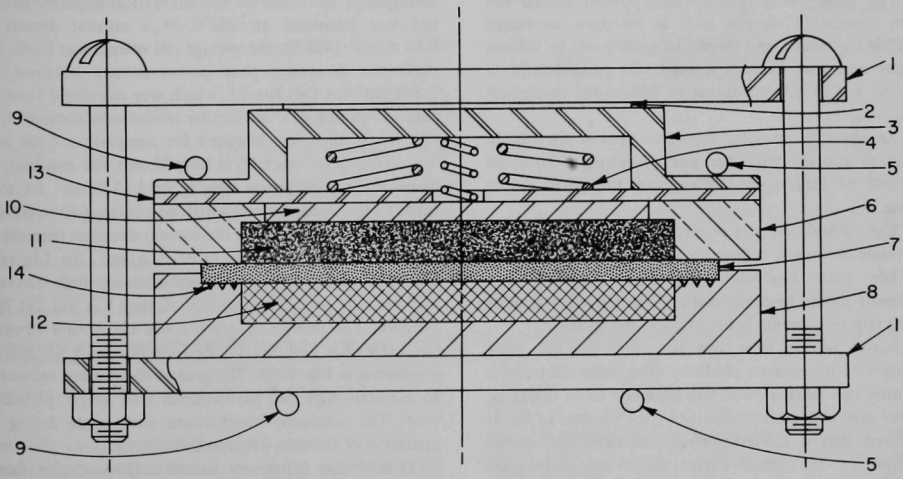

1 – Clamping Plate, SS
2 – Insulator, Al_2O_3
3 – Anode Cover, SS
4 – Springs, Inconel-X
5 – Current Lead, SS
6 – Insulator, BN
7 – Paste Electrolyte
8 – Cathode Cup, Nb-1 Zr
9 – Voltage Lead, SS
10 – Spacer Plate, Nb-1 Zr
11 – SS Feltmetal, 90% Porosity, 67-μm Mean Pore Size, Containing Li
12 – Nb Mesh, 63% Porosity, 0.23-cm Die Size, Containing Se
13 – Spring Plate, SS
14 – Grooved Cathode Sealing Surface

Fig. V-35. Components of Lithium/Selenium Cell with 7.5-cm Dia Paste Electrolyte. ANL Neg. No. 308-2393.

TABLE V-18. Lithium/Selenium Cells with 7.5-cm Diameter Paste Electrolytes

Cell Number	Theoretical Capacity[a] (A-hr)	Anode: Lithium Content (g)	Cathode: Selenium Content (g)	Paste Electrolyte: Electrolyte Content[b] Major (wt %)	Electrolyte Content[b] Coating (wt %)	Filler $LiAlO_2$ (wt %)	Filler BN (wt %)	Fraction of Theoretical Density	Thickness (cm)
9	18.6	12.7	27.3	60	0	40	0	0.94	0.24
10	16.5	10.3	24.2	60	0	40	0	0.97	0.30
11	14.1	9.0	20.8	47.7	20.4	31.8	0	0.95	0.26
12	19.7	11.7	29.0	48.8	18.7	32.4	0	0.93	0.32
13	15.3	12.4	22.5	60	0	40	0	0.98	0.29
14	17.9	12.3	26.3	57.4	4.4	38.2	0	0.95	0.29
15	20.8	12.6	30.5	60	0	0	40	0.85	0.28
16	18.8	6.6	27.7	52.5	12.5	35.0	0	0.96	0.29
17	16.9	10.3	24.9	54.4	15.6	18.6	11.4	0.94	0.25
18	16.2	10.0	23.8	59.7	7.4	20.4	12.5	0.94	0.25
19	16.2	9.8	23.8	70.0	0	30.0	0	0.96	0.25
20	21.1	8.8	31.0	61.0	12.9	26.1	0	0.96	0.25
21	21.8	5.3	32.1	55.5	13.9	19.0	11.6	0.94	0.25
22	16.0	5.6	23.5	50.0	12.2	18.9	18.9	0.95	0.25
L-1	12.7	9.5	18.7	55.7	13.5	19.2	11.7	0.94	0.25
L-2	17.0	8.3	25.0	51.2	9.8	19.5	19.5	0.97	0.25
L-3	17.3	5.2	25.5	50.6	11.0	19.2	19.2	0.94	0.25

[a]This theoretical capacity was based upon Li_2Se as the fully discharged composition and the quantity of selenium loaded into the cathode.
[b]The major electrolyte was the LiF-LiCl-LiI eutectic; mp = 340.9°C. The coating electrolyte was the LiCl-LiBr-LiI-KI-CsI eutectic, mp = 184°C, except for Cells No. 11 and 12 (LiBr-RbBr; mp = 259°C) and Cell No. 18 (LiF-LiCl-LiI).

should be spring-loaded to provide good electrical contact with the paste electrolyte.

2) The paste electrolyte molding powder should not contain sources of oxygen such as moisture, unreacted Al_2O_3, or carbonate, and should be readily wet by lithium and selenium. Also, for high strength, the paste electrolyte should have a density in excess of 90% of the theoretical value.

3) An electrical insulator should be used at the lithium housing in contact with the paste electrolyte to avoid deposition of lithium at the edge of the paste during charging.

4) The cathode current collector should be welded to the cathode housing to reduce the internal resistance.

5) The paste electrolyte should be impervious to selenium or should be coated with a low-melting eutectic in order to reduce selenium penetration to the anode.

6) Boron nitride filler can be added to the paste electrolyte to improve its plasticity. The paste electrolytes containing this filler showed less tendency to be displaced from the cathode current collector by the product Li_2Se. It is believed that a modest amount of extrusion of the electrolyte into the cathode current collector provides good adherence.

7) For cells operated in the vertical position, an electrical insulator should be used at the cathode housing sealing surface to avoid product formation at this surface during discharge if a selenium leak should occur.

(2) Electrical Performance. A summary of the electrical performance, purpose of the experiment, and results for the cells tested most recently are presented in Table V-19. The maximum capacity density obtained for a 7.5-cm dia paste electrolyte cell was 0.36 A-hr/cm^2 (11.4 A-hr) for Cell No. 7 in the vehicular series tested earlier. This value corresponds to 58.8% of the theoretical capacity density and was measured at 400°C at a current density of 0.15 A/cm^2 (4.8 A); the average cell voltage was 1.6 V. The maximum short-time peak power density obtained was 2.3 W/cm^2 for Cell No. 21, which was calculated from the data shown in Fig. V-36. Similar results were obtained from Cell No. 9; these are included for comparison. Cells using 7.5-cm dia paste electrolyte have shown the capability of delivering a peak power density of 1–3 W/cm^2 for short times (a few seconds) and a high percentage (40 to 60%) of the theoretical capacity at the current densities required for electric vehicular applications (0.27 A/cm^2, the 1-hr rate). The additional objective of maintaining high electrical performance over long periods of time has not yet been satisfied. The maximum cell life was 120 hr and 13 cycles (to 1.0 V) for Cell No. 17. Performance data for this cell are shown in Fig. V-37. The goal of the present cell tests is to maintain high cell performance over longer periods of time. The following observations were made during the operation of the cells listed in Table V-19:

1) Selenium apparently leaked to the sealing surface in some cells tested in the vertical position, and Li_2Se formed at this surface during discharge, breaking the cathode seal. This problem can be solved by heating cells initially in a horizontal position (eliminating exposure of the sealing surface to liquid selenium) and rotating the cell to the vertical testing position after being heated above the electrolyte melting point.

2) Cells in which the paste electrolyte was coated with LiCl-LiBr-LiI-KI-CsI showed better charging characteristics

TABLE V-19. Electrical Performance of 31.6-cm² Lithium/Selenium Cells at 380°C

Cell No.	Peak Power Density[a] (W/cm²)	Discharge Current Density (A/cm²)	Average Discharge Voltage (V)	Discharge Time (hr)	Capacity Density[b] (A-hr/cm²)	Energy Density (W-hr/cm²)	Fraction of Fraction of Theoretical Capacity	Fraction of 1-hr Rate Current Density[c]	No. of Cycles	Testing Period (hr)	Purpose of Experiment	Results
9	2.2	0.15	1.8	0.27	0.04	0.07	0.074	0.59	5	72	Test cathode seal-grooves	Li_2Se at anode;[d] poor seal; low O.C.V. at end of test.
10[e]	0.8	-	-	-	-	-	-	-	-	24	Test paste (60 wt % eutectic) permeability to Se vapor	Li_2Se at anode; good seal;[f] low O.C.V. at end of test.
11[e]	-	-	-	-	-	-	-	-	-	-	Test LiBr-RbBr coated paste	Li_2Se at anode; electrical short.
12[e]	-	-	-	-	-	-	-	-	-	24	Test LiBr-RbBr coated paste	Li_2Se at anode; good seal; low O.C.V. at end of test.
13[e]	0.9	-	-	-	-	-	-	-	-	30	LiCl-LiBr-LiI-KI-CsI in seal grooves[g]	Li_2Se at anode; good seal; low O.C.V. at end of test.
14	1.7	0.29	1.7	0.78	0.23	0.39	0.40	1.1	6	60	LiCl-LiBr-LiI-KI-CsI coated paste	Li_2Se at anode and at outer cathode perimeter; no Se loss; normal O.C.V. at end of test.[h]
15	0.4	0.15	1.3	1.70	0.25	0.32	0.38	0.55	2	30	Test BN filler paste	Li_2Se at anode and outer cathode perimeter; no Se loss; mushy paste.
16	0.6	0.26	1.4	0.77	0.20	0.28	0.33	1.0	6	56	LiCl-LiBr-LiI-KI-CsI coated paste	Li_2Se at anode and at outer cathode perimeter; no Se loss.
17	0.7	0.27	1.5	0.65	0.18	0.27	0.33	1.0	13	120	LiCl-LiBr-LiI-KI-CsI coated BN and $LiAlO_2$ filler paste	Li_2Se at anode and at outer cathode perimeter; no Se loss; longest testing period; paste fractured near seal.
18[e]	0.7	-	-	-	-	-	-	-	-	-	LiF-LiCl-LiI coated paste	Se leakage; distorted paste.
19	1.6	0.27	1.7	1.0	0.27	0.46	0.52	1.0	2	8	70 wt % LiF-LiCl-LiI paste and salt in Se	Paste cracked; good capacity.
20	1.2	0.26	1.6	1.2	0.31	0.50	0.43	1.0	2	8	LiCl-LiBr-LiI-KI-CsI coated 70 wt % paste	Li_2Se at anode and at outer cathode perimeter; no Se loss.
21	2.3	0.27	1.6	1.0	0.27	0.43	0.39	1.0	5	60	LiCl-LiBr-LiI-KI-CsI coated BN & $LiAlO_2$ paste	Li_2Se at anode and at outer cathode perimeter; no Se loss; paste fractured near seal.
22	0.7	0.12	1.6	1.0	0.12	0.19	0.23	0.44	3	40	Insulator on cathode seal	Li_2Se at anode and at outer cathode perimeter; no Se loss.
L-1	0.6	0.26	1.3	0.13	0.04	0.05	0.09	1.0	1	45	LiCl-LiBr-LiI-KI-CsI coated paste	Paste cracked.
L-2	0.4	0.21	1.3	0.51	0.12	0.14	0.22	0.8	3	20	LiCl-LiBr-LiI-KI-CsI coated paste	Li_2Se at anode; poor seal.
L-3	0.3	0.30	1.2	0.28	0.08	0.10	0.15	1.1	2	28	LiCl-LiBr-LiI-KI-CsI coated paste	Li_2Se at anode; poor seal.

[a]These values are short-time peak power density and represent measurements taken a few seconds after closing the circuit.
[b]These values represent the capacity density measured for the first discharge during the first hour of cell testing, to a 1.0 V cut-off.
[c]This current-density ratio is the discharge current density divided by the current density (0.27 A/cm²) for a 1-hour discharge time to 1.0 V.
[d]The presence of Li_2Se at the anode interface was determined by electron microprobe for 3% of the cells tested. Most of the determinations for Li_2Se were made from visual examination of the anode section.
[e]No capacity measurements were made for these cells. The purpose of these experiments was to determine selenium permeability of the paste electrolyte in the absence of electrical measurements.
[f]A good seal was one of no selenium leakage nor product deposited at the outer cathode perimeter.
[g]All subsequent cells contained LiCl-LiBr-LiI-KI-CsI eutectic in the cathode seal grooves.
[h]Unless stated otherwise, the open-circuit voltage at cell shut-down was above 2.0 V.

than cells using uncoated paste and maintained an open-circuit voltage greater than 2.0 V. It has not been determined if this electrolyte is required in the sealing grooves to prevent selenium leakage, but this practice was adopted as part of the normal cell operating procedure.

3) Paste-electrolyte cells with the highest LiF-LiCl-LiI content (Cells No. 14 and 19 to 21 containing 57 to 70 wt % LiF-LiCl-LiI) showed the highest capacity density (at 0.27 A/cm², the 1-hr rate) and the highest short-time peak power density. Addition of electrolyte to selenium (Cell No. 19) also increased the capacity density achieved. There is some indication, however, that pastes of very high LiF-LiCl-LiI content (70 wt % for Cell No. 19) are susceptible to cracking due to thermal expansion of the electrolyte. Further tests are required to verify this observation.

4) The percent of selenium utilized at the 1-hr rate appears to be directly related to the weight percent LiF-LiCl-LiI eutectic in the paste electrolyte, as shown by the data for Cells No. 14, 16, 17, 19, 20, 21, L-2, and L-3 plotted in Fig. V-38. This relation may result from an increase in the reaction zone available for Li_2Se formation

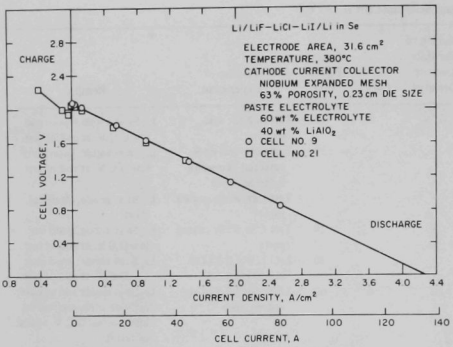

Fig. V-36. Voltage-Current Density Characteristics of Lithium/Selenium Cells No. 9 and 21. ANL Neg. No. 308-2561.

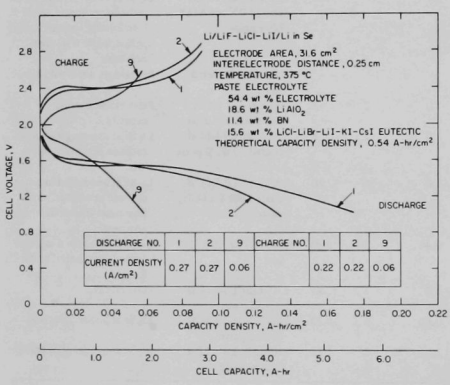

Fig. V-37. Voltage-Capacity Density Curves for Lithium/Selenium Cell No. 17. ANL Neg. No. 308-2392.

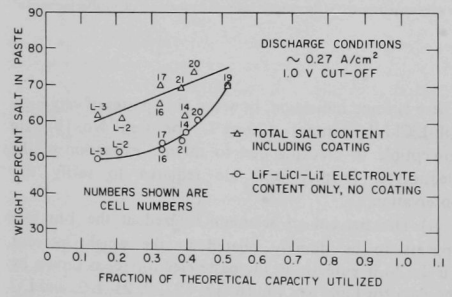

Fig. V-38. Effect of Paste Electrolyte Composition on Selenium Utilization. ANL Neg. No. 308-2562.

owing either to solubility of the electrolyte in the cathode materials or to salt flooding at the electrolyte-cathode interface. More information is required at the higher and lower LiF-LiCl-LiI weight percentages to verify the observed 37% selenium utilization change for a 20 wt % LiF-LiCl-LiI composition change.

5) The problem that appears unaffected by the changes made in these cell tests is formation of Li_2Se at the anode and cathode perimeter. Changes will be made in the cell construction and testing procedures for future cell tests in an attempt to minimize this problem.

b. Paste Electrolyte Studies (L. E. Trevorrow, J. G. Riha)

Development work on paste electrolytes consisting of molten LiF-LiCl-LiI eutectic and lithium aluminate filler has emphasized two properties of the pastes, ionic resistivity and permeability to selenium.

(1) Resistivity of Paste Electrolytes. Measurements of the minimum, empirically realizable paste resistivities were carried out because they would indicate the minimum realizable internal cell resistances. Resistances were, therefore, measured for paste samples with varying salt-filler ratios and surface treatments. The paste samples used in resistance measurements were 13-mm dia disks with nominal thicknesses of 2.5 mm, pressed at 1050 kg/cm^2 *in vacuo* at 25°C from filler-salt mixtures. Pulverization and sintering at 400°C had been carried out thrice on each mixture. One set of disks was conditioned by exposure to lithium vapor at 500–600°C, a second set was conditioned by coating disk faces with thin films of lithium through vacuum evaporation, and a third set received no conditioning. The purpose of conditioning was to improve contact between the paste electrolyte and the lithium electrode.

Resistance measurements were carried out by a dc, potentiometric technique with each paste disk held between two lithium-impregnated, stainless steel Feltmetal disks. Paste resistivities were derived from the resistance measurements and the dimensions of a sample; resistivity = resistance $\times$ (A/L), where A and L are the geometrical facial area and the thickness of the disk, respectively. Figure V-39 shows resistivity ratios of paste at 350°C as a function of volume fraction of electrolyte, both for experimental values and for theoretical values based on Maxwell's equation [96] for conduction in heterogeneous systems: paste resistivity/salt resistivity = $(2+f)/(2-2f)$, where f = volume fraction of filler. Figure V-39 indicates that conditioning had no effect on paste resistivities for samples containing 40 and 50 wt % salt, and also that paste-electrolyte resistivities can be realized that are no greater than 1.1 to 1.4 times those predicted from Maxwell's theory.

(2) Permeability of Paste Electrolytes. The permeability of paste electrolytes to gaseous helium implies the existence of mechanical imperfections, which may be related to the

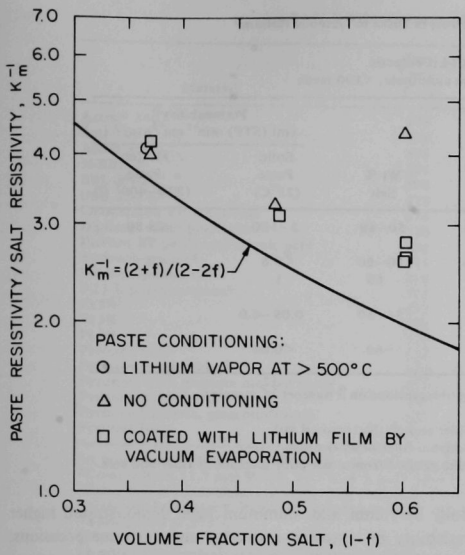

Fig. V-39. Dependence of Resistivity Ratios at 350°C on Salt Content for Paste Electrolyte Samples Prepared From Lithium Aluminate and the LiF-LiCl-LiI Eutectic. ANL Neg. No. 308-2391.

interelectrode leakage of selenium observed in cell tests. The development of pastes with minimum permeability was, therefore, considered a basic objective. The studies described below demonstrated that the fabrication procedure can be altered to produce pastes with significantly lower permeability to helium. Permeabilities were obtained from measurements of flow rates through paste disks at measured pressure drops through the disks.

To determine which fabrication variables significantly affect permeability, an experimental design discussed by Stowe and Mayer [97] was used in which an 8 X 8 matrix allowed testing five variables at two levels with two degrees of freedom. The variables and levels chosen for the study, using paste disks with 13-mm diameter and 2.5-mm thickness, were (1) filler drying temperature, 200 and 430°C, (2) salt-filler ratio, 50 and 60 wt %, (3) atmosphere for sintering the salt-filler mixture, helium and vacuum, (4) pressing temperature, 25 and 100°C, and (5) pressing pressure, 700 and 1050 kg/cm^2.

At the 95% confidence level, the following conclusions were obtained from the study: (1) Below the salt melting point, the permeability of pastes is significantly decreased by using the lower salt/filler ratio and higher pressing temperature and is significantly increased by higher pressing pressures. (2) Above the salt melting point, the permeability is significantly decreased by using higher pressing temperatures.

The second area of experimental work on paste permeability, development of an infiltration method of paste fabrication, resulted in a more pronounced reduction of permeability. An infiltration method was discussed by Tantram *et al.* [98], who prepared electrolytes by first pressing a cake from a salt-poor mixture of filler and salt, then allowing the remainder of the required salt to melt into the cake. We have observed that paste electrolytes prepared by infiltration are less permeable to helium than pastes prepared by the conventional method of pressing a mixture containing filler and all of the required salt. Further, we have observed that paste electrolytes prepared by allowing all the required salt to melt into a cake of pure filler are less permeable to gaseous helium than those prepared by allowing only a fraction of the required salt to melt into a cake of salt-poor mixtures.

The cracking of pure filler disks of 7.5-cm diameter during infiltration by molten salt was the main difficulty to be overcome in the development of this method. Pure filler disks pressed at 1000–1200 kg/cm^2 almost invariably cracked. Pure filler disks of 7.5-cm diameter were successfully infiltrated, however, under the following conditions: A filler disk was pressed at 600 kg/cm^2. The disk was heated to 450–460°C while resting on a tantalum plate protected from drafts. The heat source was on the bottom face and the edges of the disk. About 60–75% of the required salt was added as a powder to the top face, mainly near the edges, in small increments that melted immediately. The salt distributed itself throughout the disk by flowing from the edges to the center. The disk was slowly cooled to 25°C at 1–3°C/min, then it was turned over and the remainder of the required salt was added to the opposite face by repeating the procedure described above. Table V-20, listing the permeabilities of various samples, indicates the significantly lower permeability that is characteristic of pastes prepared by the infiltration of pure filler disks.

c. Materials of Construction (M. L. Kyle, F. J. Martino)

The development of reliable, long-lived lithium/selenium secondary batteries requires corrosion-resistant materials. Selenium, lithium, and the molten salts utilized in these cells are relatively reactive and consequently are corrosive to many common materials.

Current emphasis is on the cathode compartment, which requires a material resistant to the selenium and lithium-selenium alloys that are present in the cathode compartment in the partially discharged state. Most corrosion tests are performed with a 20 at. % lithium-selenium mixture, which was chosen as representative of the cathode composition of a partially discharged cell.

Figure V-40 summarizes the corrosion data for the more corrosion-resistant materials examined in this program. The

TABLE V-20. Permeabilities of Paste Electrolyte Disks to Gaseous Helium[a]

Salt Component of Disk: LiF-LiCl-LiI eutectic
Filler Component of Disk: Lithium aluminate, <100 mesh

Fabrication Method	Disk Dia (cm)	Disk Pressing Pressure (kg/cm^2)	Disk Pressing Temp. (°C)	Wt % Salt	Permeability[b] [ml (STP) min^{-1} cm^{-2} atm^{-1}] Solid Paste (25°C)	Molten Paste (370–400° C)
Conventional[c]	1.3	700–1050	25–100	50–60	2–100	<3-30
Infiltration of pure filler[d]	1.3	700–1050	25–100	50–60	<0.8	<3
Conventional[c]	7.5	1300	200	60	1	-
Infiltration of mixture[e]	7.5	1200	150	56–57	0.09–4.0	-
Infiltration of pure filler	7.5	600	150	~60	<0.04	-

[a]The permeabilities and conditions listed are ranges representing observations on a number of samples.
[b]Corrected to 0.25-cm thickness.
[c]Disks were pressed from a pulverized and sintered mixture of filler and all the required salt.
[d]All the salt was added by allowing it to melt into a cake pressed from filler powder only.
[e]A fraction of the salt was added by allowing it to melt into a cake pressed from a salt-poor mixture of filler and salt.

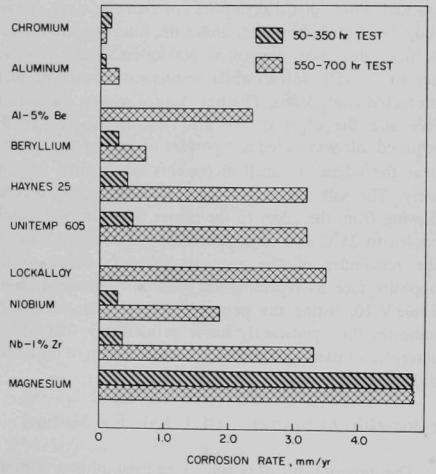

Fig. V-40. Corrosion Rates Observed in 20 at. % Li-Se Mixtures (temperature, 375°C; dynamic isothermal capsule tests). ANL Neg. No. 308-2375.

results of both short-term (50–350 hr) and longer-term (550–700 hr) dynamic isothermal capsule tests (in which the corrosion specimen is sealed in an evacuated quartz capsule along with a 20 at. % Li-Se mixture and the capsule is rotated during equilibration to produce uniform specimen exposure) are included. Chromium has consistently demonstrated the best corrosion resistance to lithium-selenium mixtures and is the prime candidate for use in the construction of cells that will be used in the initial life tests. Both beryllium and aluminum have demonstrated higher variability in corrosion resistance and, on some occasions, have yielded corrosion rates lower than that of chromium. If the cause of this variability could be determined, one of these materials might prove to be a better choice for long-lived cells.

d. Seals and Insulators (M. L. Kyle, F. J. Martino)

Lithium/selenium cells require electrically insulating materials resistant to lithium, selenium, lithium-selenium alloys, and molten halide salts. These cells may also require a sealant resistant to these substances in order to produce a hermetically sealed battery.

Several high-temperature polymers with reported good thermal stability were tested for corrosion resistance to lithium, molten salts, and selenium. Polymers were investigated because they potentially offered both electrical insulating and hermetic sealing capabilities in a thin, lightweight form which could reduce both the size and weight of the battery. Table V-21 presents the results of the corrosion tests that were performed.

None of the polymers appeared satisfactory for long-term cell application. Consequently, efforts to hermetically seal the cell will now be directed primarily toward the development of suitable metal-ceramic seals.

3. High-Specific-Energy Lithium/Sulfur Cells for Electric Vehicles [99]

Battery-powered electric automobiles are a possible means of reducing significantly the amount of air pollution caused by vehicles. However, an all-electric automobile is not practical at the present time because available batteries

TABLE V-21. Corrosion Resistance of Insulating Polymers

Material	Test Temp. (°C)	Test Duration (hr)	Exposure Condition	Results
Astrel[a] 360	375	72	Li	Destroyed
Astrel 360	375	72	Se	Destroyed
Astrel 360	375	72	Electrolyte[b]	Destroyed
M-BBB-2[c]	375	113	Electrolyte	Brittle
BBL-SN-2[c]	375	125	Argon	Brittle
BBB-33-1-C[c,d]	375	113	Electrolyte	Brittle
Chemstrand TR-BX-2-ICO	375	125	Argon	Brittle, cracked
Diphenyl ether polyimide	375	125	Argon	Brittle, cracked
DuPont XP perfluorosulfonic acid	375	125	Argon	Brittle, cracked
Hydrophenazine[e]	375	113	Electrolyte	Brittle, cracked
Polybenzimidazole[e]	375	113	Electrolyte	Brittle, cracked
P-11-E polypyrrolone[e]	375	113	Electrolyte	Brittle, cracked
P13N[f]	375	72	Li	Destroyed
P13N	375	72	Se	14 mm/yr corrosion
P13N	375	72	Electrolyte	7.4 mm/yr corrosion
Pyronne film[g]	400	232	Argon	Destroyed
Pyronne molded block	400	232	Argon	Brittle, cracked
Pyronne–15% graphite molded block	400	232	Argon	Brittle, cracked
Pyronne welded block	400	232	Argon	10% wt loss
Pyronne laminate, glass reinforced	400	232	Argon	Destroyed
Pyronne foam	400	232	Argon	40% wt loss

[a]A polyarylsulfone product of the Chemical Divison, 3M Company.
[b]Composition 11.7 mol % LiF, 29.1 mol % LiCl, 59.2 mol % LiI.
[c]Benzimidazobenzophenanthroline polymers cast from CH_3SO_3H obtained from Dr. R. L. Van Deusen, Air Force Materials Laboratory, Wright-Patterson Air Force Base, Ohio.
[d]Yarn drawn at 575°C.
[e]Samples obtained from Dr. D. H. White, The University of Arizona.
[f]A polyimide laminating varnish product of TRW, Inc. Sample was 50/50 mixture of polymer and chopped glass fibers.
[g]Heterocyclic aromatic polymers having the following recurring unit in the polymer chain.

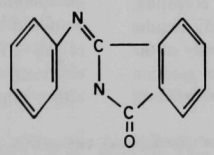

have an insufficient energy-storage capacity per unit weight and are, therefore, heavy, bulky, and too costly for general consumer acceptance. Recent studies [100–102] have shown that a major improvement in specific energy (W-hr/kg) must be achieved without a corresponding sacrifice in specific power (W/kg) before electric passenger vehicles can become technically attractive. For such a vehicle to have a reasonable range, say 200 miles, and acceptable acceleration and hill-climbing ability, the battery should have a specific energy of at least 200 W-hr/kg. To be economically feasible (i.e., competitive with present internal-combustion engines), the battery should cost no more than about \$2/kg (~\$0.92/lb), or about \$10/kW-hr.

The ultimate goal of the current experimental program is to develop the technology required to construct a multi-kilowatt secondary battery capable of meeting the above requirements. The immediate program is concerned with electrical performance evaluations of small experimental cells (~1–5 cm^2 electrode area), materials testing, supporting chemical studies, and preliminary battery design calculations for electric vehicles. The electrical performance studies have involved cells of the type Li/LiX/S, Li/LiX/P_4S_{10}, and Li/LiX/P_4S_3, where LiX represents a molten halide salt containing lithium cations.

a. Single-Cell Studies (M. L. Kyle, H. Shimotake, R. Rubischko [103], F. J. Martino)

The experimental cells were operated at temperatures of 325 to 400°C under a high-purity helium atmosphere to avoid contamination of the lithium anode and the electrolyte by nitrogen, oxygen or moisture. The anode and cathode reactants and the electrolyte are all liquid at these temperatures. The effects of cell configuration, cathode current-collector structure, and cathode material were evaluated by means of electrical performance tests. In general, the anode consisted of liquid lithium contained in stainless steel Feltmetal, and the cathode was molten sulfur, P_4S_{10}, or P_4S_3 contained in a porous current-collector structure. The anode and cathode assemblies were immersed in the molten-salt electrolyte with an interelectrode spacing of 0.3 to 1.0 cm.

Electrical performance tests were conducted on a series of cells to determine the effects of different operating

conditions and variations in the cell design. The performance of the cells was evaluated during constant-current operation on the basis of voltage-current density data, voltage-capacity density data, the relationship between current density and capacity density, and the cycle life. In general, the open-circuit potential of a fully charged lithium/sulfur cell was 2.1 to 2.3 V, and the short-circuit current densities ranged between 4.8 and 8.5 A/cm^2. The results show that these cells can be charged and discharged at high current densities.

The effect of temperature on cell performance, which was investigated briefly, is illustrated by the results from two identical cells that were operated at different temperatures but at the same current density (1.0 A/cm^2). One cell, which was operated at 364°C, had a capacity density of 0.022 A-hr/cm^2 (above 1.0 V), compared with 0.052 A-hr/cm^2 for the other cell at 385°C. Another cell with a molybdenum-foam cathode current collector was operated between 350 and 400°C at current densities of 0.33 and 1.0 A/cm^2. The capacity density of this cell nearly doubled with a 50°C increase in the temperature (0.092 vs 0.056 A-hr/cm^2 above 1.0 V and 0.033 vs 0.021 A-hr/cm^2 above 1.0 V, respectively, at the current densities of 0.33 and 1.0 A/cm^2. These results indicate that attempts to decrease the temperature to about 300°C to ease certain design problems (e.g., corrosion, sulfur containment, and thermal insulation) may require the use of chemical additives to reduce the viscosity of the sulfur and increase the diffusion rate of the reaction product within the cathode. Some additives also perform the useful function of lowering the vapor pressure of the cathode material.

The possibility of using phosphorus as an additive to the cathode of lithium/sulfur cells was explored by operating similar cells with sulfur, P_4S_{10}, and P_4S_3 cathodes to determine which one provides the highest capacity density. The characteristics of the cells and the results are presented in Table V-22. The performance of the P_4S_3 cell was inferior to that of both of the other cells in terms of capacity density and energy density. The short-circuit current densities of the sulfur and P_4S_{10} cells were between 6 and 7 A/cm^2. Data of this type were not obtained for the P_4S_3 cell. If the sulfur can be more fully utilized (sulfur utilization is indicated in Table V-22 by the percent of theoretical capacity density achieved, assuming the final cell reaction product to be Li_2S), the lithium/sulfur cell shows greater promise of achieving the required performance because of its higher capacity per unit volume or weight. However, the P_4S_{10} cell warrants further investigation because a higher energy density may be attainable (i.e., the voltage of the Li/P_4S_{10} cell, during constant-current discharge, is slightly higher than that of the Li/S cell) and because some practical design problems may be alleviated by the lower vapor pressure of P_4S_{10}.

The low electronic conductivities of sulfur and phosphorus-sulfur compounds (about 10^{-9} and 10^{-7} ohm^{-1} cm^{-1}, respectively, at 375°C) necessitate the use of an efficient current collector structure to provide electrical conduction paths to the electrochemical reaction sites at the cathode-electrolyte interface. Earlier

TABLE V-22. Comparison of Lithium/Sulfur, Lithium/P_4S_{10}, and Lithium/P_4S_3 Cells

Anode: lithium
Cathode: as indicated
Electrolyte: LiBr-RbBr eutectic salt (mp ~278°C)
Interelectrode distance: 1 cm
Cathode current collector: stainless steel Feltmetal, 80% porosity, 29 μm mean pore dia

Cathode Material	Temp. (°C)	Current Density (A/cm^2)	Theoretical Capacity Density (A-hr/cm^2)	Capacity Density above 1.0 V (A-hr/cm^2)	Short-Circuit Current Density (A/cm^2)	Open-Circuit Voltage (V)
Sulfur	375	0.57	0.50	0.114	-	2.3
Sulfur	355	0.46	0.73	0.119	6.5	2.3
	365	0.34		0.124		
	364	1.03		0.022		
	363	0.34		0.103		
P_4S_{10}	375	0.12	0.40	0.074	-	2.5
P_4S_{10}	368	0.21	0.39	0.015	-	2.5
		0.31		0.009		
		0.52		0.007		
P_4S_{10}	373	0.21	0.39	0.069	-	2.4
		0.31		0.073		
P_4S_{10}	340	0.31	0.41	0.082	6.2	2.7
	357	0.60		0.092		
	372	0.31		0.116		
P_4S_3	377	0.13	0.28	0.053	-	2.2
		0.33		0.029		
		0.41		0.027		
		0.64		0.037		

investigations (ANL-7675, pp. 143–146) had shown that cell performance is related to the porosity and pore size of the cathode current collector. These and subsequent results showed that the capacity density increased and the total overvoltage decreased with increasing porosity of the current collector at porosities up to 80% or higher. Additional data on the effect of the cathode current-collector structure upon capacity density are presented in Table V-23. At current densities in the vicinity of 0.5 A/cm^2, capacity densities from 0.003 to 0.143 A-hr/cm^2 were obtained as the material and structure of the cathode current collector were varied. The highest capacity densities were obtained with the molybdenum foam (75% porosity, 30 μm pore size) and the stainless steel Feltmetal (80% porosity, 29 μm pore size). Small differences in the porosity of the molybdenum foam appeared to have little effect upon cell performance. The relatively high performance obtained with the foam is encouraging because several materials, such as beryllium, niobium and chromium, which are not available as Feltmetal, can be fabricated into foams.

Three similar lithium/sulfur cells were operated to determine the effect of cathode thickness upon the capacity density. This information is necessary to determine the optimum cathode thickness in a practical cell design. The three cells used the LiBr-RbBr electrolyte with an interelectrode distance of 1 cm and were operated at 400°C. The difference in the cells was that the cathode current collectors (Type 302 stainless steel Feltmetal, 80% porosity, 29 μm pore size, 0.7-cm^2 surface area) had thicknesses of 0.16, 0.32, and 0.48 cm, respectively. The thickness of the cathode, within the above range, had no significant effect upon the capacity densities at various current densities, indicating that the effective thickness of the cathode was less than 0.16 cm.

In view of the above results, a new cathode structure was designed with the objective of increasing the sulfur-electrolyte interfacial area within a given volume. A cell incorporating this cathode design is illustrated in Fig. V-41. The cathode consisted of four 11 X 11 X 1.6-mm pieces of

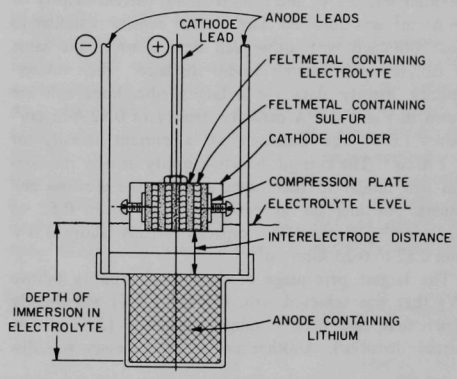

Fig. V-41. Laminated-Cathode Lithium/Sulfur Cell. ANL Neg. No. 308-2390.

TABLE V-23. Effect of Cathode Current Collector on Lithium/Sulfur Cell Performance

Anode: lithium
Cathode: sulfur
Electrolyte: LiBr-RbBr eutectic salt (mp ~278°C)
Interelectrode distance: 1.0 cm
Cathode current collector: as indicated

Cathode Current Collector						
Material	Porosity (%)	Mean Pore Dia (μm)	Temp. (°C)	Current Density (A/cm^2)	Theoretical Capacity Density (A-hr/cm^2)	Capacity Density above 1.0 V (A-hr/cm^2)
Stainless steel Feltmetal (Huyck)	80	29	375	0.57	0.50	0.114
Stainless steel Fibermetal (Brunswick)	85	40	375	0.41	0.26	0.048
Molybdenum foam	75	30	400	0.44	0.46	0.143
			400	0.88		0.051
Molybdenum foam	82	a	385	0.43	0.62	0.121
				0.85		0.060
				1.39		0.023
Niobium Expanded Mesh	76	(0.24 cm)[b]	385	0.58	1.2	0.005
Chromium foam	68	25	385	0.60	0.43	0.004
Stainless steel Fibermetal (Brunswick)	92	30	385	0.44	0.32	0.003

[a]Not available.
[b]Die size.

Huyck Type 302 stainless steel Feltmetal impregnated with sulfur, which were sandwiched between five similarly sized pieces of Feltmetal impregnated with electrolyte to form a laminated structure. The projected area of the cathode, i.e., the cathode-electrolyte surface directly facing the anode, was 1.58 cm^2. The cathode assembly was immersed in the LiBr-RbBr electrolyte to a depth of 0.3 cm, with an interelectrode distance of 1 cm.

The voltage-current density data for a cell with laminated cathode are shown in Fig. V-42. The open-circuit potential was 2.2 V, and a short-circuit current density of 6.6 A/cm^2 was obtained. This current density is similar to those obtained with other cell designs using the same electrolyte and interelectrode distance. The voltage-capacity density data for a laminated-cathode cell are shown in Fig. V-43. A capacity density of 0.52 $A\text{-}hr/cm^2$ above 1.0 V was obtained at a current density of 0.52 A/cm^2. The current density-capacity density relationship was similar to that obtained with the previous cell designs. An increase in current density from 0.52 to 1.04 A/cm^2 decreased the capacity density above 1.0 V from 0.52 to 0.23 $A\text{-}hr/cm^2$.

The largest percentage of theoretical capacity (above 1 V) that was achieved with this cell (24%) was slightly higher than had been obtained previously (22% at low current densities). Another cell of this design was discharged as far as practicable to determine the maximum utilization of sulfur that could be achieved. The cell was discharged to zero voltage, placed on open circuit to allow diffusion to proceed, and discharged again to zero voltage. When this procedure had been repeated 19 times, 0.67 $A\text{-}hr/cm^2$ had been withdrawn from the cell. This value corresponds to about 52% utilization of the sulfur, assuming that Li_2S is the reaction product. This result suggests that reasonably high utilization of the sulfur may be achieved if the cathode can be designed to permit adequate diffusion of the product.

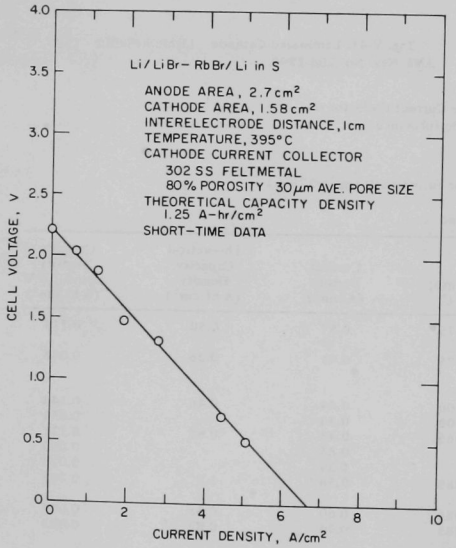

Fig. V-42. Voltage-Current Density Characteristics of a Lithium/Sulfur Cell with a Laminated Cathode. ANL Neg. No. 308-2389.

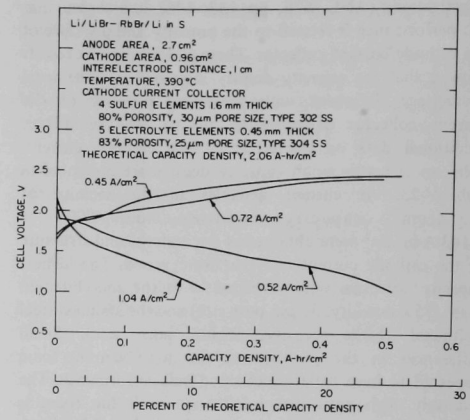

Fig. V-43. Voltage-Capacity Density Characteristics of Lithium/Sulfur Cell with Laminated Cathode. ANL Neg. No. 308-2388.

A cell with a laminated cathode consisting of five porous graphite plates (1.15 X 1.15 X 0.094 cm, 63% porosity, mean pore size 1.4 μm) and six molybdenum foam plates (1.15 X 1.15 X 0.165 cm, 75% porosity, mean pore size ~20 μm) was assembled and tested. The graphite was filled with P_4S_{10}. The anode and cathode assemblies were immersed in LiCl-KCl eutectic electrolyte (interelectrode distances, 1.0 cm), and the cell was ooperated at 400°C. Although the P_4S_{10} utilization above 1.0 V was low (15 to 17% of the sulfur), the cell performance remained constant over 15 discharge-charge cycles at current densities of 0.1 to 0.5 A/cm^2. For use in electric vehicles, a lithium/sulfur battery should have a cycle life of at least 300 charge-discharge cycles and a lifetime of three years or more. At present, the cycle life and lifetime of the experimental cells appear to be limited by the loss of sulfur or P_4S_{10} from the cathode.

The above results indicate that improved utilization of the cathode reactant and improved cell cycle life may be achieved with the laminated cathode structure. However, additional development work is needed to determine the

most appropriate materials for this purpose and the optimum dimensions and configurations of the laminated cathode structure.

b. Studies of Molten-Salt Electrolytes (J. P. Ackerman, D. M. Gruen [104], A. Zielen [104], C. H. Liu [105]

In the selection of a molten-salt electrolyte and a cathode material for a practical lithium/chalcogen secondary cell, it is necessary to have pertinent information on the phase relationships and mutual solubilities of these two materials and on possible chemical reactions that could decrease the capacity or cycle life of the cell. A basic chemical study is being undertaken to understand the nature of the solutions of sulfur-bearing species in molten-salt electrolytes and to find methods of minimizing or eliminating the solubility. The initial work, directed to the formation and study of the chemical behavior of sulfur-bearing species in molten halide salts will involve the preparation, characterization, and analysis of molten salt solutions containing known concentrations of sulfur and sulfide.

c. Materials Testing (M. L. Kyle, F. J. Martino)

Additional corrosion tests have been performed to evaluate various electrically conducting materials for use as cell housings and current collectors. Specimens of the materials were exposed to molten 20 at. % lithium-80 at. % sulfur mixtures at 375°C in rotating-paddle or dynamic isothermal capsule tests. Two types of tests have been performed. Shorter-term tests of about 100–300 hr duration were used to screen a variety of metals and alloys. Longer-term (~600-hr) tests were used to investigate some of the more promising materials.

The results of both types of tests are presented in Table V-24. In general, the corrosion rates of the stainless steels were less than about 0.15 mm/year in the shorter-term tests, and the corrosive attack occurred by a surface reaction that produced an adherent, electrically conductive film. The nickel-base alloys proved to be more variable in their performance, as shown by the difference in the results for Hastelloy B and Monel as opposed to those for Hastelloy X and Inconel 702. Of the other materials tested, molybdenum, chromium, Zircaloy-2, and niobium showed

TABLE V-24. Comparison of Corrosion Rates of Metals by 20 at. % Lithium-Sulfur at 375°C

Test Material	Shorter-Term Tests: Exposure Period (hr)	Shorter-Term Tests: Corrosion Rate[a] (mm/yr)	Longer-Term Tests: Exposure Period (hr)	Longer-Term Tests: Corrosion Rate (mm/yr)	Remarks
Stainless Steels (Ni-Cr)					
2 RK 65	311	0.03	620	0.67	Conductive film
347	311–331	0.02–0.09	620	1.5–1.9	Conductive film
2 RN 65	311	0.10	-	-	Conductive film
2 RE 10	311	0.12	-	-	Conductive film
Worthite	311	+0.07	-	-	Conductive film
Croloy 16-1	304	+0.14	-	-	Conductive film
Carpenter 20	304	+0.21	-	-	Conductive film
Durimet 20	100	+0.24	-	-	Adherent film
Stainless Steels (Mn-Cr)					
205	309	0.05	620–642	0.35–5.4	Poorly conductive film
Tenelon	304	0.18			
Nickel-Base Alloys					
Hastelloy X	331	0.02	620–642	0.17–2.0	Conductive film
Inconel 702	311	0.02	615	0.07	Nonconductive film
Inconel 800	331	0.23			Conductive film
Hastelloy B	309	1.93			Dissolution
Monel	304	3.68			Dissolution
Inconel 718	100	+0.12	642	0.07–0.10	Adherent film
Inconel 600			620	0.54	Nonconductive film
Hastelloy C			615	0.49	Poorly conductive film
Other					
Molybdenum	100	0.01	615	0.001–0.07	No detectible corrosion
Chromium	100–328	0.01–+0.17	642	0.01–0.16	Poorly conductive film
LT-1	101	0.03			Al_2O_3 reduction
Zircaloy-2	101–136	0.05–+0.01	620	0.94–1.1	Nonconductive film
Niobium	306	0.09	615	1.6–2.4	
Magnesium	304–331	0.11–0.24			Nonconductive film
Aluminum	304–331	0.02–0.85	620–642	0.01–2.4	Nonconductive film
Titanium	304	0.48			
Beryllium	233	0.55			Sample pitted
Tantalum	101	0.56	615	2.0	Dissolution
Nickel	100	1.80			Dissolution
Iron	100	2.36			Dissolution

[a]"+" indicates a weight gain of the specimen as a result of film formation.

the greatest corrosion resistance. Although the results for magnesium and aluminum are somewhat variable, these metals and their alloys are of considerable interest because of their light weight and low cost.

The 600-hr tests were conducted to determine the effect of exposure time upon corrosion rates and to check the validity of using linear extrapolation to obtain annual rates. Several of the materials, such as niobium, Type 205 stainless steel, Hastelloy X, and Zircaloy-2, showed significantly higher rates in the 600-hr tests than in the shorter-term tests (see Fig. V-44). The reason for this behavior is not fully understood, but it may be related to intergranular attack or to the temporary formation of a protective film. Additional tests are needed to investigate this phenomenon more fully. Other materials which had low corrosion rates in the shorter-term tests, such as molybdenum and chromium, continued to show low corrosion rates in the 600-hr tests. Aluminum had highly variable corrosion behavior in the longer tests. Most of the observed corrosion rates were similar to those obtained in the short-term tests.

Although these corrosion data are useful for a preliminary evaluation of potential cell materials, they should not be regarded as corrosion rates in an operating cell, since they do not reflect the electrochemical effects resulting from potential differences within the cell. The performance of the more promising materials will be further evaluated by long-term cell tests.

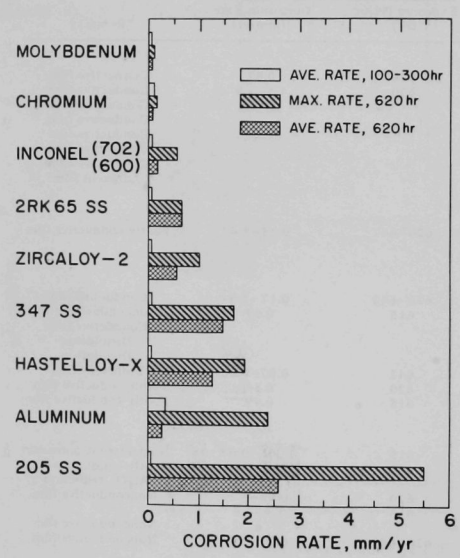

Fig. V-44. Comparison of Corrosion Rates in Li-S Mixtures (temperature, 375°C; composition, 20 at. % Li-80 at. % S; est duration, 100-300 or 620 hr as shown). ANL Neg. No. 308-2387.

d. Seals and Insulators (M. L. Kyle, F. J. Martino)

Data on the corrosion rates of several ceramic insulating materials in molten lithium and lithium-sulfur mixtures were reported previously (ANL-7675, pp. 149, 162). A subsequent 1168-hr immersion test at 375°C showed hot-pressed, high-purity beryllia to be the most resistant to lithium attack of any insulator tested to date. The average corrosion rate was 0.011 mm/yr. Other types of beryllia (commercial grade, recrystallized grade) have exhibited corrosion rates as high as 12 mm/yr. The purity and method of fabrication appear to have a marked influence on the corrosion rate of beryllia.

e. Design Calculations for Electric Vehicles (M. L. Kyle, M. S. Foster [106], H. Shimotake, E. J. Cairns)

Preliminary calculations were made to estimate the performance that might be expected of a battery-powered family automobile. The results represent the maximum possible performance for a particular battery because of several simplifying assumptions that were used in the calculations. The most important of these assumptions was that the battery would deliver a specific energy of 220 W-hr/kg [107], regardless of the power density and depth of discharge throughout the driving profile. At high power levels, the deliverable specific energy of a battery is significantly lower than that at low power. More refined calculations are in progress in which these factors are taken into account. The new calculations will result in a downward revision of the reported vehicle ranges.

The automobile was assumed to have a curb weight of 1588 kg (3500 lb) and to carry a playload (passengers and luggage) of 227 kg (500 lb). The battery weight was 397 kg (875 lb) with a deliverable specific energy of 220 W-hr/kg (100 W-hr/lb). Other assumptions related to the vehicle are listed in Table V-25. The calculations of the vehicle range and maximum specific power requirements for the battery were based either upon constant velocity or upon urban [108], suburban, and cross-country driving [109] profiles which involve acceleration, deceleration, and hill-climbing in typical traffic-flow patterns.

The results of the calculations are presented in Table V-26 and Fig. V-45. These results, obtained with the urban and suburban driving profiles, indicate that an electric vehicle with normal accessories would have a maximum range of 326 to 364 km (203–226 mi) with a battery having a specific power of 152–161 W/kg (69–73 W/lb) and a deliverable specific energy of 200 W-hr/kg (100 W-hr/lb). Under constant-velocity

TABLE V-25. Assumptions Used in Vehicle Calculations

Curb weight of vehicle	1588 kg (3500 lb)
Payload of vehicle	227 kg (500 lb)
Tire rolling-resistance coefficient	0.0175
Air-drag coefficient	0.35
Frontal area of vehicle	2.32 m^2 (25 ft^2)
Efficiency (battery output to wheels)	0.82
Conversion factor from linear to total acceleration (including rotational)	1.1
Air density	1.25×10^{-6} g-sec^2/cm^4 (2.4×10^{-3} lb-sec^2/ft^4)
Battery specific energy (delivered)	220 W-hr/kg (100 W-hr/lb)
Accessory Power	
No accessories	0 W
Normal service accessories (lights, windshield wipers, heater-blower, defrosters, radio, etc.)	230 W
Convenience option (normal service accessories plus air conditioning, power steering)	6530 W

conditions, the range would be about twice that for the normal traffic-flow situations.

The calculations were extended to determine the increase in performance that could be obtained if the vehicle employed regenerative braking (an electromechanical system to recover part of the energy normally dissipated during braking and deceleration). The calculations made with the urban driving profile indicate that regenerative braking could increase the range of the vehicle by as much as 40%, assuming that 50% of the braking and deceleration energy could be recovered.

In the above calculations, the battery weight was assumed to be 25% of the curb weight of the vehicle, which is approximately equivalent to the weight of the power plant (engine, transmission, exhaust system, fuel and fuel tank) in a conventional internal-combustion-engine vehicle. If an electric vehicle were designed specifically to allocate a higher percentage of the total vehicle weight to the battery, a significant increase in power and range could be achieved.

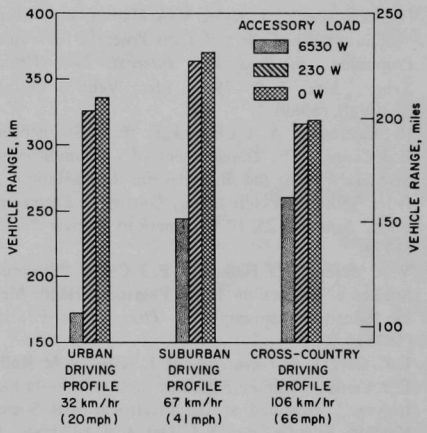

Fig. V-45. Vehicle Range Under Selected Driving Profiles. ANL Neg. No. 308-2386.

TABLE V-26. Range of Electric Vehicle Under Various Driving Conditions

Driving Profile	Accessory Load (W)	Range km	Range mi	Specific Power[a] W/kg	Specific Power[a] W/lb
Urban	0	336	208	150	68
(31.6 km/hr,	230	326	202	152	69
19.6 mi/hr)	6530	172	107	170	77
Suburban	0	370	230	160	73
(66.6 km/hr,	230	364	226	161	73
41.3 mi/hr)	6530	244	151	180	82
Cross-country	0	318	197	271	123
(106 km/hr,	230	317	197	273	124
65.8 mi/hr)	6530	260	162	291	132
32 km/hr, constant	0	731	454	53	24
(19.9 mi/hr)	230	682	423	54	25
	6530	238	148	73	33
64 km/hr, constant	0	546	339	107	48
(39.8 mi/hr)	230	532	330	108	49
	6530	308	191	128	58
96 km/hr, constant	0	384	238	163	74
(59.6 mi/hr)	230	379	235	164	74
	6530	282	175	181	82

[a]Minimum specific power required to accomplish driving profile.

REFERENCES AND FOOTNOTES

1. A summary of this section is given on pp. 11 to 13.
2. R. Sridhar, C. E. Johnson, E. J. Cairns, "Phase Diagrams of the Systems LiI-KI and LiI-RbI," *J. Chem. Eng. Data 15*, 244 (1970).
3. V. A. Maroni, E. J. Cairns, "Raman Spectra of Fused Carbonates," *J. Chem. Phys. 52*, 4915 (1970).
4. V. A. Maroni, D. M. Gruen, R. L. McBeth, E. J. Cairns, "Raman Spectrum and Vibrational Analysis for Gaseous Aluminum Chloride," *Spectrochim. Acta 26A*, 418 (1970).
5. H. Shimotake, M. L. Kyle, V. A. Maroni, E. J. Cairns, "Lithium/Sulfur Cells and Their Potential for Vehicle Propulsion" in *Proc. First Internat. Elec. Vehicle Symp., Nov. 5–7, 1969*, Elec. Vehicle Council, New York (1969).
6. H. Shimotake, A. A. Chilenskas, R. K. Steunenberg, E. J. Cairns, "The Development of Lithium/Selenium Secondary Cells and Batteries for Implantation" in *Proc. Fifth Intersociety Energy Conversion Engineering Conf., Sept. 21–25, 1970*, American Nuclear Society (1970).
7. V. A. Maroni, E. J. Hathaway, E. J. Cairns, "Structural Studies of Magnesium Halide-Potassium Halide Melts by Raman Spectroscopy," *J. Phys. Chem. 75*, 155 (1971).
8. E. C. Gay, L. E. Trevorrow, M. L. Kyle, V. M. Kolba, E. J. Cairns, "Lithium/Selenium Cells with Paste Electrolytes," presented at the Electrochemical Society Meeting, Atlantic City,, N.J., Oct. 4–8, 1970; see also *Extended Abstracts*, p. 150.
9. E. J. Cairns, G. H. Kucera, P. T. Cunningham, "Thermodynamic Studies of the Lithium-Selenium System by an Emf Method," presented at the CITCE Meeting, Prague, Sept. 28–Oct. 2, 1970; see also *Extended Abstracts*, p. 95.
10. R. Sridhar, E. J. Cairns, "Electrical Resistivities of Liquid Mixtures of Selenium and Tellurium," presented at the Electrochemical Society Meeting, Los Angeles, May 10–15, 1970; see also *Extended Abstracts*, p. 765.
11. J. G. Eberhart, *J. Amer. Chem. Soc. 53*, 223 (1970).
12. J. G. Eberhart, *J. Colloid. and Interfacial Sci. 33*, 191 (1970).
13. J. G. Eberhart, F. A. Cafasso, H. M. Feder, W. A. Kremsner, in *Corrosion by Liquid Metals*, pp. 461–467, Plenum Press, New York (1970).
14. Wilfred W. Scott, *Standard Methods of Chemical Analyses*, 5th ed., D. Van Nostrand Co., Princeton, N.J. (1939).
15. T. G. Pearson, P. L. Robinson, *J. Chem. Soc. 1931*, 413.
16. D. J. Rose, submitted for publication in *Science*.
17. D. J. Rose, *Nuclear Fusion, 1969*, p. 183.
18. A. J. Hatch *et al., Argonne National Laboratory Reviews 6*(1), 30 (1970).
19. T. Alexander, *Fortune*, p. 94 (June 1970).
20. Proceedings of the British Nuclear Energy Society Conference on Nuclear Fusion Reactors held at the UKAEA Culham Laboratory, September 17–19, 1969.
21. Ibid., p. 54.
22. Ibid., p. 441.
23. A. P. Fraas, H. Postma, USAEC report ORNL-TM-2822 (1970).
24. J. D. Lee, USAEC report UCRL-72493 (1970); presented at the Symposium on Fusion Reactor Design, Texas Tech. Univ., Lubbock, Texas, June 2–5, 1970.
25. R. W. Werner, UCRL-72329 (1970); presented at the Fifth IECEC, Las Vegas, Nevada, September 21–25, 1970.
26. E. J. Cairns *et al.*, USAEC report ANL-7316 (1967).
27. E. Veleckis, R. K. Edwards, *J. Phys. Chem. 73*, 683 (1969).
28. G. W. Johnson, R. Shuttleworth, *Phil. Mag. 4*, 957 (1959); L. F. Epstein, KAPL-MEMO-LFE-10 (1952); H. Mandel, NAA-SR-MEMO-10745; T. Emi, R. D. Pehike, *Met. Trans. 1*, 2733 (1970).
29. H. Reiss, *Advan. Chem. Phys.*, Vol. IX, I. Prigogine, ed., Interscience Publishers, New York (1965).
30. M. S. Wertheim, *Phys. Rev. Letters 10*, 321 (1963).
31. E. Thiele, *J. Chem. Phys. 39*, 474 (1963).
32. The Ostwald coefficient is defined as the volume of gas dissolved per unit volume of solvent.
33. J. M. Ziman, *Phil. Mag. 6*, 1013 (1961).
34. D. Pines, P. Nozieres, *The Theory of Quantum Liquids*, Vol. I, p. 168, W. A. Benjamin, Inc., New York (1966).
35. Ibid., p. 292.
36. J. Friedel, *Nuovo Cim. Suppl. 7*, 287 (1958).
37. B. Linder, *Advan. Chem. Phys.*, Vol. XII, p. 225, J. O. Hirschfelder, ed., Interscience Publishers, New York (1967).
38. Ref. 33, p. 220.
39. P. W. Langhoff, M. Karplus, *J. Chem. Phys. 53*, 233 (1970).
40. P. W. Langhoff, M. Karplus, *J. Opt. Soc. Amer. 59*, 863 (1969).
41. J. Lindhard, *Kgl. Danske Videnskab. Selskab, Mat. Fys. Medd. 28*(8) (1954).
42. E. Veleckis, G. Redding, ANL-7675, p. 64 (1970).
43. K. Thormeier, *Atomkernenerg. 14*, 449 (1969).
44. E. Veleckis, R. Blomquist, R. Yonco, M. Perin, ANL-7325, p. 128 (1967).
45. E. Veleckis, W. Kremsner, ANL/ST-4 (1970).
46. W. A. Harrison, *Pseudopotentials in the Theory of Metals*, p. 52, W. A. Benjamin, Inc., New York (1966).
47. J. Friedel, *Phil. Mag. 43*, 153 (1952).

48. A. S. Skapski, *J. Chem. Phys. 16*, 389 (1948).
49. J. K. Mackenzie, A. J. W. Moore, J. F. Nicholas, *J. Phys. Chem. Solids 23*, 185 (1962).
50. J. F. Nicholas, *Aust. J. Phys. 21*, 21 (1968).
51. Consultant, University of Louisville, Louisville, Kentucky.
52. A. I. Gerbanov, *Quantum Theory of Amorphous Conductors*, Consultants Bureau, New York (1965).
53. F. Feher, H. D. Lutz, *Z. Anorg. Chem. 333*, 216 (1964).
54. B. Meyer, *Elemental Sulfur*, Interscience, New York (1965).
55. Zygmunt Tomczuk of Chemical Engineering Division analytical group assisted in designing and carrying out the sulfide analysis.
56. Spectra-Mat., Inc., Watsonville, California.
57. W. W. Mullins, *J. Appl. Phys. 28*, 333 (1957).
58. W. W. Mullins, *Trans. Met. Soc. AIME 218*, 354 (1960).
59. B. C. Allen, *Trans. Met. Soc. AIME 236*, 915 (1966).
60. J. M. Blakely, H. Mykura, *Acta Met. 11*, 399 (1963).
61. W. K. Burton, N. Cabrera, F. C. Frank, *Phil. Trans. Roy. Soc. 243A*, 299 (1951).
62. W. W. Mullins, *J. Appl. Phys. 28*, 333 (1957).
63. W. W. Mullins, *Trans. Met. Soc. AIME 218*, 354 (1960).
64. W. W. Mullins, P. G. Shewmon, *Acta. Met. 7*, 163 (1959).
65. N. A. Gjostein, *Trans. Met. Soc. AIME 221*, 1039 (1961).
66. J. Y. Choi, P. G. Shewmon, *Trans. Met. Soc. AIME 224*, 589 (1962).
67. G. E. Rhead, *Acta. Met. 11*, 1035 (1963).
68. R. Chang, in *Proc. of the Conf. on Nuclear Applications of Nonfissionable Ceramics, Washington, D.C., 1966*, p. 101, A. Boltax, ed., American Nuclear Society, Hinsdale, Ill.
69. N. A. Gjostein, Scientific Laboratory, Ford Motor Co., Dearborn, Mich., private communication.
70. S. J. Rothman, N. L. Peterson, *Phys. Stat. Sol 35*, 305 (1969).
71. A. Kuper *et al.*, *Phys. Rev. 96*, 1224 (1954); *Phys. Rev. 98*, 1870 (1955).
72. M. S. Maier, H. R. Nelson, *Trans. Met. Soc. AIME 147*, 39 (1942).
73. J. Steigman *et al.*, *Phys. Rev. 56*, 13 (1939).
74. B. V. Rollin, *Phys. Rev. 55*, 231 (1939).
75. P. G. Shewmon, *Diffusion in Solids*, p. 100, McGraw-Hill Book Co., New York (1963).
76. D. M. Gruen (Chemistry Division) has indicated that the solubility of sulfur in LiCl-KCl is extremely low based on results of absorption spectral studies.
77. K. Irgolic, R. A. Zingaro, M. Kudchadker, *Inorg. Chem. 4*, 1421 (1965).
78. C. W. F. T. Pistorius, *J. Chem. Phys. 29*, 1421 (1958).
79. H. Gerding, J. W. Maarsen, P. C. Nobel, *Rev. Tran. Chem. 76*, 757 (1957).
80. W. A. Rodger, S. L. Reese, *Reactor and Fuel-Processing Technology 12*(2), 173 (1969).
81. S. C. Wait, Jr., A. T. Ward, G. J. Janz, *J. Chem. Phys. 45*, 133 (1966).
82. J. R. Durig, O. D. Bonner, W. H. Breazeale, *J. Phys. Chem. 69*, 3886 (1965).
83. G. J. Janz, T. R. Kozlowski, S. C. Wait, Jr., *J. Chem. Phys. 39*, 1809 (1963).
84. L. H. Ahrens, *Nature 174*, 644 (1954).
85. G. E. Walrafen, D. E. Irish, *J. Chem. Phys. 40*, 911 (1964).
86. K. Nakamoto, *Infrared Spectra of Inorganic and Coordination Compounds*, 2nd ed., p. 318, John Wiley & Sons Inc., New York (1970).
87. Ibid., p. 55.
88. E. J. Cairns, E. C. Gay, V. M. Kolba, M. L. Kyle, A. D. Tevebaugh, L. E. Trevorrow, *Interim Tech. Summary Report No. 2, Nov. 23, 1969–May 22, 1970, to U.S. Army Mobility Equip. R&D Center, Ft. Belvoir, Va., Project Order No. MERDC 175 - 69*, p. 37 (June 1970); ANL-7745 (1971).
89. A registered name of a product of the Westinghouse Electric Corporation with the approximate composition (wt %): Fe, 53.7; Ni, 29.0; Co, 17.0; Mn, 0.3.
90. Trade name of a product of the Huyck Metals Company with a porosity of 80 to 87% and a mean pore diameter of 0.02 cm.
91. The plane of the electrolyte disk was oriented vertically.
92. Kapton is a product of E. I. du Pont de Nemours; aluminizing was performed by the Norton Co., Inc.
93. Pyre ML manufactured by E. I. du Pont.
94. DC-63-502 manufactured by Dow Corning.
95. This work is sponsored by the U.S. Army Mobility Equipment Research and Development Center, Ft. Belvoir, Virginia.
96. R. E. Meredith, C. W. Tobias, in *Advances in Electrochemistry and Electrochemical Engineering*, Vol 2, Interscience, New York, p. 15 (1962).
97. R. Stowe, R. Mayer, *Ind. Eng. Chem. 58*, 36 (1966).
98. A. Tantram, A. Tseung, B. Harris, *Hydrocarbon Fuel Cell Technology*, pp. 187–211, B. Baker, ed., Academic Press, New York (1965).
99. This work was sponsored by the National Air Pollution Control Administration (NAPCA) of CPE, Public Health Service, U.S. Department of Health, Education and Welfare; the current sponsor is the Air Pollution Control Office of the Environmental Protection Agency.
100. R. S. Morse, "The Automobile and Air Pollution, A Program for Progress, Parts I and II," Report of the Panel on Electrically Powered Vehicles, U.S. Department of Commerce (Dec. 1967).

101. J. H. B. George, L. J. Stratton, R. G. Action, "Prospects for Electric Vehicles. A Study of Low Pollution–Potential Vehicles–Electric," A. D. Little Report to NAPCA, U.S. Department of Health, Education, and Welfare.
102. J. H. B. George, "Directions for Electric Vehicle Development," in *Proc. 1st Intern. Electric Vehicle Symposium, Nov. 5–9, 1969, Phoenix, Ariz.*, p. 29, Electric Vehicle Council.
103. Resident Associate from Gould, Inc.
104. ANL Chemistry Division.
105. Consultant, Arizona State University.
106. Chemical Engineering Division, computer applications consultant.
107. For comparison, conventional lead-acid storage batteries have specific energies in the range of about 5–25 W-hr/kg.
108. *Federal Register*, Vol. 35, No. 136 (July 15, 1970).
109. G. Hagey, Air Pollution Control Office, private communication (1970).

VI. NUCLEAR SAFEGUARDS STUDY [1]

(S. Lawroski)

At the request of the AEC's Office of Safeguards and Materials Management (OSMM), a program study has been initiated on nuclear safeguards, that is, measures designed to detect and guard against the diversion of strategically significant nuclear materials for unauthorized uses. It is desired that these measures will provide credible assurance that no diversion has occurred. Argonne's efforts in this regard are specifically directed at provisions for future privately owned plants for conversion, preparation, and fabrication of nuclear fuels into finished nuclear reactor fuel assemblies. Of primary concern are materials of such high strategic value as ^{239}Pu, ^{233}U and highly enriched ^{235}U fuels. Of secondary concern are low enriched (less than 20%) uranium fuels.

The study will include materials accountability, physical protection, and surveillance. Results of the study are for use by the AEC-OSMM in developing general criteria for future U.S. plants to assure that adequate safeguards are established and maintained. The OSMM will ultimately apply the study results for (1) current international (IAEA) negotiations under the Non-Proliferation Treaty, and (2) input to the development of safeguards criteria required in connection with licensing and regulation of future private domestic facilities.

The Argonne study is being performed principally by Chemical Engineering Division personnel. Significant assistance to the study is being given by people from other parts of ANL. The initial efforts were devoted to becoming familiar with existing reactor fuel conversion, preparation, and fabrication facilities. This was followed by visits to a number of these plants. Thus far, preliminary general design criteria have been formulated and discussed with the personnel of OSMM and Division of Regulation. Initial drafts of the criteria were made available to the AEC-OSMM by the end of this calendar year for internal and later external comment.

Discussions are now under way between ANL and the AEC-OSMM for possible future support and interest of further work in this general area.

REFERENCES AND FOOTNOTES

1. A summary of this section is given on p. 13.

VII. FLUIDIZATION PROCESSES [1]

(D. S. Webster, A. A. Jonke)

A. FLUIDIZED-BED COMBUSTION OF FOSSIL FUELS

(G. J. Vogel, E. L. Carls, L. Anastasia, R. L. Jarry, M. Haas, J. Pavlik, C. Schoffstoll)

Fluidized-bed combustion is being studied at Argonne National Laboratory as a method of reducing the quantity of atmospheric pollutants (oxides of sulfur and nitrogen) released during the combustion of fossil fuels. This work, which is being carried out under contract with the National Air Pollution Control Administration, is part of a large program involving numerous governmental agencies and industrial firms. A fluidized-bed combustor offers, in addition to *in situ* control of SO_2 emission, high heat-transfer rates and efficient contacting for gas-solids reactions. Also, combustion can be carried out at lower temperatures in a fluidized bed than in conventional combustors, and nitrogen oxide emission may be lower at the lower combustion temperatures.

The concept of fluidized-bed combustion involves burning fuel (coal or natural gas) in a fluidized bed of solids with simultaneous, continuous feeding of crushed or pulverized limestone to control sulfur dioxide emission. An upward flow of combustion air, distributed by a gas-distributor plate at the bottom of the combustor, expands the bed to a dense suspension. The limestone calcines to lime, then reacts with sulfur dioxide to form $CaSO_4$.

The results of bench-scale and laboratory-scale investigations performed during the report period are summarized here. Detailed data are presented in an annual report [2] on the fluidized-bed combustion program.

1. Bench-Scale Investigations

a. Equipment and Materials

The bench-scale stainless steel combustor employed in these studies has a 6-in. diameter and 6-ft length; upstream from the combustor is a preheater. Vibratory-screw feeders deliver the coal and the limestone additive from hoppers into transport-air streams for injection into the fluidized-bed combustor. A schematic diagram of the equipment is shown in Fig. VII-1. The fuels used in the bench-scale experiments reported here were pulverized coal and natural gas. In some bench-scale experiments with natural-gas fuel at ANL, the natural gas contained high-purity SO_2. The starting bed materials were particulate refractory alumina, fresh limestone powder, and partially sulfated particulate limestone; additives included limestone No. 1359 (97.8% $CaCO_3$, 1.3% $MgCO_3$), limestone No. 1360 (78% $CaCO_3$, 22% $MgCO_3$), dolomite No. 1337 (53.4% $CaCO_3$, 46.5% $MgCO_3$), and Tymochtee dolomite (49.3% $CaCO_3$, 36.6% $MgCO_3$). The flue gas from the

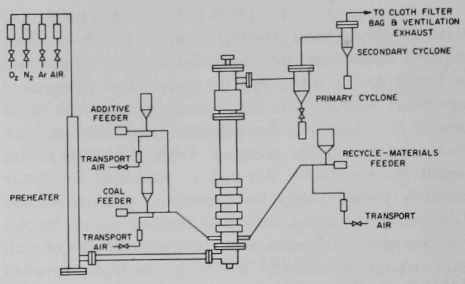

Fig. VII-1. Simplified Flowsheet of Bench-Scale Fluidized-Bed Combustor and Associated Equipment. ANL Neg. No. 308-2563.

combustor first passes through cyclone separators and a glass-fiber final filter, where entrained solids are removed; an aliquot passes through a gas-analysis system.

b. Procedure

The startup procedure for a bench-scale experiment commences with preheating the fluidized bed to approximately 1000°F by passing heated air through the bed and also employing resistance heaters installed on the combustor. Coal fed through a variable-drive volumetric screw feeder is then introduced into the bed by entrainment in a transport-air stream, and ignition occurs. (In natural-gas experiments, the bed is heated from 1000°F to the ignition temperature of natural gas with propane.) The bed temperature rises and is stabilized at 1600°F (or another selected temperature) by means of air passed through the annular coolant chambers on the lower section of the reactor. After 1 hr of steady-state operation (i.e., with relatively constant levels of oxygen, sulfur dioxide, and nitric oxide in the flue gas), additive injection is initiated.

During combustion, a small fraction of the coal, additive, and ash is elutriated by the gas and carried out of the bed before the coal is completely consumed. The bed and overhead solids are sampled periodically for analysis. To reduce carbon losses, it would be necessary to recycle the fly ash or to feed it to a second fluidized bed to complete combustion. Some experiments at ANL employed the recycle of fines. Most of the elutriated solids that had been removed from the gas stream by the primary cyclone were batch-fed into a variable-drive volumetric screw feeder and reintroduced into the bed.

At least two alternative modes of operation of a desulfurizing fluidized-bed combustor are possible. In one mode, the combustion bed is composed of a mixture of partially sulfated limestone of relatively coarse particle size

and any coarse ash produced by combustion of the fuel; the bed level is controlled by continuously withdrawing excess bed material. Since the limestone fed to the combustor becomes a principal constituent of the fluidized bed, selection of the particle size of the limestone feed is based primarily on the combustor operating conditions, especially gas velocity. The feed limestone particle size for this mode of operation is approximately the same as the coal particle size.

In the second mode of operation, the fuel is burned in a bed composed chiefly of ash or other refractory material, to which finely pulverized limestone is fed. Since the fine limestone particles are readily elutriated by the gas, they have a relatively short residence time in the bed. To improve reagent utilization efficiency and the fuel combustion efficiency, a portion of the elutriated limestone and fly ash can be recycled.

The operating conditions that were varied, in addition to type of starting bed material, type of additive, and fuel, were superficial gas velocity, additive particle size, combustion temperature, and Ca/S mole ratio in the feed streams. The effects of the different operating conditions on SO_2 removal, NO removal, regeneration of additive, CaO utilization, and combustion efficiency were measured in various series of experiments.

c. Results and Discussion

A series of coal-combustion experiments was carried out to evaluate the relative effectiveness for SO_2 removal of limestone No. 1359, limestone No. 1360, and dolomite No. 1337. These additives had average particle sizes of about 500 to 600 μm so that as much additive as possible would be retained in the fluidized bed and steady-state composition might be approached rapidly. At steady state [3], bed composition (i.e., Ca/S ratio) does not change with continued addition of fresh limestone and removal of reacted limestone. Also, the initial fluid beds were large-particle-size limestone that had been presulfated to nearly the expected steady-state level to shorten the experimental time.

These experiments were performed with a combustion temperature of 1600°F, a superficial gas velocity of 3 ft/sec, a 2-ft-deep fluidized bed, and Ca/S mole ratios in the feed streams of 2.3 to 2.6. SO_2 removals of 74 to 86% were achieved for the three additives. The results indicate that SO_2 removal is relatively independent of the type of additive material used in these studies.

In coal-combustion experiments with starting beds of limestone performed over the temperature range 1400–1800°F, a marked effect of combustion temperature on SO_2 removal was noted for both a limestone (No. 1359) and a dolomite (No. 1337). At 1500 to 1550°F and a Ca/S mole ratio of 2.5 with limestone No. 1359, SO_2 removal was 91%. At temperatures above and below this temperature range, lower SO_2 removals were observed as shown in Fig. VII-2. When dolomite was the additive, the temperature effect was nearly identical.

Coal-combustion experiments with a fluidized bed of partially sulfated limestone were performed to determine the effect of superficial gas velocity in the combustor on SO_2 removal by limestone No. 1359 additive. Coarse particles of limestone No. 1359 averaging 1010 μm diameter were fed to the fluid bed to ensure their retention in the bed at the highest gas velocity tested. The tests were made at 1550°F with a Ca/S mole ratio in the feed of ~4 (3.8 to 4.2 range) and at gas velocities of 3.5, 5.5, and 7.4 ft/sec. Calcium oxide utilizations were 20, 19, and 15% at these gas velocities. The greatest removal of SO_2 (83%) was observed at the lowest gas velocity, 3.5 ft/sec; similarly, at the highest gas velocity, 7.4 ft/sec, SO_2 removal (65%) was lowest. These results show that the fluidizing gas velocity has a significant effect on the removal of SO_2 by large-particle-size limestone during the combustion of coal.

Coal-combustion experiments were performed to determine the effect of Ca/S mole ratio in the feed streams on SO_2 removal in experiments of extended duration. No. 1359 limestone having an average particle size of 490 μm was added to a bed of sulfated limestone at three different rates. Run durations at the three operating conditions were 27, 19, and 20 hr to ensure that equilibrium conditions were closely approached in the fluid bed. At a cumbustion temperature of 1550°F and with Ca/S stoichiometric ratios of 2.5, 4.6, and 5.5, SO_2 removals were 78, 95, and 94%, respectively. This is in agreement with earlier results indicating that the rate of fresh limestone addition to the combustor fluid bed has a significant effect on the quantity of SO_2 removed from the

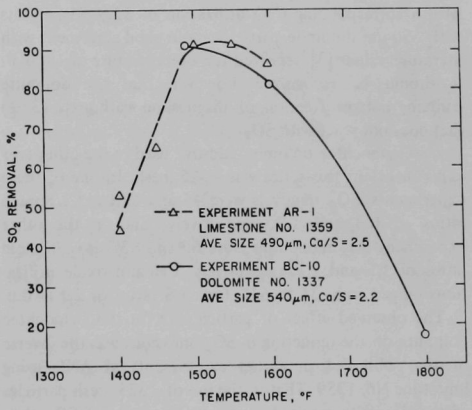

Fig. VII-2. Effect of Fluidized-Bed Combustion Temperature on SO_2 Removal. ANL Neg. No. 308-2564.

combustion gases. As the stoichiometric ratio was increased, CaO utilization decreased from 31 to 21% and then to 17%.

The SO_2 removal at a 2.5 Ca/S mole ratio with limestone No. 1359 at 1500°F was 78%, which is similar to those obtained with limestone No. 1360 and dolomite No. 1337 at combustion temperatures of 1550–1600°F and indicates that the effects of the additive types used are not significant.

In four bench-scale experiments, dolomite of two particle sizes (<44 and 650 μm) from the Tymochtee formation in western Ohio was evaluated as an additive for SO_2 removal during the combustion of coal at 1600°F. A purpose of these experiments was to compare SO_2 removal observed with our apparatus and conditions with SO_2 removals reported in the literature [4] for this type of limestone and a different apparatus.

In the first experiment with Tymochtee dolomite additive, a superficial gas velocity of 2.8 ft/sec and 650-μm particles of dolomite were employed. The dolomite particles were observed to remain in the fluidized bed. In contrast to previous experiments with 600–1400-μm particles of limestone No. 1359, the coarse Tymochtee dolomite apparently retained chemical reactivity in the fluidized bed; consequently, as the dolomite content of the fluidized bed increased, the emission of SO_2 gradually decreased. The minimum SO_2 level in the flue gas, obtained at a Ca/S mole ratio of 1.6, corresponded to a reduction of 87% in SO_2 emission and a CaO utilization of 54%. These results are significantly better than those obtained with 25-μm limestone No. 1359 at similar Ca/S mole ratios.

The introduction of Tymochtee dolomite of 650-μm average particle size at a Ca/S mole ratio of 1.5 in a second experiment yielded a reduction in SO_2 emission of 78%, with a corresponding CaO utilization of 52%. The results with 650-μm dolomite particles are in good agreement with literature values [4] reported for a temperature of 1800°F. It should be recognized, however, that the dolomite contains a large fraction of magnesium carbonate (37%) that does not react with SO_2.

The Tymochtee dolomite additive used in the other two experiments in this series was −325 mesh. In one of these experiments, SO_2 removals were 45 and 69% at Ca/S mole ratios of 0.6 and 1.2, respectively, and in the other experiment SO_2 reductions were 66 and 83% at Ca/S mole ratios of 1.5 and 2.1, respectively. Calcium oxide utilizations ranged from 31 to 64% for Ca/S ratios of 2.1 to 0.6.

The observed effect of particle size for the Tymochtee dolomite on the reduction in SO_2 emissions was the inverse of that observed in earlier experiments at ANL using limestone No. 1359. That is, the use of −325 mesh particles of the dolomite resulted in poorer removals of SO_2 than when the larger sized particles (650-μm) were employed. The poorer SO_2 removal for the finer Tymochtee dolomite is evidently related to decreased solids residence time due to elutriation. In earlier work at ANL, the greater reactivity of fine limestone No. 1359 particles more than compensated for the increased elutriation.

The effectiveness of Tymochtee dolomite for SO_2 removal was compared with the effectiveness of limestone No. 1359. The dolomite particles had an average particle size of <44 μm, and the limestone particle size was 25 μm. Reaction conditions were a combustion temperature of 1600°F, a superficial gas velocity of 3 ft/sec, 10–20% excess air, a fluidized-bed depth of 2 ft, and feed rates giving a Ca/S mole ratio of 2.5 in the feed streams. SO_2 removals by these additives did not differ markedly.

2. Recycle of Elutriated Solids

As reported earlier (ANL-7675, p. 167), SO_2 removal was not increased by recycling a finely divided limestone-flyash mixture that had been elutriated from the bench-scale combustor. Increased SO_2 removal had been expected because of the additional reaction potential of the partially sulfated limestone in the elutriated solids. During those recycle experiments, all reaction was apparently due to the addition of fresh limestone, and SO_2 removal was the same as that in the absence of recycle. Laboratory-scale experiments were performed to compare the reactivity of partially sulfated limestone (elutriated with the flyash) with the reactivity of fresh limestone. Results showed that partially sulfated limestone contained in elutriated solids has a reactivity with SO_2 comparable to that of fresh limestone.

In an attempt to explain the discrepancy between the poor reactivity of recycled fines in the combustor and the normal reactivity of similar fines in laboratory-scale experiments, the extent of sulfation and calcination of material in the final alumina bed and of material in the overhead was determined by analysis of solids streams from SA-series experiments. The materials and conditions for this series of experiments are given in Table VII-1. The results show that material retained in the fluid bed had the highest extent of CaO utilization (70%) and the greatest extent of calcination (~100%). Material collected in the primary cyclone had the lowest CaO utilization (18%) and also the lowest extent of calcination (~75%). Material collected in the secondary cyclone was intermediate (CaO utilization of 43% and calcination of ~90%). Table VII-1 presents values for CaO utilization.

The low values for both sulfation and calcination for material collected in the cyclones suggest that these materials were blown through the bed with little time for reaction and had a brief residence time. These results lend support to the belief that the lack of additional SO^2 removal when elutriated fines are recycled to the combustor is due to the short residence time of the fines in the bed.

TABLE VII-1. Extent of Reaction of CaO in Various Solids Streams, Expts. SA-1 to SA-4

Additive, Limestone No. 1359: 25 μm SA-1 and SA-2
103 μm SA-3 and SA-4

Combustion Temperature: 1550°F SA-1 and SA-4
1650°F SA-2 and SA-3

Expt.	Solids Stream Sampled	No. of Samples	Range of Ca/S Mole Ratios	Avg Ca/S Mole Ratio	Avg CaO Utiliz. (%)
SA-1	Fluid Bed	5	1.2–2.0	1.5	67
	Primary Cyclone	5	4.0–6.5	5.3	19
	Secondary Cyclone	2	2.0–2.3	2.2	45
	Final Filter	1	-	1.3	77
SA-2	Fluid Bed	6	1.3–1.4	1.4	71
	Primary Cyclone	4	4.8–7.2	6.3	16
	Secondary Cyclone	3	1.8–3.0	2.6	38
	Final Filter	1	-	1.6	62
SA-3	Fluid Bed	5	1.3–1.5	1.4	71
	Primary Cyclone	4	1.5–6.3	4.1	24
	Secondary Cyclone	4	2.0–2.5	2.2	45
	Final Filter	1	-	0.7	>100
SA-4	Fluid Bed	3	1.3–1.4	1.4	71
	Primary Cyclone	4	4.8–11.8	7.1	14
	Secondary Cyclone	4	1.8–3.4	2.4	42

3. Removal of Nitrogen Oxides

Nitrogen oxides, principally nitric oxide (NO), are formed during the combustion of fossil fuels and are a major contributor to air pollution. The quantities of NO observed in the flue gas from high-temperature combustors can be accounted for by the equilibrium of the nitrogen-fixation reaction, $1/2\,N_2 + 1/2\,O_2 \rightleftharpoons NO$, between the nitrogen and oxygen in the combustion air.

The potential of fluidized-bed combustion of natural gas as a means of reducing NO emission was investigated. The level of NO was a major item of investigation. Because a relatively low combustion temperature (1600°F) is feasible in fluidized-bed combustion of natural gas, NO content of the flue gas is held to the level dictated by the nitrogen fixation equilibrium, about 60 ppm.

The NO concentration has been observed to be lowered when limestone was added to the fluidized bed in earlier coal-combustion experiments (see ANL/ES-CEN-1002). The NO concentration was lowered by as much as 40% of its original concentration concomitantly with a reduction in SO_2 concentration.

An additional series of coal-combustion experiments has been performed in which changes in nitric oxide concentration during the addition of limestone to a fluid-bed combustor were observed. The greatest reduction in NO emission (from an initial concentration of about 600 to 200–300 ppm) was achieved when the initial fluid bed was composed entirely of limestone. An interesting observation pertaining to NO removal when limestone was added was that NO concentration did not decrease immediately, but only after SO_2 removal had occurred. This suggests that the sulfate formed by the reaction between SO_2 and limestone may be responsible for NO removal. That calcium sulfate influences the reduction of NO concentration is also apparently indicated by results obtained with Tymochtee dolomite, for which the extent of NO removal was inversely proportional to the Ca/S mole ratio in the feed. With lower Ca/S mole ratios in the feed, higher concentrations of $CaSO_4$ in the bed would be expected.

Catalytic decomposition was considered as a means of reducing nitric oxide emission. However, in coal-combustion experiments, metal oxides (Al_2O_3, Co_3O_4, and ZrO_2) were not effective as catalysts for the decomposition of NO. In fact, when Co_3O_4 was tested, NO concentration in the flue gas increased.

4. Removal of Added SO_2 in Natural Gas Combustion Experiments

In other natural-gas combustion experiments, artificially generated SO_2 was reacted with limestone at 1600°F. The SO_2 removals were 95 to 99% at a low Ca/S mole ratio of 1.5. These excellent results were probably due to efficient distribution of the injected SO_2 in the combustor (as compared with coal combustion experiments) and to an ash-free environment. Although combustion efficiencies for natural gas were only 94–99% in our equipment setup, a combustion efficiency greater than 99% can undoubtedly be achieved by more efficient distribution of natural gas in the fluidized bed.

5. Electron Microprobe Examination of Particle Composition

Samples of partially reacted limestone particles from bench-scale combustor experiments have been examined for calcium, magnesium, and sulfur by electron microprobe

analysis. An objective was to determine, if possible, the mode of reaction responsible for differing SO_2 removals in natural gas and coal combustions. By electron microprobe analysis, clear maps of element distribution in the particles were obtained. A typical scan is shown in Fig. VII-3.

Examination of elutriated particles from combustion experiments showed that in samples from coal-combustion experiments, the sulfur concentration usually decreased at increasing distance from the surface of the particle. For samples obtained in natural-gas experiments, sulfur concentrations appeared to be more uniform throughout the particles. Few particles exposed to either mode of combustion showed the calcium and sulfur levels that would be observed if CaO were completely converted to $CaSO_4$. Other particles, mainly from the natural-gas combustion experiment, had the calcium concentrations of $CaCO_3$, indicating that little calcination or sulfation had occurred. Although the information obtained on distributions of these elements in particles has not shed additional light on the physical or chemical mechanisms involved in the sulfur sorption process during combustion, the capability of examining particles from combustion solids streams (bed material and overheads) for specific components by an electron microprobe has been demonstrated. Controlled experiments with a small number of particles may allow the mode of the reaction mechanism to be determined by this technique.

6. Desorption of SO_2 from Sulfated Limestone

In other work, it was noted that when a bed of partially reacted limestone was heated, desorption of SO_2 commenced at slightly above 1700°F. At 1850°F with the excess air level in the feed resulting in only 1 vol % oxygen in the flue gas, SO_2 concentration in the flue gas was unexpectedly high, 5000 ppm. This degree of SO_2 desorption at a relatively low temperature (previously, a temperature of about 2200°F had been thought necessary to obtain this effect) may have been a result of partial reducing conditions in the bed at the low excess-air level employed.

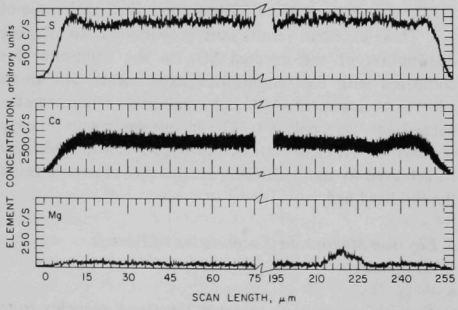

Fig. VII-3. Electron Microprobe Trace of Sulfated Limestone Particle (Experiment AR-2, bed sampled at 20th hour). ANL Neg. No. 308-2565.

7. Relationship of SO_2 Removal to Design of Bench-Scale Equipment

The maximum effective reduction in SO_2 emission obtainable with a coal feed in our bench-scale equipment appears to be ~95% with Ca/S mole ratios in the feed of 4.5 and higher. The apparent maximum SO_2 removals, demonstrated at very high Ca/S ratios when fresh beds of limestone were sulfated, were 94 and 96%. These SO_2 removals are probably not absolute limits but rather reflect combustor-design considerations such as the location of the coal injection port. For example, in the combustion of natural gas with fine limestone No. 1359 (25 μm) additive and with SO_2 from an external source injected at the preheater so that it was well mixed with the fluidization air, essentially 100% SO_2 removal was achieved; however, when SO_2 was injected at the regular coal-feeding port, 92 and 95% reductions in SO_2 emission were achieved. These results show that a procedure of using additive for SO_2 control in fluidized beds is capable of achieving 100% reduction in SO_2 emission, and that the maximum reduction in SO_2 emission may have been limited to ~95% in our bench-scale experiments because of design features.

8. Modeling Study on Coal Feeding

A modeling study is under way to predict the effects of nonuniform feeding of coal on localized reducing or oxidizing conditions at points within and above a fluidized-bed combustor. Mathematical models have been developed for predicting concentration gradients within the bed for coal injection at the base of the bed and for horizontal-jet coal injection and deep penetration into the bed. Application to the operating conditions anticipated for a large fluidized-bed coal combustor showed that coal concentration in the bed is more uniform if coal in injected as a horizontal jet with deep penetration into the bed than if coal is injected at the base of the bed.

B. BASIC MECHANISMS OF FLUIDIZATION

(J. D. Gabor, J. Hepperly)

Fluidized-bed reactors offer the advantages of good heat-transfer rates and good particle mixing for gas-solid reactions. These properties of the fluidized bed are the result of complex fluid dynamics associated with the gas bubbles rising in the bed. Although fluidization has proved to be a useful technique in many chemical processes, many uncertainties remain relative to reactor scale-up and alterations of reactor geometry. The effects of finite bed dimensions on the fluid dynamics of a bed when bubbles

rise through the bed have been investigated [5], as well as the relationship of fluidized-particle residence time to wall-to-bed heat transfer.

1. Fluid Dynamics for a Bubble Rising in a Finite Two-Dimensional Fluidized Bed

Theoretical treatments by other workers have opened the way to a mechanistic approach for fluidized-bed design. The previous work considered the fluid dynamics for bubbles rising in either an infinite or a semi-infinite fluidized bed. Obviously, actual fluidization is conducted with beds of finite dimensions. Since the effects of a finite bed on the fluid dynamics associated with a rising bubble had not been theoretically examined, a theoretical study was made for a bubble rising in a two-dimensional fluidized bed of finite width and height. Two-dimensional fluidization occurs in a rectangular column for which the thickness is so small that a rising bubble is simultaneously in contact with both opposite walls. The results of this study should qualitatively apply to three-dimensional fluidization [6,7].

The effects of finite dimensions, as predicted from the theoretical analysis [5], are summarized as follows:

1) The circulation pattern of bed particles, as a result of a bubble rising in a finite fluidized bed, is upward at the column center and downward near the column walls.

2) Particle movement is primarily in the vertical direction; horizontal particle movement occurs at the bottom and top boundaries of the bed.

3) The side walls and the top and bottom boundaries of the bed have a compressive effect on the gas cloud that surrounds a rising bubble. The compressive effect increases with a decrease in the ratio of bubble velocity to interstitial gas velocity.

These effects are in agreement with experimental observation and must be considered in reactor scale-up.

2. Basic Mechanisms of Fluidized-Bed Heat Transfer

The objective of this study is to develop a generalized correlation for the rate of heat transfer between a surface and a fluidized bed. As the initial step in this study, a model [8] has been proposed for heat transfer from a wall to particles moving past a heater within a fluidized bed. In this model, the two phases of the particulate bed are represented by a series of alternate slabs of gas and solids. The heat-transfer coefficients predicted with this model were in good agreement with reported data for moving packed beds. It was assumed that the characteristics of particles in moving packed beds are similar to those of particles moving past a heater in a fluidized bed. However, since the model was developed for packed beds, experimental verification for fluidized beds was needed.

While the bed was at the point of minimum fluidization, bubbles were periodically injected into a bed to cause particle motion, and measurements were made relating the heat-transfer coefficient to the fluidized-particle residence time at a heater surface. These measurements were made with two different columns. One was a 4-in.-dia semicylindrical column constructed so that particle movement at the extremities of a flat glass surface could be photographed through the glass surface, while simultaneously making measurements of the heat-transfer rate from a heater (1 in. by 1 in.) mounted in the curved brass portion of the column opposite the flat glass surface. Half-bubbles, which rose along the center of the glass face, were formed by injecting air at the base of the glass surface. It was assumed that the bubble (and hence particle movement) was axisymmetric. It could then also be assumed that particle movement at the extremities of the flat face (near the curved portion of the column) was identical to particle movement near the heater surface.

The second column used in this investigation was a 4-in.-dia cylinder. The heater (2 in. high by 1 1/2 in. wide) was mounted in the column wall and was interchangeable with a window that allowed photographic observation. With this column, particle residence times and heat-transfer rates could not be determined simultaneously as with the first column. Separate runs had to be made at the same fluidization conditions to obtain both the heat-transfer rates (with the heater mounted in the column wall) and the particle residence times (with the window mounted in the column wall). Measurements made with the cylindrical column were compared with the results for the semicircular column to test the assumption that particle movement is axisymmetric in the semicylindrical column. The particle movement for both columns was photographed with a Milliken Model DBM-5 motion picture camera [9] at 120 frames per second.

Heat-transfer coefficients as a function of particle residence time were measured for glass beads with 1.51×10^{-3}-ft and 1.17×10^{-3}-ft diameter and copper shot with 1.93×10^{-3}-ft diameter. The data were plotted in terms of hd (where h is the heat-transfer coefficient and d is the particle diameter) versus t/d^2 (where t is the particle residence time). In Fig. VII-4, the data for the glass particles are compared with the values predicted by the alternate slab model, and in Fig. VII-5, the data for copper particles are compared. The heat-transfer data for glass and copper particles fall near the curves (solid lines) predicted by the alternate slab model. The data for the glass and copper particles verify that the alternate slab model, which was originally used to make comparisons with moving-bed data, is applicable to fluidized beds. The data scatter is approximately the same as that for the reported data for moving packed beds. The data for heat transfer by glass beads in the cylindrical and semicylindrical columns are in agreement, verifying the assumption that axisymmetric particle movement occurs in the semicylindrical column. The semicylindrical column can serve as a useful tool in

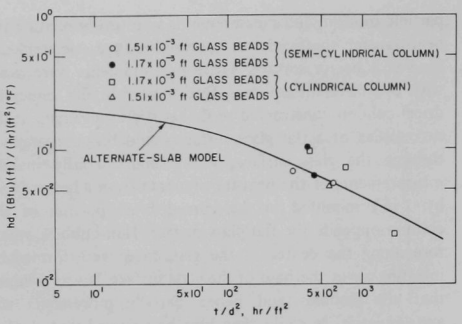

Fig. VII-4. Comparison of Data for Glass Particles with Alternate-Slab model. ANL Neg. No. 308-2566.

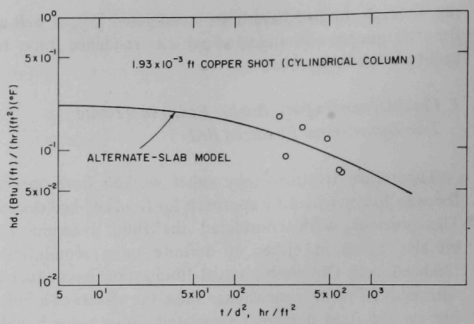

Fig. VII-5. Comparison of Data for Copper Particles with Alternate-Slab Model. ANL Neg. No. 308-2567.

future work in which particle residence times will be related to bed-bubbling conditions.

The ultimate goal of this study is to obtain a generalized heat-transfer correlation. The heat-transfer coefficient has been related to the particle residence time. The next step is to relate the particle residence time to the bubbling conditions. The final step is to determine the effect of geometry of the gas distributors and column on the bubbling conditions in the bed.

REFERENCES AND FOOTNOTES

1. A summary of this section is given on pp. 13 to 14.
2. A. A. Jonke, E. L. Carls, R. L. Jarry, L. J. Anastasia, M. Haas, J. R. Pavlik, W. A. Murphy, C. B. Schoffstoll, G. N. Vargo, "Reduction of Atmospheric Pollution by the Application of Fluidized-Bed Combustion, Annual Report, July 1969–June 1970." ANL/ES-CEN-1002 (1970).
3. The time required to reach steady state is a function of bed weight and limestone feed rate. Calculations indicated that 95% of steady-state composition would be achieved in 2 1/2 bed changes, and that each bed change would require about 25 hr.
4. C. W. Zielke, H. E. Lebowitz, R. T. Struck, E. Gorin, "Sulfur Removal During Combustion of Solid Fuels in a Fluidized Bed of Dolomite," Abstracts of Papers, American Chemical Society 158th National Meeting in New York, September 11–12, 1969, Paper Fuel 026.
5. J. D. Gabor, "Boundary Effects on a Bubble Rising in a Finite Two-Dimensional Fluidized Bed," *Chem. Eng. Sci. 26*, 1247 (1971).
6. J. D. Gabor, "Interaction Effects on the Fluid Dynamics of Bubbles in a Fluidized Bed: Chain of Rising Bubbles in an Infinite Two-Dimensional Medium," *Ind. Eng. Chem. Fundamentals 8*, 84 (1969).
7. J. D. Gabor, L. B. Koppel, "Interaction Effects on the Fluid Dynamics of Bubbles in a Fluidized Bed: Chain of Rising Bubbles in an Infinite Three-Dimensional Medium," *Chem. Eng. Progr. Symp. Ser.*, No. 105, *66*, 28 (1970).
8. J. D. Gabor, "Wall-to-Bed Heat Transfer in Fluidized and Packed Beds," *Chem. Eng. Progr. Symp. Ser.*, No. 105, *66*, 76 (1970).
9. Manufactured by D. B. Milliken Company, Arcadia, California.

ARGONNE NATIONAL LAB WEST
3 4444 00010839 9

B